Evaluation of Wettability and EOR Potential of Shale and Tight Formations

by

Mahmood Reza Yassin

A THESIS SUBMITTED IN PARTIAL FULFILLMENT OF
THE REQUIREMENTS FOR THE DEGREE OF

DOCTOR OF PHILOSOPHY

in

Petroleum Engineering

Department of Civil and Environmental Engineering

UNIVERSITY OF ALBERTA

© Mahmood Reza Yassin, 2019

Abstract

During the last decade, low-permeability unconventional reservoirs have been rapidly developed using horizontal drilling and multistage hydraulic fracturing. Despite high extent of unconventional resources, typically less than 10% of the initial oil in place (IOIP) can be recovered. This shows that complementary technologies are needed to increase the recovery percentage of IOIP. An example is enhanced oil recovery (EOR) technology. Field and laboratory results suggest that rock/fluid interactions in unconventional rocks can significantly influence well performance. The extent of this influence depends on rock wettability, reservoir conditions, and fracturing fluid formulation. Evaluation of wettability provides valuable information about 1) the low oil recovery factor of unconventional wells, 2) the location of the residual trapped oil, and 3) the potential EOR technique to produce the residual trapped oil.

This study first aims at investigating wettability of organic-rich shales of the Duvernay Formation. We recognize the key parameters controlling the wettability of shale samples and identify the location of the residual trapped oil. Using the concept of dual-wet pore network proposed in this thesis, we develop new experimental approaches for pore size distribution of unconventional rocks as well as mathematical models for two-phase gas/water relative permeability. We use tight siltstone samples of the Montney Formation to develop relative permeability curves for dual-wet rocks. Then, this study presents the experimental results of CO_2-EOR tests using a custom-designed visual cell. It also explains the principal mechanisms controlling CO_2-assisted oil recovery from dual-wet rocks.

Investigating wettability of the Duvernay shale plugs shows higher oil uptake than brine uptake. The higher oil uptake suggests that there are abundant water-repellant pores with strong affinity to

oil. Scanning electron microscopy (SEM) and energy-dispersive x-ray spectroscopy (EDS) show two different pore networks in shale sample. We observe 1) large micropores bordered by inorganic minerals such as quartz, calcite, and clays and 2) abundant small nanopores within the organic matter; forming a dual-wet/dual-porosity medium. Abundant organic pores with hydrophobic characteristics explain strong oil-wetness of the shale samples, confirmed by the positive correlation of effective porosity with total organic carbon (TOC) content.

Exploring wettability of dual-wet shales from different hydrocarbon windows indicates that besides TOC content, wettability has functional dependency on kerogen maturity level. SEM images of highly mature samples (gas window) show higher number of organic pores compared with less mature samples (oil window). It is expected to see higher oil uptake in the samples with higher TOC content. However, we observe the opposite trend in less mature shales which is explained by the poorly-developed organic pores that hinder oil uptake.

Based on the concept of dual-wet pore network, brine is the wetting and non-wetting phases in inorganic and organic pores, respectively. We use this concept and estimate inorganic and organic pore size distributions by conducting spontaneous and forced imbibition, respectively. The results indicate that cumulative pore space filled by brine is about three times higher than that in mercury injection capillary pressure (MICP). Furthermore, minimum pore-throat diameter detected in MICP test is 3.8 nm. This parameter is 1.2 nm in forced brine-imbibition test, indicating the capability of brine for characterizing smaller pore-throat sizes compared with Mercury.

The concept of gas/water relative permeability for dual-wet rocks is proposed to account for the organic nanopores inaccessible for water. By increasing the fraction of organic pore space (S_{org}) in our model, gas relative permeability decreases, for a fixed water saturation. Because by increasing S_{org}, the average size of pores for gas mobility and gas relative permeability are reduced.

The results of wettability tests demonstrate that significant volume of oil is mainly trapped in organic nanopores. Imbibition oil recovery by brine is very low (less than 7%), indicating the weak affinity of oil-saturated plugs for brine imbibition. However, supercritical CO_2 (at 2000 psig and 122^oF) can diffuse into the oil-saturated dual-wet plugs and produce about 80% of oil, indicating the significantly high potential of supercritical CO_2 for recovering residual oil trapped in organic nanopores.

Supercritical CO_2 recovers the oil in a three-step process including 1) CO_2 dissolution into the oil, 2) oil expansion, and 3) extraction (vaporization) of the oil expelled from the shale plug. The results of CO_2/oil bulk-phase tests indicate that supercritical CO_2 can rapidly dissolve into and expand the oil due to 1) extracting and condensing flows at the CO_2/oil interface and 2) density-driven convection within the bulk oil phase.

Preface

This thesis is an original work by Mahmood Reza Yassin. All or parts of Chapters 2 to 7 have been published as peer-reviewed papers or submitted for peer review and publication. I was responsible for conducting laboratory tests, model development as well as writing and editing these papers. My co-authors were responsible for conducting part of laboratory tests, analyzing scanning electron microscopy (SEM) images, computer programming, reviewing the manuscript drafts, and providing useful comments and discussions.

Chapter 2 has been published as Yassin, M. R., Begum, M., & Dehghanpour, H. (2017). Organic Shale Wettability and Its Relationship to Other Petrophysical Properties: A Duvernay Case Study. International Journal of Coal Geology.

Chapter 3 has been submitted (under review) as Begum, M., Yassin, M. R., & Dehghanpour, H. (2019). Effect of Kerogen Maturity on Organic Shale Wettability: A Duvernay Case Study. Marine and Petroleum Geology.

A part of Chapter 4 (modeling spontaneous-imbibition process in Appendix A) has been published as Shi, Y., Yassin, M.R., Yuan, L., & Dehghanpour, H. (2019). Modelling imbibition data for determining size distribution of organic and inorganic pores in unconventional rocks. International Journal of Coal Geology.

Chapter 5 has been published as Yassin, M. R., Dehghanpour, H., Wood, J., & Lan, Q. (2016). A Theory for Relative Permeability of Unconventional Rocks with Dual-Wettability Pore Network. SPE Journal.

Chapter 6 is ready for submission as Yassin, M. R. & Dehghanpour, H. (2019). Advances in Understanding CO_2/Shale Oil Interactions.

Chapter 7 has been published as Yassin, M.R., Habibi, A., Zolfaghari, A., Eghbali, S. & Dehghanpour, H. (2018). An Experimental Study of Nonequilibrium Carbon Dioxide/Oil Interactions. SPE Journal.

Dedicated to my lovely parents Ehteram and Ahmad

&

All my dear sisters and brothers.

Acknowledgements

I would like to express my gratitude and respect to my supervisor, Dr. Hassan Dehghanpour for his continuous support and guidance throughout my PhD program. I have always enjoyed working with him and I appreciate him for all academic and life lessons that he taught me during this time. I am forever indebted to him.

The efforts made by Dr. Rick Chalaturnyk, Dr. Murray Gingras, Dr. Selma Guigard, and Dr. Nobuo Maeda as my internal examiners from the University of Alberta as well as Dr. Matthew Balhoff as my external examiner from the University of Texas at Austin are gratefully acknowledged.

Support from Encana Corporation, Cenovus Energy, Athabasca Oil Corporation, Natural Resources Canada (NRCan), Future Energy Systems (FES), and the National Sciences and Engineering Research Council of Canada (NSERC) for providing field data and funding this study is gratefully acknowledged. I am grateful to James wood, Lindsay Dunn, Donald Bryan, and Glenn Karlen for their fruitful discussions and insightful guidance.

I would like to appreciate my colleagues (Ali Habibi, Ashkan Zolfaghari, Yue Shi, Momotaj Begum, Sara Eghbali, Qing Lan, Yanmin Xu, Obinna Daniel Ezulike, Yingkun Fu, Mingxiang Xu, and Lin Yuan), for their valuable help and contributions. I would like to thank Todd Kinnee, for the valuable guidance and support on designing and testing the experimental setup. Also, I appreciate the help of some administrative staff members of the civil and environmental engineering department (Trina Cattral, Arlene Figley, and Anne Jones).

Table of Contents

List of Tables

List of Figures

Chapter 1
General Introduction

1.1 General Overview of Unconventional Resources

Unconventional resources including organic-rich shale oil and shale gas have been considered as potential reserves across the world. Extraction of hydrocarbon from shale rocks in the US is considered as one of the landmark events in this century (Wang et al., 2014). The best way to define unconventional resources is to review the resource triangle (Fig. 1.1) developed by John Masters. While his exploration company (Canadian Hunter Exploration) was searching for tight gas in the deep basin of Alberta, conventional gas in the high-permeability conglomerates was also discovered. The concept of resource triangle is that all natural resources are distributed log-normally in nature. Conventional and unconventional resources are mapped at the top and base of the triangle, respectively (Fig. 1.1). Conventional resources with good reservoir quality are easy and less-expensive to exploit. However, initial hydrocarbon in place is limited. By going deeper into the base of resource triangle, there are unconventional reservoirs with vast initial hydrocarbon in place but ultralow permeability (< 0.1 mD). Better technologies and more capital are needed to exploit the unconventional resources (Ahmed and Meehan, 2016).

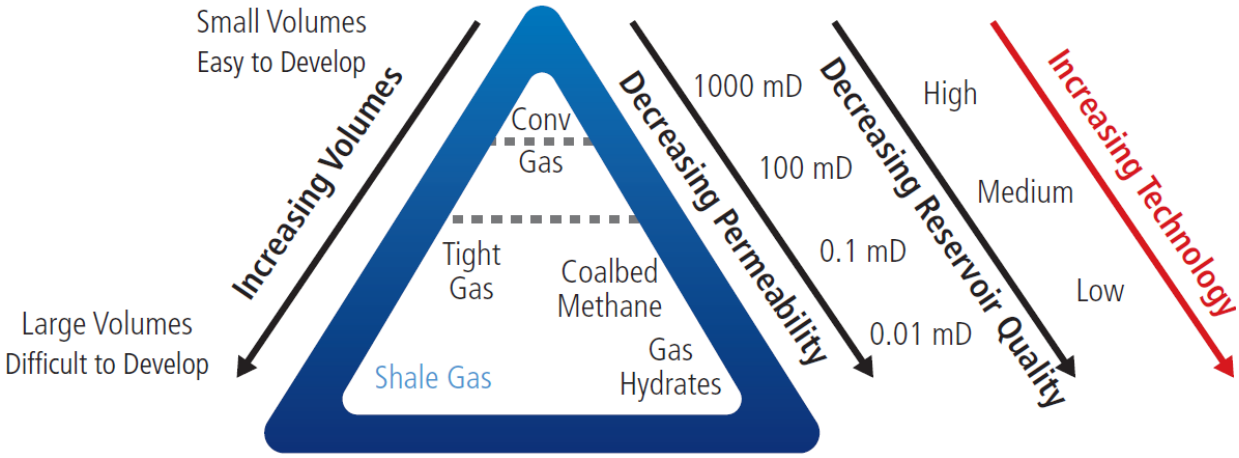

Fig. 1.1: The resource triangle (Ahmed and Meehan, 2016).

Fig. 1.2 shows the location of most prospective shale oil and shale gas formations in 41 countries. This map highlights the abundance of unconventional resources worldwide, consistent with the base of the resource triangle shown in Fig. 1.1. According to the US Energy Information Administration (EIA) report, 345 billion barrels of shale oil technically recoverable resources (TRR) and 7,299 trillion cubic feet (Tcf) of shale gas TRR exist in the world. The US and Canada are among the biggest unconventional producers. Shale oil and shale gas TRRs in the US are 58 billion barrels and 665 Tcf, respectively. In Canadian basins, shale oil and shale gas TRRs are 9 billion barrels and 573 Tcf, respectively (Ahmed and Meehan, 2016).

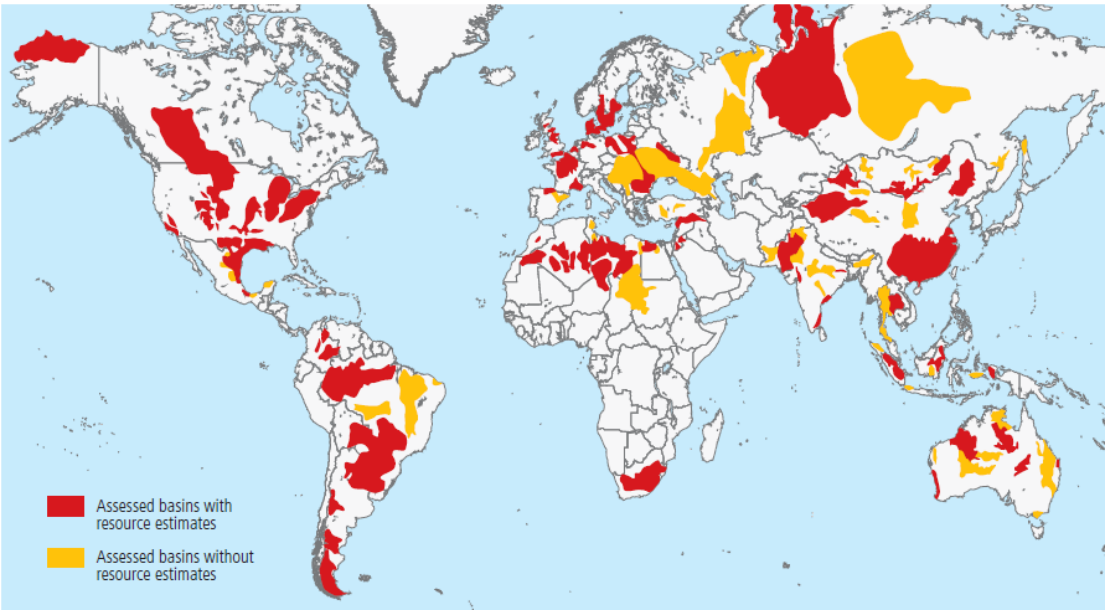

Fig. 1.2: Map of basins with assessed shale oil and shale gas formations (Ahmed and Meehan, 2016).

These unconventional rocks with ultralow permeability can produce hydrocarbons at economic rates through 1) horizontal wells and 2) multistage hydraulic fracturing (Fig. 1.3). After successful gas recovery from Barnett shale (2003), these two key elements were called US model for shale development (Ahmed and Meehan, 2016). The horizontal well has a lateral length up to 3,000 m, which can increase the contact area with shale rock. However, hydrocarbon production does not initiate economically unless the contact area is increased to a much higher value. To do this, a large volume of fracturing fluid (up to 70,000 m^3 in total) comprised of water, proppants, and chemicals is injected at high pressures, creating hydraulic fractures and new pathways. The injection of fracturing fluid is conducted in separate stages (multistage) along the horizontal section of the wellbore. Once a complex fracture network is created, hydrocarbon production from shale rock begins.

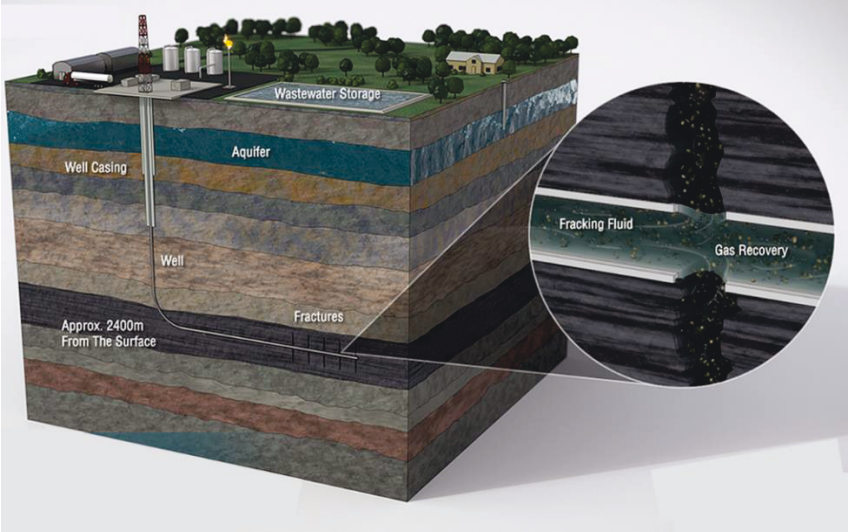

Fig. 1.3: Hydraulic fracturing of a horizontal well drilled in an unconventional reservoir (elarasystems).

Fig. 1.4 presents the total number of horizontal wells in the US. Shale boom started from 2008 and motivated the US industry to drill higher number of horizontal wells coupled with hydraulic fracturing. More than 110,000 horizontal wells were drilled till 2016 and about 18,000 new wells are drilled each year (EIA; Ahmed and Meehan, 2016).

Total cost of drilling, fracturing, and completion of an unconventional well depends on several factors such as true vertical depth, lateral length, well design, completion strategy, and location of the reservoir. The total cost of a fractured well may vary from 3.5 to 7.0 $ million for Barnett shale gas and Eagle Ford oil wells (both in the US), respectively (Ahmed and Meehan, 2016).

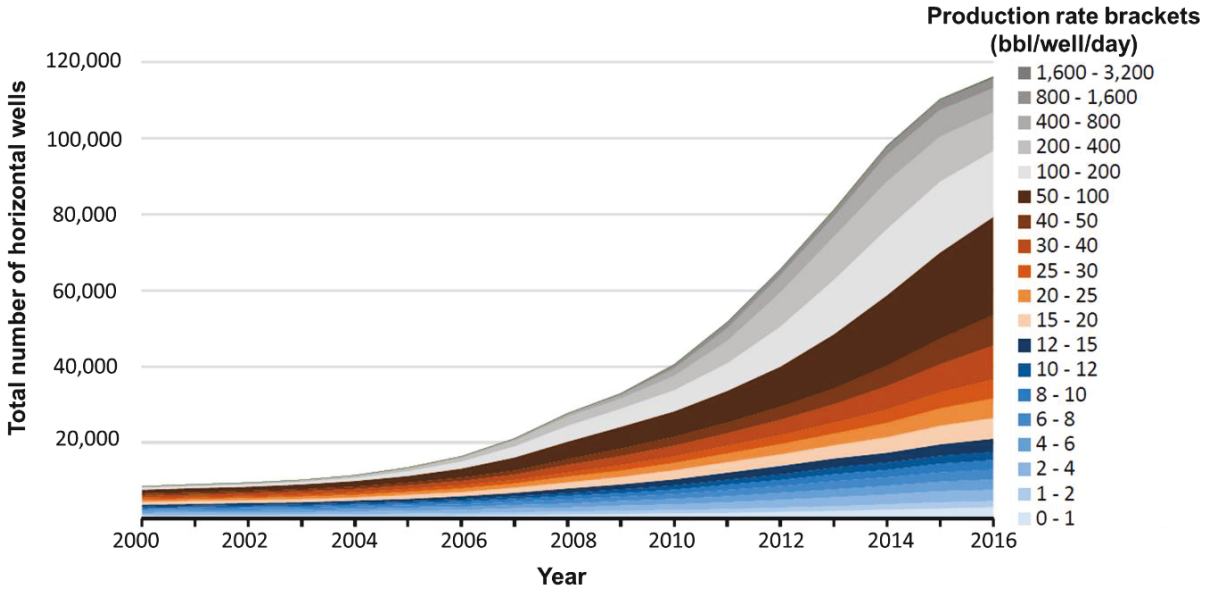

Fig. 1.4: Total number of horizontal wells in the US (Data from EIA)

1.2 Oil Recovery Factor of Unconventional Wells

Fig. 1.5 presents the typical oil production rate vs. time for a number of unconventional wells in the US. Initially, the production rate is high (Stage 1) and then declines to ~30% of initial rate just after one year (Stage 2). Fast rate decline in unconventional wells is attributed to fracture failure, fracture closure, fracture depletion, and depletion of the matrix adjacent to fracture face. After Stage 2, rate decline is less noticeable and oil rate reaches a relatively constant plateau for several years (Stage 3).

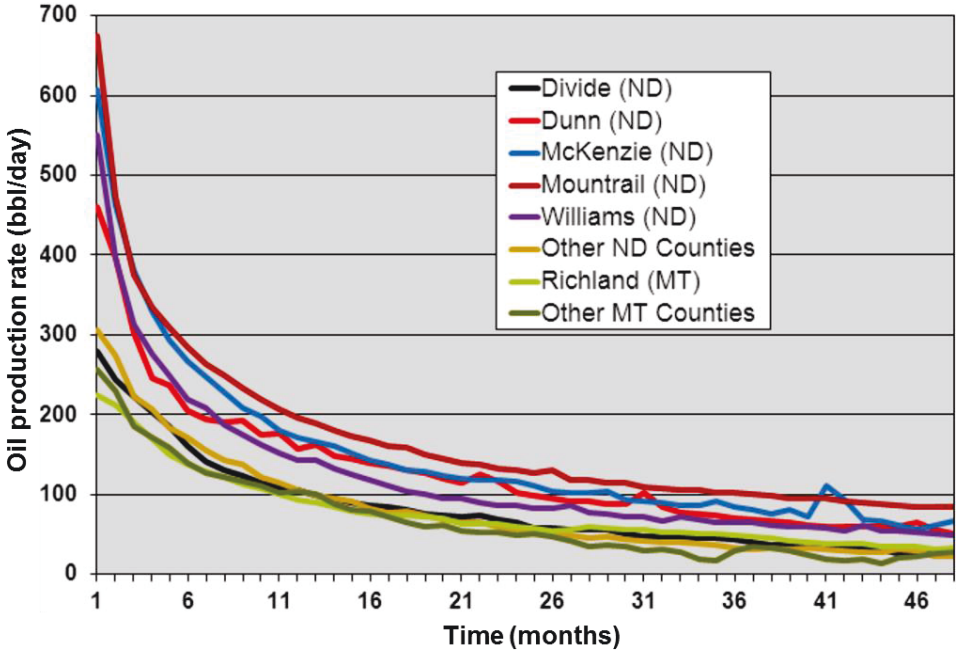

Fig. 1.5: Oil production rate vs. time in US unconventional wells (Data from Drillinginfo).

Rapid rate decline in unconventional oil wells results in a low estimated ultimate recovery (EUR), and subsequently in a low oil recovery factor (RF). Oil RF of unconventional wells is typically less than 10% of the initial oil in place (IOIP). Fig. 1.6 presents oil recovery factor of 19 Bakken wells, estimated by decline curve analysis (Clark, 2009). Most of the wells have oil RF < 10% and the average oil RF is 7%. Fig. 1.7 shows the oil RF distributions for 123 wells in the midland basin Wolfcamp (Barba, 2015). Oil RF is typically < 13% and the average oil RF is 8%.

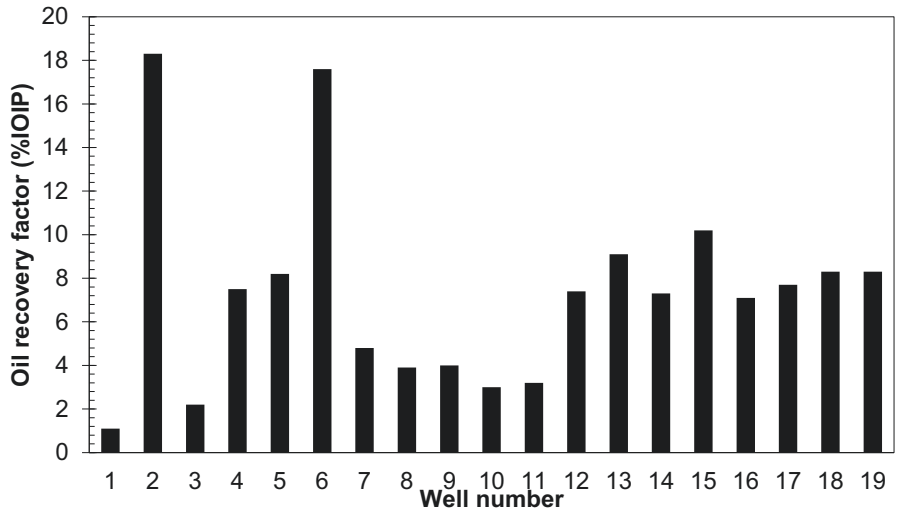

Fig. 1.6: Oil recovery factor of 19 wells in the Bakken Formation (Clark, 2009). Average oil recovery factor is 7% of initial oil place.

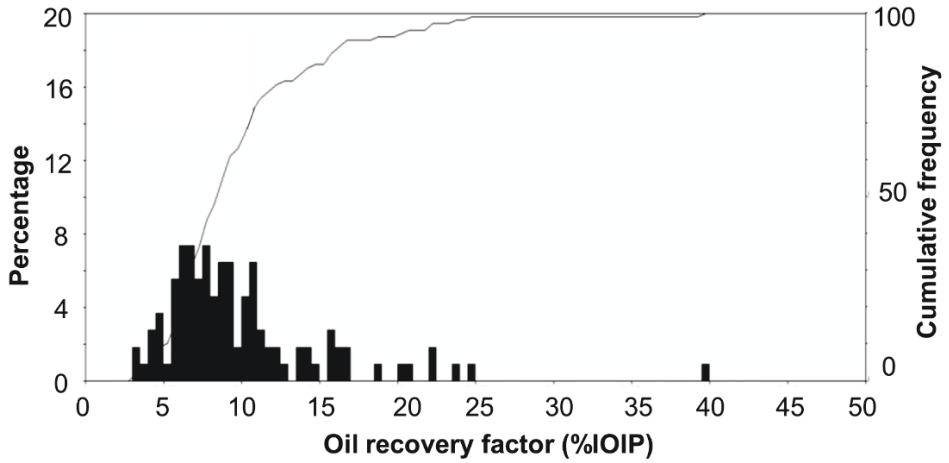

Fig. 1.7: Oil recovery factor distribution of 123 wells in the midland basin Wolfcamp (Barba, 2015). Average oil recovery factor is 8% of initial oil in place.

1.3 EOR Techniques

To compensate for the production loss due to rapid oil rate decline, the industry conventionally drills new wells and aggressively produces from them. As previously noted, drilling, fracturing, and completion of an unconventional well cost millions of dollars. A smarter cost-effective solution might be increasing the recovery factor of existing wells by 1) refracturing and/or 2) implementation of enhanced oil recovery (EOR) techniques.

There are primarily two reasons to refracture a well. One is to reopen the initial fracture network that has failed over a period of time. Another reason would be to connect the existing stimulated

reservoir volume to new sets of fractures by creating new pathways. Fracture failure may occur due to 1) closure, plugging, or degradation of fractures with time, 2) crushing the proppants, 3) production of proppants during flowback, and 4) improper selection of fracturing fluid (Ahmed and Meehan, 2016). Refracturing techniques are not investigated in this thesis.

EOR is defined as injection of a fluid for oil displacement from a matrix and reduction of residual oil saturation. Conventional well-to-well flooding of EOR fluid is not applicable in unconventional wells because of the ultralow permeability matrix that hinders fluid injection as well as the formation of oil bank. Therefore, cyclic (Huff-n-Puff) injection in a single fractured horizontal well is recommended. This process is composed of three steps: 1) injection of EOR fluid, 2) soaking the well for a certain period of time to allow interactions of the injected fluid with formation fluids, and 3) opening the well for hydrocarbon production. Fig. 1.8 presents a schematic of cyclic CO_2 injection in a fractured horizontal well.

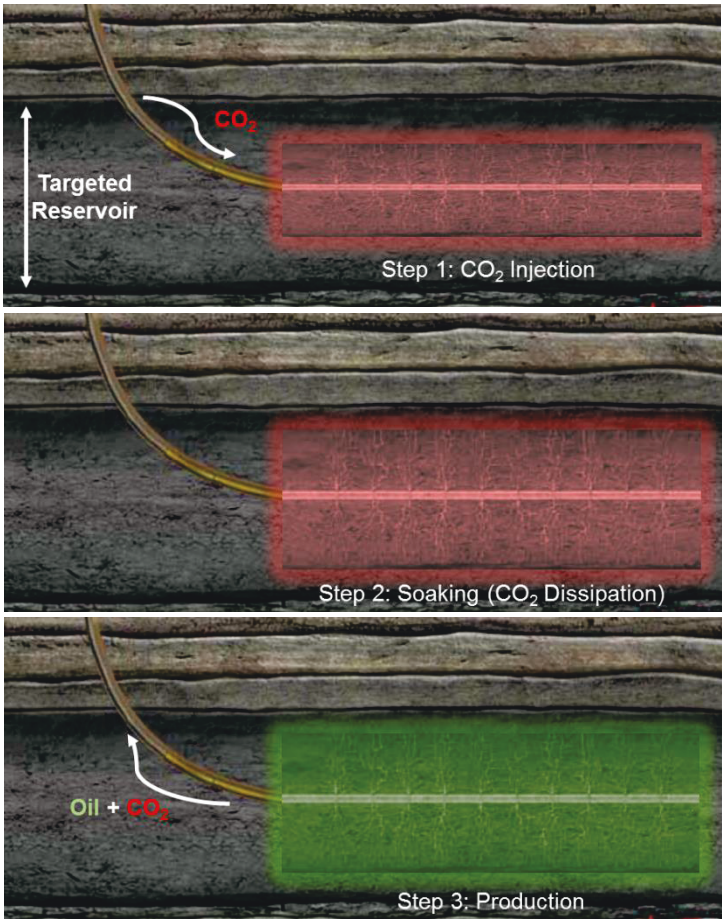

Fig. 1.8: Schematic of CO_2 cyclic (Huff-n-Puff) process in a fractured horizontal well (Revised after CSUR and Ezulike (2017)).

EOR techniques in unconventional wells are typically implemented in two different ways. In some cases, EOR fluid is injected as the fracturing fluid for creating the fracture network and also higher oil recovery upon opening the well (EOR while fracturing). Another option would be implementation of EOR years after fracturing the well and oil production; when oil rate is not economical anymore. Carpenter (2018) conducted a critical review of more than 70 studies and proposed three EOR techniques with the most promising potential for unconventional wells: 1) chemical methods, 2) smart water technique, and 3) gas injection.

1.3.1 Chemical Methods

Among different chemicals such as surfactant, polymer, and alkaline, surfactant injection is the most promising fluid to enhance oil recovery of North American liquid-rich reservoirs. These reservoirs are well-known as intermediate-wet to oil-wet. Surfactant solution can change wettability to water-wet conditions, which increases the affinity of matrix for water imbibition and displacement of oil into fractures. No one has investigated the applicability of polymer and alkaline in unconventional wells, due to injectivity problems and incompatibility with rock mineralogy, respectively.

1.3.2 Smart Water Technique

The results of recent studies show that maximum oil recovery can occur at optimum salinity of injected brine. Interfacial tension and wettability alteration are considered as two principal mechanisms for incremental oil recovery in smart water injection. Most of the experimental works and field case studies are focused on conventional high-permeability reservoirs.

1.3.3 Gas Injection

Gas injection is the most-investigated EOR technique in tight and shale reservoirs. CO_2, N_2, and enriched natural gas are among the candidates with the highest potential. However, the majority of studies have been conducted on the applicability of CO_2. Compared with methane and N_2, CO_2 has lower minimum miscibility pressure (MMP) with shale oil. CO_2 dissolution into oil can increase oil mobility by oil expansion and oil viscosity reduction mechanisms. The experimental and simulation studies show high performance of CO_2 for shale-oil EOR. However, enriched natural gas pilot tests outperform CO_2 pilot tests, indicating a lack of understanding of CO_2-related mechanisms at the field-scale.

1.4 Wettability

A key parameter that determines the performance of any EOR technique is wettability of the rock matrix. It describes the relative adhesion of two fluids to a solid surface. Wettability is an important rock/fluid property that affects primary oil recovery (Tiab et al., 1997), distribution of immiscible fluids at the pore scale, capillary pressure and relative permeability curves (Anderson, 1987a and 1987b), and water flood behavior (Morrow, 1987). In the next subsections, we describe the main differences between wettability of conventional and unconventional rocks.

1.4.1 Wettability of Rocks from Conventional Reservoirs

Wettability of unconventional rocks is typically categorized as 1) water-wet, 2) oil-wet, 3) intermediate-wet (neutral-wet), or 4) mixed-wet. In a water-wet brine/oil/rock system, brine fills the smaller pores and wets the major portion of the surfaces in the larger pores. If an oil-saturated water-wet rock is immersed in brine, brine spontaneously imbibes into the smaller pores and displaces the oil from the rock. If a brine-saturated oil-wet rock is immersed in oil, oil spontaneously imbibes into the smaller pores and displaces the brine from the rock. The system exhibits intermediate-wet behavior, if no preference is shown by the rock to either oil or brine (or both oil and brine equally wet the rock). The term “mixed-wet” refers to the condition where the larger pores of the rock are oil-wet, but the smaller pores are occupied by brine and are water-wet (Tiab et al., 1997).

The chemical compositions of the rock surfaces (mineralogy) and the fluids determine the values of surface forces, and thus wettability. The mineralogy of the rock surface contributes to the overall wettability of the rock/fluid system. By examining the chemical structures of key minerals, the wetting affinity of sandstones and carbonates to brine and crude oil are explained (Tiab et al., 1997).

1.4.2 Wettability of Rocks from Unconventional Reservoirs

Fig. 1.9a shows a scanning electron microscopy (SEM) image of a siltstone sample from the Montney tight-gas Formation, located in the Western Canadian Sedimentary Basin (WCSB). We observe that the rock is composed of 1) inorganic minerals, which are primarily quartz and illite, 2) organic matters, which are predominantly degraded bitumen/pyrobitumen, and 3) multiscale pores within the inorganic and organic parts. In general, the pores can be divided into relatively

large micropores and small nanopores. Micropores are predominantly between inorganic minerals, whereas the nanopores are mainly within the organic matter. Fig. 1.9b shows the magnified view of nanoscale pores within the organic matter of a Montney sample. Similarly, Figs. 1.9c and 1.9d show inorganic and organic pores of a Duvernay shale sample (in WCSB), respectively. The large inorganic pore is bordered by the inorganic minerals such as quartz, calcite, and feldspar/clay; while the organic pores with nanoscale size are within the organic matter of Duvernay sample.

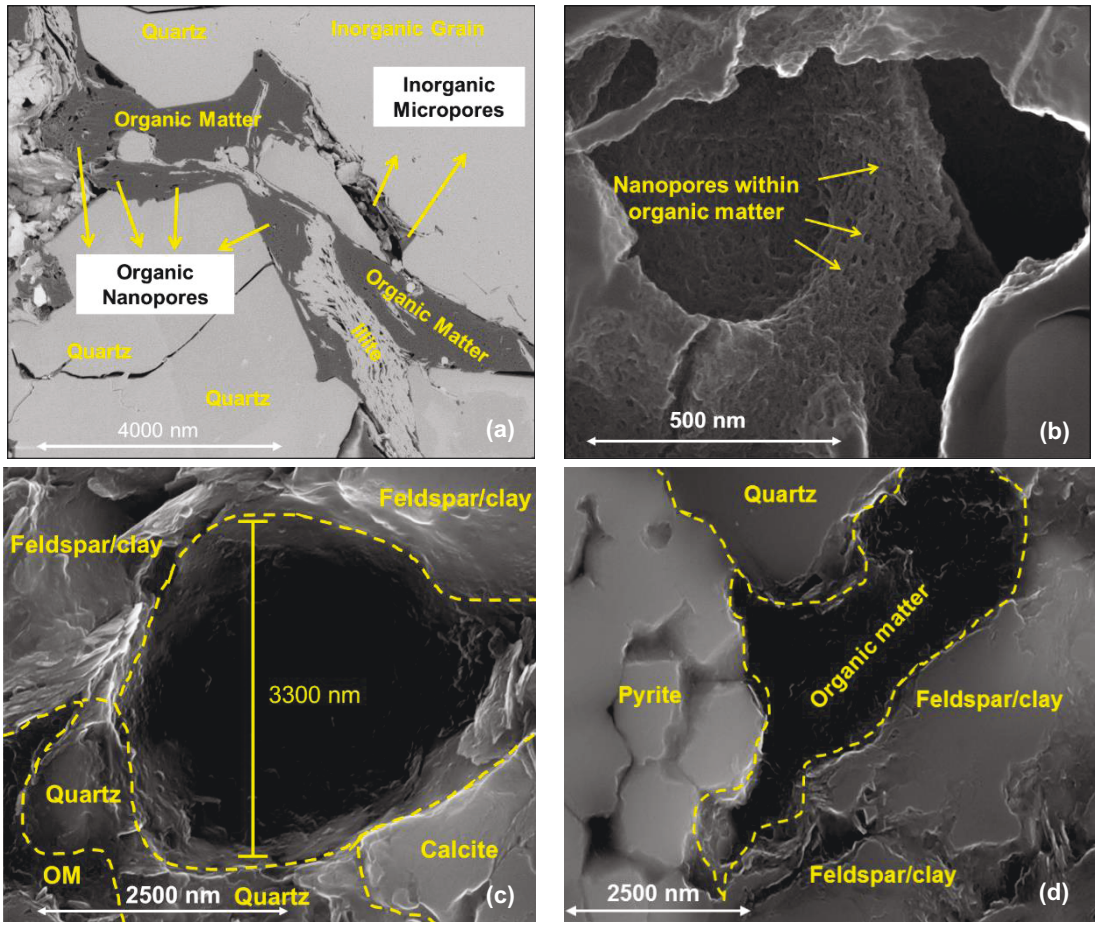

Fig. 1.9: SEM images of (a) a Montney sample (After Yassin et al., 2016), (b) organic pores of a Montney sample (After Wood et al., 2015), (c) inorganic pore of a Duvernay sample, and (d) organic pores of a Duvernay sample (After Yassin et al., 2017). The inorganic pores are bordered by inorganic minerals, and are larger than the organic pores within organic matter (OM).

In an air/liquid/rock system, organic matter is hydrophobic and is expected to have low wetting affinity to brine (Mitchell et al., 1990). Conversely, the inorganic part can be hydrophilic with preferentially high wetting affinity to brine, especially when clay minerals are present (Chenevert, 1970; Hensen and Smit, 2002). The presence of inorganic and organic pores with different wetting affinities and sizes makes a dual-wet/dual-porosity system.

The presence of hydrophobic nanopores within organic matter might be considered as the main difference between pore network of unconventional and conventional rocks. Fig. 1.10 presents SEM images of shale samples obtained at different locations worldwide. The organic nanoscale pores within the organic matter constitute a considerable portion of pore network of the shale samples. As a result of organic water-repellant pores, conventional theories of wettability, capillary pressure, relative permeability, pore size distribution, and EOR which have been developed for uniformly-wet systems, might not be fully applicable to unconventional rocks with dual-wet behavior.

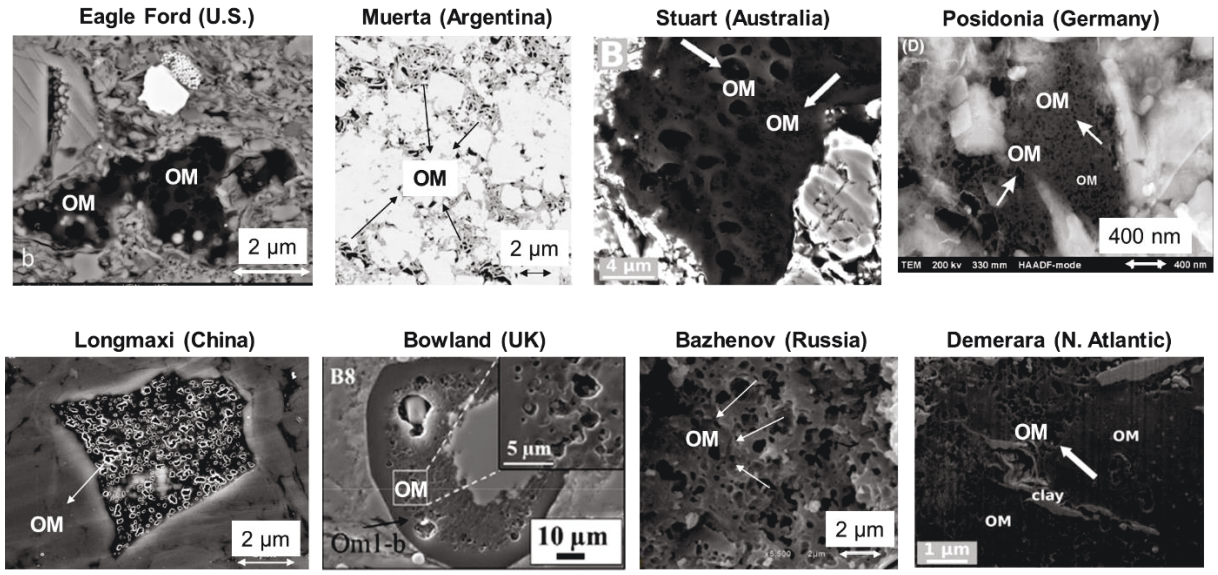

Fig. 1.10: The presence of organic nanoscale pores in shale samples worldwide.

The results of wettability tests conducted on Montney (Lan et al., 2015a) and Duvernay (Yassin et al., 2017) plugs show that oil imbibition is much higher than brine imbibition, in the presence of air. The samples exhibit a strongly oil-wet behavior, explained by hydrophobic organic pores with high affinity for oil uptake (Yassin et al., 2017; Lan et al., 2015a). In this thesis, unconventional shale and tight rock samples with oil-wet behavior are referred to as "dual-wet" samples.

The results of wettability tests conducted on the US shale plugs of Bakken (Wang et al., 2012), Wolfcamp (Neog and Schechter, 2016), Eagle Ford (Nguyen et al., 2014), Permian (Alvarez and Schechter, 2017), and Marcellus (Engelder et al., 2014) show that these samples are typically intermediate-wet to dual-wet. Odusina et al. (2011) used Nuclear Magnetic Resonance (NMR) analysis and studied the wettability of shale samples from Barnett, Floyd, and Woodford

Formations located in the US. They concluded that the pores within organic matter contribute to the strong dual-wet behavior. Combined analyses of oil recovery, wettability, and SEM results demonstrate that the strong dual-wet behavior of shale samples is due to the abundant water-repellant pores within organic matter (Yassin et al., 2018a). As a result, significant volume of oil may be trapped in nanoscale oil-wet pores, mainly within organic matter. Recovering this trapped oil is challenging, both technically and economically.

1.5 Research Motivation

Evaluation of wettability of unconventional rocks is significant for 1) investigating the spatial distribution and morphology of oil-wet and water-wet pores, 2) selecting the type of fracturing fluid (or EOR fluid) and its chemical additives (such as surfactants) for higher hydrocarbon production, 3) selecting appropriate capillary pressure and relative permeability curves for reservoir engineering calculations, 4) mitigating low fracturing fluid recovery after fracturing operations, 5) investigating fracture-face damage and subsequent cleanup strategies after fracturing operations, and 6) evaluating the consequences of condensate dropout below dewpoint pressure.

In this research, evaluation of wettability of shale and tight siltstone rocks will provide valuable information about 1) the low oil recovery factor of unconventional wells, 2) the location of the residual trapped oil, and 3) the potential EOR technique to produce the residual trapped oil. Therefore, this study investigates wettability of unconventional rocks and proposes new experimental and modeling approaches for characterizing their dual-wet pore network. After evaluation of wettability, this research explores EOR mechanisms for producing the residual trapped oil from organic-rich shale samples.

1.6 Research Objectives

This research has the following four objectives:

- to measure and model wettability of shale and tight siltstone samples and investigate the functional dependence of wettability on petrophysical properties.
- to develop mathematical models and experimental techniques for characterizing water-wet (hydrophilic) and water-repellant (hydrophobic) pore size distributions of dual-wet rock samples.

- to modify conventional relative permeability models, and develop new models for unconventional rocks with dual-wet pore network.
- to evaluate the performance of CO_2 and brine for EOR from oil-saturated dual-wet shales.

1.7 Organization of Thesis

This work is divided into 8 chapters. Chapters 1 and 8 are the "General Introduction" and "Conclusions and Recommendations".

Chapter 1 gives a general introduction about the massive extent of unconventional resources worldwide, hydraulic fracturing operations, EOR techniques, as well as wettability and pore network of unconventional rocks. At the end of this chapter, the research motivation, the objectives, and the organization of this thesis are elaborated.

Chapter 2 investigates wettability of organic-rich shale samples from the Lower Duvernay Formation. It also examines the existence of possible correlations between the measured oil wettability index and petrophysical properties measured in the laboratory. A large data set from rock samples of 5 Lower Duvernay wells are presented to study the effect of organic-matter content on petrophysical properties.

Chapter 3 follows the subject of Chapter 2, and focuses mainly on the effect of kerogen thermal maturity level on shale wettability. It provides the wettability results of two sets of Duvernay plugs from gas window (Lower Duvernay) and oil window (Upper Duvernay) with different thermal maturity levels.

Chapter 4 is based on the conclusions of Chapter 2 regarding the dual-wet behavior of Duvernay samples. It provides an experimental technique assisted with mathematical models for separate estimation of hydrophilic and hydrophobic pore size distributions. The results are compared with those of mercury injection capillary pressure (MICP) to emphasize on the advantages of the proposed methodology over MICP.

Chapter 5 modifies the conventional relative permeability model, and develops a new model for unconventional rocks with dual-wet pore network. This chapter first reviews and discusses the results of SEM images, MICP, organic petrography, and comparative oil/brine imbibition

experiments conducted on the Montney siltstone samples. On the basis of these analyses, the dual-wet behavior of the Montney samples is identified, and then a modified relative permeability model is proposed.

Chapters 6 gives the results of CO_2-EOR tests conducted on the oil-saturated Duvernay plugs. A high-pressure and high-temperature visual cell is used for CO_2-soaking tests to visually explain governing mechanisms of oil production. This chapter also compares the results of CO_2-soaking tests with those of brine-soaking tests and investigates the potentials of brine and CO_2 for oil production from dual-wet shale plugs.

Chapter 7 complements the results of Chapter 6 by analyzing the results of bulk-phase tests and visualizing the interactions at CO_2/oil interface under high-pressure and high-temperature conditions. The results of bulk-phase visualization tests are used to explain the mechanisms of CO_2 dissolution into Montney and Duvernay oil samples.

Chapter 8 provides key conclusions from this thesis and proposes some recommendations for future studies.

The references from all chapters are combined together and presented after Chapter 8. Appendix A is presented after the references.

Chapter 2

Organic Shale Wettability and Its Relationship to Petrophysical Properties

2.1 Introduction

Organic-rich shales have been considered as potential reserves across the world (Gonzalez et al., 2013). Extraction of hydrocarbons from shale rocks in the United States is considered as one of the landmark events in this century (Wang et al., 2014). These unconventional resources with ultralow permeability can produce hydrocarbons at economic rates by hydraulically fractured horizontal wells. However, successful hydrocarbon recovery from such reservoirs requires characterization of rock/fluid properties such as wettability, relative permeability, and capillary pressure. Wettability affects other rock/fluid properties including capillary pressure, water flood behavior, relative permeability, and electrical characteristics of rock (Anderson, 1986b). Evaluation of shale wettability is significant for 1) mitigating low fracturing fluid recovery after fracturing operations (Cheng, 2012; Ghanbari and Dehghanpour, 2015 and 2016), 2) investigating water blockage in shale matrix followed by rapid decline in production rate (Bertoncello et al., 2014), 3) selecting the type of fracturing fluid (water-based or oil-based) and its additives (Montgomery, 2013), and 4) investigating the consequences of condensate dropout below dewpoint pressure (Sheng et al., 2016; Meng and Sheng, 2016).

Anderson (1986a) described several quantitative and qualitative methods for evaluating the wettability. Contact-angle measurement (Johnson and Dettre, 1969), Amott method (Amott, 1959), USBM wettability index (Donaldson et al., 1969), combined Amott/USBM method (Sharma and Wunderlich, 1987), spontaneous imbibition (Bobek et al., 1958), flotation technique

(American Petroleum Institute, 1962), glass slide method (Reisberg and Doscher, 1956), Craig rules of thumb in relative permeability curves (Craig, 1971), water flood method (Batycky et al., 1981), displacement capillary pressure (Benner et al., 1942), electrical resistivity log (Graham, 1958), and Nuclear Magnetic Resonance (NMR) (Brown and Fatt, 1956; Odusina et al., 2011; Sulucarnain et al., 2012) are different approaches for evaluation of wettability. Among these methods, contact-angle measurement (Siddiqui et al., 2018), spontaneous imbibition (Makhanov et al., 2014; Dehghanpour et al., 2015; Lan et al., 2015a), and NMR (Sulucarnain et al., 2012) have been used for characterizing the wettability of tight and shale rocks with ultralow permeability.

In our previous studies, we conducted spontaneous-imbibition tests on downhole rock samples from the Horn River Basin (HRB) gas shales (Dehghanpour et al., 2012 and 2013; Xu and Dehghanpour, 2014), Montney tight-gas (Lan et al., 2015a and 2015b), and Montney tight-oil (Habibi et al., 2016) Formations. The experiments on the HRB samples show the strong water uptake of gas shales which are oil-wet based on contact-angle measurements (Dehghanpour et al., 2012 and 2013; Xu and Dehghanpour, 2014). Clay hydration, micro-fracture induction, lamination, osmotic effect, and electrical double-layer expansion are collectively responsible for the excess water uptake (Xu and Dehghanpour, 2014; Binazadeh et al., 2016). The contact-angle tests and air/liquid imbibition data on tight samples of the Montney tight-gas Formation show that the samples have stronger wetting affinity to oil compared with brine. The wettability results are explained by the strong adsorption of oil on the surface of a well-connected organic pore network that is partly composed of degraded bitumen/pyrobitumen (Lan et al., 2015a and 2015b). The results of tests on the samples from the Montney tight-oil Formation are different from those from the Montney tight-gas Formation. Tight-oil samples similarly imbibe both oil and brine, while tight-gas samples imbibe more oil than brine. The pore network of the tight-oil samples exhibits a mixed-wet behavior (Habibi et al., 2016). In these studies, the authors investigated the relationships of wettability with other petrophysical properties. Lan et al. (2015a) observed that the normalized imbibed mass of oil and brine are lower at higher total organic carbon (TOC) content in the Montney tight-gas samples. They concluded that the samples with higher TOC content have higher amount of degraded bitumen/pyrobitumen that can clog the pores and reduce the oil and brine uptake.

In Chapter 2, we characterize the wettability of 9 shale plugs with different maturity levels from 5 wells completed in the Lower Duvernay (LD) Formation which is a self-sourced reservoir. We

present and analyze the petrophysical properties, mineralogy, and the results of rock-eval pyrolysis to characterize the shale samples. Then, we present the results of contact-angle and spontaneous-imbibition tests on the plugs. To investigate the role of pore connectivity, we also conduct spontaneous-imbibition and contact-angle tests on crushed shale pack (CSP) samples and compare the results with those of similar tests on the plugs. To investigate the size, abundance, and morphology of pores, we analyze scanning electron microscopy (SEM) and energy-dispersive x-ray spectroscopy (EDS) of the shale samples. We also analyze 147 data points from samples of 5 wells completed in the LD Formation and examine the effect of TOC content on effective porosity (φ_{eff}), pressure-decay permeability (k_{Decay}), bulk density (ρ_{Bulk}), matrix density (ρ_{Matrix}), and oil saturation (S_o). We use the results of spontaneous-imbibition tests on the plugs to define oil wettability index (WI_o) and pore wettability index of oil (PWI_o) and brine (PWI_w). Finally, we investigate the correlations of WI_o with TOC content, φ_{eff}, ρ_{Bulk}, and oxygen index (OI). OI measured by rock-eval pyrolysis is used as the indicator of organic-matter maturity level.

2.2 Materials and Data

We select 9 twin plugs, and the reservoir oil and brine from 5 wells drilled in the Lower Duvernay Formation located in the Western Canadian Sedimentary Basin (WCSB). The shale samples have a wide range of φ_{eff}, TOC content, and kerogen maturity level which allows investigation of the aforementioned properties on wettability. The samples are characterized by tight-rock analysis (TRA), x-ray diffraction (XRD) analysis, and rock-eval pyrolysis.

2.2.1 Plugs

The Duvernay shale Formation is a stratigraphical unit of Frasnian age in the WCSB (Fig. 2.1a). This formation has been characterized as a source rock for many of the large Devonian oil and gas pools in Alberta (Low, 2012). The Duvernay Basin covers an area of over 50,000 mi^2 in central Alberta. The prospective area for the Duvernay shale is 23,250 mi^2 and is divided into Kaybob in the north, Edson-Willesden Green in the center, and Innisfail in the south as shown in Fig. 2.1b. By increasing the depth of Duvernay Formation from east to west, there is an extensive oil prospective area in the east (13,000 mi^2), a gas-condensate prospective area in the center (7,350 mi^2), and a smaller dry-gas prospective area in the west (2,900 mi^2) (US Energy Information Administration, EIA). The gross shale thickness in the prospective area ranges from 30 ft to over

200 ft. The shale thickness averages 41 ft in the oil prospective area, 54 ft in the gas-condensate prospective area, and 63 ft in the dry-gas prospective area (US Energy Information Administration, EIA).

We select 9 twin plugs from Minhik (MIN), Wahigan (WAH), Ferrier (FER), Saxon (SAX), and Cecilia (CEC) wells. We have one twin plugs from SAX and two twin plugs from each well. WAH, SAX, and CEC wells are in the Kaybob region, while MIN and FER wells are located in the Innisfail region. Unique well identifiers (UWI) of MIN, WAH, FER, SAX, and CEC are 2-6-44-5, 6-6-64-22w5, 12-4-42-8, 11-08-62-24w5, and 11-34-57-23, respectively. The location of the 5 Duvernay wells are shown in Fig. 2.1c.

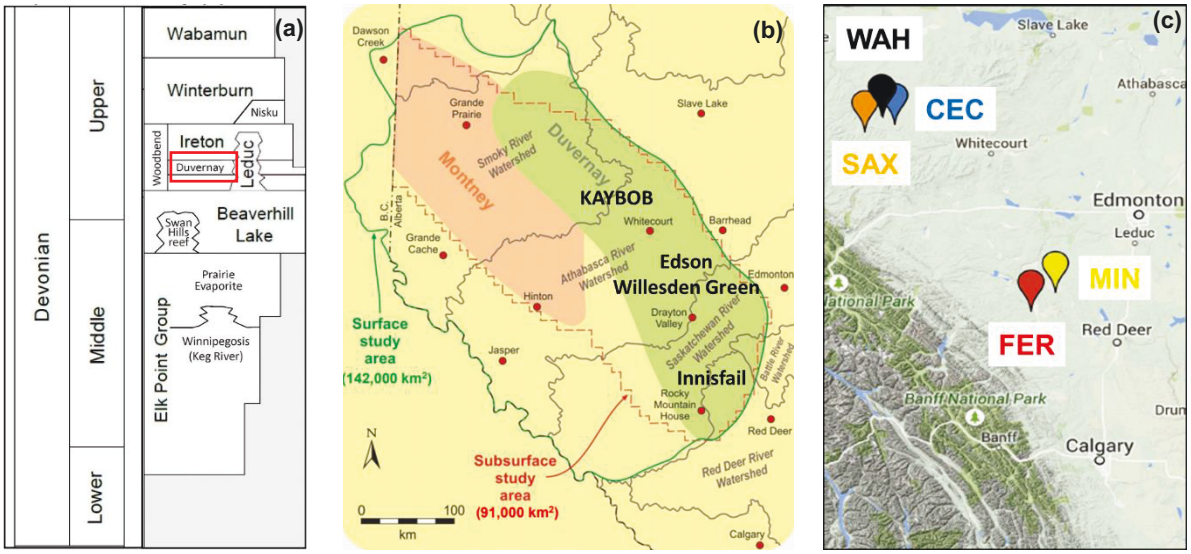

Fig. 2.1: (a) Stratigraphic column of east central plain of Alberta (rockstone-research) (b) Location of Duvernay Formation (Revised from Canadian Society of Petroleum Geoscientists, CSPG). (c) Location of the 5 Duvernay wells.

2.2.2 Tight-Rock Analysis (TRA)

The petrophysical properties of the plugs are listed in Table 2.1. The plugs with 3.8 cm diameter were drilled horizontally from the full-diameter core samples. The depth of the plugs ranges from 3,095.32 m for MIN1 to 3,963.02 m for CEC2. The downhole temperatures of MIN, WAH, FER, SAX, and CEC are 112, 111, 113, 110, and 124°C, respectively. The values of φ_{eff}, k_{Decay}, ρ_{Matrix}, and ρ_{Bulk} correspond to the offset samples located near the original twin plugs. The depth difference between offset samples and original plugs ranges from 10 to 40 cm. A commercial lab used crushed grains of the samples and measured the φ_{eff} and k_{Decay} by Boyle's law helium porosimetry and

pressure-decay methods, respectively. The size of crushed grains is larger than pore size and each grain particle contains an abundant number of pores. Using crushed grains for measuring φ_{eff} and k_{Decay} allows access to pore space and removal of artifacts or induced features (Handwerger et al., 2011). ρ_{Bulk} is measured by dividing the mass of dry rock by the bulk volume (BV) of the sample. In addition, ρ_{Matrix} is measured via Boyle's law helium porosimetry on crushed grains of the rock.

Since the plugs are not fully preserved, it is expected that the original formation brine and oil are partly or completely evaporated and the plugs are mainly saturated with air. It is important to mention that initial reservoir pressure is well above the dewpoint pressure (P_{Dew}) and oil saturation is zero at reservoir conditions for all wells. The condensate is formed when the full-diameter core samples are drilled and taken out of the well. We tested all plugs as-received and did not use any washing fluids such as toluene or methanol.

Table 2.1: Depth, dry mass, length, pressure-decay permeability, effective porosity, matrix density, and bulk density of the plugs. The diameter of all plugs is 3.8 cm. Subscripts o and w represent oil and brine, respectively.

Plug ID	Depth (m)	Dry mass (g)	Length (cm)	k_{Decay} (nD)	φ_{eff} (%BV)	ρ_{Matrix} (g/cm^3)	ρ_{Bulk} (g/cm^3)
$MIN1_w$	3095.32	93.779	3.3	288	6.24	2.56	2.45
$MIN1_o$	3095.41	100.706	3.6	288	6.24	2.56	2.45
$MIN2_w$	3103.05	167.278	6.1	236	4.93	2.58	2.49
$MIN2_o$	3103.10	155.054	5.6	236	4.93	2.58	2.49
$WAH1_w$	3308.62	94.808	3.3	102	3.64	2.58	2.51
$WAH1_o$	3308.69	108.750	3.8	102	3.64	2.58	2.51
$WAH2_w$	3313.37	107.607	3.8	130	4.12	2.57	2.55
$WAH2_o$	3313.42	111.335	3.8	130	4.12	2.57	2.55
$FER1_w$	3440.14	148.026	5.3	243	4.72	2.53	2.46
$FER1_o$	3440.18	158.030	5.7	243	4.72	2.53	2.46
$FER2_w$	3464.37	128.488	4.3	131	2.00	2.50	2.44
$FER2_o$	3464.42	135.100	4.7	131	2.00	2.50	2.44
$SAX1_w$	3795.73	149.500	5.3	275	3.96	2.59	2.52
$SAX1_o$	3795.73	152.104	5.4	275	3.96	2.59	2.52
$CEC1_w$	3949.30	128.396	4.4	287	3.53	2.67	2.60
$CEC1_o$	3949.34	117.339	4.1	287	3.53	2.67	2.60
$CEC2_w$	3962.98	128.223	4.6	236	4.17	2.60	2.51
$CEC2_o$	3963.02	129.942	4.6	236	4.17	2.60	2.51

2.2.3 Mineralogy

The mineralogy of the samples is measured using XRD and is listed in Table 2.2. The XRD analysis shows that quartz (22.3-47.9 wt%), calcite (7.7-29.5 wt%), K-feldspar (1.7-9.3 wt%), and plagioclase (0.6-6.8 wt%) are the dominant non-clay minerals; whereas mixed layers of illite/mica (13.2-26.3 wt%) and illite/smectite (3.4-9.3 wt%) are the main clay minerals.

Table 2.2: Mineralogy of the shale samples. The unit of XRD results is wt%.

Plug ID	Quartz	K-Feldspar	Plagioclase	Calcite	Dolomite	Ankerite/Fe-Dolomite	Pyrite	Barite	Fluorapatite	Total non-clay	Illite/Smectite	Illite/Mica	Chlorite	Kaolinite	Total clay
	Non-clay minerals										Clay minerals				
MIN1	43.2	1.7	2.7	13.8	1.5	3.5	4.0	0.4	0.0	70.8	7.2	18.4	3.6	0.0	29.2
MIN2	36.3	8.0	0.6	20.1	2.0	1.0	1.0	1.0	0.0	70.0	9.0	17.0	4.0	0.0	30.0
WAH1	47.3	2.5	3.5	7.7	1.1	3.2	2.0	0.5	0.0	67.8	8.0	21.7	1.8	0.7	32.2
WAH2	47.9	3.3	4.6	11.4	2.0	2.0	4.0	0.8	0.0	76.0	5.0	17.0	2.0	0.0	24.0
FER1	35.5	2.3	3.8	14.6	1.8	0.4	4.1	1.4	0.3	64.2	5.1	26.3	2.8	1.6	35.8
FER2	47.8	2.2	6.5	9.6	1.9	1.0	2.9	0.1	0.0	72.0	8.2	16.9	1.9	1.0	28.0
SAX1	36.7	6.5	4.0	15.3	0.5	3.5	3.6	0.1	0.0	70.2	9.3	18.5	1.8	0.2	29.8
CEC1	22.3	3.6	5.3	29.5	4.4	3.6	2.0	0.3	0.0	71.0	6.6	18.4	3.2	0.8	29.0
CEC2	30.9	9.3	6.8	22.2	6.1	2.3	4.4	0.2	0.0	82.2	3.4	13.2	1.2	0.0	17.8

2.2.4 Rock-Eval Pyrolysis

The results of rock-eval pyrolysis are listed in Table 2.3. The TOC content is > 2 wt% and categorizes the samples as "very good" quality in terms of petroleum potential (Baskin, 1997; Law, 1999). The crossplot of Hydrogen Index (HI) vs. Oxygen Index (OI) (Fig. 2.2a) shows the type of kerogen (Law, 1999). The kerogen type of all samples is Type II owing to their marine nature, which indicates the ability of the samples to produce a mix of oil and gas (Weber and Green, 1981). The crossplot of Production Index (PI) vs. T_{max} (Fig. 2.2b) can be interpreted to identify the maturity level of kerogen (Law, 1999). This crossplot shows that WAH and SAX samples are in the wet-gas window, MIN and FER samples are in the dry-gas window, and CEC samples are over-mature.

Table 2.3: The results of rock-eval pyrolysis conducted on the shale samples.

Plug ID	TOC (wt%)	S_1 (mg/g)	S_2 (mg/g)	S_3 (mg/g)	T_{max} (°C)	HI[1]	OI[2]	PI[3]	Maturity window
MIN1	5.2	0.20	2.71	0.19	480	51.81	3.63	0.07	Dry-gas
MIN2	5.6	0.22	3.05	0.18	481	54.50	3.22	0.07	Dry-gas
WAH1	2.5	0.08	1.69	0.18	475	67.60	7.20	0.04	Wet-gas
WAH2	4.7	0.17	3.70	0.25	468	78.56	5.30	0.04	Wet-gas
FER1	6.6	0.16	3.28	0.13	476	49.70	1.97	0.05	Dry-gas
FER2	4.6	0.27	2.35	0.20	481	51.20	4.36	0.10	Dry-gas
SAX1	3.8	4.36	4.36	0.10	466	113.51	2.60	0.50	Wet-gas
CEC1	2.2	0.09	0.22	0.21	594	10.00	9.00	0.29	Over-mature
CEC2	4.9	0.10	0.45	0.24	606	9.00	5.00	0.18	Over-mature

[1] Hydrogen index (HI) = (S_2×100/TOC) [2] Oxygen index (OI) = (S_3×100/TOC)
[3] Production index (PI) = (S_1/(S_1+S_2))

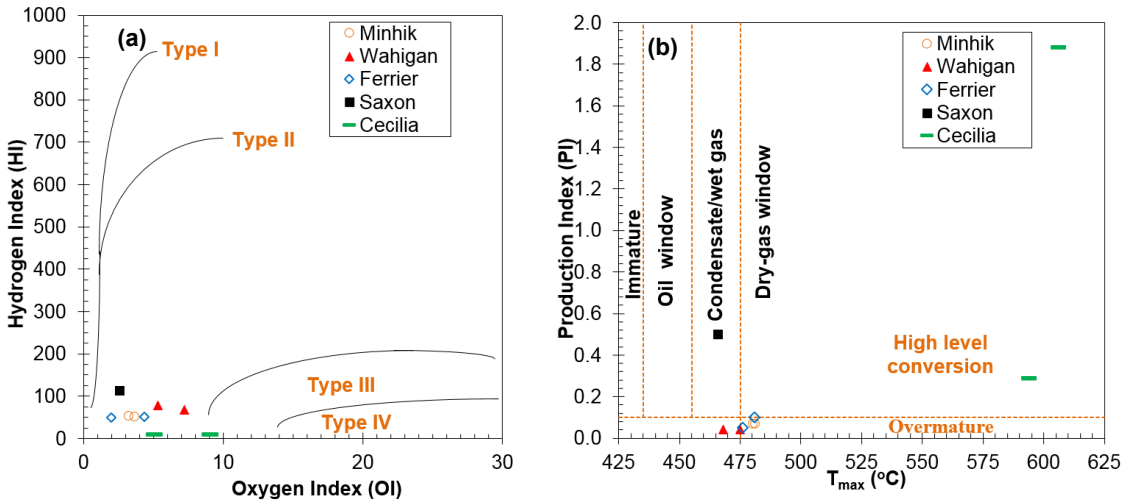

Fig. 2.2: The crossplots of (a) HI vs. OI for determining kerogen type and (b) PI vs. T_{max} for determining kerogen maturity level.

2.2.5 Reservoir Fluids

We use reservoir oil and brine for spontaneous-imbibition and contact-angle tests on the plugs. The produced oil and brine were collected from the wells next to the cored wells. Table 2.4 lists the values of viscosity, surface tension, and density of the fluids at 25°C and atmospheric pressure. We measure the surface tension of the fluids using Attension Sigma 700 (Biolin Scientific) instrument and Wilhelmy plate method. The oil surface tension is almost the same for different samples and the average value is ~23 mN/m. In most cases, the surface tension of brine increases when the salinity increases (Craig et al., 1993; Weissenborn and Pugh, 1996). The salinity of produced brine is higher than 150,000 ppm. Na^+, K^+, Ca^{2+}, Mg^{2+}, and Sr^{2+} are the major cations, while Cl^-, HCO_3^-, and SO_4^{2-} are the major anions in the produced brine. As shown in Table 2.4,

the surface tension of formation brine is less than that of deionized water (~72 mN/m). The slickwater fracturing fluid used in the Duvernay wells contains surfactant. The produced brine is contaminated with slickwater which includes surfactant, reducing the surface tension of the produced brine as listed in Table 2.4. The produced oil and brine are not available for CEC well, and we use FER fluid samples for conducting wettability tests on the CEC plugs. We use deionized (DI) water and mineral oil for wettability tests on the CSPs. The physical properties of deionized water and mineral oil are given in Table 2.5.

Table 2.4: The physical properties of produced oil and brine at 25°C.

Fluid sample	Viscosity (cp)		Surface tension (mN/m)		Density (g/cm^3)	
	Brine	Oil	Brine	Oil	Brine	Oil
MIN	1.50	1.20	47.8	23.3	1.048	0.762
WAH	1.60	2.10	62.5	23.5	1.111	0.787
FER	1.62	1.37	51.9	23.2	1.129	0.747
SAX	1.48	1.35	46.5	22.3	1.080	0.771

Table 2.5: The physical properties of deionized water and mineral oil at 25°C.

Viscosity (cp)		Surface tension (mN/m)		Density (g/cm^3)	
DI water	Mineral oil	DI water	Mineral oil	DI water	Mineral oil
0.9	29.0	72.0	31.1	0.997	0.852

2.3 Methodology

In this section, we present the procedure of conducting spontaneous-imbibition and contact-angle tests on plugs and CSPs.

2.3.1 Air/Liquid Contact Angle

Contact-angle measurements are conducted using Attension Theta (Biolin Scientific) which is equipped with Navitar lens (1984 × 1264 pixel resolution) and an LED light source. The reported contact angle for each sample is the average value ($\theta_{average}$) measured on 6 different spots on the polished surface of the sample.

2.3.2 Air/Liquid Spontaneous Imbibition

We conduct a total of 18 counter-current spontaneous-imbibition tests on 9 twin plugs. For air/liquid imbibition, 9 dry plugs are fully immersed in the brine and the other 9 plugs are fully immersed in the oil. We record the mass of rock during the time course of imbibition. Then, the imbibed volume is calculated using the liquid density. Fig. 2.3 presents the schematic of setup used for conducting counter-current spontaneous-imbibition tests.

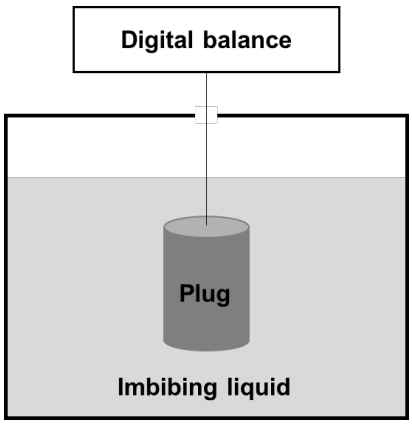

Fig. 2.3: Schematic of counter-current spontaneous-imbibition setup.

We also conduct 8 co-current spontaneous-imbibition tests on CSPs and compare the results with the results of spontaneous-imbibition tests on the plugs. This comparison is used for characterizing the connectivity of different pore networks of shale plugs. By powdering the shale plugs, we mix pore networks with different wetting behaviors and make an artificially homogenous porous medium.

To make the CSP, we use the procedure applied by Xu and Dehghanpour (2014). We break the shale sample into pieces smaller than 1 cm^3. We clean the grinding container with ethanol to eliminate the contaminations. Then, we pour the shale pieces into the grinding container and crush the shale samples using a carbide swing mill. A constant grinding time of 1 minute is used to have a similar particle size for different shale samples. The particle diameter is measured using Nikon Eclipse 50i POL polarizing microscope. Fig. 2.4a shows that the size of the shale particles is around 2000 nm. Fig. 2.4b shows the Attension Sigma 700 (Biolin Scientific) used for conducting the air/liquid spontaneous-imbibition tests on the CSPs. We fill the steel chamber with 0.2 g of shale powder and pack it using the chamber cap as much as possible. After that, we add another 0.2 g of shale powder and pack it similar to the previous step. We continue the filling and packing procedure until reaching the desired powder mass (m_{powder}). Then, the bottom face of the steel chamber is immersed in the liquid. The bottom face of steel chamber has a screen mesh equipped with filter paper that allows the liquid to pass through the chamber and to imbibe into the CSP. The steel chamber is hung from the balance and Sigma 700 measures the imbibed mass of liquid vs. time with 1 µg accuracy. Table 2.6 lists the general properties of the CSPs. The porosity (φ_{CSP}) is calculated by,

$$\varphi_{CSP} = \frac{BV_{CSP} - \frac{m_{Powder}}{\rho_{Matrix}}}{BV_{CSP}} \times 100 \quad (2.1)$$

where BV_{CSP} is the bulk volume of the CSP calculated by the diameter and length of CSP listed in Table 2.6. m_{Powder} is the powder mass and ρ_{Matrix} is the matrix density of the powder as listed in Table 2.1.

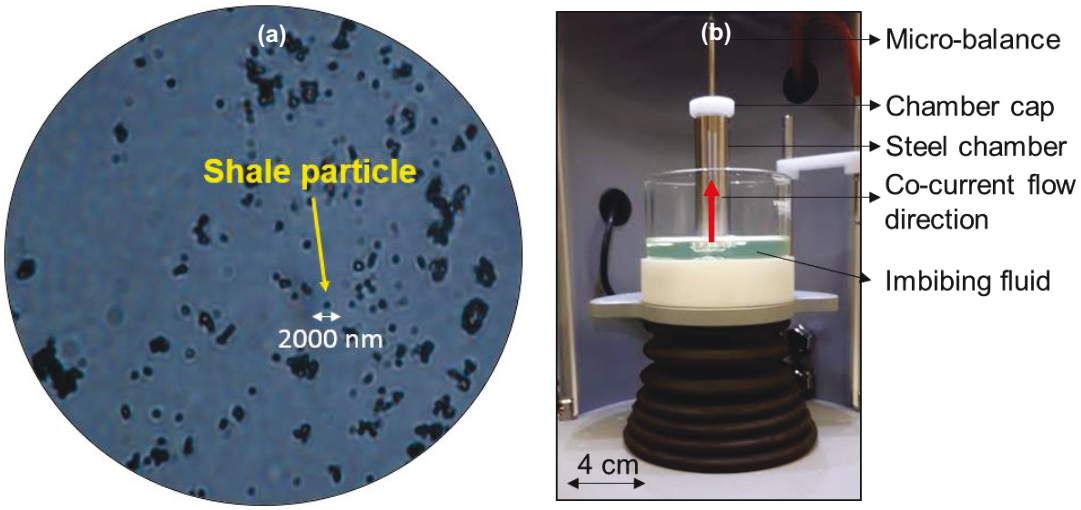

Fig. 2.4: (a) A picture of the shale particles captured by the Nikon Eclipse 50i POL polarizing microscope. The size of shale particles is around 2000 nm. (b) Attension Sigma 700 (Biolin Scientific) instrument used for co-current spontaneous-imbibition tests on crushed shale packs.

Table 2.6: The properties of the crushed shale packs.

CSP ID	Imbibing fluid	m_{Powder} (g)	Length (cm)	Diameter (cm)	φ_{CSP} (%BV)
FER1	Mineral oil	5.055	2.007	1.47	41
FER1	DI water	5.037	2.002	1.47	41
SAX1	Mineral oil	5.049	2.097	1.47	44
SAX1	DI water	5.050	2.108	1.47	44
WAH2	Mineral oil	5.038	2.030	1.47	44
WAH2	DI water	5.034	2.020	1.47	43
CEC2	Mineral oil	3.967	1.595	1.47	44
CEC2	DI water	3.960	1.590	1.47	43

The produced oil from the Duvernay Formation is very volatile and has a high vapour pressure. Evaporation of oil during spontaneous imbibition may affect the recorded mass by the Sigma 700 instrument (Fig. 2.4b). Therefore, we use mineral oil instead of reservoir oil for spontaneous-imbibition tests on the CSPs. Mineral oil has a very low vapour pressure and its vaporization is negligible compared with the reservoir oil. Moreover, we use DI water as the aqueous phase for the CSP tests.

2.3.3 SEM/EDS Analyses

To explain the results of wettability tests and characterize the size, spatial distribution, and morphology of different pores, we conduct SEM/EDS analyses. We polish the end-pieces of shale samples to obtain a smooth surface, and then, coat polished surface with carbon to mitigate the charging effects that may deteriorate the resolution and quality of the images.

2.4 Results and Discussions

2.4.1 Air/Liquid Contact-Angle Results

The contact angles of oil and brine on dry surface of SAX1 rock sample are presented in Fig. 2.5a and 2.5b, respectively. When the droplet of brine contacts the SAX1 surface, it retains as a droplet with contact angle of 76°, in the presence of air. However, the droplet of reservoir oil completely spreads. We observe that oil droplets completely spread on other samples, however, brine contact angles are different on various samples as listed in Table 2.7. MIN1 and CEC2 samples have the maximum and minimum brine contact angles of 103° and 65°, respectively. The results of air/liquid contact angles suggest that the Duvernay shale samples are strongly oil-wet in the presence of air.

Table 2.7: The contact angles of brine ($\theta_{average}$ ± standard deviation) in the presence of air on the polished surface of plugs and crushed shale packs.

Sample ID	Contact angle on plug (degrees)	Contact angle on crushed shale pack (degrees)
MIN1	103 ± 6	–
MIN2	66 ± 3	–
WAH1	78 ± 9	–
WAH2	80 ± 11	142 ± 4
FER1	90 ± 8	127 ± 3
FER2	74 ± 7	–
SAX1	74 ± 6	152 ± 5
CEC1	82 ± 4	–
CEC2	65 ± 5	132 ± 5

Fig. 2.5c shows the contact angle of brine on CSP of SAX1. As is evident, the CSP with contact angle of 150° is more water-repellant compared with the rock sample (76°). The roughness of CSP is higher than that of rock sample. Wenzel (1936) proposed Eq. 2.2 for the apparent contact angle (θ_{app}) formed by a liquid wetting a rough surface,

$$\cos(\theta_{app}) = \bar{r} \times \cos(\theta_{int}) \quad (2.2)$$

where the intrinsic contact angle (θ_{int}) is the contact angle which a liquid would make on a rigid, flat, and chemically homogeneous solid surface. $\bar{r}$ is the average roughness ratio calculated by dividing the real contact surface by the ideal flat surface ($\bar{r} \geq 1$). If we assume powdering the rock does not change θ_{int} in Eq. 2.2, θ_{app} is expected to decrease by roughening the surface (increasing $\bar{r}$). In other words, if the surface chemistry remains unaltered (constant θ_{int}) after powdering the shale, θ_{app} of brine droplet on SAX1 CSP should be smaller than 76°. However, $\theta_{app} = 150^{o}$ in Fig. 2.5c indicates that the assumption of constant surface chemistry after powdering the shale may not be valid. Similarly, powdering FER1 (Figs. 2.5d and 2.5e), WAH2, and CEC2 samples increases their hydrophobicity. The brine contact angles on CSPs are listed in Table 2.7. To explain the strong hydrophobicity of CSPs, we need to investigate the contact angle on composite solids. Cassie and Baxter (1944) derived Eq. 2.3 for θ_{app} on a two-component composite surface with varying degrees of heterogeneity,

$$\cos(\theta_{app}) = f_1 \times \cos(\theta_1) + f_2 \times \cos(\theta_2) \quad (2.3)$$

where f_1 and f_2 are the surface-area fractions of components 1 and 2 on the surface ($f_1 + f_2 = 1$), respectively, and θ_1 and θ_2 are the equilibrium contact angles of the same liquid on each of the flat surfaces of these components. The shale matrix is comprised of hydrophobic ($\cos(\theta_1) < 0$) organic matter (Mitchell et al., 1990) and hydrophilic ($\cos(\theta_2) > 0$) inorganic minerals such as quartz, calcite, feldspar, and especially clays (Chenevert, 1970; Hensen and Smit, 2002). We assume f_1 and f_2 as the surface area fractions of organic matter and inorganic minerals, respectively. The apparent contact angle of brine on SAX1 rock sample is 76° ($\cos(\theta_{app}) > 0$), that indicates $f_1 \times \cos(\theta_1) < f_2 \times \cos(\theta_2)$. After powdering SAX1, θ_{app} increases to 150° ($\cos(\theta_{app}) < 0$), that indicates $f_1 \times \cos(\theta_1) > f_2 \times \cos(\theta_2)$. The contact angles of brine on organic matter (θ_1) and inorganic minerals (θ_2) depend on surface forces, and is independent of powdering the shale. In conclusion, increasing θ_{app} after powdering the shale samples may be due to increasing the surface area fraction of organic matter (f_1) compared with that of inorganic minerals (f_2). Similarly, Xu and Dehghanpour (2014) observed that the wetting affinity to oil increases after powdering the shale samples of Horn River Basin. In Section 2.4.3, we discuss the possible reason for increasing f_1 after powdering the shale samples.

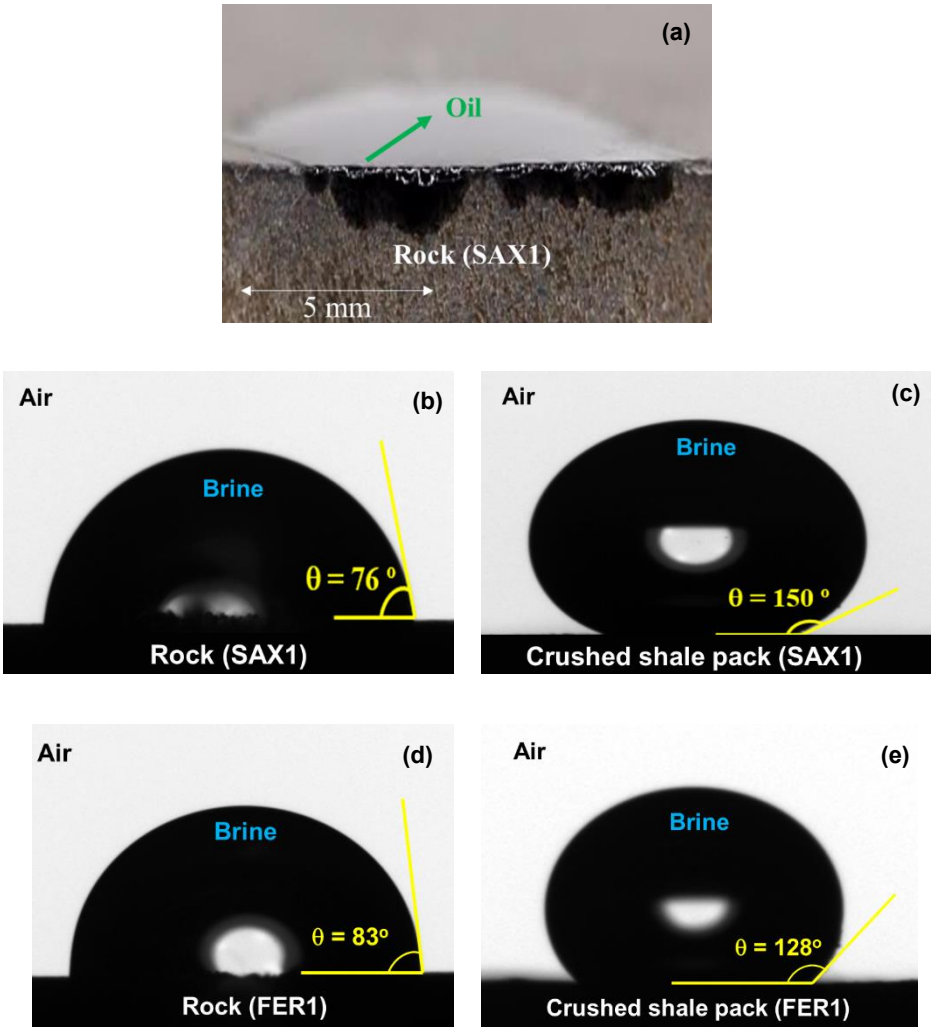

Fig. 2.5: Pictures of (a) oil droplet on dry surface of SAX1 rock sample and brine droplet on (b) dry surface of SAX1 rock sample, (c) crushed shale pack of SAX1, (d) dry surface of FER1 rock sample, and (e) crushed shale pack of FER1.

2.4.2 Air/Liquid Spontaneous-Imbibition Results

Figs. 2.6a and 2.6b present the normalized imbibed volumes of oil (I_o) and brine (I_w) vs. time for the 9 twin plugs, respectively. We calculate I_o (or I_w) by dividing the imbibed volume of oil (or brine) by the effective pore volume (PV) of the plug. The depth difference between the offset samples and the twin plugs ranges from 10 to 40 cm. Since the shale samples are very heterogeneous, calculation of effective PV using the offset φ_{eff} (Table 2.1) may be erroneous. As shown in Figs. 2.6a and 2.6b, the equilibrated I_o (I_o^{eq}) is much higher than the equilibrated I_w (I_w^{eq}). For instance, I_o^{eq} and I_w^{eq} of FER1 sample are 100% and 13% of PV, respectively. The results indicate that the wetting affinity of the shale samples to oil is significantly higher than that to brine. $I_o^{eq} > I_w^{eq}$ is in agreement with the results of air/liquid contact-angle tests presented in the previous

section. The equilibrium times are also different for brine and oil. Brine imbibition stops after almost 600 hours, while oil keeps imbibing with considerable rate even after 1,000 hours.

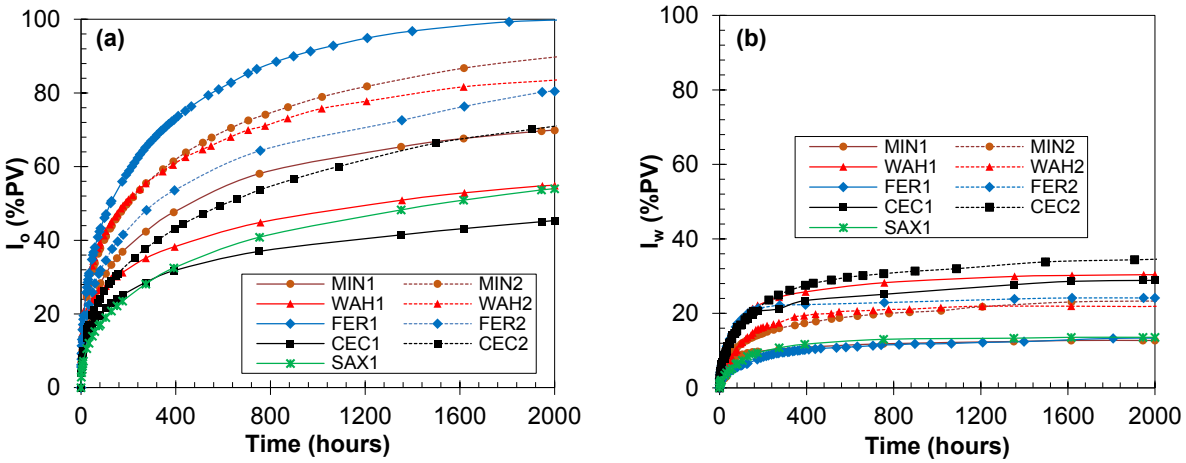

Fig. 2.6: Normalized imbibed volumes of (a) oil (I_o) and (b) brine (I_w) vs. time.

The imbibition results presented in Figs. 2.6a and 2.6b are affected by rock and fluid properties such as effective porosity (φ_{eff}), absolute permeability (k_{Decay}), viscosities of displacing (μ_1) and displaced (μ_2) phases, surface tension (σ), and geometrical parameters such as size, shape, and boundary conditions of the samples (L_s). To scale the imbibition data, we calculate dimensionless time (t_D) derived by Shouxiang et al. (1997),

$$t_D = t\sqrt{\frac{k_{Decay}}{\varphi_{eff}}}\frac{\sigma}{\sqrt{\mu_1\mu_2}}\frac{1}{L_s^2} \tag{2.4}$$

$$L_s = \frac{1}{2}\frac{DL}{\sqrt{D^2+2L^2}} \tag{2.5}$$

where L_s is the characteristic length, D is the diameter, and L is the length of plug. Figs. 2.7a and 2.7b show I_o and I_w vs. t_D, respectively. Comparing Figs. 2.7a and 2.7b indicates that the oil imbibition data for each sample are still much above the brine imbibition data. Since Eq. 2.4 does not account for the effect of wettability, the difference between oil and brine imbibition data in Figs. 2.7a and 2.7b is attributed to high wetting affinity of the shales to oil. Besides, there is considerable difference between oil imbibition data of different samples as shown in Figs. 2.7a. It clearly shows that the wetting affinity of shales to oil is different in various plugs. A similar difference is observed in Figs. 2.7b that points out to the variations in the level of wetting affinity to brine.

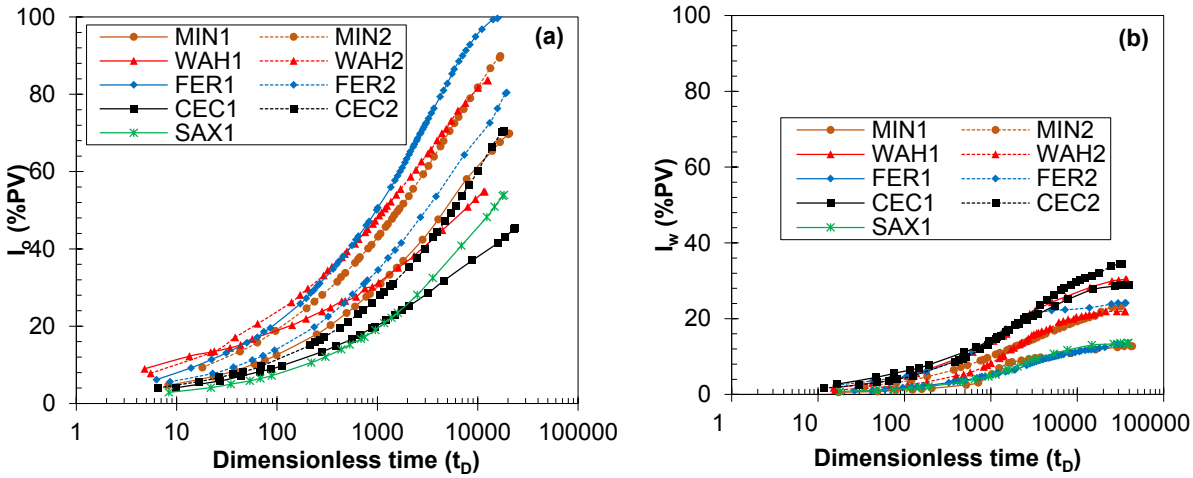

Fig. 2.7: Normalized imbibed volumes of (a) oil (I_o) and (b) brine (I_w) vs. dimensionless time (t_D).

Fig. 2.8 shows the normalized imbibed volume of mineral oil and DI water for the CSPs. The normalized imbibed volume is calculated by dividing the imbibed volume by the bulk volume of the CSP. Similar to the plugs, the equilibrated imbibed volume of oil is significantly higher than that of water. Besides, the difference between oil and water imbibition data is more pronounced for the CSPs compared with that for the plugs. For instance, I_w^{eq} and I_o^{eq} for SAX1 plug are 13.6% and 54.0% of PV, respectively. For CSP of SAX1, I_w^{eq} and I_o^{eq} are 5.9% and 100% of PV, respectively. The results show that powdering the shale plugs enhances their wetting affinity to oil. This is in agreement with the results of brine contact angles (Table 2.7), indicating that the CSPs are more water-repellant compared with the shale plugs.

The reservoir brine has lower surface tension (lower driving capillary pressure) and higher viscosity compared with DI water. If we use reservoir brine instead of DI water for CSP tests, I_w of brine is expected to be lower than that of DI water. The surface tension of mineral oil is 1.3 times higher than that of reservoir oil. Conversely, the viscosity of mineral oil is 22 times higher than that of reservoir oil. If we use reservoir oil instead of mineral oil for CSP tests, I_o of reservoir oil is expected to be higher than that of mineral oil. In summary, if we use reservoir fluids instead of mineral oil and DI water, the difference between I_o and I_w in CSP tests is expected to be higher.

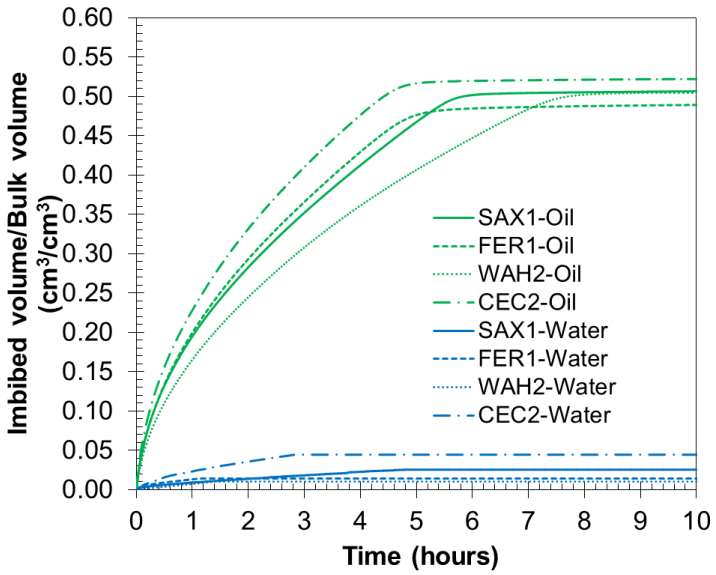

Fig. 2.8: Normalized imbibed volumes of mineral oil and deionized water in crushed shale pack tests.

Similarly, Xu and Dehghanpour (2014) observed that the CSPs imbibed more oil than water in gas shales of the HRB. However, I_w was higher than I_o in shale plugs of the HRB, which is in contrary to the Duvernay results in this study. Clay hydration, micro-fracture induction, lamination, and osmotic effect are collectively considered for the excess water imbibition in plugs of the HRB. Xu and Dehghanpour (2014) hypothesized that by powdering the shale plugs, the poorly-connected hydrophobic pores of plugs become artificially well-connected. In this study, I_o is higher than I_w in the Duvernay plugs. By powdering the shale, the oil imbibition increases, while the brine imbibition declines. For instance, by powdering SAX1 sample, I_o^{eq} increases from 54% to 100% of PV and I_w^{eq} declines from 13.6% to 5.9% of PV. We can conclude that the hydrophobic pores are relatively well connected in the Duvernay plugs and powdering the plugs enhances the connectivity of hydrophobic pores.

2.4.3 Discussion of Wettability Results

The key results of the spontaneous-imbibition and contact-angle tests presented so far are as follows:

1- Oil completely spreads on the shale plugs, while brine retains as a droplet with measurable contact angle, in the presence of air. Moreover, the contact angle of brine droplet on the CSPs is higher than that on the shale plugs.

2- I_o^{eq} is higher than that of I_w^{eq} for the shale plugs. This is in agreement with the air/liquid contact-angle results. Furthermore, brine stops imbibing after 600 hours, while oil continues imbibing with considerable rate even after 1,000 hours (Fig. 2.6).

3- The difference between I_o^{eq} and I_w^{eq} is more pronounced for the CSPs (Fig. 2.8) compared with that for the plugs. I_o^{eq} is higher for the CSPs compared with that for the plugs. In contrast, I_w^{eq} is higher for the plugs compared with that for the CSPs.

Observation 1 indicates that the Duvernay plugs are strongly oil-wet, in the presence of air. In addition, the CSPs are more hydrophobic compared with the shale plugs. The shale matrix is comprised of organic matter and inorganic minerals such as quartz, calcite, feldspar, plagioclase, and clays. The TOC content of the plugs ranges from 2.2 to 6.6 wt%. Organic matter is expected to have high wetting affinity to oil (Mitchell et al., 1990). Conversely, the inorganic part can be hydrophilic, especially when clay minerals are present (Chenevert, 1970; Hensen and Smit, 2002).

Powdering the shale plugs generates more hydrophobic and hydrophilic sites by increasing the surface areas of organic matter and clay minerals, respectively. The volume contents of clay minerals and organic matter for SAX1 sample are 27.3% and 7.7%, respectively. Since the volume content of clay minerals is higher than that of organic matter, it is expected to see an increase in the wetting affinity to brine after powdering SAX1. Surprisingly, the brine contact angle increases from 76° for the rock to 150° for the CSP. This observation suggests that powdering the shale facilitates the accessibility to the organic matter which is hydrophobic. Zhu et al. (2016) conducted multiple analyses on clay-sized particles (< 2000 nm) of shales. They categorized the TOC into mobile organic carbon (MOC) and stable organic carbon (SOC). The authors used 6 wt% NaClO solution and extracted 60.4% of TOC and called it MOC. MOC adsorbs on the mineral surfaces of the pores. The rest of organic matter (39.6%) could not be extracted by NaClO solution and was called SOC. SOC occurs in interlayer spacing of clay minerals. By powdering the Duvernay plugs, we increase the effective surface area of clay minerals. By increasing the surface area of clays, we may enhance the accessibility to SOC. Therefore, brine droplet can be in contact with both MOC and SOC in the CSPs. Higher accessibility to SOC may be responsible for the stronger hydrophobicity of the CSPs, leading to the contact angle of 150° for CSP of SAX1.

Observation 2 confirms the strong wetting affinity of the shale plugs to oil, suggesting that the majority of pores are hydrophobic. The SEM images of FER1, CEC2, and MIN2 samples are

shown in Figs. 2.9a, 2.9b, and 2.9c, respectively. The organic matter detected by EDS analysis is surrounded by quartz, feldspar/clay, pyrite, and carbonates minerals. The magnified SEM images in Fig. 2.9 indicate that the diameter of pores within the organic matter is generally < 100 nm. The statistical analysis of several SEM images shows that majority of pores exist in the organic matter of the rock. The abundant hydrophobic organic pores may explain the higher imbibition of oil compared with brine (Fig. 2.6).

The size and number of hydrophilic and hydrophobic pores affect the equilibrium time of oil and brine imbibition. Considering the porous medium as a bundle of capillary tubes, the liquid uptake is faster in larger diameter capillaries. In other words, the fluid first imbibes into larger diameter capillaries, and moves through them into the smaller capillaries (Handy, 1960; Gruener et al., 2016). According to Fig. 2.6, the brine imbibition reaches equilibrium before 600 hours, while oil continues imbibing with considerable rate even after 1000 hours. The significant oil imbibition rate even after 1000 hours suggests that there are abundant small nanopores in the samples with low wetting affinity to brine, and high wetting affinity to oil. This observation is backed by small organic nanopores observed in Fig. 2.9. There are many pores with diameter < 100 nm in the organic matter. These small hydrophobic pores may be responsible for the late equilibrium of oil compared with brine.

Figs. 2.10a through 2.10c show the large micropores with diameter > 1000 nm bordered by inorganic minerals such as quartz, feldspar/clay, calcite, and dolomite. These micropores with diameters larger than organic nanopores, have almost no hydrophobic organic matter, and can be considered as hydrophilic conduits for brine imbibition. According to Handy's (1960) model, larger pores fill faster than smaller pores. Brine can spontaneously imbibe into these hydrophilic micropores (Fig. 2.10) and can fill them first. The brine uptake in hydrophobic organic nanopores (Fig. 2.9) may be negligible and brine stops imbibing into these pores. In conclusion, faster brine imbibition in hydrophilic micropores and negligible brine uptake in hydrophobic nanopores may explain the early equilibrium of brine compared with the late equilibrium of oil.

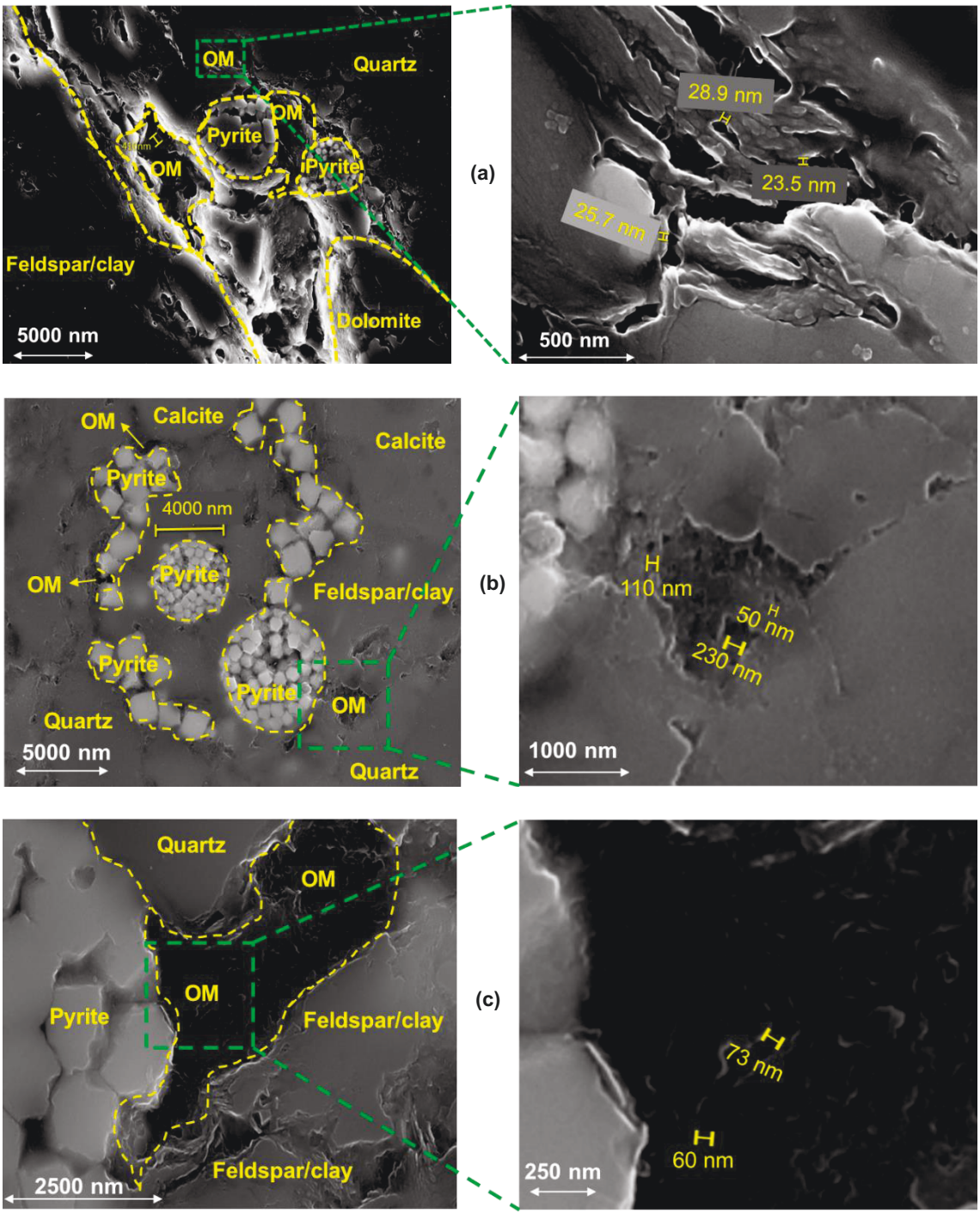

Fig. 2.9: The SEM images of (a) FER1 (TOC = 6.6 wt%), (b) CEC2 (TOC = 4.9 wt%), and (c) MIN2 (TOC = 5.6 wt%) samples show that organic matter is surrounded by quartz, carbonate, pyrite, and feldspar/clay minerals. A large number of small nanopores (< 100 nm) in the organic matter supports $I_o^{eq} > I_w^{eq}$, and the late equilibrium of oil in the imbibition experiments. The organic matter is detected by energy-dispersive x-ray spectroscopy (EDS) analysis. OM is organic matter.

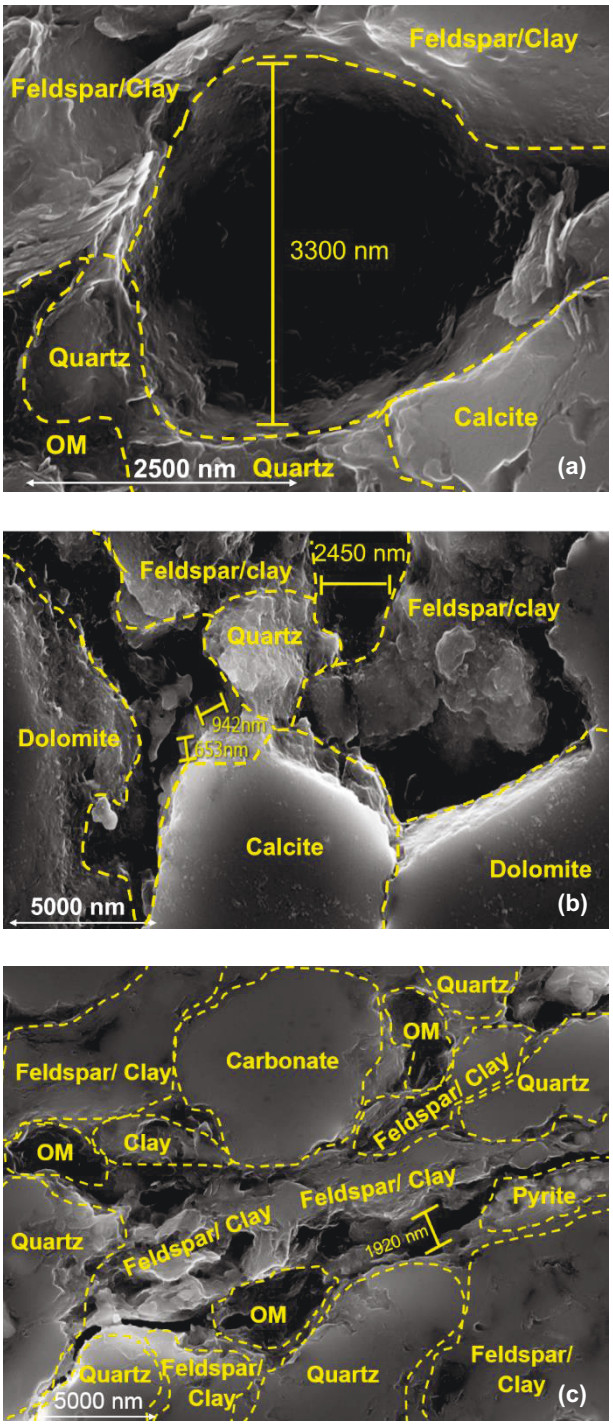

Fig. 2.10: The SEM images of (a) FER1, (b) CEC2, and (c) MIN2 samples show the large inorganic micropores bordered by quartz, feldspar/clay, calcite, and dolomite minerals. These large micropores may support the early equilibrium of brine in the imbibition experiments. Different minerals are detected by energy-dispersive x-ray spectroscopy (EDS) analysis. OM is organic matter.

The pore-throat size distribution also supports the abundant number of nanopores. Fig. 2.11 shows the pore-throat size distribution of FER2 sample measured by Mercury Injection Capillary Pressure (MICP) method. The maximum applied mercury pressure and the corresponding minimum pore-throat diameter are 55,110 psig and 3.8 nm, respectively. The maximum mercury saturation at 55,110 psig is 36.4% of PV. The high inaccessible pore volume by mercury (63.6% of PV) may be attributed to tiny nanopores within the organic matter. As shown in Fig. 2.11, the majority of pores have diameters < 100 nm, occupying 27.1% out of 36.4% of PV.

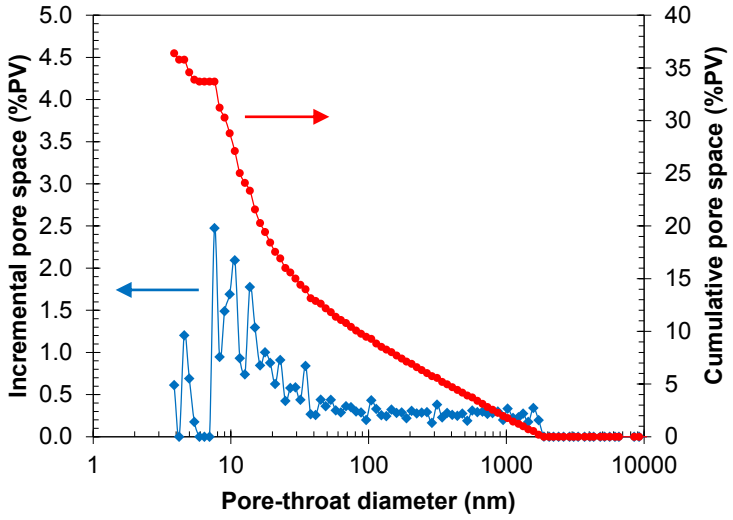

Fig. 2.11: Pore-throat size distribution of FER2 sample measured by MICP method. The maximum applied mercury pressure and the corresponding minimum pore-throat diameter are 55,110 psig and 3.8 nm, respectively. The maximum mercury saturation at 55,110 psig is 36.4% of pore volume.

Observation 3 suggests that the CSPs are more oil-wet than the shale plugs. The results of contact angles (Observation 1) show that powdering the shale samples generates more hydrophobic interface and increases the wetting affinity to oil. Higher hydrophobic interface in CSPs enhances I_o^{eq} (to almost 100% of PV); while significantly reduces I_w^{eq} (< 7% of PV). Although the porosity and permeability of CSPs are significantly higher than those of the plugs, brine imbibition is higher in the plugs compared with that in the CSPs. As discussed in Observation 1, higher accessibility to SOC may be responsible for enhancing the water-repellency of the CSPs.

2.5 Data Analysis; Effect of TOC Content on Petrophysical Properties

The results of wettability tests show that the wetting affinity of the shale plugs to oil is higher than that to brine. The SEM/EDS analyses suggest that the abundant number of hydrophobic nanopores within organic matter may be responsible for the higher oil uptake. To see the effects of organic matter on petrophysical properties, we investigate the correlations of TOC content with φ_{eff}, k_{Decay}, ρ_{Bulk}, ρ_{Matrix}, and S_o. We use 147 data points corresponding to the samples from 5 wells drilled in the Duvernay Formation. These correlations assist in better characterization of shale pore network and understanding shale wettability.

2.5.1 Effective Porosity (φ_{eff}) and Permeability (k_{Decay})

φ_{eff} of the samples from MIN, WAH, FER, SAX, and CEC wells are plotted vs. TOC content, as shown in Figs. 2.12a through 2.12e, respectively. φ_{eff} generally increases by increasing the TOC content. These positive correlations suggest that the majority of connected pores exist in the organic part of the rock. The positive correlations of φ_{eff} with TOC content demonstrate the significant role of organic porosity in the Duvernay Formation. Furthermore, Figs. 2.13a through 2.13e show that the samples with higher TOC content have generally higher k_{Decay}. The higher TOC content leads to higher φ_{eff} that subsequently increases k_{Decay}. The positive correlation of φ_{eff} with TOC content has been reported in other gas shales as well. For example, Jarvie (2012) observed that φ_{eff} has a positive covariation with TOC content of Barnett shale samples, consistent with the fact that most of the connected pores are within the organic matter. Kale et al. (2010) investigated the petrophysical properties of three petrofacies in Barnett shale and observed that φ_{eff} is typically higher in the samples with higher TOC content.

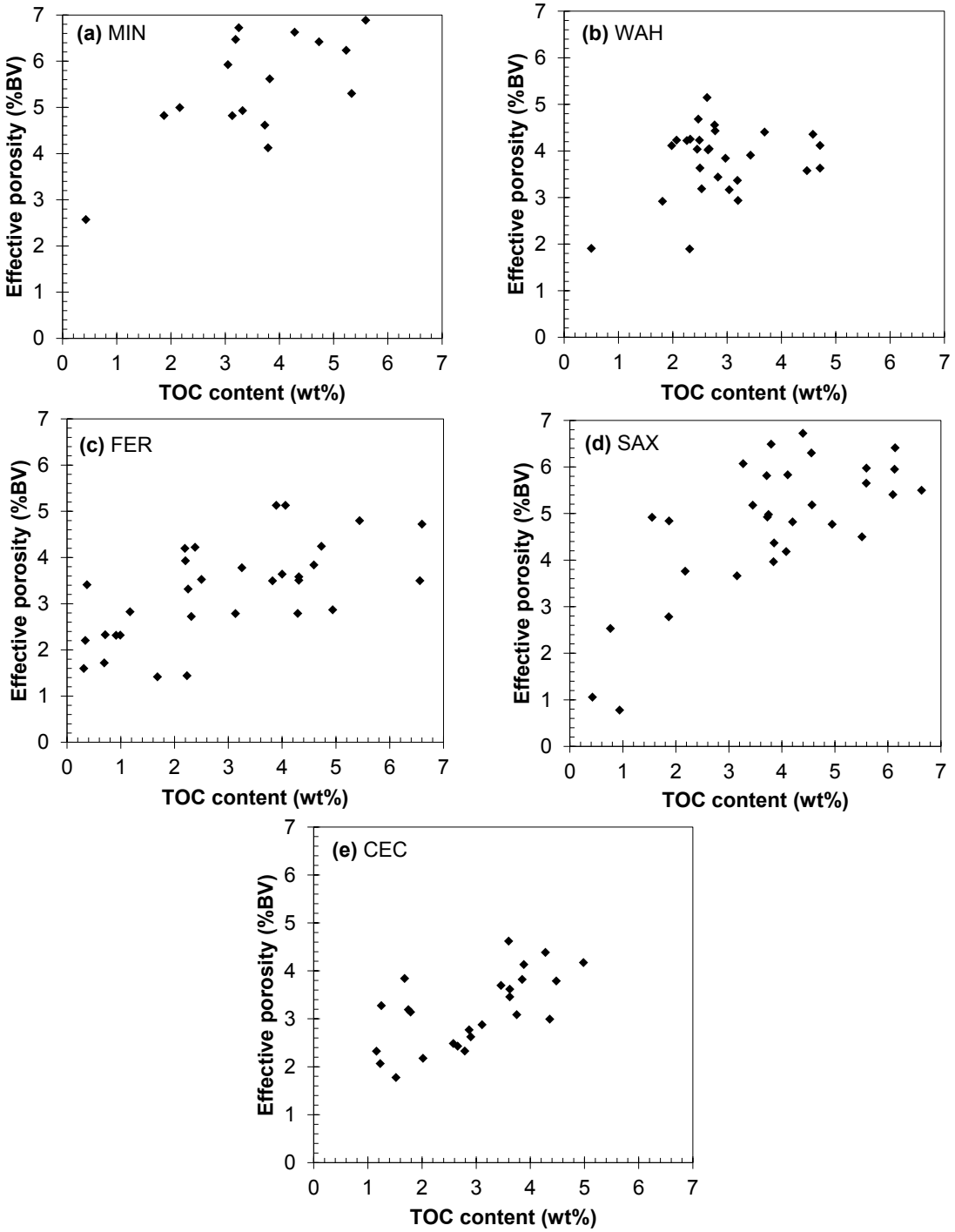

Fig. 2.12: The correlations of effective porosity vs. TOC content for the shale samples of (a) Minhik, (b) Wahigan, (c) Ferrier, (d) Saxon, and (e) Cecilia wells.

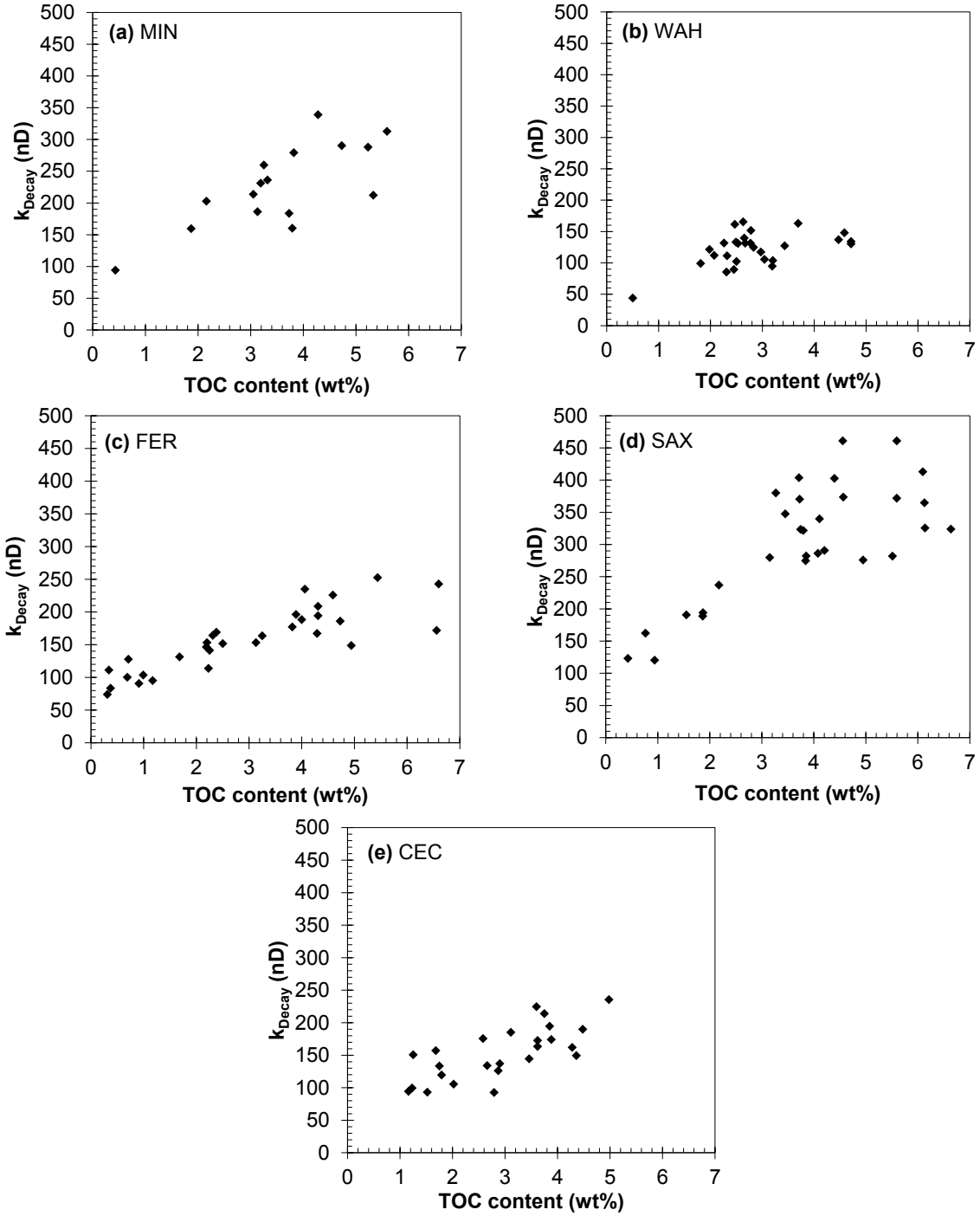

Fig. 2.13: The correlations of pressure-decay permeability vs. TOC content for the shale samples of (a) Minhik, (b) Wahigan, (c) Ferrier, (d) Saxon, and (e) Cecilia wells.

2.5.2 Bulk Density (ρ_{Bulk}) and Matrix Density (ρ_{Matrix})

Fig. 2.14a shows the negative correlation of ρ_{Bulk} with TOC content of 147 samples. ρ_{Bulk} is calculated by dividing the total mass of dry rock by the bulk volume as follows,

$$\rho_{Bulk} = \frac{\text{Matrix mass}}{\text{Bulk volume}} = \frac{\text{Matrix mass}}{\text{Matrix volume} + \text{Pore volume}} \tag{2.6}$$

Based on Eq. 2.6, lower matrix mass (or matrix density) and higher pore volume (or φ_{eff}) lead to lower ρ_{Bulk}. The negative correlation of ρ_{Bulk} with TOC content may be due to the effect of TOC content on 1) φ_{eff} and 2) ρ_{Matrix}.

Firstly, Fig. 2.12 show that the samples with higher TOC content generally have higher φ_{eff}, leading to lower ρ_{Bulk}. Secondly, higher TOC content leads to lower ρ_{Matrix} as shown in Fig. 2.14b. ρ_{Matrix} is related to organic-matter density and mineral densities by Eq. 2.7,

$$\rho_{Matrix} = (1 - \omega_{TOC}) \times \left(\sum_{i=1}^{n} w_i \rho_i\right) + \omega_{TOC} \times \rho_{TOC} \tag{2.7}$$

where ω_i and ω_{TOC} are the weight fractions of minerals and organic matter, respectively. The densities of minerals (ρ_i) such as quartz, calcite, and illite are 2.65, 2.71, and 2.66 g/cm^3, respectively (Schön, 2011). The density of organic matter (ρ_{TOC}) is around 1.25 g/cm^3 (Boyd, 1995). Consequently, the samples with higher fraction of organic matter (the lightest component) have lower ρ_{Matrix}, leading to the negative correlation of ρ_{Bulk} with TOC content (Fig. 2.14a).

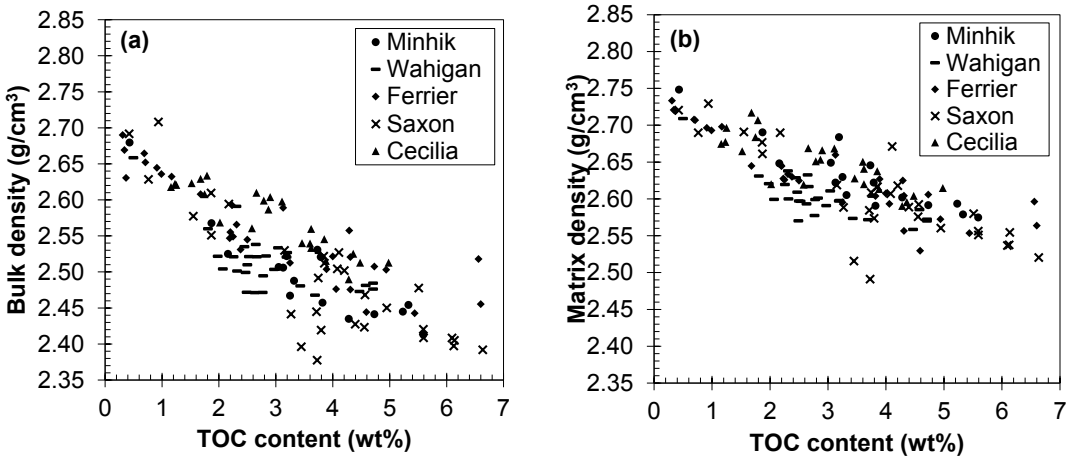

Fig. 2.14: The correlations of (a) bulk density and (b) matrix density with TOC content for 147 shale samples from 5 wells in the Duvernay Formation. The shale samples with higher TOC content generally have lower bulk and matrix densities.

2.5.3 Oil Saturation (S_o)

Figs. 2.15a through 2.15e show the crossplots of S_o vs. TOC content for the samples of MIN, WAH, FER, SAX, and CEC wells, respectively. The initial reservoir pressure is higher than P_{Dew} in the target wells. Therefore, S_o at initial reservoir conditions is zero. As reservoirs pressure drops below P_{Dew}, the oil starts to form in gas condensate wells (Danesh, 1998; Sheng et al., 2016). When the full-diameter core sample is drilled and taken out of the well, the pressure drops below P_{Dew} and oil is formed. Figs. 2.15a through 2.15e show that the samples with higher TOC content generally have higher S_o. The positive correlations of S_o with TOC content are explained by 1) formation and 2) preservation of oil in the shale samples.

The total gas content in shales is comprised of free gas in the pore space and adsorbed gas on the pore walls of organic matter (Wang and Reed, 2009). The gas molecules adsorb on nanopores of the organic matter due to favorable wettability of nanopores (Li et al., 2013). Wang and Reed (2009) showed that the adsorbed gas content stored in organic pores increases linearly with TOC content. As discussed in Fig. 2.12, the majority of connected pores are within the organic matter of the shale samples. Moreover, SEM images and MICP data show that the size of organic pores is generally < 100 nm. The free gas in the pore space and adsorbed gas on the pore walls convert to oil as pressure declines below P_{Dew}. Higher TOC content provides higher number of nanopores for adsorption of gas molecules, and subsequently higher S_o in the form of condensed oil as shown in Fig. 2.15.

After formation of the condensed oil, a portion of the oil may evaporate at surface conditions. The evaporation of oil is less pronounced in smaller pores compared with larger pores, due to higher van der Waals forces in the smaller pores (Brunauer et al., 1940). Higher TOC content provides higher number of nanopores for preservation of oil against vaporization, leading to the positive correlation of S_o with TOC content. In summary, the arguments regarding Fig. 2.15 indicate that the samples with higher TOC content generally have higher potential for the formation and preservation of oil at pressures below P_{Dew}.

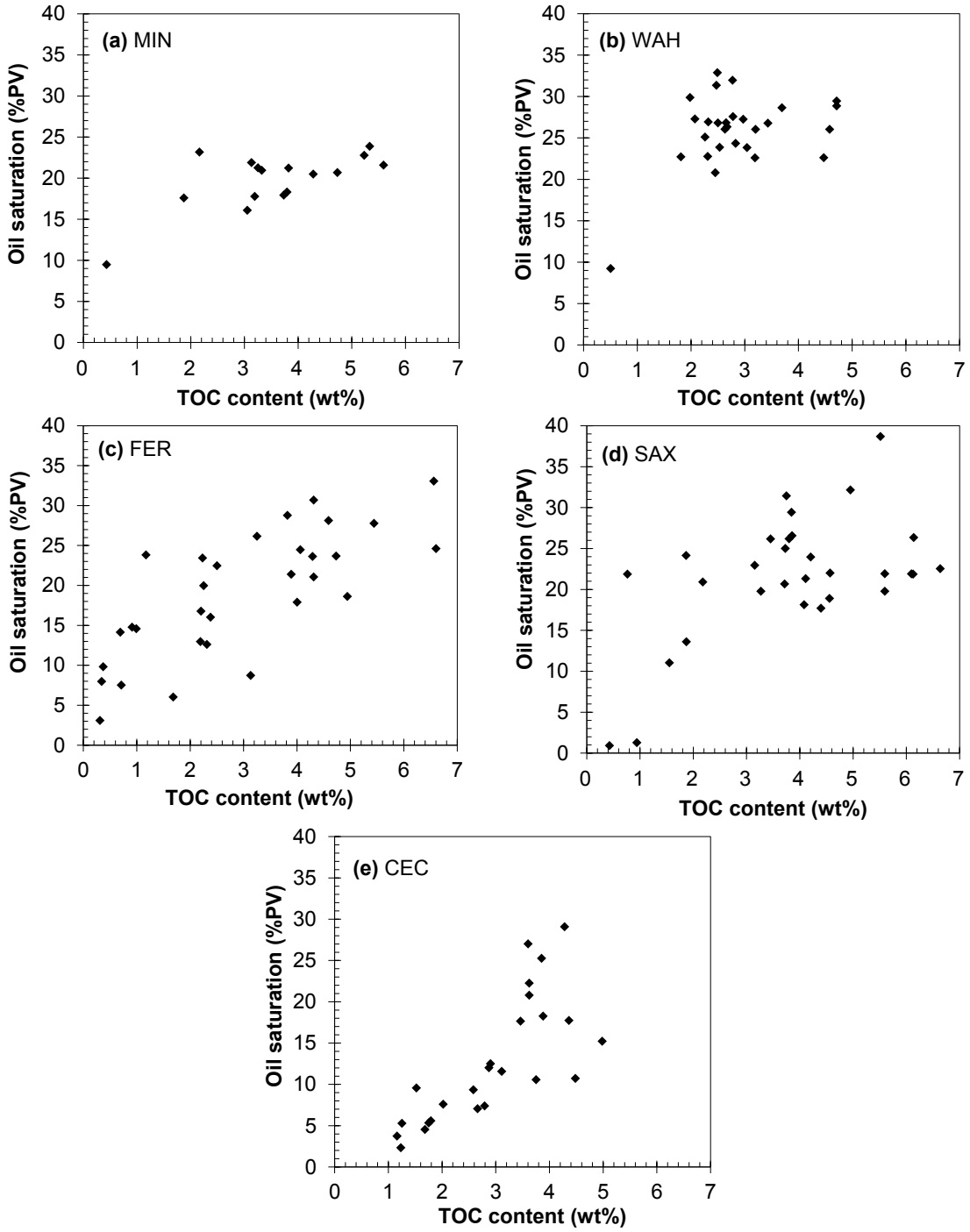

Fig. 2.15: The correlations of oil saturation vs. TOC content for the shale samples of (a) Minhik, (b) Wahigan, (c) Ferrier, (d) Saxon, and (e) Cecilia wells.

2.6 Wettability Indices Using Spontaneous-Imbibition Data

To analyze the results of wettability tests quantitatively, we use the imbibition data and define wettability indices. The imbibition rate data and Handy's (1960) model are incorporated to define an index referred to as "pore wettability index" of oil (PWI_o) and brine (PWI_w). Furthermore, I_o^{eq} and I_w^{eq} are used to calculate oil wettability index (WI_o).

2.6.1 Pore Wettability Index (PWI)

In this part, we define pore wettability index (PWI) using the initial rate of spontaneous imbibition. By calculating PWI for brine and oil imbibition experiments, we can compare the size and wetting affinity of pores that imbibe brine and oil. Handy (1960) showed that there is a linear relationship between square of imbibed volume (Q^2) and time (t) in 1-dimensional piston-like displacement (Eq. 2.8). Handy (1960) used the imbibition slope and calculated the effective capillary pressures (P_c),

$$Q^2 = \left(\frac{2P_c k_e \varphi_{acc} A^2 S_f}{\mu}\right) t \tag{2.8}$$

where Q is the volume of imbibed liquid, k_e is the effective permeability, φ_{acc} is the porosity accessible for liquid imbibition, A is the cross sectional area of the sample, S_f is the liquid saturation behind the imbibition front, μ is the liquid viscosity, and P_c is the capillary pressure. We use normalized imbibed volume (I_o or I_w) to account for the difference in pore volume of different plugs. Dividing both sides by square of effective pore volume ($A^2L^2\varphi_{eff}^2$) and also approximating the capillary pressure by the Young-Laplace equation (Young, 1805; Laplace, 1805) ($P_c = 2\sigma\cos\theta/r$), we have,

$$\left(\frac{Q}{AL\varphi_{eff}}\right)^2 = \left(\frac{2\left(\frac{2\sigma\cos\theta}{r}\right)k_e\varphi_{acc}A^2S_f}{\mu(A^2L^2\varphi_{eff}^2)}\right) t \tag{2.9}$$

where σ is the surface tension, θ is the contact angle, and r is the pore radius. Assuming $S_f = 1$, k_e and φ_{acc} are substituted by the absolute permeability (k_{Decay}) and the effective porosity (φ_{eff}), respectively. Moreover, $Q/AL\varphi_{eff}$ is substituted by I (I_o or I_w). The rock and fluid properties such as L, φ_{eff}, μ, σ, and k_{Decay} are shifted to the left side as shown in Eq. 2.10,

$$I^2 \times \left(\frac{L^2 \varphi_{eff} \mu}{4\sigma k_{Decay}}\right) = \left(\frac{\cos\theta}{r}\right) \times t \qquad (2.10)$$

If we plot $I^2 \times ((L^2 \varphi_{eff} \mu) / 4 \sigma k_{Decay})$ vs. time (t), we expect a straight line with the slope of cosθ/r which we refer to as "pore wettability index" (PWI). Higher PWI means higher wetting affinity to the imbibing liquid and/or smaller pores available for liquid uptake.

Figs. 2.16a and 2.16b show typical crossplots of $I^2 \times ((L^2 \varphi_{eff} \mu)/4 \sigma k_{Decay})$ vs. time for brine and oil imbibition experiments (FER1 and CEC2 samples), respectively. The slope of the fitted line represents PWI. The pore wettability indices of oil (PWI_o) and brine (PWI_w) for all 9 twin plugs are shown in Fig. 2.17, indicating that $PWI_o > PWI_w$. The rock wettability (cosθ) and pore radius (r) may be individually or collectively responsible for $PWI_o > PWI_w$. Figs. 2.5a and 2.5b show that oil completely spreads on the shale, while brine forms a droplet with non-zero contact angle. Complete spreading of oil means stronger wetting affinity of rock to oil, leading to higher cosθ. Moreover, the magnified SEM images in Fig. 2.9 show that majority of small nanopores exist in the organic part of the rock. The diameter of organic pores is generally < 100 nm and they have a strong wetting affinity for oil uptake. Smaller size of hydrophobic organic pores may lead to $PWI_o > PWI_w$ as shown in Fig. 2.17.

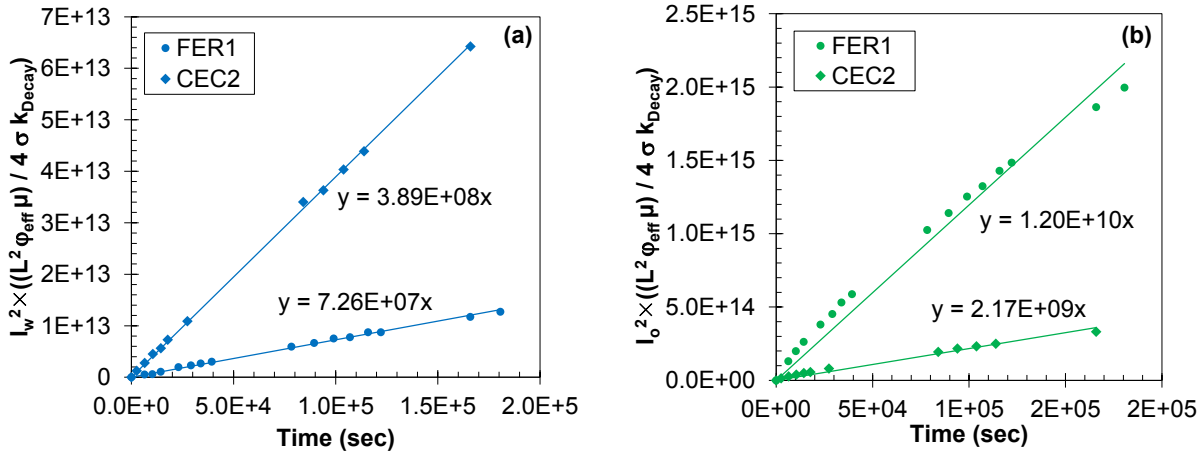

Fig. 2.16: The crossplots of $I^2 \times ((L^2 \varphi_{eff} \mu)/4 \sigma k_{Decay})$ vs. time for (a) brine and (b) oil imbibition tests of FER1 and CEC2 plugs. The slope of fitted line represents pore wettability index (PWI).

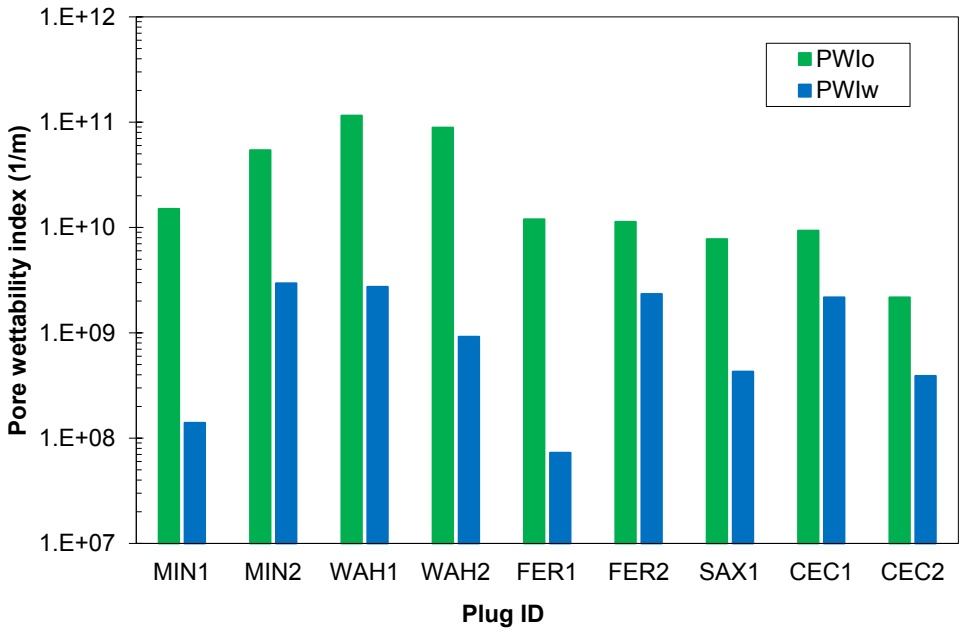

Fig. 2.17: The values of PWI_o and PWI_w for the twin plugs.

It is important to mention that we assumed $k_e = k_{Decay}$ and $\varphi_{acc} = \varphi_{eff}$. Assuming the same values of k_e and φ_{acc} for calculations of PWI_o and PWI_w may not be valid due to dual-wet behavior of shales (Yassin et al., 2016; Lan et al., 2015a). In a dual-wet system, hydrophobic organic pores may not have strong wetting affinity to brine. Therefore, the values of φ_{acc} and k_e may be different for oil and brine. In other words, the difference between PWI_o and PWI_w may be attributed to the dual-wet characteristics of the shale samples.

2.6.2 Oil Wettability Index (WI_o)

On the basis of oil and brine imbibition data vs. time (Figs. 2.6a and 2.6b), Lan et al. (2015a) defined WI_o that shows the comparative capacity of the rock for oil and brine uptake,

$$WI_o = \frac{I_o^{eq}}{I_o^{eq} + I_w^{eq}} \tag{2.11}$$

WI_o is calculated for twin plugs with the assumption that all petrophysical properties are the same. The values of I_w^{eq}, I_o^{eq}, and WI_o are listed in Table 2.8.

Table 2.8: The values of I_w^{eq}, I_o^{eq}, and WI_o.

Plug ID	I_w^{eq} (%PV)	I_o^{eq} (%PV)	WI_o
MIN1	12.7	69.9	0.85
MIN2	23.2	89.5	0.79
WAH1	30.4	54.9	0.64
WAH2	21.9	83.6	0.79
FER1	13.3	99.6	0.88
FER2	24.0	80.0	0.77
SAX1	13.6	54.0	0.80
CEC1	28.8	45.4	0.61
CEC2	34.5	70.6	0.67

In this section, we investigate the correlations of WI_o with petrophysical data including φ_{eff}, TOC content, ρ_{Bulk}, and oxygen index (OI).

2.6.2.1 TOC Content and φ_{eff}

The effective porosity (Table 2.1) of the 9 plugs is plotted vs. TOC content in Fig. 2.18a. Similar to Fig. 2.12, φ_{eff} generally increases by increasing the TOC content. This correlation suggests that the majority of connected pores exist within the organic part of the rock. Fig. 2.18b shows the positive correlation of WI_o with TOC content. This correlation suggests that the samples with higher organic matter generally have stronger affinity for oil imbibition and lower affinity for brine uptake as shown in Figs. 2.18c and 2.18d, respectively. The positive correlation between WI_o and TOC content is explained by the organic porosity of the samples. The pores in the organic matter constitute a significant portion of the effective porosity. Higher TOC content provides higher number of organic nanopores, and subsequently higher specific surface area (Zhu et al., 2016). It leads to higher oil adsorption on the surface of organic matter (Wang et al., 2015), and higher oil imbibition into organic pores. According to Figs. 2.18e and 2.18f, the samples with higher φ_{eff} generally imbibe more oil and less brine, respectively. Similar to the previous arguments, the samples with higher φ_{eff} have higher number of pores within the organic matter. The existence of more hydrophobic pathways within the organic matter leads to higher oil imbibition.

It is important to mention that the negative correlations of I_w^{eq} with TOC content and φ_{eff} (Figs. 2.18d and 2.18f) are not as strong as the positive correlations of I_o^{eq} with TOC content and φ_{eff} (Figs. 2.18c and 2.18e). The weaker correlations of I_w^{eq} compared with I_o^{eq} suggest that I_w^{eq} may not have functional dependence on the organic-matter content. As discussed in Fig. 2.10, brine can

only imbibe into hydrophilic inorganic pores which are independent of hydrophobic pores within the organic matter.

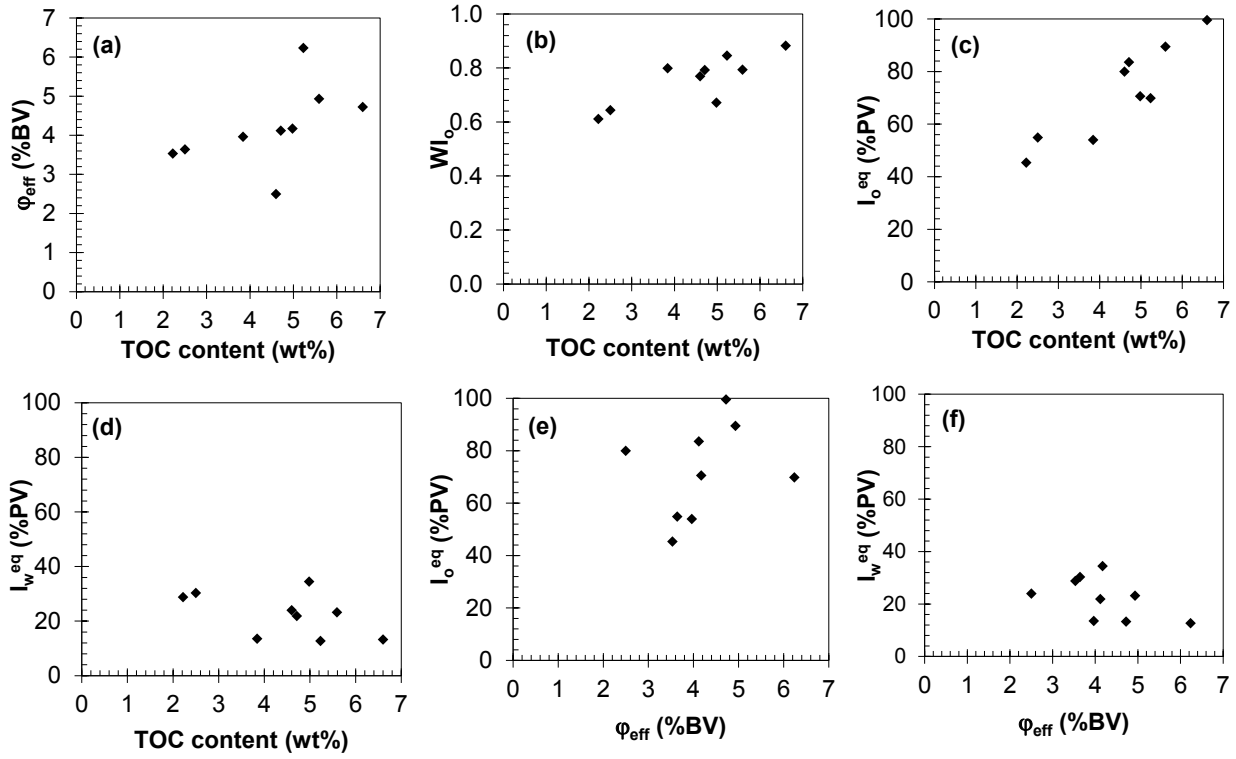

Fig. 2.18: The crossplots of (a) φ_{eff} vs. TOC content, (b) WI_o vs. TOC content, (c) I_o^{eq} vs. TOC content, (d) I_w^{eq} vs. TOC content, (e) I_o^{eq} vs. φ_{eff}, and (f) I_w^{eq} vs. φ_{eff}.

2.6.2.2 Bulk Density (ρ_{Bulk})

Fig. 2.19a presents the negative correlation of ρ_{Bulk} (Table 2.1) vs. TOC content, which is explained by the positive and negative correlations of TOC content with φ_{eff} and ρ_{Matrix}, respectively. Fig. 2.19b shows the crossplot of WI_o vs. ρ_{Bulk}, indicating that the samples with higher ρ_{Bulk} generally have lower WI_o. It can be explained by the fact that the shale samples with higher ρ_{Bulk} generally have lower organic matter (Fig. 2.19a), and consequently lower wetting affinity to oil.

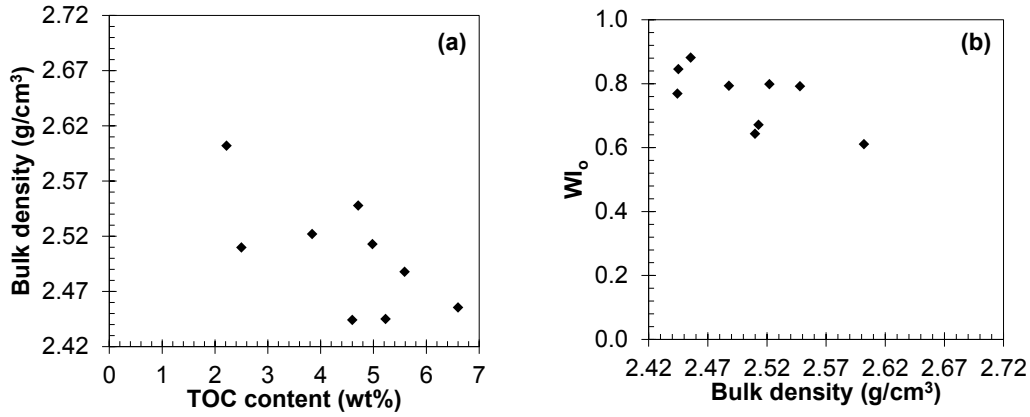

Fig. 2.19: The crossplots of (a) ρ_{Bulk} vs. TOC content and (b) WI_o vs. ρ_{Bulk}.

2.6.2.3 Oxygen Index (OI)

Fig. 2.20a presents the crossplot of WI_o vs. OI. The samples with higher OI generally have lower WI_o. This negative correlation suggests that the samples with higher OI have lower wetting affinity for oil imbibition and higher wetting affinity for brine imbibition as shown in Figs. 2.20b and 2.20c, respectively.

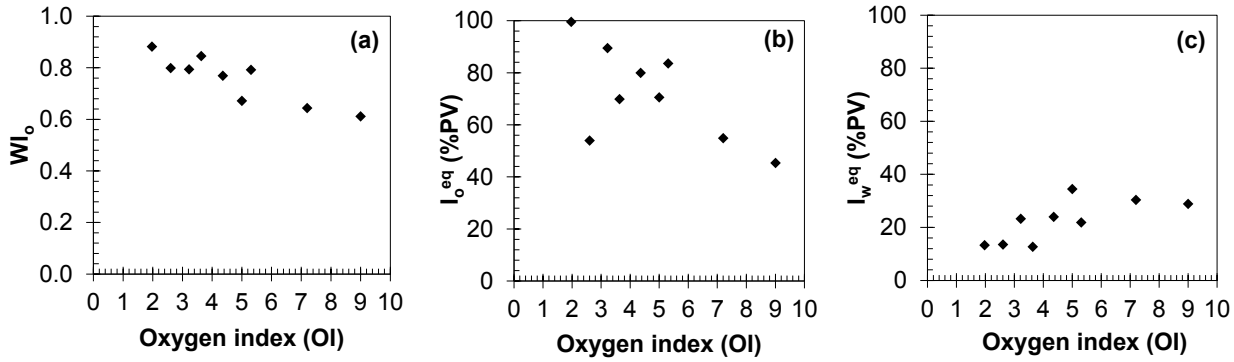

Fig. 2.20: The crossplots of (a) WI_o, (b) I_o^{eq}, and (c) I_w^{eq} vs. oxygen index (OI).

OI is used for determining the type of kerogen (Lafargue et al., 1998), and shows the oxygen content of the source rock (Hu et al., 2014). OI represents the oxygen/carbon ratio of kerogen in the Van Krevelan diagram (Krevelen, 1950), and can be attributed to the level of kerogen maturity. Hetényi (1998) found relatively good correlations of OI with vitrinite reflectance index (%R_o) in numerous samples from organic-rich sediments. Vitrinite reflectance index is a measure of the percentage of incident light reflected from the surface of vitrinite particles, and is used for determining the maturation level of organic matter. The reflectance of light increases by increasing the maturation level (Hunt, 1979). Hetényi (1998) suggested that OI can be used as an indicator

for the level of maturity. The samples with higher maturity levels are expected to have lower values of OI (Tissot and Welte, 1984). To explain the negative trend shown in Fig. 2.20a, we investigate the effects of kerogen maturity on 1) the abundance of organic pores and 2) the hydrophobicity of organic matter.

1) Kerogen maturity and abundance of organic pores. Loucks et al. (2009) conducted a comprehensive study on morphology, genesis, and distribution of nanopores in siliceous mudstones of the Barnett shale. They reported a strong correlation between pore abundance in organic matter and vitrinite reflectance; suggesting that pore formation is the result of thermal maturation and conversion of the organic matter to hydrocarbon. Loucks et al. (2009) used SEM analysis and observed that organic matter in less mature samples ($R_o < 0.7\%$) has few or no pores compared with that in highly mature samples ($R_o > 0.8\%$). Cao and Zhou (2015) also showed that the number of organic pores is higher in samples with higher kerogen maturity. According to Fig. 2.20a, the shale samples with higher OI may have lower kerogen maturity, and subsequently lower number of organic pores. A reduction in the number of organic pores may lead to lower specific surface area for adsorption and imbibition of oil into organic matter (Zhu et al., 2016), and therefore lower WI_o (Fig. 2.20a).

2) Kerogen maturity and kerogen wettability. Hu et al. (2016) conducted pore-scale molecular dynamics simulations to understand the relationship between kerogen maturity and kerogen wettability. The results of simulations demonstrated that kerogen maturity affects the wettability of organic pores. The authors showed that kerogen may be hydrophobic at high maturities, neutral-wet at intermediate maturities, or even hydrophilic at very low maturities. Higher hydrophobicity of kerogen in the samples with higher kerogen maturity (lower OI) may be another possibility to explain the negative correlation of WI_o with OI.

2.7 Summary

In this chapter, we conducted spontaneous-imbibition tests and measured air/oil and air/brine contact angles of 9 twin plugs from 5 wells drilled in the Duvernay Formation, which is a self-sourced reservoir located in the Western Canadian Sedimentary Basin (WCSB). We investigated wettability of the shale samples with a wide range of total organic carbon (TOC) content (2.2-6.6 wt%), effective porosity (φ_{eff}, 2.0-6.2% BV), and kerogen maturity (wet-gas, dry-gas, and over-

mature). We characterized the samples by measuring φ_{eff}, pressure-decay permeability (k_{Decay}), oil saturation (S_o), bulk density (ρ_{Bulk}), matrix density (ρ_{Matrix}), mineralogy, TOC content, and conducting rock-eval pyrolysis test. To investigate the role of pore connectivity, we also measured spontaneous imbibition and contact angles of oil and water in crushed shale packs (CSP) and compared the results with those of similar tests on the plugs. To examine the role of organic matter on petrophysical properties, we also investigated the crossplots of φ_{eff}, k_{Decay}, ρ_{Bulk}, ρ_{Matrix}, and S_o vs. TOC content, by using 147 data points from shale samples of the 5 Duvernay wells. Finally, to analyze the results of wettability tests quantitatively, the imbibition data were used to define pore wettability index (PWI) and oil wettability index (WI_o).

The key findings of this chapter are the following:

1- The results of contact-angle and spontaneous-imbibition tests on shale plugs show that the wetting affinity of the samples to oil is much stronger than that to brine. High wetting affinity to oil is attributed to abundant hydrophobic nanopores within the organic matter, confirmed by the SEM/EDS analyses. These hydrophobic nanopores with diameter < 100 nm may explain high imbibed volume of oil compared with that of brine as well as late equilibrium of oil imbibition.

2- SEM/EDS analyses also show large micropores bordered by inorganic minerals such as quartz, calcite, and feldspar/clays. These hydrophilic micropores with diameter > 1000 nm may explain early equilibrium of brine in spontaneous-imbibition tests.

3- The results of spontaneous-imbibition tests and contact-angle measurements show that powdering the shale samples generates more hydrophobic surface area, and subsequently increases wetting affinity of CSPs to oil. Higher accessibility to static organic carbon (SOC) may be responsible for stronger hydrophobicity of the CSPs compared with the plugs.

4- Analysis of 147 Duvernay shale samples shows that there is a positive correlation between TOC content and φ_{eff}. This positive correlation indicates that the pores within the organic matter constitute a significant portion of effective porosity. Moreover, the positive relationship of TOC content with k_{Decay} indicates that the majority of pores in the organic matter are well connected.

5- The results of spontaneous-imbibition tests on the plugs show that the samples with higher TOC content generally have higher WI_o. WI_o also has negative correlations with ρ_{Bulk} and oxygen index (OI). The negative correlation of WI_o with OI is explained by 1) higher number of organic

nanopores and 2) stronger hydrophobicity of kerogen in the samples with higher kerogen maturity (lower OI).

Nomenclature

A = Surface area, L^2 [cm^2, m^2]
BV = Bulk volume, L^3 [cm^3, m^3]
BV_{CSP} = Bulk volume of CSP, L^3 [cm^3]
D = Diameter, L [cm, m]
f = Fractions of solid components, dimensionless
HI = Hydrogen index, dimensionless
I_o = Normalized imbibed volume of oil, [%PV]
I_o^{eq} = Equilibrated I_o, L^3/L^3 [%PV]
I_w = Normalized imbibed volume of brine,[%PV]
I_w^{eq} = Equilibrated I_w, L^3/L^3 [%PV]
k_e = Effective permeability, L^2 [m^2]
k_{Decay} = Pressure-decay permeability, L^2 [nD, m^2]
L = Length of plug, L [cm, m]
L_s = Characteristic length of plug, L [m]
m_{powder} = Powder mass, M [g]
MOC = Mobile organic carbon, [%TOC]
OI = Oxygen index, dimensionless
P_c = Capillary pressure, $ML^{-1}t^{-2}$ [pa]
PI = Production index, dimensionless
PV = Pore volume, L^3 [cm^3, m^3]
PWI_o = Pore wettability index of oil, L^{-1} [1/m]
PWI_w = Pore wettability index of brine, L^{-1} [1/m]
Q = Imbibed volume of liquid, L^3 [m^3]
r = Pore radius, L [m]
$\bar{r}$ = Average roughness ratio, dimensionless
R_o = Reflectance index, %
S_1 = Free hydrocarbons, M/M [mg/g]
S_2 = Hydrocarbons from kerogen, M/M [mg/g]
S_3 = CO_2 yield in kerogen pyrolysis, M/M [mg/g]
S_f = Front saturation of liquid, L^3/L^3 [%PV]
S_o = Oil saturation, L^3/L^3 [%PV]
SOC = Static organic carbon, [%TOC]
TOC = Total organic carbon, M/M% [wt%]
t = Time, t [s, hour]
t_D = Dimensionless time, dimensionless
T_{max} = Temperature of maximum hydrocarbon yield
WI_o = Oil wettability index, dimensionless
ω_{TOC} = Weight fraction of TOC, dimensionless
φ_{eff} = Effective porosity, L^3/L^3 [%BV]
φ_{CSP} = Porosity of CSP, L^3/L^3 [%BV]
ρ = Density, ML^{-3} [kg/m^3]
ρ_{Bulk} = Bulk density, ML^{-3} [kg/m^3]
ρ_{Matrix} = Matrix density, ML^{-3} [kg/m^3]
ρ_{TOC} = Organic-matter density, ML^{-3} [kg/m^3]
θ = Contact angle, degree
θ_{app} = Apparent contact angle, degree
θ_{int} = Intrinsic contact angle, degree
ω = Weight fraction, dimensionless
σ = Surface tension, Mt^{-2} [mN/m]
μ = Viscosity, $ML^{-1}t^{-1}$ [cp]

Abbreviations

CEC = Cecilia
CSP = Crushed shale pack
EDS = Energy-dispersive x-ray spectroscopy
FER = Ferrier
LD = Lower Duvernay
MIN = Minhik
MICP = Mercury injection capillary pressure
P_{Dew} = Dewpoint pressure
SAX = Saxon
SEM = Scanning electron microscopy
TRA = Tight-rock analysis
WAH = Wahigan
WCSB = Western Canadian Sedimentary Basin
XRD = x-ray diffraction

Chapter 3

Effect of Kerogen Maturity on Shale Wettability

3.1 Introduction

Unconventional oil and gas resources are becoming the largest contributors of hydrocarbons in North America (Stark et al., 2008; Wang et al., 2014). Due to the concern that conventional resources will not meet the growing demand for energy worldwide, unconventional resources are considered as viable and economically important sources of energy in the future (Law and Curtis, 2002; Stark et al., 2008). In particular, organic-rich shales are now considered as potential hydrocarbon resources across the world (Gonzalez et al., 2013). Producing hydrocarbons from these resources is challenging due to their ultralow porosity and permeability (Jarvie, 2014).

Unconventional oil and gas resources with low porosity (< 10%) and ultralow permeability (microdarcy for tight siltstones and nanodarcy for shale source rocks) (Jarvie, 2014) can produce hydrocarbons at economic rates by the technologies of horizontal drilling and multistage hydraulic fracturing (Montgomery and Smith, 2010). During the hydraulic fracturing operation, a large volume of water is injected into reservoir, resulting in a complex fracture network for hydrocarbon production (Britt, 1985). The water injected into reservoir interacts with reservoir rock, depending on rock/fluid properties such as wettability. Due to such interactions, usually a small fraction of the injected water can be recovered during flowback process (Ghanbari et al., 2013; Dehghanpour et al., 2012 and 2013). Wettability describes the affinity of rock to a certain fluid in the presence of another immiscible fluid (Dake, 1977), and controls pore-scale distribution of reservoir fluids (Morrow, 1990; Anderson, 1986a and 1987b). Evaluating wettability of shales is challenging due to the presence of organic matter and clay minerals but is essential for designing optimum fluids for fracturing as well as enhanced oil recovery operations. In general, wettability is a complicated parameter which

depends on the rock texture and composition, pore morphology, and physicochemical properties of reservoir fluids (Drummond and Israelachvili, 2004; Buckley, 2001).

Various techniques such as Nuclear Magnetic Relaxation (NMR) (Brown and Fatt, 1956), contact angle (Johnson and Dettre, 1969), spontaneous imbibition (Bobek et al., 1958), and USBM wettability index (Donaldson et al., 1969) have been introduced to measure wettability of reservoir rocks. Measuring wettability of shales is challenging due to their complex pore structures within organic and inorganic materials (Passey et al., 2010; Curtis et al., 2011; Clarkson et al., 2013). Different researchers have demonstrated the dependence of shale wettability on pore structure and connectivity (Kibria et al., 2018; Lan et al., 2015a). Recent studies show that measuring contact angle may lead to inconsistent results for wettability of shales (Habibi et al., 2016; Lan et al., 2015b; Dehghanpour et al., 2012; Xu and Dehghanpour, 2014). Instead, measuring spontaneous imbibition of oleic and aqueous phases has been successfully used to evaluate wettability of shales and tight rocks (Habibi et al., 2016; Lan et al., 2015b; Zhou et al., 2002; Takahashi et al., 2010).

It is of great interest to understand the functional dependence of wettability on other petrophysical and petrographic properties such as porosity, permeability, mineralogy, total organic carbon (TOC) content, and kerogen maturity level. Recent studies show that wettability of organic shales strongly depends on TOC content (Lan et al., 2015b; Begum et al., 2017; Yassin et al., 2017 and 2018a). However, in addition to TOC content, thermal maturity level can influence the wettability of organic shales. Several studies demonstrated the dependence of wettability on type of source rock as well as thermal maturity of kerogen (Odusina et al., 2011; Peng et al., 2015; Gupta et al., 2018). Boult et al. (1997) found that organic-rich shales become oil-wet as kerogen becomes more mature. Hu et al. (2014 and 2016) conducted molecular dynamics simulations and found that highly mature kerogen is hydrophobic whereas immature kerogen tends to be hydrophilic. Furthermore, the number and size of organic pores depend on the thermal maturity of kerogen. It has been shown that organic porosity evolves by increasing kerogen maturity level (Curtis et al., 2011; Cao and Zhou, 2015). Munson (2015) analyzed shale samples with different kerogen maturity levels and found that organic pore morphology varies with the maturity level. The organic pores of source rocks host the hydrocarbon produced over geological time-scales (Curtis et al., 2011; Akkutlu et al., 2012; Xiong et al., 2012). The residual hydrocarbon in organic pores may affect the wettability of plugs analyzed by laboratory tests.

In Chapter 3, we evaluate the wettability of several plugs from 6 wells drilled in the Duvernay Formation. The samples were collected from zones with different thermal maturity levels. We characterize the shale samples by measuring pressure-decay permeability (k_{Decay}), effective porosity (φ_{eff}), initial oil and water saturations (S_o and S_w), mineralogy, and TOC content. We conduct scanning electron microscopy (SEM) and energy-dispersive x-ray spectroscopy (EDS) to characterize the type, size, and spatial distribution of pores, and to explain the results of wettability tests. Finally, we analyze the functional dependence of wettability on petrophysical and petrographic properties of the shale samples, and in particular, on thermal maturity of kerogen.

3.2 Geological Background of the Duvernay Formation

3.2.1 Origin and Geology

The Duvernay Formation is one of the stratigraphic units of Upper Devonian age deposited during the maximum transgressive stage of the Woodbend Group (Fig. 2.1a) in the Western Canadian Sedimentary Basin (Stoakes, 1980; Switzer et al., 1994). Transgressive and high-stand sea levels along with high rates of primary productivity provided favourable conditions to preserve high amounts of organic matter, forming a world-class source rock and now a self-sourced reservoir (Fothergill et al., 2014). Duvernay has been characterized as a source rock for many of the large Devonian oil and gas pools in Alberta (Low, 2012). This Formation is characterized by three lithofacies: 1) siliceous organic-rich mudstones, 2) argillaceous mudstones, and 3) non-reservoir carbonates (Dunn and Humenjuk, 2014).

3.2.2 Location

Duvernay Formation covers an area of over 50,000 mi^2 in central Alberta. The prospective area of the Duvernay shale is divided into Kaybob in the north, Edson-Willesden Green in the center, and Innisfail in the south (Fig. 2.1b in Chapter 2). We select 17 twin plugs from 6 wells called AOK, MIN, WAH, FER, SAX, and CEC. MIN and FER wells are located in the Innisfail region, while AOK, WAH, SAX, and CEC wells are in the Kaybob region. Unique well identifiers (UWI) of AOK, MIN, WAH, FER, SAX, and CEC are 2-7-65-18W5, 2-6-44-5, 6-6-64-22w5, 12-4-42-8, 11-08-62-24w5, and 11-34-57-23, respectively.

We divide the Duvernay Formation into Upper (UD) and Lower (LD) parts. UD (Depth < 3000 m) and LD (Depth > 3000 m) samples have different properties in terms of organic-matter content and kerogen maturity level. In Chapter 2, we evaluated the wettability of the LD plugs.

3.3 Materials and Data

3.3.1 Rock Samples

As listed in Table 3.1, we select 8 twin plugs from AOK well drilled in the UD Formation. The plugs are named AOK1 to AOK8 as depth increases from 2783.66 m (AOK1) to 2802.94 m (AOK8). We also select 9 twin plugs from 5 wells in the LD Formation. We have two twin plugs for all LD wells, except for SAX with only one twin plugs. The depth of LD plugs ranges from 3095.32 m (MIN1) to 3963.02 m (CEC2). All plugs were drilled horizontally from the full-diameter cores. The downhole temperatures of MIN, WAH, FER, SAX, and CEC wells are 112, 111, 113, 110, and 124°C, respectively; while the downhole temperature of AOK well is 93°C.

3.3.2 Tight-Rock Analysis (TRA)

Table 3.1 lists the results of TRA, including effective porosity (φ_{eff}), pressure-decay permeability (k_{Decay}), and initial saturations of gas (S_g), oil (S_o), and water (S_w). A commercial laboratory used offset crushed samples to measure φ_{eff} and k_{Decay} by Boyle's law helium-porosimetry and pressure-decay methods, respectively. Using crushed samples for measuring φ_{eff} and k_{Decay} allows access to tight pore space and reduces the effects of artifacts such as non-natural features (Handwerger et al., 2011). LD plugs generally have higher values of φ_{eff} and k_{Decay}. The ranges of φ_{eff} for UD and LD samples are 2.83-3.93% and 2.50-6.24% of bulk volume (BV), respectively. The ranges of k_{Decay} for UD and LD samples are 98.27-141.51 nD and 102.15-287.82 nD, respectively.

Table 3.1 also lists the values of S_g, S_o, and S_w measured by retort method on offset crushed samples. To measure S_w, crushed samples are heated up to 120°C, and the extracted vapor is condensed by cooling. The accumulated condensed liquid is comprised of water and oil. The temperature is further increased to 315°C to extract the rest of oil remained in crushed samples. The water content condensed from 120 to 315°C is considered as clay-bound water (Handwerger et al., 2012), which is not taken into account for the calculation of S_w data listed in Table 3.1. S_w

is less than 14% of pore volume (PV), suggesting sub-irreducible water saturation conditions. It is important to mention that we received the plugs two months after saturation measurements by the commercial laboratory. Despite preserving the plugs in cellophane coatings, it is expected that a portion of water and oil contents were evaporated after two months. Therefore, the actual S_o and S_w at the start of experiments are expected to be lower than those listed in Table 3.1. We tested all plugs as-received and did not use any washing fluids such as toluene or methanol.

3.3.3 XRD Analysis

Table 3.2 lists the mineralogy of the plugs measured by x-ray diffraction (XRD) method. Quartz, calcite, K-feldspar, and plagioclase are the dominant non-clay minerals; whereas mixed layers of illite/mica and illite/smectite are the main clay minerals in both UD and LD samples.

3.3.4 Rock-Eval Pyrolysis

Table 3.3 lists the results of rock-eval pyrolysis tests on offset samples for determining kerogen type, kerogen maturity, and TOC content. The values of TOC content, S_1, S_2, S_3, T_{max}, hydrogen index (HI), oxygen index (OI), and production index (PI) are listed in this table. TOC content is the total amount of organic carbon present in the shale sample and represents the quality of the source rock in terms of petroleum potential (Baskin, 1997). TOC content is more than 2 wt%, classifying the samples as "very good" source rock in terms of petroleum potential (Baskin, 1997). S_1 is the amount of free hydrocarbons present in the rock, S_2 represents the amount of hydrocarbons after thermal cracking of kerogen, and S_3 represents the amount of oxygen-containing compounds (such as CO_2) that are produced over thermal cracking of kerogen (Lafargue et al., 1998). T_{max} is the maximum temperature needed to release the highest amount of hydrocarbons by thermal cracking of kerogen (S_2). HI, OI, and PI are calculated using S_1, S_2, S_3, and TOC content, as listed in Table 3.3 (Tissot and Welte, 1984).

Table 3.1: Tight-rock analysis (TRA) of the UD and LD plugs. The diameters of UD and LD plugs are 2.5 and 3.8 cm, respectively. Subscripts o and w represent oil and brine, respectively.

Formation	Plug ID	Depth (m)	Length (cm)	φ_{eff} (%BV)	k_{Decay} (nD)	S_g (%PV)	S_o (%PV)	S_w (%PV)
Upper Duvernay (UD)	$AOK1_o$	2783.66	7.6	2.83	98.27	56.70	40.41	2.89
	$AOK1_o$	2783.97	7.6	2.83	98.27	56.70	40.41	2.89
	$AOK2_o$	2786.94	7.6	3.24	112.35	56.43	40.67	2.90
	$AOK2_o$	2786.97	7.6	3.24	112.35	56.43	40.67	2.90
	$AOK3_o$	2789.24	7.6	2.97	102.85	54.76	42.01	3.23
	$AOK3_w$	2789.27	7.6	2.97	102.85	54.76	42.01	3.23
	$AOK4_o$	2791.85	7.6	3.08	105.72	46.85	47.55	5.60
	$AOK4_o$	2791.88	7.6	3.08	105.72	46.85	47.55	5.60
	$AOK5_o$	2794.88	7.6	3.32	115.69	59.84	34.42	5.74
	$AOK5_w$	2794.91	7.6	3.32	115.69	59.84	34.42	5.74
	$AOK6_o$	2798.36	7.6	3.62	127.68	66.93	28.94	4.13
	$AOK6_w$	2798.39	7.6	3.62	127.68	66.93	28.94	4.13
	$AOK7_o$	2800.57	7.6	3.93	141.51	60.08	32.44	7.48
	$AOK7_w$	2800.60	7.6	3.93	141.51	60.08	32.44	7.48
	$AOK8_o$	2802.91	7.6	3.33	115.75	57.41	31.38	11.21
	$AOK8_o$	2802.94	7.6	3.33	115.75	57.41	31.38	11.21
Lower Duvernay (LD)	$MIN1_w$	3095.32	3.3	6.24	287.82	74.36	22.79	2.85
	$MIN1_o$	3095.41	3.6	6.24	287.82	74.36	22.79	2.85
	$MIN2_w$	3103.05	6.1	4.93	236.20	73.58	20.95	5.47
	$MIN2_o$	3103.10	5.6	4.93	236.20	73.58	20.95	5.47
	$WAH1_w$	3308.62	3.3	3.64	102.15	72.92	26.82	0.26
	$WAH1_o$	3308.69	3.8	3.64	102.15	72.92	26.82	0.26
	$WAH2_w$	3313.37	3.8	4.12	130.21	68.32	29.47	2.21
	$WAH2_o$	3313.42	3.8	4.12	130.21	68.32	29.47	2.21
	$FER1_w$	3440.14	5.3	4.72	242.75	66.33	24.61	9.06
	$FER1_o$	3440.18	5.7	4.72	242.75	66.33	24.61	9.06
	$FER2_w$	3464.37	4.3	2.50	131.31	93.29	6.04	0.67
	$FER2_o$	3464.42	4.7	2.50	131.31	93.29	6.04	0.67
	$SAX1_w$	3795.73	5.3	3.96	274.78	67.50	29.44	3.06
	$SAX1_o$	3795.73	5.4	3.96	274.78	67.50	29.44	3.06
	$CEC1_w$	3949.30	4.4	3.53	286.66	76.93	9.50	13.57
	$CEC1_o$	3949.34	4.1	3.53	286.66	76.93	9.50	13.57
	$CEC2_w$	3962.98	4.6	4.17	235.65	78.26	15.22	6.52
	$CEC2_o$	3963.02	4.6	4.17	235.65	78.26	15.22	6.52

Table 3.2: Mineralogy of UD and LD samples. The unit of XRD results is wt%.

Formation	Plug ID	Depth (m)	Quartz	K-Feldspar	Plagioclase	Calcite	Dolomite	Ankerite/Fe-Dolomite	Pyrite	Barite	Fluorapatite	Total non-clay	Illite/Smectite	Illite/Mica	Chlorite	Kaolinite	Total clay
			Non-clay minerals										Clay minerals				
Upper Duvernay (UD)	AOK1	2783.66	62.6	1.1	2.9	11.7	1.0	5.2	1.5	0.1	0.5	86.6	4.6	7.6	1.2	0.0	13.4
	AOK2	2786.94	50.5	6.2	0.7	16.3	2.0	2.8	3.0	0.0	0.0	81.5	5.5	11.9	1.1	0.0	18.5
	AOK3	2789.27	46.9	0.6	3.8	15.2	1.5	3.4	2.9	0.2	0.0	74.5	5.5	18.6	1.3	0.1	25.5
	AOK4	2791.85	39.6	6.9	5.9	12.1	0.9	2.4	3.4	0.2	0.0	71.4	10.5	15.8	1.6	0.7	28.6
	AOK5	2794.91	51.8	1.2	4.1	13.1	1.5	2.7	2.7	0.4	0.0	77.5	9.0	12.8	0.7	0.0	22.5
	AOK6	2798.36	64.2	1.7	3.0	8.7	1.9	2.2	2.1	0.2	0.0	84.0	2.8	12.4	0.8	0.0	16.0
	AOK7	2800.60	54.2	1.7	2.9	9.7	1.2	3.4	2.5	0.2	0.1	75.9	10.8	10.7	1.1	1.5	24.1
	AOK8	2802.94	54.1	3.7	3.6	8.8	1.5	2.0	2.0	0.6	0.0	76.3	11.0	11.3	0.6	0.8	23.7
Lower Duvernay (LD)	MIN1	3095.45	43.2	1.7	2.7	13.8	1.5	3.5	4.0	0.4	0.0	70.8	7.2	18.4	3.6	0.0	29.2
	MIN2	3103.48	36.3	8.0	0.6	20.1	2.0	1.0	1.0	1.0	0.0	70.0	9.0	17.0	4.0	0.0	30.0
	WAH1	3308.73	47.3	2.5	3.5	7.7	1.1	3.2	2.0	0.5	0.0	67.8	8.0	21.7	1.8	0.7	32.2
	WAH2	3313.22	47.9	3.3	4.6	11.4	2.0	2.0	4.0	0.8	0.0	76.0	5.0	17.0	2.0	0.0	24.0
	FER1	3441.85	35.5	2.3	3.8	14.6	1.8	0.4	4.1	1.4	0.3	64.2	5.1	26.3	2.8	1.6	35.8
	FER2	3464.29	47.8	2.2	6.5	9.6	1.9	1.0	2.9	0.1	0.0	72.0	8.2	16.9	1.9	1.0	28.0
	SAX1	3795.88	36.7	6.5	4.0	15.3	0.5	3.5	3.6	0.1	0.0	70.2	9.3	18.5	1.8	0.2	29.8
	CEC1	3948.54	22.3	3.6	5.3	29.5	4.4	3.6	2.0	0.3	0.0	71.0	6.6	18.4	3.2	0.8	29.0
	CEC2	3963.81	30.9	9.3	6.8	22.2	6.1	2.3	4.4	0.2	0.0	82.2	3.4	13.2	1.2	0.0	17.8

Table 3.3: Results of rock-eval pyrolysis.

Formation	Plug ID	Depth (m)	TOC (wt%)	S_1 (mg/g)	S_2 (mg/g)	S_3 (mg/g)	T_{max} (^oC)	HI[1]	OI[2]	PI[3]	Maturity window
Upper Duvernay	AOK1	2783.66	2.75	2.03	2.60	0.14	452	155.69	8.38	0.44	Oil
	AOK2	2786.94	3.13	2.42	3.43	0.19	451	147.84	8.19	0.41	Oil
	AOK3	2789.27	2.90	2.78	4.94	0.23	455	154.86	7.21	0.36	Oil
	AOK4	2791.85	3.01	2.73	5.02	0.22	455	140.22	6.15	0.35	Oil
	AOK5	2794.91	3.21	2.38	4.57	0.19	458	150.33	6.25	0.34	Oil
	AOK6	2798.36	3.49	3.16	5.26	0.15	456	167.52	4.78	0.38	Oil
	AOK7	2800.60	3.80	3.30	4.47	0.20	456	156.84	7.02	0.37	Oil
	AOK8	2802.94	3.25	2.55	4.93	0.19	458	157.01	6.05	0.34	Oil
Lower Duvernay	MIN1	3095.45	5.2	0.20	2.71	0.19	480	51.81	3.63	0.07	Dry-gas
	MIN2	3103.48	5.6	0.22	3.05	0.18	481	54.50	3.22	0.07	Dry-gas
	WAH1	3308.73	2.5	0.08	1.69	0.18	475	67.60	7.20	0.04	Wet-gas
	WAH2	3313.22	4.7	0.17	3.70	0.25	468	78.56	5.30	0.04	Wet-gas
	FER1	3441.85	6.6	0.16	3.28	0.13	476	49.70	1.97	0.05	Dry-gas
	FER2	3464.29	4.6	0.27	2.35	0.20	481	51.20	4.36	0.10	Dry-gas
	SAX1	3795.88	3.8	4.36	4.36	0.10	466	113.51	2.60	0.50	Wet-gas
	CEC1	3948.54	2.2	0.09	0.22	0.21	594	10.00	9.00	0.29	Over-matured
	CEC2	3963.81	4.9	0.10	0.45	0.24	606	9.00	5.00	0.18	Over-matured

[1] Hydrogen index = (S_2×100/TOC) [2] Oxygen index = (S_3×100/TOC)

[3] Production index = (S_1/(S_1+S_2))

According to the Van Krevelen diagram (Krevelen, 1950) presented in Fig. 3.1a, the crossplot of HI vs. OI can be interpreted to determine the type of kerogen. Fig. 3.1a shows that the kerogen types of both UD and LD samples are Type II, indicating the potential of the shale samples to produce a mix of oil and gas. Lower values of OI and HI represent higher maturity of kerogen (Krevelen, 1950), suggesting that the maturity of LD samples is generally higher than that of UD samples.

The crossplot of PI vs. T_{max} (Fig. 3.1b) can be interpreted to identify kerogen maturity level. T_{max} ranging from 435 to 455°C indicates that kerogen has reached the thermal maturity to produce oil (Baskin, 1997). As shown in Fig. 3.1b, most of the UD samples are located around the boundaries of oil and wet-gas windows, indicating that the UD samples have been producing oil and wet-gas. The crossplot of PI vs. T_{max} for LD samples suggests that WAH and SAX samples are in the wet-gas window, MIN and FER samples are in the dry-gas window, and CEC samples are over-mature. T_{max} (LD) is typically higher than T_{max} (UD), indicating that the thermal maturity of LD samples is typically higher than that of UD samples (Lafargue et al., 1998).

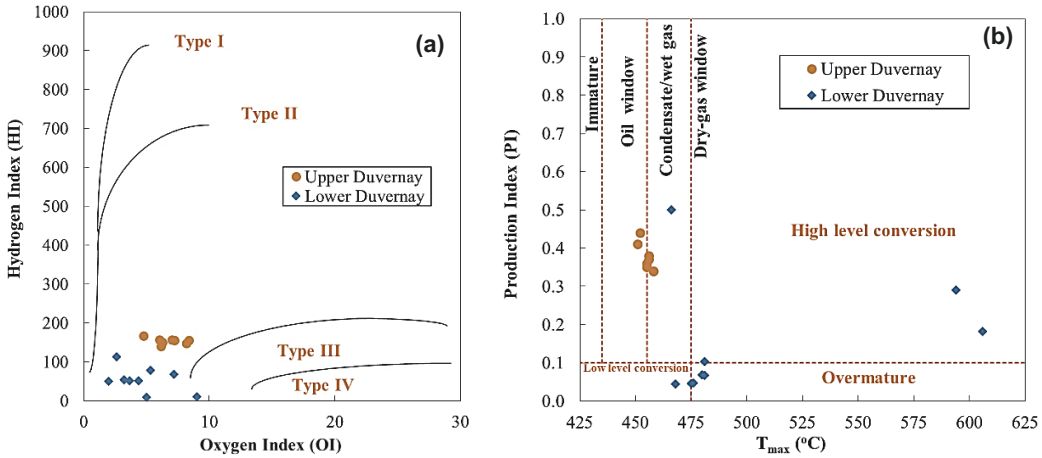

Fig. 3.1: The crossplots of (a) HI vs. OI for determining kerogen type and (b) PI vs. T_{max} for determining kerogen maturity level.

3.3.5 Reservoir Fluids

We use reservoir oil and brine (flowback brine) for conducting wettability tests. The produced oil and brine were collected from the wells next to the UD and LD cored wells. Table 3.4 lists the values of viscosity, surface tension, and density of the fluids at 25°C and atmospheric pressure, measured by concentric cylinder rheometer, Wilhelmy plate, and displacement method (Archimedes' principle), respectively. The slickwater used as fracturing fluid in the Duvernay

wells, contains a surfactant that reduces surface tension and facilitates fracture-face cleanup after fracturing process. During fracturing operations, a portion of fracturing fluid mixes with the formation brine, and thus, the produced flowback brine may have lower surface tension than the original formation brine. Table 3.4 also lists the total dissolved solids (TDS) of brine samples ranging from 153,000 (MIN) to 182,000 (AOK) ppm.

Table 3.4: Physical properties of oil and brine at 25°C and atmospheric pressure.

Well		Viscosity (cP)		Surface tension (mN/m)		Density (g/cm^3)		TDS (ppm)
		Brine	Oil	Brine	Oil	Brine	Oil	Brine
UD	AOK	1.38	2.97	40.0	24.7	1.09	0.80	182,000
LD	MIN	1.50	1.20	47.8	23.3	1.05	0.76	153,000
	WAH	1.60	2.10	62.5	23.5	1.11	0.79	176,000
	FER	1.62	1.37	51.9	23.2	1.13	0.75	156,000
	SAX	1.48	1.35	46.5	22.3	1.08	0.77	171,000

3.4 Methodology

3.4.1 Air/Liquid Spontaneous Imbibition

To conduct spontaneous-imbibition tests for wettability evaluation, one plug of each twin is fully immersed in oil and the other plug is fully immersed in brine. We conduct the tests on 9 twin plugs of LD and 4 twin plugs of UD including AOK3, AOK5, AOK6, and AOK7. We conduct only oil-imbibition tests on AOK1, AOK2, AOK4, and AOK8 plugs.

During imbibition process, we record the mass of plugs by using a digital balance with 0.001 g accuracy. The initial mass of plug is subtracted from the recorded mass to calculate the imbibed mass of liquid. Then, we calculate the imbibed volume by dividing the imbibed mass by the liquid density. Normalized imbibed volumes of oil (I_o) or brine (I_w) are calculated by diving the imbibed volumes of oil or brine by the effective pore volume, respectively. We define oil wettability index (WI_o) using the equilibrated values of I_o (I_o^{eq}) and I_w (I_w^{eq}) for each twin plugs as,

$$\text{Oil wettability index } (WI_o) = \frac{I_o^{eq}}{I_o^{eq} + I_w^{eq}} \tag{3.1}$$

According to Eq. 3.1, $0 < WI_o < 1$ and higher value of WI_o is interpreted as the stronger wetting affinity of rock to oil compared with that to brine.

3.4.2 SEM/EDS Analyses

In order to explain the results of wettability tests and characterize the size and spatial distribution of different pores, we conduct SEM/EDS analyses. We polish the end-pieces of shale samples to obtain a smooth surface, and then, coat the polished surface with carbon to mitigate the charging effects that may deteriorate the resolution and quality of images.

3.5 Results and Discussions

3.5.1 Results of Spontaneous-Imbibition Tests

Figs. 3.2a through 3.2d show I_o and I_w vs. time for the UD and LD plugs. I_o^{eq} is higher than I_w^{eq} for all twin plugs, indicating that the wetting affinity of the Duvernay plugs to oil is stronger than that to brine. Also, $WI_o > 0.5$ for all plugs, suggesting that the shale samples are strongly oil-wet.

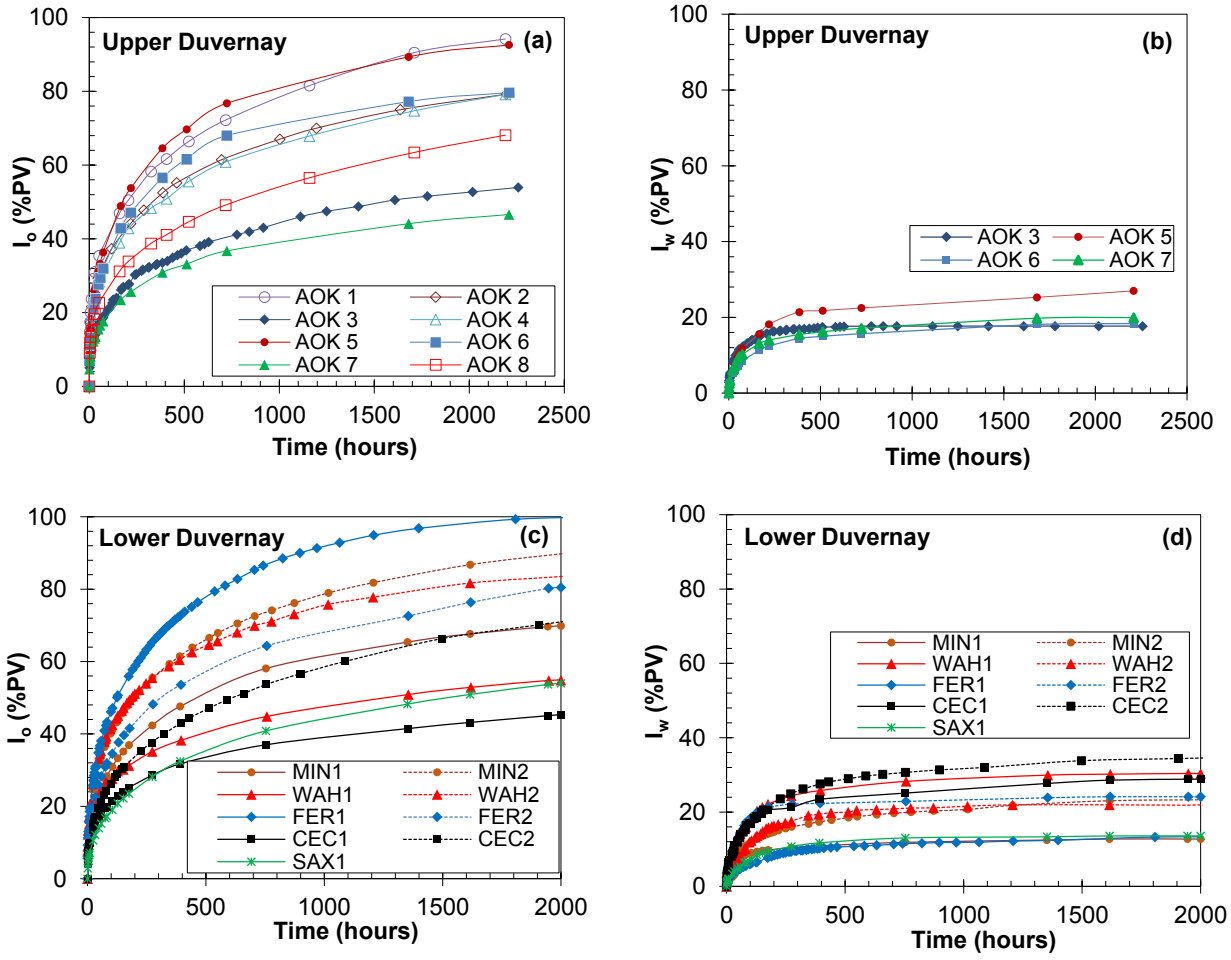

Fig. 3.2: Normalized imbibed volumes of (a) oil and (b) brine vs. time for the UD plugs. Normalized imbibed volumes of (c) oil and (d) brine vs. time for the LD plugs.

Figs. 3.3a through 3.3d show the crossplots of φ_{eff} and k_{Decay} vs. TOC content of 16 UD and 147 LD samples. Figs. 3.3a and 3.3c show that φ_{eff} generally increases by increasing the TOC content, suggesting that most pores are within the organic matter (OM). Figs. 3.3b and 3.3d show that the samples with higher TOC content typically have higher k_{Decay}, suggesting that the pores within OM are relatively well connected. In addition to TOC content, thermal maturity of OM may also affect the connectivity of organic pores. The relationship between organic-pore connectivity and kerogen maturity will be discussed after presenting the results of wettability tests.

The shale samples are mainly comprised of inorganic minerals such as quartz, plagioclase, calcite, K-feldspar, and clays (Table 3.2) and OM (Table 3.3). Inorganic minerals can be hydrophilic, especially when clay minerals are present (Chenevert, 1970; Hensen and Smit, 2002). Conversely, OM with hydrophobic characteristics is expected to have lower wetting affinity to brine (Mitchell et al., 1990). The distribution of pores bordered by inorganic minerals or within OM affects wettability of shale, and consequently spontaneous imbibition. The positive correlations of φ_{eff} and k_{Decay} with TOC content (Fig. 3.3) suggest the presence of abundant pores within OM, leading to strong hydrophobicity of the shale plugs.

According to Fig. 3.2, brine imbibition reaches equilibrium state faster than oil imbibition. For instance, brine imbibition stops at ~ 700 hours, while oil imbibition rate is considerable even after 1000 hours for AOK6 sample. Considering the pore network of rock samples as an idealized bundle of capillary tubes with different pore sizes, the wetting phase first imbibes into the larger pores, followed by the smaller pores (Shi et al., 2018; Handy, 1960). Late equilibrium of oil compared with brine profiles suggests the presence of abundant small hydrophobic pores with strong wetting affinity to oil. Oil can imbibe into and fill these small hydrophobic pores at late imbibition times, however, brine reaches equilibrium state earlier than oil as brine cannot imbibe into such hydrophobic pores.

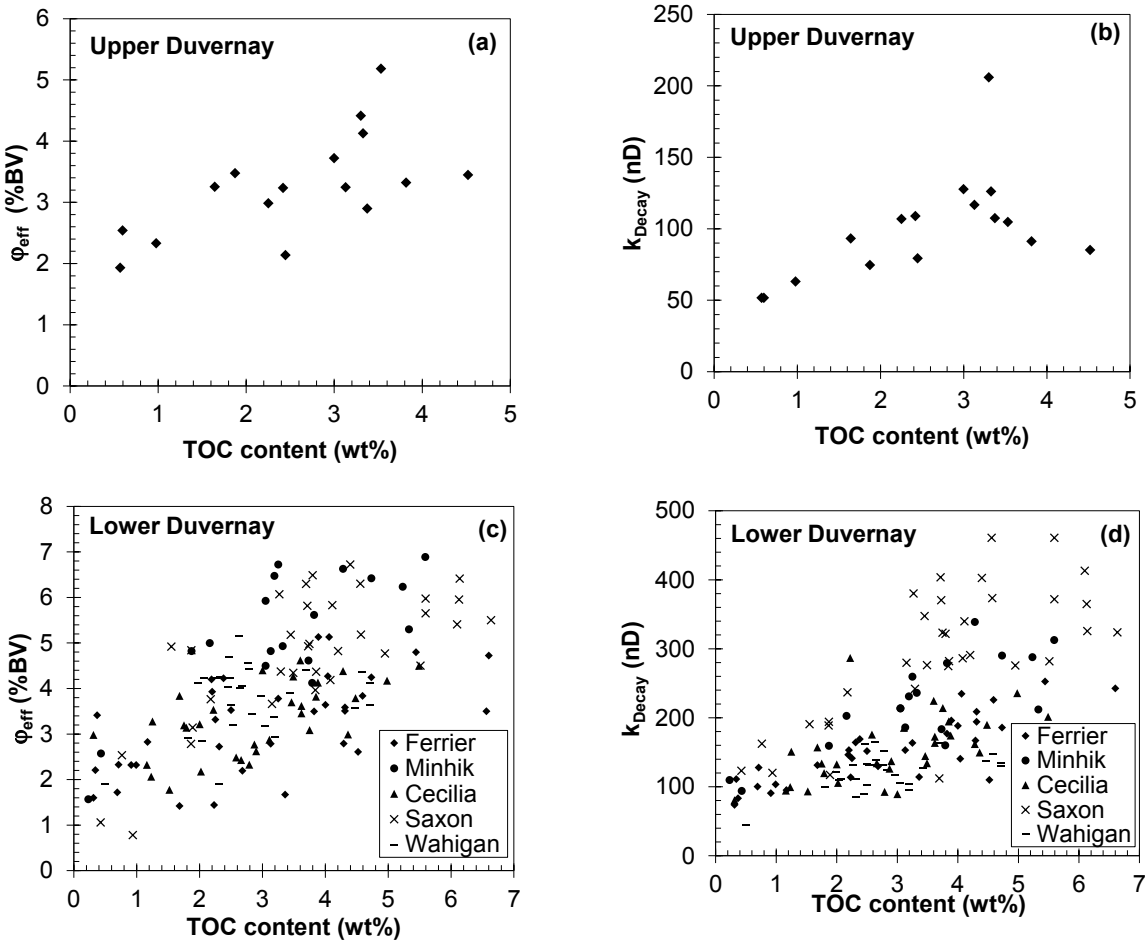

Fig. 3.3: The crossplots of (a) effective porosity and (b) pressure-decay permeability vs. TOC content for 16 UD samples. The crossplots of (c) effective porosity and (d) pressure-decay permeability vs. TOC content for 147 LD samples.

3.5.2 Effect of Kerogen Maturity on Wettability

Oxygen index (OI) represents the oxygen/carbon ratio of kerogen in Van Krevelan diagram (Krevelen, 1950), and can be attributed to the level of kerogen maturity. Hetényi (1998) found relatively good correlations of OI with T_{max} and vitrinite reflectance index (%R_o) in numerous samples from organic-rich sediments. Vitrinite reflectance is a measure of the percentage of incident light reflected from the surface of vitrinite particles and is used as a technique for determining the maturation of organic matter. The reflectance of light increases by increasing the maturation level (Hunt, 1979). Hetényi (1998) suggested that OI can be used as an indicator for the level of maturity, caused by natural evolution of kerogen. The samples with higher kerogen maturity are expected to have lower values of OI (Tissot and Welte, 1984). Fig. 3.4 shows that WI_o generally decreases with increasing OI, suggesting that the samples with higher kerogen

maturity have a higher wetting affinity to oil and vice versa. To explain the negative trend shown in Fig. 3.4, we investigate the effects of kerogen maturity on 1) the abundance of organic pores and 2) the hydrophobicity of organic matter.

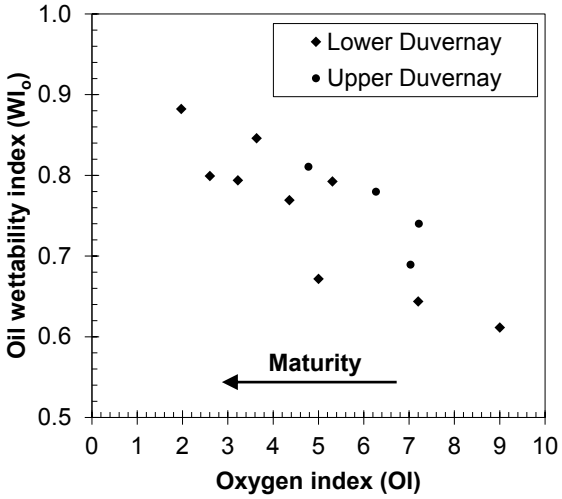

Fig. 3.4: Oil wettability index (WI_o) vs. oxygen index (OI) of UD and LD samples. The samples with higher kerogen maturity level (lower OI) generally have higher WI_o.

1) Kerogen Maturity and Abundance of Organic Pores. Loucks et al. (2009) conducted a comprehensive study on morphology, genesis, and distribution of nanopores in siliceous mudstones of the Barnett shale. The authors showed a strong correlation between the abundance of organic pores and vitrinite reflectance index, suggesting that pore formation is the results of thermal maturation and conversion of OM to hydrocarbons. Loucks et al. (2009) analyzed SEM images and observed that OM in less mature samples ($R_o < 0.7\%$) has fewer pores compared with that in highly mature samples ($R_o > 0.8\%$). Cao and Zhou (2015) also showed that the number of organic pores is higher in samples with higher maturity. According to Fig. 3.4, the samples with lower OI may have higher maturity, and subsequently higher number of organic pores. Increasing the number of organic pores may lead to higher specific surface area for adsorption of oil on the surface of OM (Zhu et al., 2016) and higher organic pore space accessible for oil imbibition. Therefore, it causes higher oil wettability index at higher maturity levels.

2) Kerogen Maturity and Kerogen Wettability. Hu et al. (2016) conducted pore-scale molecular dynamics simulations to understand the relationship between kerogen maturity and kerogen wettability. The results demonstrated that kerogen may be oil-wet at high maturities, neutral-wet at intermediate maturities and even water-wet at very low maturities. Thus, the stronger

hydrophobicity of kerogen in the samples with higher kerogen maturity (lower OI) may be another explanation for the negative correlation of WI_o with OI.

Figs. 3.5a and 3.5b show the crossplots of I_o^{eq} vs. TOC content of UD and LD samples, respectively. I_o^{eq} has a positive correlation with TOC content of LD samples (Fig. 3.5b). The presence of organic matter with high wetting affinity to oil (Borysenko et al., 2009) may explain the positive correlation of I_o^{eq} with TOC content, observed for the LD samples. However, I_o^{eq} generally reduces with increasing the TOC content of UD samples (Fig. 3.5a), which is in contrary with the positive trend observed for the LD samples. The results suggest that in addition to TOC content, there might be other contributing factors that affect wettability, and subsequently the imbibed volume of oil. The results of TRA and XRD tests listed in Tables 3.1 and 3.2 show that the UD and LD samples are generally similar to each other in terms of petrophysical properties and mineralogy. However, the results of rock-eval pyrolysis presented in Table 3.3 and Fig. 3.1 show that the UD and LD samples are different in terms of kerogen maturity level. To explain the different trends observed in Figs. 3.5a and 3.5b for UD and LD samples, we investigate the effect of kerogen maturity level on 1) the abundance and size of pores within the organic matter and 2) the amount of free hydrocarbons (S_1) and accessible pore volume for oil imbibition.

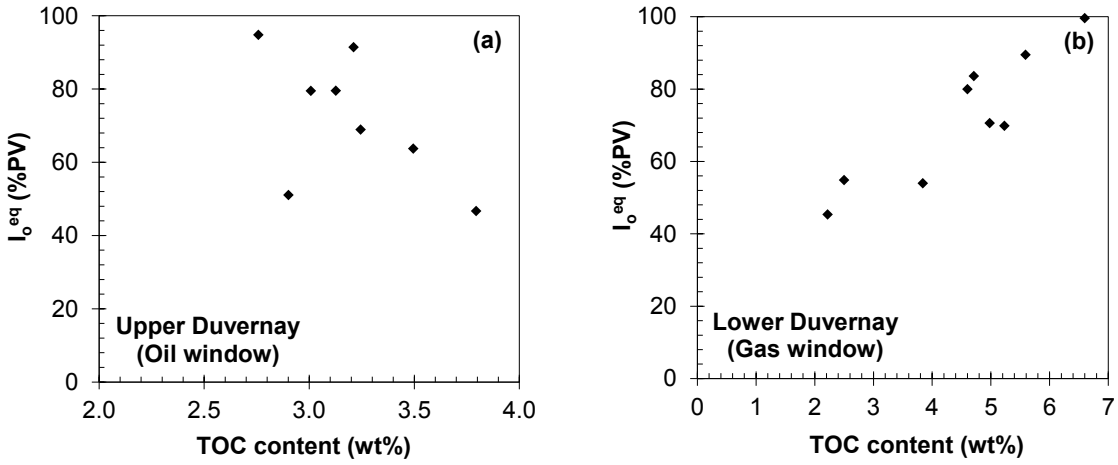

Fig. 3.5: I_o^{eq} vs. TOC content of (a) UD and (b) LD samples.

3.5.2.1 Effect of Kerogen Maturity on Organic Porosity

The kerogen type of all Duvernay samples is Type II, which indicates the ability of the samples to produce a mix of oil and gas. Average TOC content of LD samples is 4.5 wt%, with the thermal maturity level corresponding to gas production. On the other hand, the UD samples contain lower average TOC content of 3.3 wt%, with the thermal maturity level corresponding to oil production (Fig. 3.1b). The thermal maturity of LD samples is higher than that of UD samples. Figs. 3.6a and 3.6b show the SEM images of OM for UD and LD samples, respectively, with the OM detected by using EDS analysis. Comparing Fig. 3.6a with 3.6b indicates that OM of the UD sample has a sponge-like fabric with fewer number of pores compared with the LD sample.

Loucks et al. (2009) demonstrated that pore formation in source rocks is the result of thermal maturation and conversion of the kerogen to hydrocarbons. Lower maturity level of UD samples (oil window) compared with LD samples (gas window) may explain the lower number of organic pores in the UD samples. As discussed in Figs. 3.3a through 3.3d, the pores of shale samples are mainly within OM. Connectivity of organic pores affects the wettability, and consequently, the imbibed volume of oil. Compared with the UD samples, the LD samples with higher thermal maturity have higher number of organic pores (Fig. 3.6b) that may lead to their stronger conductivity to each other. For LD samples, I_o^{eq} generally increases by increasing TOC content, as shown in Fig. 3.5b. However, the number of organic pores may not be high enough to form a well-connected pore network in the less mature UD samples. Therefore, OM may act as a clogging agent against oil imbibition, leading to lower values of I_o^{eq} in the samples with higher TOC content (Fig. 3.5a). Lan et al. (2015b) investigated wettability of Montney tight-gas samples, and similarly, observed a strong negative correlation between I_o^{eq} and TOC content. OM in the form of pyrobitumen/degraded bitumen could clog the pores and reduce the rock pore-space available for oil imbibition in the Montney samples (Lan et al., 2015a).

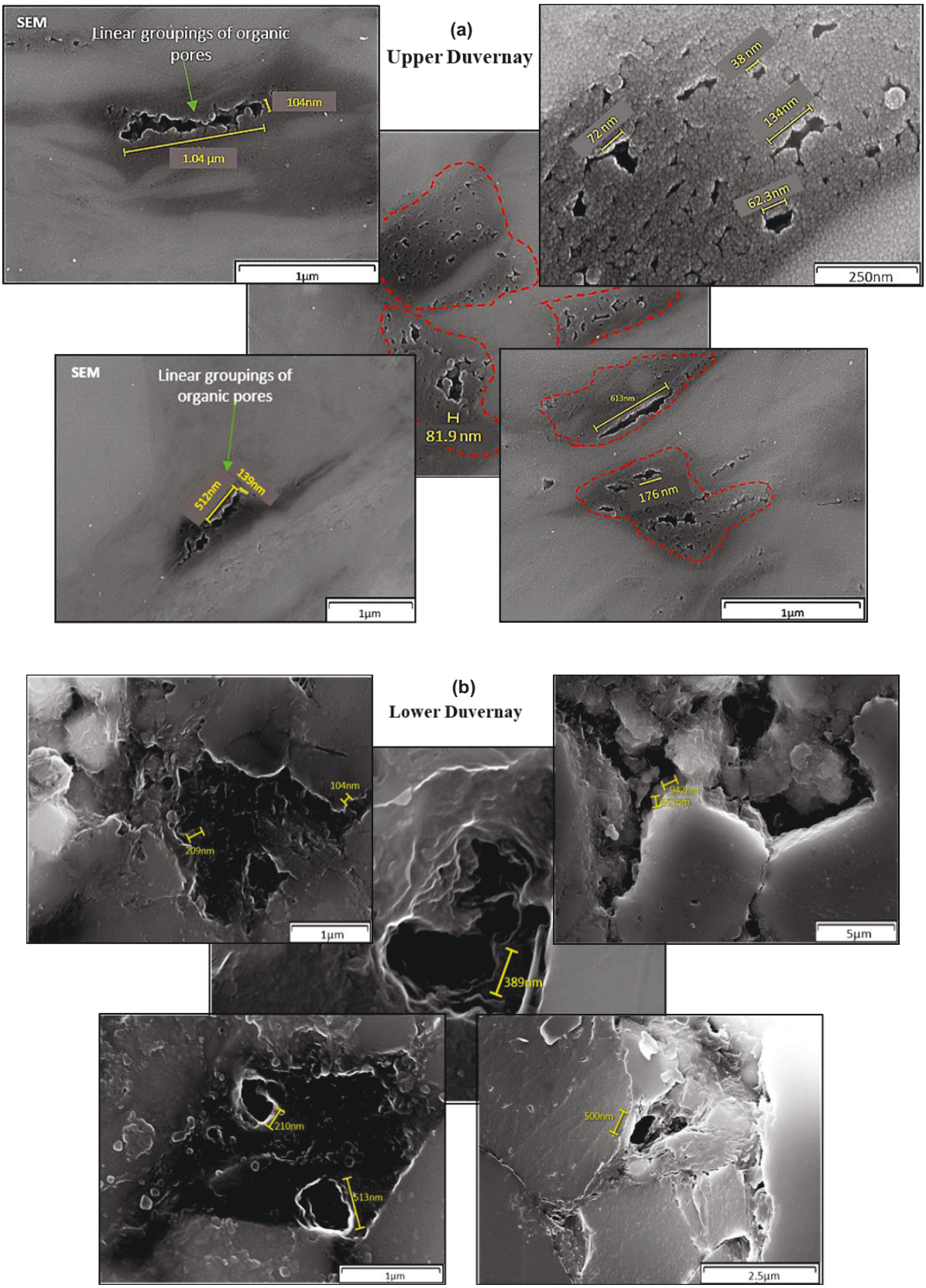

Fig. 3.6: SEM images of (a) UD and (b) LD organic pores. Organic matter is detected by EDS analysis. The number and occurrence of organic pores in the LD samples are higher than those in the UD samples.

Munson (2015) analyzed SEM images of Duvernay samples from 4 wells with different maturity levels. He found that the size and occurrence of organic pores systematically increase with maturity from the approximate onset of the oil window. The SEM analysis of early oil-window Duvernay samples in Fig. 3.7 shows limited visible porosity overall. Organic matter is generally non-porous; however, some OM-hosted porosity is observed (Fig. 3.7c and 3.7f). OM-hosted porosity within the early oil-window samples consists of pores with maximum diameter of approximately 30 nm.

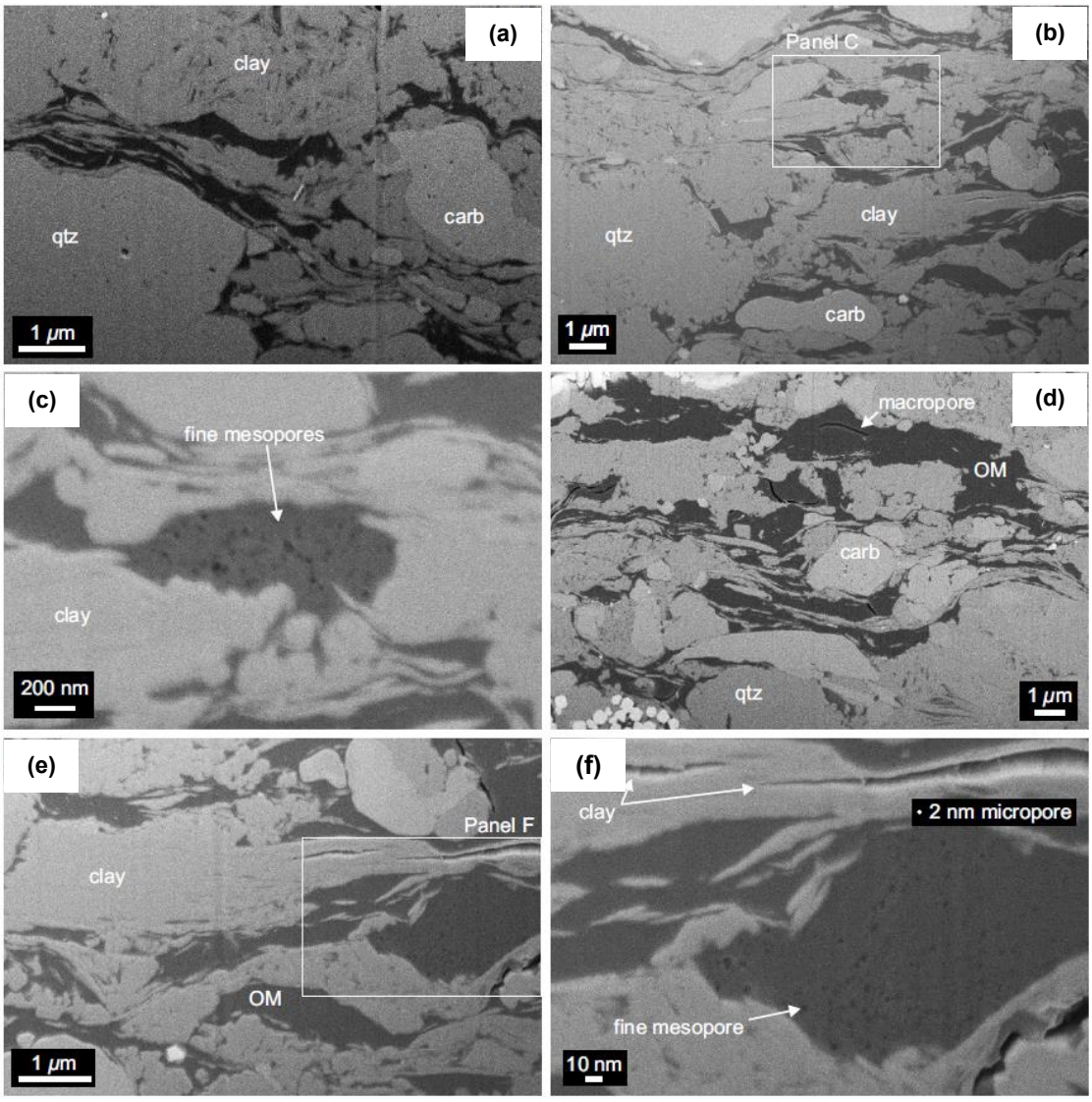

Fig. 3.7: SEM images of Duvernay samples from a well in the early oil-window. Organic matter (OM) is generally non-porous, however fine mesopores (2-10 nm, Figure c) and coarse micropores (d) are imaged in two separate locations. Macropores (> 50 nm) exist in crack-like distributions within or at the boundaries of OM particles (d). Intra-particle clay hosted porosity is also evident (e) (SEM images and caption from Munson (2015)).

Duvernay samples from the gas window (Fig. 3.8) show much better developed OM-hosted porosity compared with the samples from the oil window (Fig. 3.7). The size of organic-hosted pores exceeds 200 nm in apparent diameter, as shown in Figs. 3.8d and 3.8e (Munson, 2015). As noted previously, the number of organic pores in highly mature samples is high enough to form a well-connected pore network, leading to higher I_o^{eq} in the samples with higher TOC content. However, OM may act as a clogging agent in less mature samples due to poor connectivity of organic pores. It may explain the negative correlation of I_o^{eq} with TOC content in less mature samples (Fig. 3.5a).

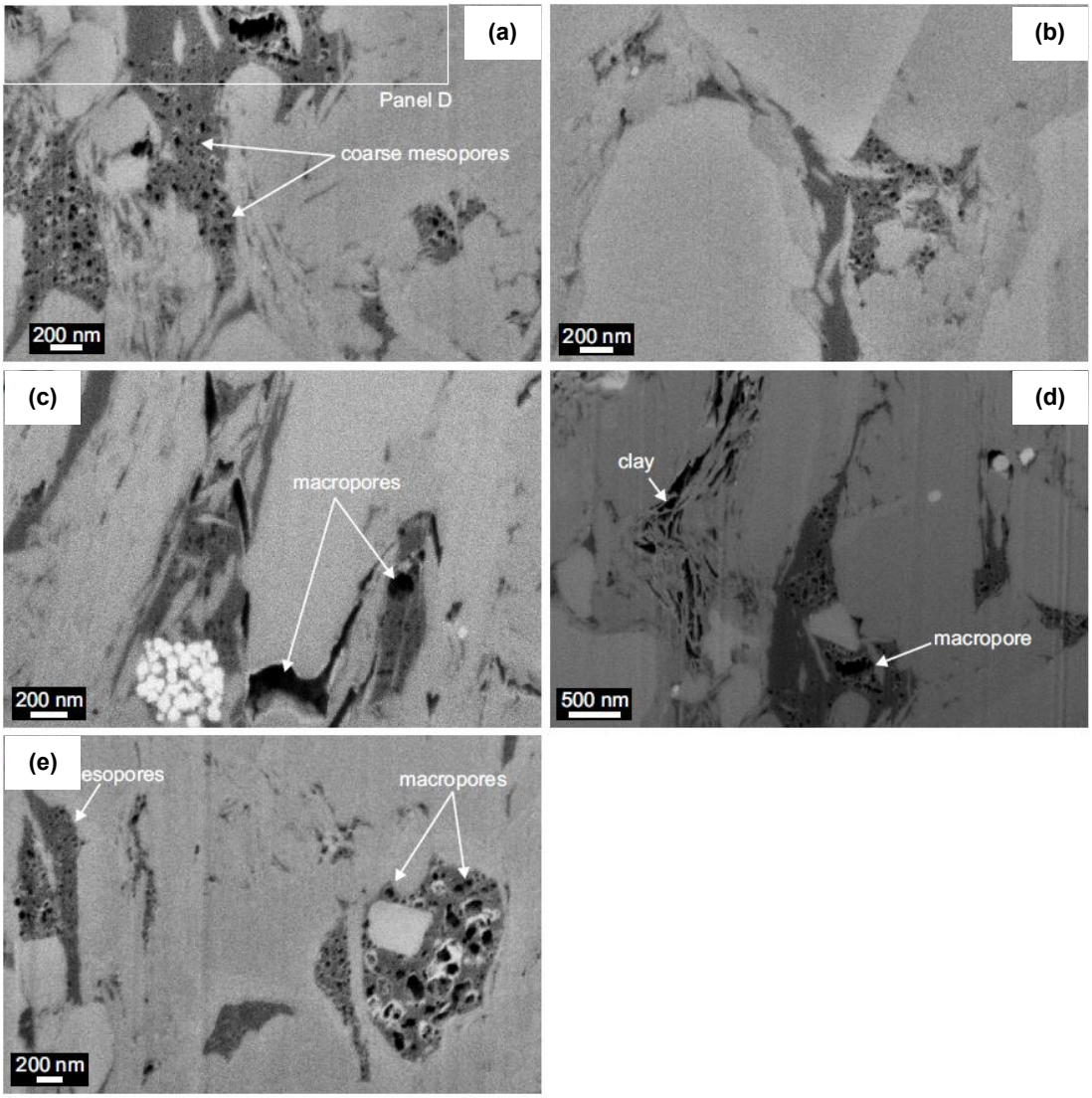

Fig. 3.8: SEM images of Duvernay samples from a well in the gas window. Organic matter is meso-porous (2-50 nm, Figure a) to macro-porous (> 50nm, Figure e) and exhibits larger organic pores compared with the oil-window samples. Inter-crystalline porosity is associated with clay minerals (d) and carbonate grains (c) (SEM images and caption from Munson (2015)).

Furthermore, Munson (2015) used the results of N_2 BJH method and indicated the systematic variation of pore size distribution with kerogen maturity level. Less mature samples from the oil window (Fig. 3.9a) show a pore size distribution peak around approximately 20-70 nm with pore volume progressively decreasing toward smaller pore sizes associated with OM-hosted porosity. However, organic pores with diameters smaller than 10 nm constitute a significant fraction of pores volume in the highly mature samples from the gas window (Fig. 3.9b). Pore volume within the fine mesopores (2-10 nm) of gas-window samples is commonly four time higher than the pore volume of oil-window samples at a given pore size.

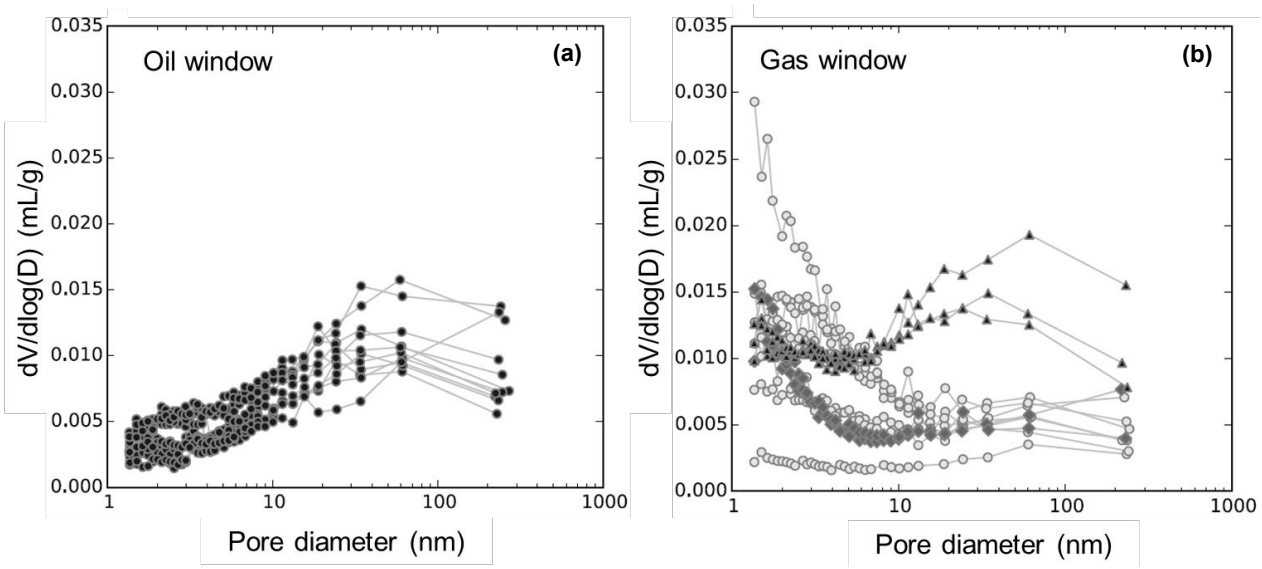

Fig. 3.9: Nitrogen BJH pore size distribution for the Duvernay samples of two wells in the (a) oil and (b) dry-gas windows. The highly mature gas-window samples generally have higher fraction of OM-hosted porosity (diameters < 10 nm) compared with the less mature oil-window samples (Munson, 2015).

3.5.2.2 Effect of Free Hydrocarbons (S_1) on Accessible Pore Space

Kerogen type of the Duvernay samples is Type II, with the potential to produce oil and then gas by increasing kerogen maturity. As kerogen reaches the required thermal maturity, hydrocarbons expulsion occurs, generating organic pores within kerogen (Cao and Zhou, 2015). Thereafter, the organic pores within kerogen act as hydrocarbon storage (Curtis et al., 2011). The values of S_1 listed in Table 3.3 represent the amount of free hydrocarbons that can be flushed out of the rock during the early part of rock-eval pyrolysis at temperatures ranging from 200 to 300°C. Average value of S_1 in the UD samples except SAX1 is about 16 times higher than average S_1 in the LD samples. S_1 (UD) > S_1 (LD) is explained by the fact that UD kerogen produces oil, while LD

kerogen with higher thermal maturity mostly produces gas. In other words, the pore spaces of UD and LD samples are predominantly occupied by oil and gas, respectively.

Figs. 3.10a and 3.10b show the crossplots of S_1 vs. TOC content of the UD and LD samples, respectively. S_1 typically increases with TOC content for both sets of plugs. Higher OM content corresponds to higher generation and storage of hydrocarbons from kerogen, explaining the positive correlations of S_1 with TOC content.

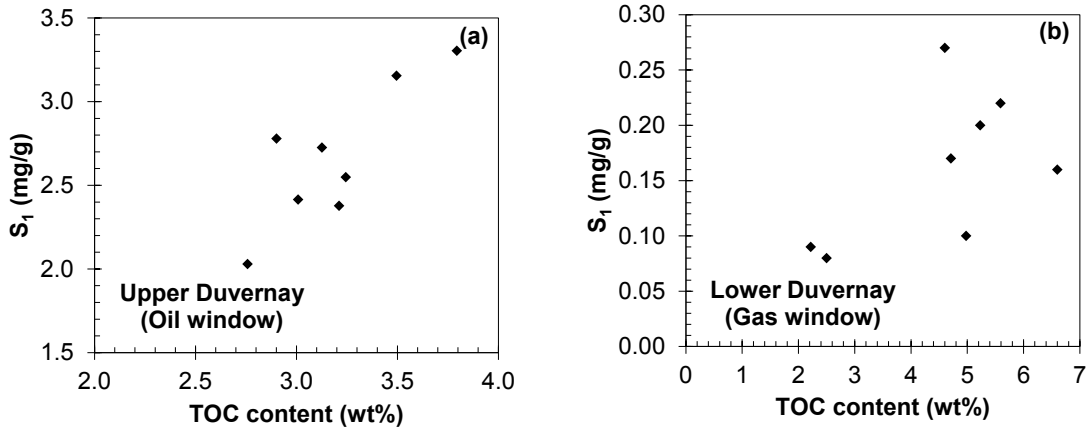

Fig. 3.10: Free hydrocarbons (S_1) vs. TOC content of (a) UD and (b) LD plugs. SAX1 data point is not included in these plots.

Figs. 3.11a and 3.11b present the crossplots of I_o^{eq} vs. S_1 for the UD and LD samples, respectively. Similar to Fig. 3.5a, I_o^{eq} generally decreases with increasing S_1 in UD samples, suggesting that oil imbibition may also depend on free hydrocarbons present in the pores. If the thermally-produced oil exists in the pore system of kerogen as free hydrocarbons, there will be less void space available for oil imbibition. The UD samples with higher TOC content have generally higher S_1 (Fig. 3.10a), leading to less available pore space for oil imbibition as well as negative correlation of I_o^{eq} with TOC content (Fig. 3.5a). On the other hand, LD samples are in the gas window with lower value of S_1 in the form of oil compared with the UD samples. S_1 (UD) > S_1 (LD) suggests relatively higher volume of clean pores accessible for oil imbibition in the LD samples. In other words, as TOC content increases in the LD samples with low S_1, the available pore space for oil imbibition increases, leading to the positive correlation of I_o^{eq} with TOC content (Fig. 3.5b).

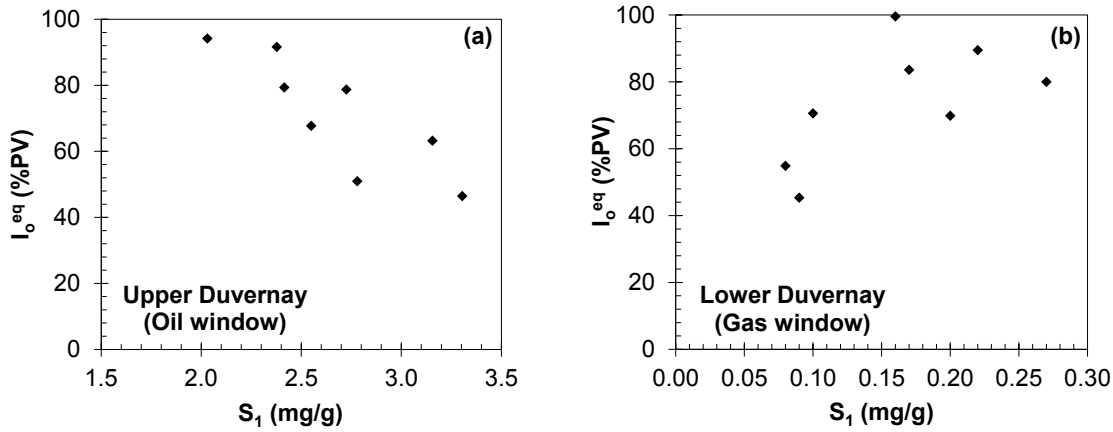

Fig. 3.11: I_o^{eq} vs. S_1 of (a) UD and (b) LD plugs. SAX1 data point is not included in these plots.

3.6 Summary

The primary objective of Chapter 3 was to investigate the functional dependence of wettability on thermal maturity of shale samples from the Duvernay Formation. We evaluated the wettability of organic-rich shale plugs from 6 wells drilled in the Upper Duvernay (UD) and Lower Duvernay (LD) Formations. We measured and compared spontaneous imbibition of oil and brine for 17 twin plugs with wide ranges of kerogen maturity and total organic carbon (TOC) content. We characterized the shale samples by conducting tight-rock analysis (TRA), x-ray diffraction (XRD), and rock-eval pyrolysis tests to identify the petrophysical properties, mineralogy, and organic-carbon properties, respectively. To investigate the size, abundance, and morphology of pores, we analyzed scanning electron microscopy (SEM) of the shale samples. Finally, we investigated the relationships between the results of spontaneous-imbibition tests and geochemical properties to understand the effect of kerogen maturity on shale wettability. The key findings of this chapter are the following.

1- The results of wettability tests show that oil imbibition is significantly higher than brine imbibition, indicating the strong wetting affinity of the shales to oil.

2- The positive correlations of effective porosity (φ_{eff}) and pressure-decay permeability (k_{Decay}) with TOC content suggest that most pores are within the organic matter, confirmed by SEM/EDS analyses.

3- The observed negative correlation between oil wettability index (WI_o) and oxygen index (OI) can be explained by the higher number of organic pores in the samples with higher kerogen

maturity (lower OI) and the stronger hydrophobicity of organic matter in the samples with higher kerogen maturity.

4- In contrary to the highly mature LD plugs, the equilibrated imbibed volume of oil (I_o^{eq}) is negatively correlated with TOC content of the less mature UD plugs. The negative correlation is explained by the poor development of organic-hosted porosity and lack of well-connected organic pores in the less mature UD samples. Furthermore, the higher content of free hydrocarbons (S_1) in the UD samples reduces the accessible pore space for oil imbibition, leading to the negative correlation of I_o^{eq} with TOC content.

Nomenclature

BV = Bulk volume, L^3 [cm^3]
HI = Hydrogen index, dimensionless
I_o = Normalized imbibed volume of oil [%PV]
I_o^{eq} = Equilibrated I_o, L^3/L^3 [%PV]
I_w = Normalized imbibed volume of brine [%PV]
I_w^{eq} = Equilibrated I_w, L^3/L^3 [%PV]
k_{Decay} = Pressure-decay permeability, L^2 [nD]
OI = Oxygen index, dimensionless
PI = Production index, dimensionless
PV = Pore volume, L^3 [cm^3]
R_o = Reflectance index, %
S_1 = Free hydrocarbons, M/M [mg/g]
S_2 = Hydrocarbons from kerogen, M/M [mg/g]
S_3 = CO_2 yield in kerogen pyrolysis, M/M [mg/g]
S_g = Gas saturation, L^3/L^3 [%PV]
S_o = Oil saturation, L^3/L^3 [%PV]
S_w = Water saturation, L^3/L^3 [%PV]
TOC = Total organic carbon, M/M% [wt%]
t = Time, t [hour]
T_{max} = Temperature of maximum hydrocarbon yield
WI_o = Oil wettability index, dimensionless
φ_{eff} = Effective porosity, L^3/L^3 [%BV]

Abbreviations

AOK = Core plugs of UD Formation
CEC = Cecilia
EDS = Energy-dispersive x-ray spectroscopy
FER = Ferrier
LD = Lower Duvernay
MIN = Minhik
OM = Organic matter
SAX = Saxon
SEM = Scanning electron microscopy
TRA = Tight-rock analysis
UD = Upper Duvernay
WAH = Wahigan
WCSB = Western Canadian Sedimentary Basin
XRD = x-ray diffraction

Chapter 4

Pore Size Distribution of Unconventional Rocks with Dual-Wet Behavior

4.1 Introduction

Mercury injection capillary pressure (MICP) is a common method for characterizing total pore-size distribution (PSD_{tot}) of rock samples. In this method, mercury which is the non-wetting phase is forced into pores. Then, incremental mercury saturation at different pressures is converted to PSD_{tot} using the Young-Laplace (Y-L) equation (Young, 1805; Laplace, 1805). However, the validity MICP results to predict PSD_{tot} of shale and tight rocks is questionable due to either limited accessibility to small nanopores (Al Hinai et al., 2014; Lan et al., 2015a) or the need to apply extremely high pressures up to 60,000 psig. Mercury injection at ultrahigh pressures may compress a rock sample's grains and change its total pore volume (PV_{tot}) and PSD_{tot} (Labani et al., 2013).

Unconventional rocks generally exhibit a dual-wet behavior. This is attributed to hydrophilic inorganic and hydrophobic organic pores with strong and low wetting affinities to brine, respectively (Yassin et al., 2016). However, mercury is the non-wetting phase in both pore networks. Therefore, it is not possible to distinguish inorganic and organic PSDs using MICP data. Yassin et al. (2016) used PSD_{tot} estimated from MICP of Montney siltstone samples to qualitatively attribute different wetting characteristics to pores with different sizes. They divided PSD_{tot} into two parts: 1) a tail part representing very small hydrophobic pores within the organic matter (PSD_{org}) and 2) a bell-shaped part representing relatively larger hydrophilic pores, bordered by inorganic minerals (PSD_{inorg}).

Spontaneous imbibition is another technique for characterizing pore network of shales. (Lan et al., 2015a). Gruener et al. (2016) analyzed the advance of imbibition front using gravimetrical,

optical imaging, and neutron radiography techniques. They applied classical Lucas-Washburn (L-W) law (Lucas, 1918; Washburn, 1921) to estimate PSD_{tot}. The difference between PSD_{tot} calculated from imbibition front and isotherm N_2-sorption was attributed to a sticking liquid layer adjacent to the pore wall, which reduces the mobility of the imbibing liquid (Gruener et al., 2016).

Fractal theory is applied to characterize the pore network of sedimentary rocks and to model spontaneous imbibition in porous media. Li and Zhao (2012) used fractal dimension (FD) and derived an analytical model to predict spontaneous-imbibition rate in rocks with different values of porosity and permeability. Cai et al. (2012) idealized the pore network of rock as a bundle of capillary tubes with different diameters. They applied fractal theory for pore size distribution of rock and used the L-W law to model piston-like displacement of air by spontaneous imbibition of brine. Shi et al. (2018) modified the imbibition model proposed by Cai et al. (2012) and assumed non-piston-like displacement of the non-wetting phase (air) by the wetting phase (liquid). They applied a history-matching technique to fit their model to experimental air/oil and air/brine imbibition data of dual-wet Montney plugs and estimated PSD_{tot} and PSD_{inorg}, respectively (Shi et al., 2019). They estimated PSD_{org} by decoupling PSD_{tot} and PSD_{inorg} and concluded that the average size of organic pores (D_{org}) is generally smaller than the average size of inorganic pores (D_{inorg}).

Isotherm gas-sorption technique such as Brunaur-Emmett-Teller (BET) (Brunauer et al., 1938) is another method for characterizing PSD_{tot} of porous media. Recently, several researchers used BET analysis to calculate PSD_{tot} and specific surface area of shale samples (Adesida et al., 2011; Labani et al., 2013; Kuila & Prasad, 2013; Al Hinai et al., 2014). Clarkson et al. (2013) concluded that comparison of PSD_{tot} of shale samples obtained from N_2- and CO_2-sorption analyses can be effectively used to characterize micro-meso-macroporosity up to a limit of 100 nm. They compared the results of PSD_{tot} from MICP with N_2- and CO_2-sorption tests, and claimed that discrepancies in certain pore-size ranges may be due to deviation from a slit-shaped pore geometry or compression of grains at ultrahigh mercury pressures. Labani et al. (2013) observed smaller pore sizes from MICP compared with N_2-sorption test and attributed this discrepancy to compression of shale samples at ultrahigh mercury pressures. Furthermore, MICP and N_2-sorption tests give pore-throat and pore-body sizes, respectively, leading to the discrepancies between the results of these two tests (Al Hinai et al., 2014).

Water molecules can simultaneously adsorb on clays and condense in inorganic pores in water-sorption test. To eliminate the effect of adsorbed water by clay minerals, Zolfaghari et al. (2017a) developed a modified water-sorption technique and estimated PSD_{inorg}. By decoupling PSD_{inorg} and PSD_{tot} from water- and N_2-sorption tests, respectively, they estimated PSD_{org} (Zolfaghari et al., 2017b).

Radiation methods such as scanning electron microscopy (SEM) combined with energy-dispersive x-ray spectroscopy (EDS) are widely used to visualize the pore structure (Chalmers et al., 2012; Klaver et al., 2012) and characterize PSD_{tot} of shales (Loucks et al., 2009). Curtis et al. (2012) conducted 2-D and 3-D SEM/EDS analyses on 9 different shale samples and reported the values of kerogen content and porosity. They indicated that although organic pores with diameter of ~ 6 nm dominate in number, they are not necessarily dominant in pore-volume contribution. SEM analysis of Longmaxi shale samples classified the nanometer-sized pores into organic pores, inorganic pores, and micro-fractures (Zhou et al., 2016). The results show that the average D_{org} ranges from 5 to 200 nm. Zolfaghari et al. (2017b) used helium ion microscope-energy dispersive spectrometer (HIM-EDS) technique and reported the average size of D_{org} ~ 13 nm for shales samples of the Horn Riven Basin.

Most of the studies discussed so far are focused on predicting PSD_{tot} of shales by MICP, isotherm gas-sorption, and image-processing techniques. Separate characterization of PSD_{org} and PSD_{inorg} is important to understand the fluid storage and transport mechanisms in unconventional rocks with dual-wet pore network, and to develop more accurate multi-phase flow models for enhanced oil recovery (EOR) purposes. Both Shi et al. (2019) and Zolfaghari et al. (2017b) indirectly estimated PSD_{org} by decoupling PSD_{tot} and PSD_{inorg}. In Chapter 4, we propose a new experimental technique to directly estimate PSD_{org} and PSD_{inorg} without any decoupling practice. Furthermore, She et al. (2019) and Zolfaghari et al. (2017b) used two individual pieces of rock for estimation of PSD_{tot} and PSD_{inorg}, and assumed that rock samples are homogenous in terms of petrophysical properties and pore-network characteristics. Using a single rock sample for estimation of PSD_{org} and PSD_{inorg} in this chapter mitigates the possible heterogeneity effects.

We first introduce the concept of dual-wet behavior in Section 4.2. Section 4.3 describes the basic theory and assumptions regarding the wettability of different pore networks of shale samples. Section 4.4 presents the materials and data. Section 4.5 shows the mathematical and experimental

procedure for calculation of PSD_{inorg} and PSD_{org}. Section 4.6 presents the experimental results and Section 4.7 discusses the limitations of our proposed technique.

4.2 Review of Dual-Wet Behavior in Unconventional Rocks

The results of air/liquid spontaneous-imbibition tests (Fig. 2.6) on 9 Duvernay twin plugs were presented in Chapter 2. The twin plugs were initially saturated with air ($S_w = 0$) and were fully immersed in reservoir oil and brine for counter-current imbibition tests. $I_o > I_w$, suggesting that the Duvernay plugs have stronger wetting affinity to oil compared with brine, in the presence of air. Consistently, the results of air/liquid contact-angle tests (Fig. 2.5) indicate that oil droplet completely spreads on the dry surface of the rock sample, while brine contact angle is higher than 65 degrees. The SEM/EDS images (Figs. 2.9 and 2.10) indicate two different pore networks in the Duvernay samples. The images show that majority of pores are present within the organic matter of the rock. Organic matter with hydrophobic characteristics is expected to have strong wetting affinity to oil (Mitchell et al., 1990), explaining higher oil uptake than brine uptake. There are also intergranular pores bordered by inorganic minerals such as quartz, feldspar, calcite, and clays. The pores bordered by inorganic minerals are expected to be hydrophilic and may act as conduits for brine imbibition. Furthermore, 2-D visualization of the pores using SEM/EDS analyses indicates that D_{org} is generally smaller than D_{inorg} (Figs. 2.9 and 2.10). Lan et al. (2015a) conducted imbibition tests as well as SEM/EDS analyses on 9 twin plugs of the Montney tight-gas Formation. Similar to the Duvernay plugs, the Montney plugs have strong wetting affinity to oil. To explain this behavior, Yassin et al. (2016) proposed the theory of dual-wet pore network that divides the pores of unconventional rocks into two categories: 1) organic pores mainly within the organic matter are hydrophobic with little or no wetting affinity to brine, and 2) inorganic pores bordered by inorganic minerals with strong wetting affinity to brine.

4.3 Basic Theory and Assumptions

The results of spontaneous-imbibition tests conducted on the Duvernay shale plugs (Fig. 2.6) show that the equilibrated I_o (I_o^{eq}) is higher than the equilibrated I_w (I_w^{eq}). This suggests the strong wetting affinity of the plugs to oil. According to dual-wet theory (Yassin et al., 2016), we propose the following assumptions:

1- Higher value of I_o^{eq} compared with I_w^{eq} suggests that oil can spontaneously imbibe into most pores, including hydrophobic organic pores within the organic matter as well as hydrophilic inorganic pores bordered by inorganic minerals.

2- Low value of I_w^{eq} suggests that brine can imbibe only into hydrophilic inorganic pores. In other words, brine is the non-wetting phase in hydrophobic organic pores and cannot spontaneously imbibe into them. In terms of pore size distribution, the preference of brine for spontaneous imbibition into large inorganic pores is higher than that into smaller organic pores.

4.4 Materials and Data

Table 4.1 lists the petrophysical properties of the 3 Duvernay plugs used in this study. Oven-dried crushed grains of the offset samples are used to measure the effective porosity (φ_{eff}) and absolute permeability (k_{Decay}) by Boyle's law helium porosimetry and pressure-decay methods, respectively. Total organic carbon (TOC) content of the plugs measured by rock-eval pyrolysis test is also listed in Table 4.1. More details about the results of tight-rock analysis, rock-eval pyrolysis, and mineralogy of the plugs were presented in Chapter 2.

Figs. 4.1a through 4.1c present the results of pore-throat size distribution as well as cumulative PV invaded by mercury in MICP test. The maximum applied mercury pressure and the corresponding minimum pore-throat diameter are 55,110 psig and 3.8 nm, respectively. The cumulative PVs invaded by mercury at maximum pressure of 55,110 psig are 21.7%, 22.3%, and 36.4% for SAX1, CEC1, and FER2, respectively. In other words, the inaccessible PVs by mercury are 78.3%, 77.7%, and 63.6% for SAX1, CEC1, and FER2, respectively, leading to invalidity of the results of MICP tests. The significantly high inaccessible PVs by mercury may be attributed to the tiny pores within the organic matter.

Table 4.1: Petrophysical properties of the Duvernay plugs. The diameter of the plugs is 3.8 cm.

Plug ID	Depth (m)	Dry mass (g)	Length (cm)	φ_{eff} (%BV)	k_{Decay} (nD)	TOC content (wt%)
FER2	3464.29	127.922	4.32	2.00	131	4.6
SAX1	3795.88	72.459	2.55	3.96	275	3.8
CEC1	3948.54	128.074	4.40	3.53	287	2.2

Lan et al. (2015a) reported the results of MICP test for Upper and Lower Montney siltstone samples. The PSD_{tot} curves are composed of two parts: 1) a bell-shaped part and 2) a tail part. They claimed that the peak of the bell-shaped part represents "clean" pore throats without organic

matter, and the tail part represents pore throats with smaller sizes within the organic matter. Depending on permeability of the Montney plugs, inaccesible pore volume by mercury ranges from 7.8% to 66.1% of PV.

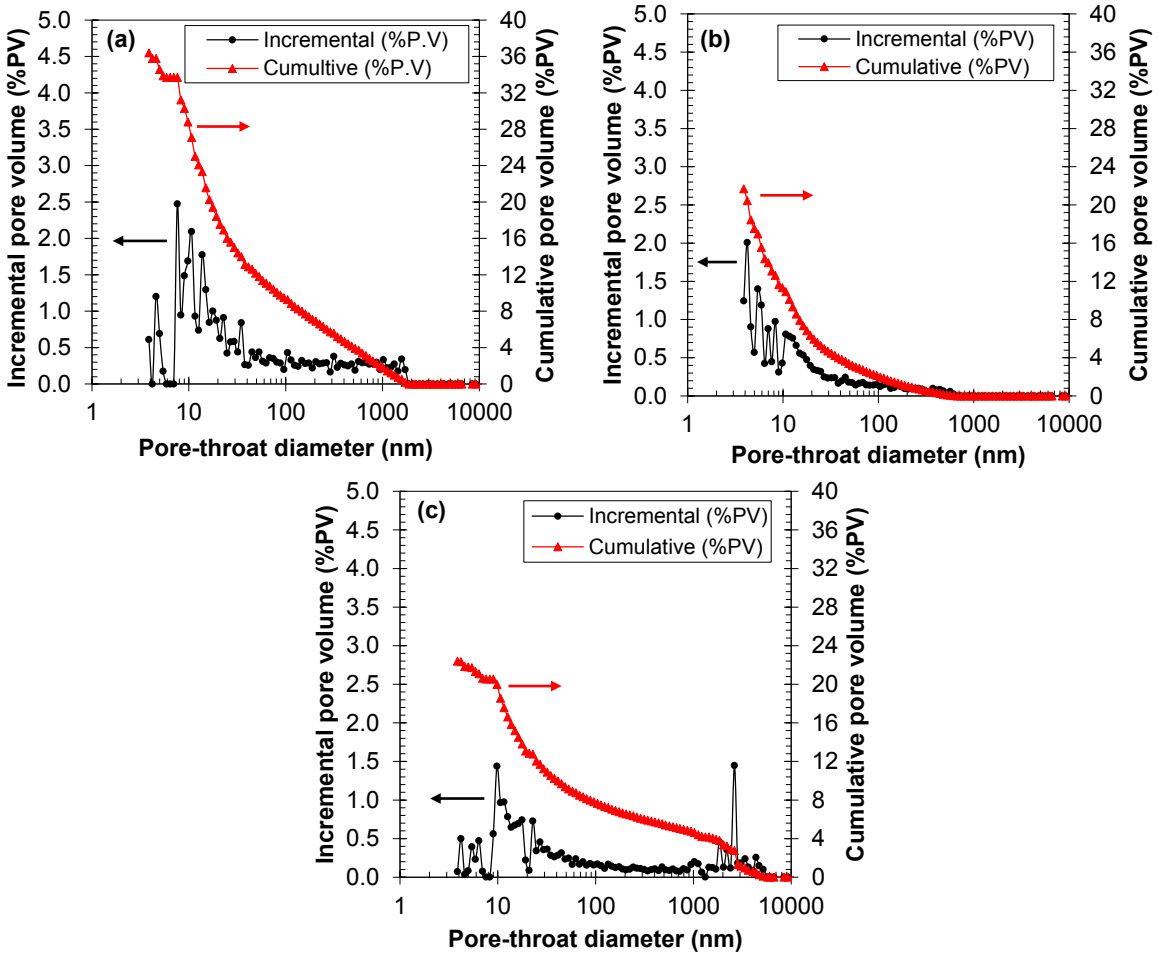

Fig. 4.1: Pore-throat size distribution of (a) FER2, (b) SAX1, and (c) CEC1 samples measured by MICP method. The maximum applied mercury pressure and the corresponding minimum pore-throat diameter are 55,110 psig and 3.8 nm, respectively.

In this study, we use reservoir brine with density, viscosity, and surface tension of 1.111 g/cm^3, 1.6 cp, and 62.5 mN/m, respectively. The measured total dissolved solids of brine is 187,000 ppm. Table 4.2 lists the composition of brine used in the spontaneous- and forced-imbibition tests.

Table 4.2: Concentrations of anions and cations of the reservoir brine.

Cations (mg/L)		Anions (mg/L)	
Na	56960	**Cl**	107480
Ca	8370	**SO_4**	289
K	1350	**HCO_3**	182
Sr	698	-	-
Mg	678	-	-
Fe	50	-	-
Ba	7	-	-

4.5 Methodology

As mentioned in Section 4.3, hydrophilic inorganic pores have stronger affinity for spontaneous brine uptake; while brine cannot spontaneously imbibe into hydrophobic organic pores with smaller pore sizes compared with inorganic pores. In our proposed methodology, we assume that the two pore networks are well connected to each other. Initially, the plug is dry and all pores are almost saturated with air ($S_w = 0$). To characterize the hydrophilic and hydrophobic pores, we conduct spontaneous (Step I) and forced imbibition (Step II), respectively.

Step I: Spontaneous Imbibition. Brine is the wetting phase in hydrophilic pores ($\theta_{inorg} < 90^o$), leading to the positive gas/brine capillary pressure ($P_{cgw} = P_g - P_w$) and spontaneous brine uptake into hydrophilic pores. The spontaneous imbibition of brine can be considered as laminar flow described by the Lucas-Washburn (L-W) equation (Lucas, 1918; Washburn, 1921). Based on the L-W equation, the imbibition rate of brine is positively proportional to the square root of pore diameter (D_{inorg}). In other words, the larger pores fill up fasters, followed by filling the smaller pores. Spontaneous imbibition proceeds until hydrophilic inorganic PV (PV_{inorg}) fills with brine and brine saturation reaches the equilibrated state (I_w^{eq}). We use the normalized imbibed volume of brine (I_w) vs. time and develop Imbibition Transient Analysis (ITA) to calculate PSD_{inorg}.

Step II: Forced Imbibition. At the end of Step I, brine partly saturates the plug. Brine is the non-wetting phase in hydrophobic organic pores with contact angle (θ_{org}) higher than 90^o, and cannot spontaneously imbibe into them ($P_{cgw} < 0$). To fill the hydrophobic pores, we need to increase brine pressure (P_w) by applying external force. Technically speaking, this is a drainage process in which brine as the non-wetting phase displaces air. Similar to MICP test, first larger pores fill at low brine pressure (P_w), followed by filling the smaller pores at higher P_w. The forced imbibed-volume of brine at the end of Step II corresponds to organic pore volume (PV_{org}).

4.5.1 PSD_{inorg} by Co-Current Spontaneous Imbibition (Step I)

Fig. 4.2 presents the schematic of setup used for conducting co-current spontaneous-imbibition tests. The shale plug is initially dry and is saturated with air (S_w = 0). Then, the bottom face of plug is immersed in brine. A digital balance with 0.001 g accuracy is used to measure the mass of rock during the course of spontaneous imbibition. A cap isolates the imbibition setup from outside environment to prevent evaporation of the imbibed brine. The imbibed volume of brine is divided by the effective PV to obtain the normalized imbibed volume of brine (I_w) vs. time. Using the crossplot of I_w vs. time, PSD_{inorg} is estimated by the model developed by Shi et al. (2018). I_w^{eq} at the end of the test is referred to as PV_{inorg}.

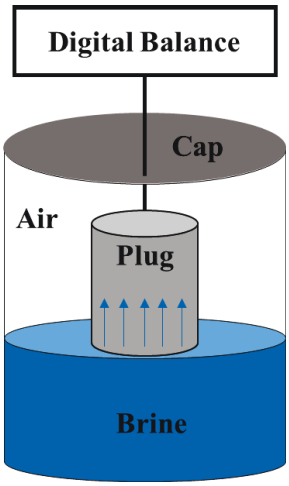

Fig. 4.2: The schematic of co-current spontaneous-imbibition setup.

To model the spontaneous-imbibition process, we idealize the pore network of rock samples as a bundle of tortuous capillary tubes with different diameters (Fig. 4.3) and consider capillary pressure ($4\sigma\cos\theta_{inorg} / D_{inorg}$) as the only driving force for liquid uptake. The idealized pore network consists of small organic and large inorganic pores. We expose both pore networks to brine at the start of the imbibition process. However, according to the presented theory and assumptions, brine can only imbibe into the larger inorganic pores. Based on the L-W equation, incorporated with the tortuosity term (τ in Eq. 4.1), the imbibition rate of brine in a single capillary is positively proportional to the square root of capillary diameter (D_{inorg}),

$$L_s = \sqrt{\frac{D_{inorg}\sigma\cos\theta_{inorg}}{4\mu\tau^2}}\sqrt{t} \tag{4.1}$$

where L_s is the straight length of brine column inside a capillary, σ is the air/brine surface tension, θ_{inorg} is the air/brine contact angle in inorganic pores (< 90°), μ is the viscosity of brine, t is time, and τ is the tortuosity which is defined as the ratio of the tortuous length (L_f) over the straight length (L_s) (Carman, 1937),

$$\tau = \frac{L_f}{L_S} \tag{4.2}$$

Cai et al., (2012) modeled the imbibition process by assuming the piston-like displacement in which imbibition rate is the same in the pores with different sizes. However, brine first fills the larger diameter capillaries, followed by filling the smaller capillaries (Handy, 1960; Gruener et al., 2016). Shi et al. (2018) modified Cai's model by assuming the non-piston-like displacement in which larger pores fill faster than smaller pores, as schematically shown in Fig. 4.3.

To extend the L-W equation and model the imbibition of brine in the bundle of tortuous pores, Shi et al. (2018) used the fractal theory (Mandelbrot, 1967; Mandelbrot and Pignoni, 1983). Based on this theory (Krohn, 1988; Mandelbrot, 1967; Yu and Cheng, 2002), the number of pores with a particular diameter is a function of 1) pore diameter (D_{inorg}) and 2) fractal dimension (FD),

$$N(\geq D_{inorg}) = (\frac{D_{max}}{D_{inorg}})^{FD} \tag{4.3}$$

N is the total number of pores with diameter equal to or larger than D_{inorg}, D_{max} is the maximum pore diameter in a self-similar unit or porous medium, and FD is the fractal dimension which controls pore size distribution. In 2-D space, 1 < FD < 2 (Cai et al., 2012). According to Eq. 4.3, N increases with decreasing D_{inorg}, which is also schematically illustrated in Fig. 4.3.

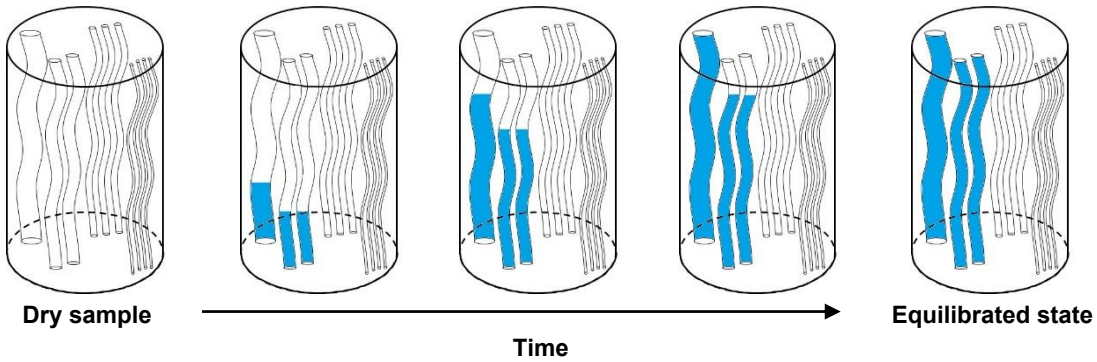

Fig. 4.3: Schematic illustration of co-current spontaneous imbibition of brine into a bundle of dual-wet capillaries with different diameters.

Shi et al. (2018) proposed semi-analytical and analytical solutions with considering and ignoring the hydrostatic term, respectively. The role of hydrostatic term is generally negligible compared with the role of capillary pressure, especially for the plugs with small height (H). Eq. 4.4 shows the analytical solution without considering the hydrostatic term for imbibition of brine in a dual-wet system (Shi et al., 2019),

$$M_T = \frac{A_f \rho}{2D_{max}^{2-FD}} \frac{\varphi'_{aw}}{1-\left(\frac{D_{min}}{D_{max}}\right)^{2-FD}} \sqrt{\frac{\sigma \cos\theta_{inorg}}{\mu}} \left(\frac{2-FD}{2.5-FD}\right) \left[D_C^{2.5-FD} - D_{min}^{2.5-FD}\right] \sqrt{t} + \frac{A_f \rho H}{D_{max}^{2-FD}} \frac{\varphi_{aw}}{1-\left(\frac{D_{min}}{D_{max}}\right)^{2-FD}} \left[D_{max}^{2-FD} - D_C^{2-FD}\right] \quad (4.4)$$

M_T is the total imbibed mass of brine at a certain time. A_f and H are the cross-sectional area and height of the plug. D_{max} and D_{min} are the maximum and minimum pore diameters, respectively. ρ is the density of brine. Brine porosity (φ_{aw}) is the ratio of the equilibrated imbibed volume of brine (V_{iw}) to the bulk volume (BV). Brine surface porosity (φ'_{aw}) is the ratio of effective pore area open to brine imbibition (A_w) to A_f. Eq. 4.5 and Fig. 4.4 show the relationship between φ_{aw} and φ_{aw}',

$$\varphi_{aw} = \tau \varphi'_{aw} \quad (4.5)$$

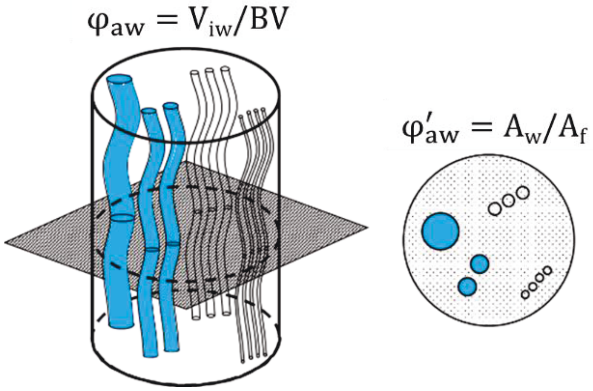

Fig. 4.4: Schematic illustration of the relationship between φ_{aw} and φ'_{aw} in spontaneous-imbibition test (Shi et al., 2019).

D_C is the critical diameter, which is defined as the diameter of the capillaries that just fill with brine at time t,

$$D_C = \frac{4\mu\tau^2 H^2}{\sigma \cos\theta_{inorg} t} \quad (4.6)$$

D_C is a time-dependent parameter whose value falls within D_{min} and D_{max}. As shown in Fig. 4.3, D_C decreases with time as the smaller pores fill later than the larger pores. We present the detailed derivation of Eq. 4.6 in Appendix A.

Once the unknown parameters of D_{min}, D_{max}, FD, and τ are specified, we can model the imbibition profile by Eq. 4.4, and subsequently estimate PSD_{inorg} by Eq. 4.3. She et al. (2019) used a history matching technique to estimate the unknown parameters and calculated PSD_{inorg}.

4.5.2 PSD_{org} by Forced Imbibition (Step II)

After conducting the co-current spontaneous-imbibition test, we assume that brine has already filled all hydrophilic pores, and I_w^{eq} corresponds to PV_{inorg}. In other words, the residual PV already saturated with air, corresponds to PV_{org}, with little or no wetting affinity to brine,

$$PV_{org} = 100 - PV_{inorg} \tag{4.7}$$

Since brine cannot spontaneously imbibe into hydrophobic pores ($\theta_{org} > 90^o$), we need to conduct forced-imbibition test by increasing P_w. The concept of forced-imbibition test is similar to that of MICP test. Mercury is the non-wetting phase in both hydrophilic and hydrophobic pores and is forced into them by increasing mercury pressure. However, brine is the non-wetting phase only in hydrophobic pores.

Fig. 4.5 shows the schematic of the forced-imbibition setup mainly comprises of an ISCO pump and an accumulator, both with maximum operating pressure of 10,000 psig. To start the test, we fill the upper part of the accumulator with the brine (Table 4.2) used for the spontaneous-imbibition tests. Then, we immerse the partly brine-saturated plug in the brine and tighten the top cap of the accumulator. Next, the pump is run at constant pressure mode and injects deionized water into the lower part of the accumulator to reach the set pressure. As shown in Fig. 4.5, a piston isolates the deionized water from the brine. Once the DI water is injected into the accumulator, the piston moves upward and compresses the brine surrounding the plug. In this study, we apply 400 psig as the first set pressure and wait for 48 hours to ensure that the brine saturation has reached the equilibrated state. Then, we reduce the pressure to atmospheric conditions and take the plug out of the accumulator. The plug is weighed to obtain incremental brine saturation ($V(D_{org})$) at 400 psig. Assuming the pore network of the plug as an idealized bundle of cylindrical capillary tubes, the Young-Laplace equation (Eq. 4.8) is used to convert P_w to D_{org},

$$P_{cgw} = P_g - P_w = -P_w = \frac{4\sigma\cos\theta_{org}}{D_{org}} \quad (4.8)$$

where P_{cgw} is the gas/brine capillary pressure, P_g is the gas pressure, P_w is the brine pressure, σ is the surface tension of brine, θ_{org} is the brine contact angle at the pore scale, and D_{org} is the organic pore-diameter. P_g is 0 psig, and we have $P_{cgw} = -P_w$. The brine surface tension is 62.5 mN/m as mentioned before. Lenormand (2012) treated sandstone and carbonate samples with siliconate solution and altered the wettability from strongly water-wet to gas-wet conditions. After changing the rock wettability, he used water to conduct forced-imbibition test and obtained PSD_{tot} by assuming $\theta = 130^o$ in Eq. 4.8. Similarly, we use $\theta_{org} = 130^o$ to calculate D_{org} at a certain P_w. For instance, $D_{org1} = 29.2$ nm corresponds to $P_w = 400$ psig. According to Eq. 4.8, brine can intrude into smaller organic pores by increasing P_w. In other words, brine fills pores with $D_{org} < 29.2$ nm if P_w exceeds 400 psig.

After measuring the incremental brine saturation at 400 psig, we immerse the plug in the brine and apply 800 psig (corresponds to $D_{org2} = 14.6$ nm). Then, we follow the same procedure to obtain incremental brine saturation at 800 psig. Incremental brine saturation from 400 to 800 psig corresponds to pore space occupied by organic pores with D_{org} ranging from 14.6 to 29.2 nm.

We repeat the aforementioned procedure up to $P_w = 9{,}500$ psig ($D_{org} = 1.2$ nm) which is close to the maximum operating pressures of the pump and accumulator. It is important to mention that the initial P_w as well as the incremental pressure steps are optional and can be different from what we conducted in this study. Smaller incremental pressure steps result in higher resolution of PSD_{org}.

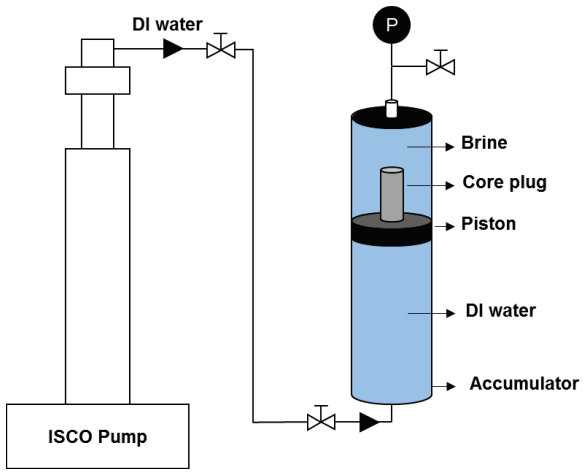

Fig. 4.5: Schematic of the setup for conducting forced imbibition of brine.

4.6 Results

Fig. 4.6 shows the plot of I_w vs. time for the 3 Duvernay plugs. As discussed before, I_w^{eq} corresponds to PV_{inorg} in Step I. According to Fig. 4.6, PV_{inorg} are 32.5%, 12.6%, and 25.8% of PV for FER2, SAX1, and CEC1 plugs, respectively. We consider PV_{org} as the uninvaded pore space by brine after Step I. Based on Eq. 4.7, PV_{org} are 67.5%, 87.4%, and 74.2% of PV for FER2, SAX1, and CEC1 plugs, respectively.

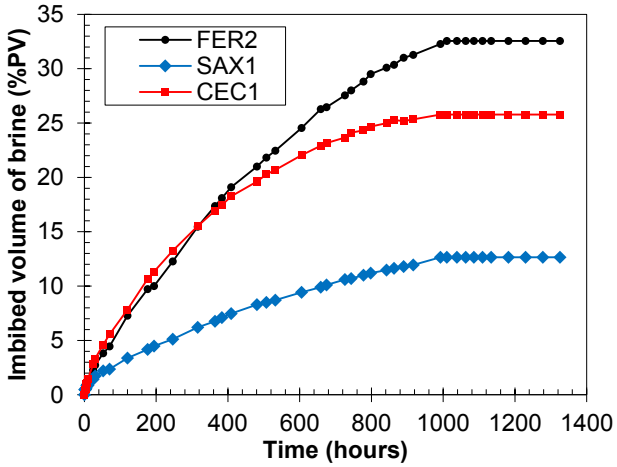

Fig. 4.6: Co-current spontaneous imbibition of brine for the 3 Duvernay plugs.

After spontaneous imbibition (Step I), we start Step II by conducting forced-imbibition test. Figs. 4.7a through 4.7c present capillary pressure ($-P_w$) vs. brine saturation for FER2, SAX1, and CEC1 samples, respectively. PV_{tot} invaded by brine (spontaneous + forced) at P_w = 9,500 psig are 96.6%, 98.3%, and 89.2% for FER2, SAX1, and CEC1 samples, respectively. The maximum operating pressures of the pump and accumulator are 10,000 psig, limiting our forced-imbibition tests to 9,500 psig. Applying P_w > 9,500 psig may result in filling 100% of PV of the shale samples.

Fig. 4.8 compares the pore volumes (%PV) filled by brine and mercury in different tests. Comparing relatively low PV_{inorg} with significantly high PV_{org} indicates that brine can be forced into a portion of hydrophobic pores inaccessible in spontaneous-imbibition test, and drain the air out. Furthermore, PV_{org} is higher than PV_{tot} from MICP, suggesting that brine can be forced into a portion of the pores inaccessible for mercury. Comparing PV_{tot} in brine imbibition (spontaneous + forced) with PV_{tot} in MICP indicates that brine can fill more that 90% of PV, while mercury can fill less than 40% of PV. Low PV_{tot} in MICP tests results in inaccurate estimation of PSD_{tot} by mercury.

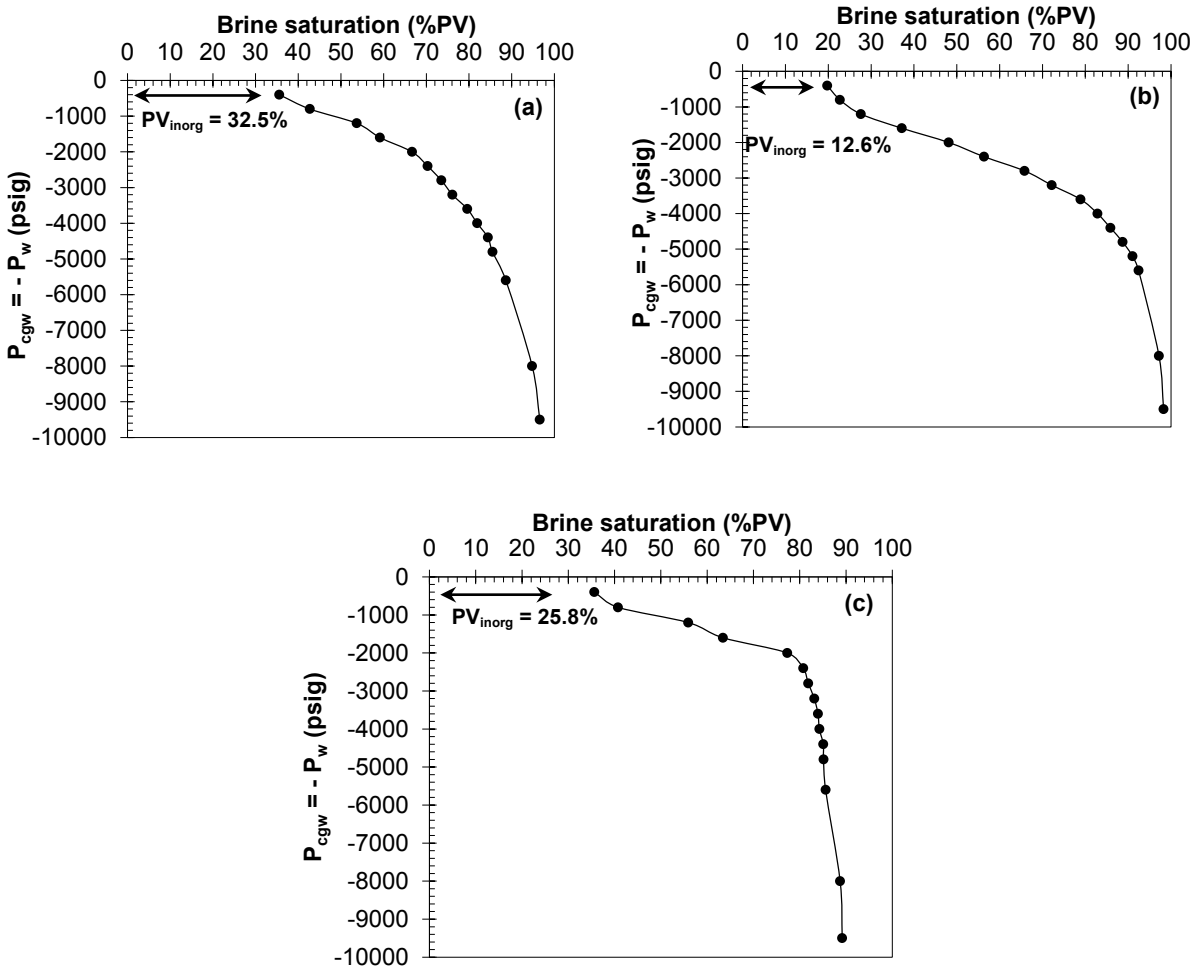

Fig. 4.7: Capillary pressure vs. water saturation for (a) FER2, (b) SAX1, and (c) CEC1 samples in forced-imbibition tests.

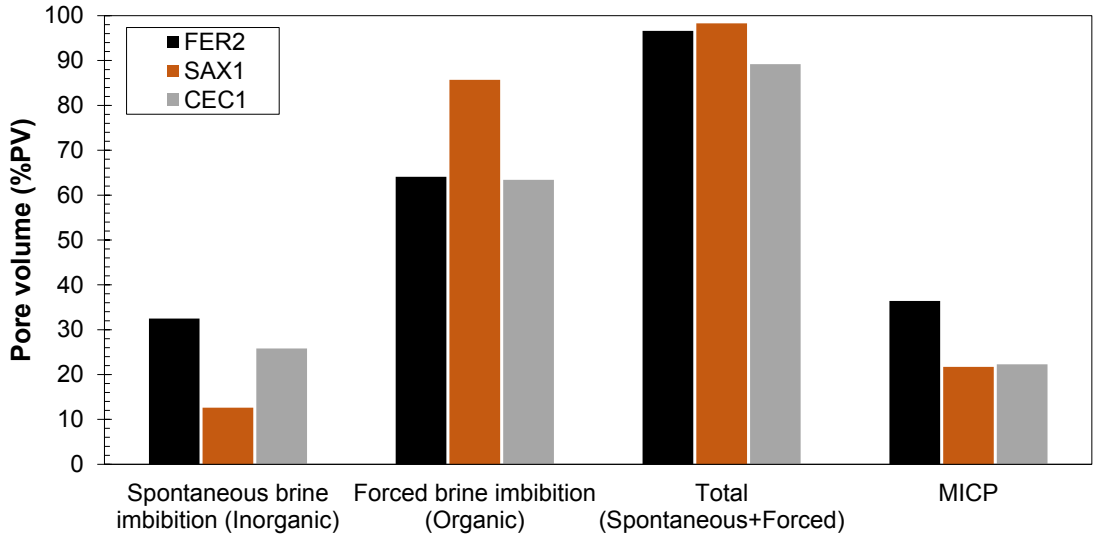

Fig. 4.8: Pore volumes filled by brine and mercury in different tests.

Figs. 4.9a through 4.9c present PSD_{org} of FER2, SAX1, and CEC1, estimated by forced brine-imbibition, respectively. The residual PV inaccessible for brine at maximum pressure of 9,500 psig is attributed to the pores with $D_{org} < 1.2$ nm. For instance, the PVs corresponding to $D_{org} < 1.2$ nm are 3.4%, 1.7%, and 10.8% of PV for FER2, SAX1, and CEC1, respectively.

Organic peak pore-diameters ($D_{peak\text{-}org}$) are 9.7-14.6 nm for FER2 and CEC1 samples, and 5.8-7.3 nm for SAX1 sample. Zolfaghari et al. (2017b) obtained PV_{org} and PSD_{org} of Horn River Basin shales by decoupling the results of N_2-sorption and modified water-sorption tests, respectively. They concluded that $D_{peak\text{-}org}$ is 3-5 nm. Zolfaghari et al. (2017b) also analyzed the HIM-EDS images of organic matter and estimated D_{org} by image processing techniques. The reported range of $D_{peak\text{-}org}$ is 3-6 nm. Curtis et al. (2012) prepared 3-D SEM images of nine different North American shale samples by using sequential focused ion beam (FIB) and 2-D SEM images. They indicated that pores with diameter of ~ 6 nm dominate in number. However, they are not necessarily predominant in pore-volume contribution.

Also, Figs. 4.9a through 4.9c present PSD_{tot} of FER2, SAX1, and CEC1 samples, measured by MICP. We use the MICP data of Fig. 4.1 to get the incremental PV corresponding to a certain pore-size range. The minimum pore sizes detected by brine and mercury are 1.2 and 3.8 nm, respectively. In other words, mercury cannot estimate PSD of pores with diameters smaller than 3.8 nm. According to Fig. 4.9, brine could fill the pore space corresponding to $D_{org} < 3.8$ nm and intrude into organic pores down to $D_{org} = 1.2$ nm. The pore spaces occupied by organic pores with $1.2 \text{ nm} \leq D_{org} \leq 3.8$ nm are 20.5%, 26.1%, and 6.0% of PV for FER2, SAX1, and CEC1 samples, respectively.

Maximum applied pressures by brine and mercury are 9,500 and 55,110 psig, respectively. Considering the Y-L equation (Eq. 4.8), brine with the surface tension of 62.5 mN/m requires lower pressure to invade into the pores, compared with mercury with the high surface tension of 485 mN/m. Labani et al. (2013) reported that characterizing PSD_{tot} of shales by MICP technique at ultrahigh pressures may yield erroneous results due to compression of grains and pores. Using brine for estimation of PSD_{tot} may be less destructive to shale pores, due to applying lower brine pressure. The results presented in Fig. 4.9 suggest that brine can be used as an alternative fluid for characterizing PSD of unconventional rocks with nanoscale pores and ultralow permeability.

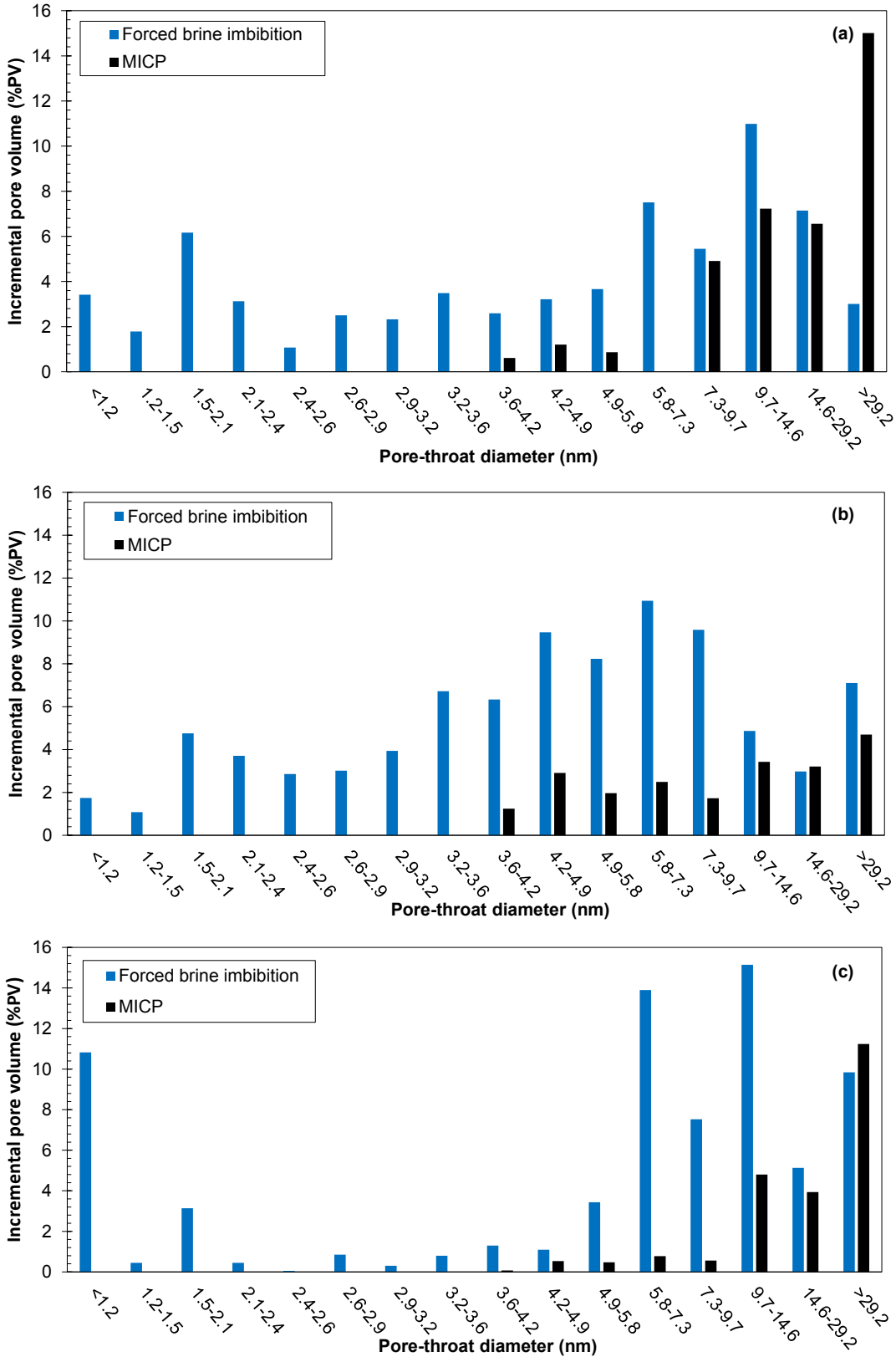

Fig. 4.9: Pore-throat size distributions of (a) FER2, (b) SAX1, and (c) CEC1 samples estimated by forced imbibition of brine and MICP. Maximum applied pressures by brine and mercury are 9,500 and 55,110 psig, respectively.

4.7 Limitations

In this part, we discuss the limitations of experimental setup and tests:

1- We consider capillary pressure as the driving force for spontaneous imbibition of brine and ignore other driving mechanisms such as water adsorption by clay minerals (Bernard, 1967), osmotic effect (Chenevert, 1989; Neuzil, 2000), and electrical double-layer expansion (Holmberg et al., 2002; Nasralla & Nasr-El-Din, 2014). The clay content of the Duvernay plugs used in this study is higher than 20 wt% (Yassin et al, 2017). Certain clay minerals can adsorb brine and expand. The expansion of clay minerals may create induced micro-fractures. The excess brine uptake by clay minerals and induced micro-fractures may cause the overestimation of PV_{inorg}.

2- We idealize the inorganic pore-network as a bundle of tortuous capillary tubes without any interconnections. In our proposed model, the larger pores first fill with brine before the smaller pores. In natural porous medium with pore interconnectivity, the sequence of pore filling may be different from our model. Due to the meniscus arrest mechanism at Y-shaped junctions (Sadjadi & Rieger, 2013; Gruener et al., 2012), first the smaller pore fills with brine, followed by air trapping in the larger pore. In our modeling approach, we did not consider the role of meniscus arrest mechanism in the sequence of pore filling.

3- In spontaneous-imbibition test, we assume that brine fills all hydrophilic inorganic pores. In other words, we consider I_w^{eq} as PV_{inorg}. However, the capillary effects such as air trapping by snap-off (Ransohoff et al., 1987), pore-doublet (Chatzis & Dullien, 1983), and backfilling (Chandler et al., 1982) increase the inaccessible pore volume for spontaneous imbibition of brine, leading to underestimation of PV_{inorg}. In other words, PV_{org} measured by forced-imbibition test may be overestimated.

4- The brine contact angle in spontaneous-imbibition model (θ_{inorg}) is measured on the polished surface of the plug. However, θ_{inorg} in Eq. 4.4 should be at the pore scale. In this study, we assume that the contact angle on the surface of plug is the same as the pore-scale contact angle. To calculate D_{org} in the forced-imbibition test, we use $\theta_{org} = 130^o$ (Lenormand, 2012) in the Young-Laplace equation (Eq. 4.8). The uncertainties in the values of θ_{inorg} and θ_{org} may lead to uncertain estimations of PSD_{inorg} and PSD_{org}.

5- To measure incremental brine saturation in forced-imbibition test, we reduce pressure to atmospheric conditions and take the plug out of the accumulator. In MICP test, the incremental mercury saturation is recorded by volume-balance measurements without reduction of mercury pressure to atmospheric conditions. The pressure drop in our forced-imbibition test leads to capillary-pressure hysteresis effects that influence brine saturation, and subsequently estimation of PSD_{org}. To resolve this problem, we recommend a modification of the experimental setup by applying the volume-balance technique for recording the incremental brine saturation (Lenormand, 2012).

4.8 Summary

In this study, we used reservoir brine and conducted spontaneous- and forced-imbibition tests to estimate the hydrophilic inorganic and hydrophobic organic pore size distributions (PSD_{inorg} and PSD_{org}) of the Duvernay shale samples with dual-wet pore network. Assuming a fractal geometry for pore network of shale samples, we developed a non-piston-like displacement model to fit the experimental spontaneous-imbibition profile, and estimated PSD_{inorg} (Step I). We used the partly brine-saturated plug from Step I and conducted forced imbibition of brine to estimate PSD_{org} (Step II). The key findings of Chapter 4 are the following.

1- Cumulative pore space filled by brine in the spontaneous and forced imbibition at 9,500 psig is more than 90% of pore volume. However, mercury could fill less than 40% of pore volume in mercury injection capillary pressure (MICP). Therefore, pore size distribution estimated by brine would be more representative compared with MICP.

2- - The organic peak-pore sizes ($D_{peak\text{-}org}$) estimated by forced imbibition of brine are approximately 9.7-14.6 nm for two of the samples, and 5.8-7.3 nm for one of the samples. Consistently, 2-D visualization of pores using scanning electron microscopy (SEM) gives a similar pore-size range for organic pores in previous studies.

3- Minimum pore diameters detected by forced mercury (55,110 psig) and forced brine (9,500 psig) injections are 3.8 nm and 1.2 nm, respectively. Therefore, brine is capable of characterizing smaller pore sizes at significantly lower pressures compared with mercury. It leads to less compression of grains and less alteration of shale pore network in forced imbibition of brine.

Nomenclature

A_f = Cross-sectional area of plug, L^2 [m^2]
A_w = Pore area open to brine imbibition, L^2 [m^2]
BV= Bulk volume, L^3 [cm^3, m^3]
D = Pore diameter, L [nm]
D_c = Critical diameter, L [nm]
D_{inorg} = Inorganic pore diameter, L [nm]
D_{org} = Organic pore diameter, L [nm]
D_{max} = Maximum D_{inorg}, , L [nm]
D_{min} = Minimum D_{inorg}, L [nm]
$D_{peak\text{-}organic}$ = Organic peak pore-throat size, L [nm]
FD = Fractal dimension, dimensionless
H = Height of the plug, L [cm, m]
I_w = Normalized imbibed volume of brine, [%PV]
I_w^{eq} = Equilibrated I_w, [%PV]
L_f = Tortuous length of liquid column, L [m]
L_s = Straight length of liquid column, L [m]
M_T = Total imbibed mass, M [kg]
N = Total number of pores with diameter ≥ D_{inorg}
P_{cgw} = Capillary pressure, $ML^{-1}t^{-2}$ [pa, psi]
P_g = Gas pressure, $ML^{-1}t^{-2}$ [pa, psi]
P_w = Brine pressure, $ML^{-1}t^{-2}$ [pa, psi]
S_w = Water saturation, L^3/L^3 [%PV]
t = Time, t [s, hour]
t^{eq} = Equilibrium time, t [s, hour]
TOC = Total organic carbon, M/M% [wt%]
V_{iw} = Imbibed volume of brine, L^3 [m^3]
θ = Liquid contact angle, degree
θ_{inorg} = Inorganic brine contact angle, degree
θ_{org} = Organic brine contact angle, degree
σ = Surface tension of brine, Mt^{-2} [mN/m]
ρ = Density of brine, ML^{-3} [kg/m^3]
τ = Tortuosity, dimensionless
μ = Viscosity of brine, $ML^{-1}t^{-1}$ [cp]
φ = Effective porosity, L^3/L^3 [%BV]
φ_{aw} = Brine porosity, L^3/L^3 [%BV]
φ'_{aw} = Brine surface porosity, L^2/L^2

Abbreviations

CEC = Cecilia
EDS = Energy-dispersive x-ray spectroscopy
FER = Ferrier
LD = Lower Duvernay
L-W = Lucas-Washburn
PV = Pore volume
PV_{inorg} = Inorganic pore volume
PV_{org} = Organic pore volume
PV_{tot} = Total pore volume
PSD = Pore size distribution
PSD_{inorg} = Inorganic pore size distribution
PSD_{org} = Organic pore size distribution
PSD_{tot} = Total pore size distribution
SAX = Saxon
TRA = Tight-rock analysis
SEM = Scanning electron microscopy
XRD = x-ray diffraction
Y-L = Young-Laplace

Chapter 5

Relative Permeability of Unconventional Rocks with Dual-Wet Behavior

5.1 Introduction

The world's consumption of natural gas is expected to grow faster than that of any other energy commodities. Tight/shale oil and gas reservoirs, also known as unconventional resources, are emerging as an important source of energy supply in North America (Frantz and Jochen, 2005; Zahid et al., 2007; Khlaifat et al., 2011). Recent advances in drilling and completion of multilateral/fractured horizontal wells have unlocked these challenging unconventional resources. However, several aspects of unconventional shale reservoirs such as origin and geologic evolution differ extensively from the nature of conventional sandstone and carbonate reservoirs (Dernaika et al., 2015). Tight rocks are composed of very fine-grained particles with very low porosity and ultralow permeability (nanodarcy scale). The affinity of a reservoir rock for a particular fluid and rock/fluid properties, such as capillary pressure (P_c), wettability, and relative permeability (k_r), depend on the rock mineralogy and the properties of the organic matter that coats and fills the pores (Lan et al., 2014).

Reliable relative permeability data are necessary input parameters in reservoir engineering, especially for reservoir simulation. Laboratory measurement of relative permeability for tight rocks is very challenging because of their extremely low permeability (Sulucarnain et al., 2012). Therefore, some researchers used other indirect methods to calculate the relative permeability of unconventional rocks. Wood (2013) integrated water saturation of full-diameter core samples with other petrophysical data, well-log information, and geological data, and found a reliable understanding of water distribution in the Triassic Montney tight-gas play. He developed two sets

of correlations to calculate absolute permeability and gas relative permeability as a function of porosity and water saturation, respectively. Dacy (2010) applied relative permeability principles of conventional rocks for unconventional gas reservoirs. He concluded that the trapped gas in tight rocks is similar to that in conventional rocks, and it depends on the relative proportions of microporosity and secondary porosity resulting from grain dissolution. He found that the water relative permeability derived from mercury injection capillary pressure (MICP) data is representative for tight rocks. Bertoncello et al. (2014) used the lattice Boltzmann method to calibrate the results of core flood experiments for calculating relative permeability curves and for investigating the water blockage in shale-gas reservoirs. Digital rock physics along with the lattice Boltzmann method were applied for estimating relative permeability of unconventional rocks (Cantisano et al., 2013).

In all aforementioned methods, gas/water relative permeability curves were calculated without considering the effect of wettability. On the basis of the conventional approach, all pores have strong affinity to water in a gas/water system, regardless of the difference in their pore-throat size. In a previous paper (Lan et al., 2015a), we observed and discussed the dual-wet behavior of several plugs from the Montney tight-gas Formation. The comparative imbibition tests show that the wetting affinity of the Montney samples to oil is significantly higher than that to water. This behavior was explained by the presence of water-repellant pores within or coated by solid bitumen/pyrobitumen.

In Chapter 5, we further analyze the dual-wet hypothesis by reviewing and discussing the results of focused ion beam/scanning electron microscopy (FIB/SEM), MICP, organic petrography, and comparative oil/water imbibition experiments. On the basis of these analyses, we extend Purcell's relative permeability model (Purcell, 1949) to describe two-phase flow of gas and water through dual-porosity and dual-wet systems such as the Montney rock samples. A sensitivity analysis is performed on the proposed dual-wet model to test the effect of the model's parameters on the relative permeability curves. The model results are then compared with the measured relative permeability data. Finally, the proposed relative permeability model is used as an input for a black-oil simulator to model water imbibition in gas-saturated plugs.

5.2 Dual-Wet Behavior: Review of Previous Measurements

In this section, we review and discuss the petrophysical and petrographic data to investigate the dual-wet behavior of the rock samples from the Montney Formation. We also present and interpret several crossplots to investigate the correlation between the observed dual-wetness and the rock pore structure represented by MICP and SEM analyses. The Montney Formation is located within a large area of British Columbia trending toward the northwest from the Alberta border to Fort St. John (Nieto et al., 2009). This formation is one of the largest economically feasible resource plays in North America (Keneti and Wong, 2010). The Montney fairway forms an indirect basin-centered gas accumulation (Law, 2002), which is a regionally unconventional gas resource (Wood et al., 2015).

5.2.1 FIB/SEM Images

Fig. 5.1 shows FIB/SEM images of two different samples from the Montney dry-gas window. We observe that the rock is composed of: 1) inorganic minerals, which are primarily quartz, feldspar, dolomite, and clays, 2) organic matter, which is predominantly solid bitumen/pyrobitumen that will be discussed later, and 3) multiscale pores within the inorganic and organic parts. In general, the pores can be divided into relatively large micropores and small nanopores. Micropores are predominantly among inorganic minerals, whereas the nanopores are primarily within the solid bitumen/pyrobitumen. In the following subsections, we argue that this dual-porosity system exhibits a dual-wet behavior.

5.2.2 Organic Petrography

A photomicrograph of a Montney sample under white reflected light with immersion oil (Fig. 5.2) shows the distribution of organic matter within the intergranular pore spaces of the rock matrix. On the basis of recent organic petrology and pyrolysis studies (Chalmers and Bustin, 2012; Freeman, 2012; Sanei et al., 2015; Wood et al., 2015), virtually all the organic matter in the Montney Formation is in the form of solid bitumen/pyrobitumen which represent a previous liquid oil phase that substantially filled the pore space of the marine siltstone during hydrocarbon charging. With increasing depth of burial and temperature, the migrated and trapped oil was thermally cracked into solid bitumen/pyrobitumen and gas.

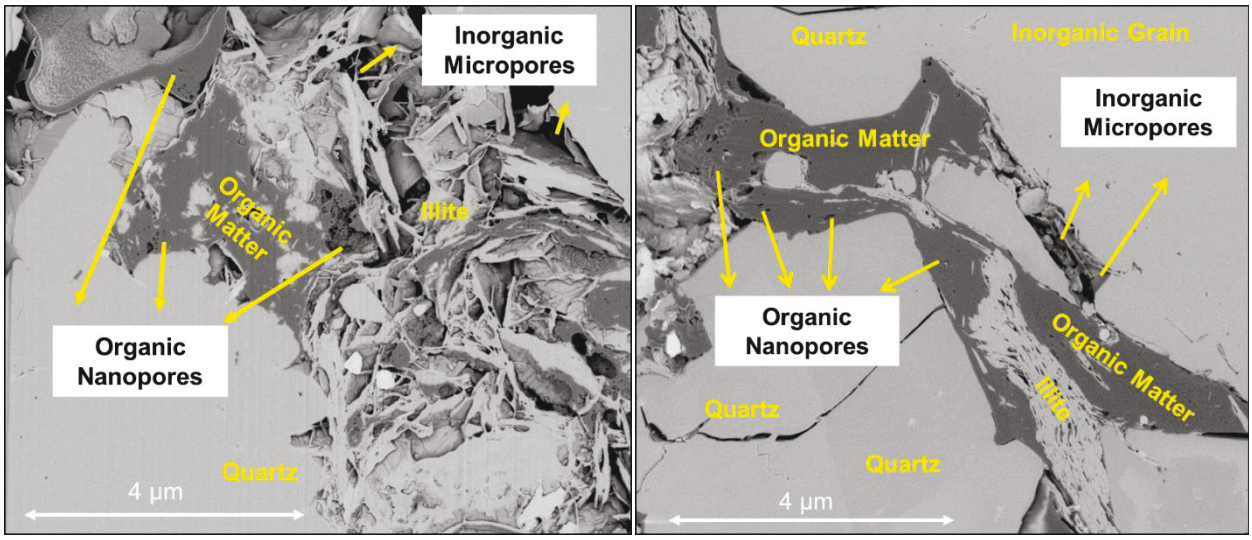

Fig. 5.1: FIB/SEM images of two Montney samples from the dry-gas window. Images courtesy of Mark Curtis, University of Oklahoma.

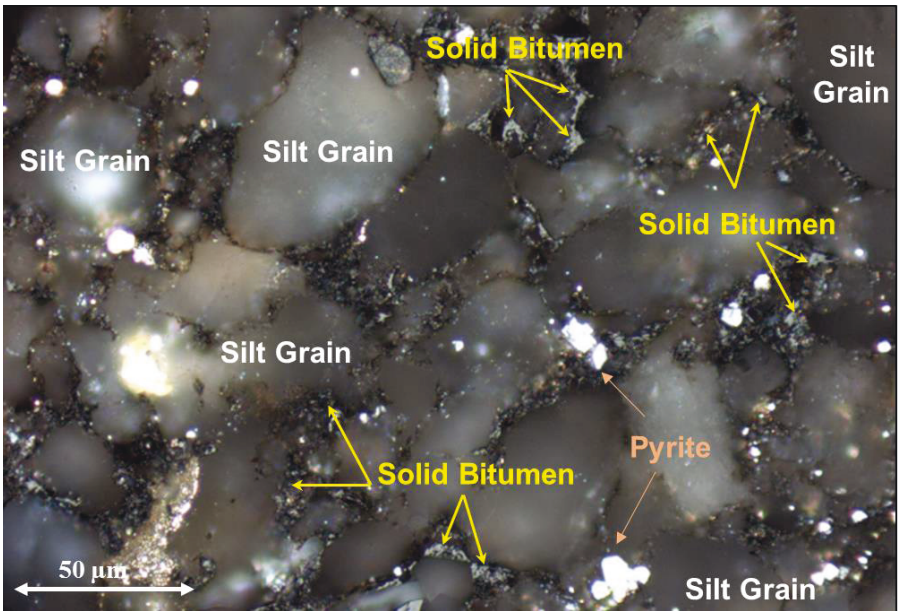

Fig. 5.2: Photomicrograph of a Montney sample under white reflected light with immersion oil showing distribution of organic matter within the intergranular pore spaces in the rock matrix. Courtesy of Hamed Sanei, Geological Survey of Canada.

5.2.3 Pore-Throat Size Distribution

Pore-throat size distributions from MICP measurements of Montney samples are usually composed of two distinct parts: 1) a tail part representing very small pores/throats and 2) a bell-shaped part representing relatively larger pores, which are predominantly bordered by inorganic minerals (Lan et al., 2015a). For example, Fig. 5.3 shows a well-developed peak at approximately 0.086 μm radius and a long tail extending from approximately 0.036 μm down to 0.002 μm. It has

been hypothesized that the pores represented by the tail part and those that cannot be accessed by mercury are mainly within or coated by solid bitumen/pyrobitumen. The corresponding pore volume (PV) of nanopores in the tail part is 36% of the total PV. This hypothesis is supported by the FIB/SEM images shown in Fig. 5.1.

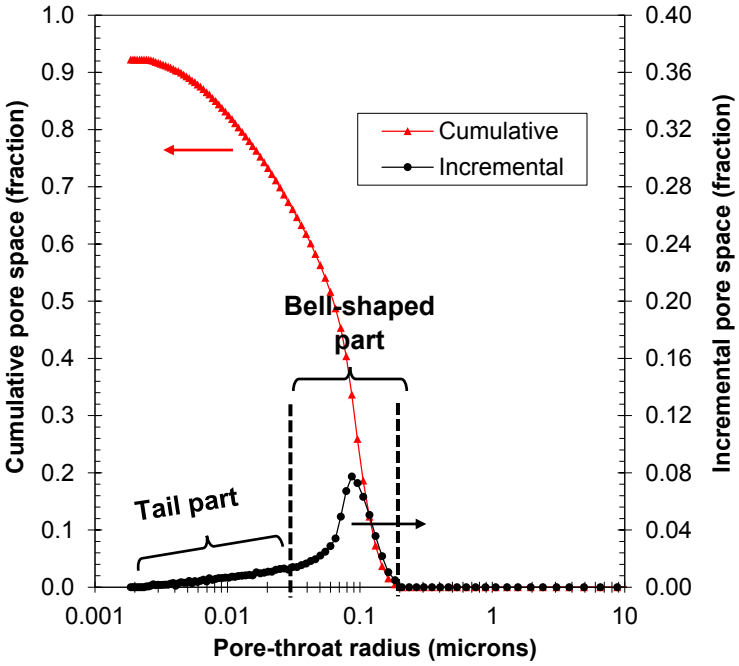

Fig. 5.3: Pore-throat size distribution curve from MICP of a Montney sample. The maximum injection pressure is 400 MPa.

5.2.3.1 Correlation Between Peak Pore-Throat Radius and Bitumen Saturation

Wood et al. (2015) developed the concept of bitumen saturation as the proportion of paleopore volume filled with solid bitumen, and demonstrated its influence on Montney reservoir quality. Fig. 5.4a shows the correlation between peak pore-throat radius and bitumen saturation for samples from 17 cored Montney wells. In general, the samples with higher bitumen saturation show a lower peak pore-throat size. This relatively strong negative correlation indicates that the peak pore-throat size of the Montney samples is controlled predominantly by the amount of solid bitumen that fills and occludes the paleopore network (Wood et al., 2015). This observation supports the hypothesis that small pores represented by the tail part, which are not accessed by mercury, are within or coated by solid bitumen.

5.2.3.2 Correlation Among Peak Pore-Throat Radius, Porosity, and Bitumen Saturation

Fig. 5.4b presents the same peak pore-throat radius vs. the total porosity. The data are divided into two groups: 1) the samples with less than 30% bitumen saturation are shown by blue, and 2) those with bitumen saturation higher than 30% are shown by green. For samples with low bitumen saturation, pore-throat size generally increases with porosity. In these samples, porosity and pore-throat size are mainly affected by reservoir qualities such as grain size and cementation (Wood et al., 2015). However, we do not observe this correlation for samples with relatively high bitumen saturation because a significant proportion of the porosity exists as nanopores within or adjacent to solid bitumen.

5.2.3.3 Correlation Among Peak Pore-Throat Radius, Water Saturation, and Bitumen Saturation

Fig. 5.4c plots the initial water saturation (S_w) vs. peak pore-throat size of the same samples. On the basis of classical theories of capillarity, the samples with smaller throat size are expected to have higher initial water saturation. This trend is roughly observed for samples with relatively higher throat size (pore-throat radius larger than 0.01 μm) and lower bitumen saturation. Interestingly, when the peak throat size is less than 0.01 μm, the samples with lower throat size have lower initial water saturation, which is contrary to the classical theories (Wood et al., 2015). As discussed previously, these samples have relatively higher bitumen saturation, which significantly influences pore-throat size and initial water saturation.

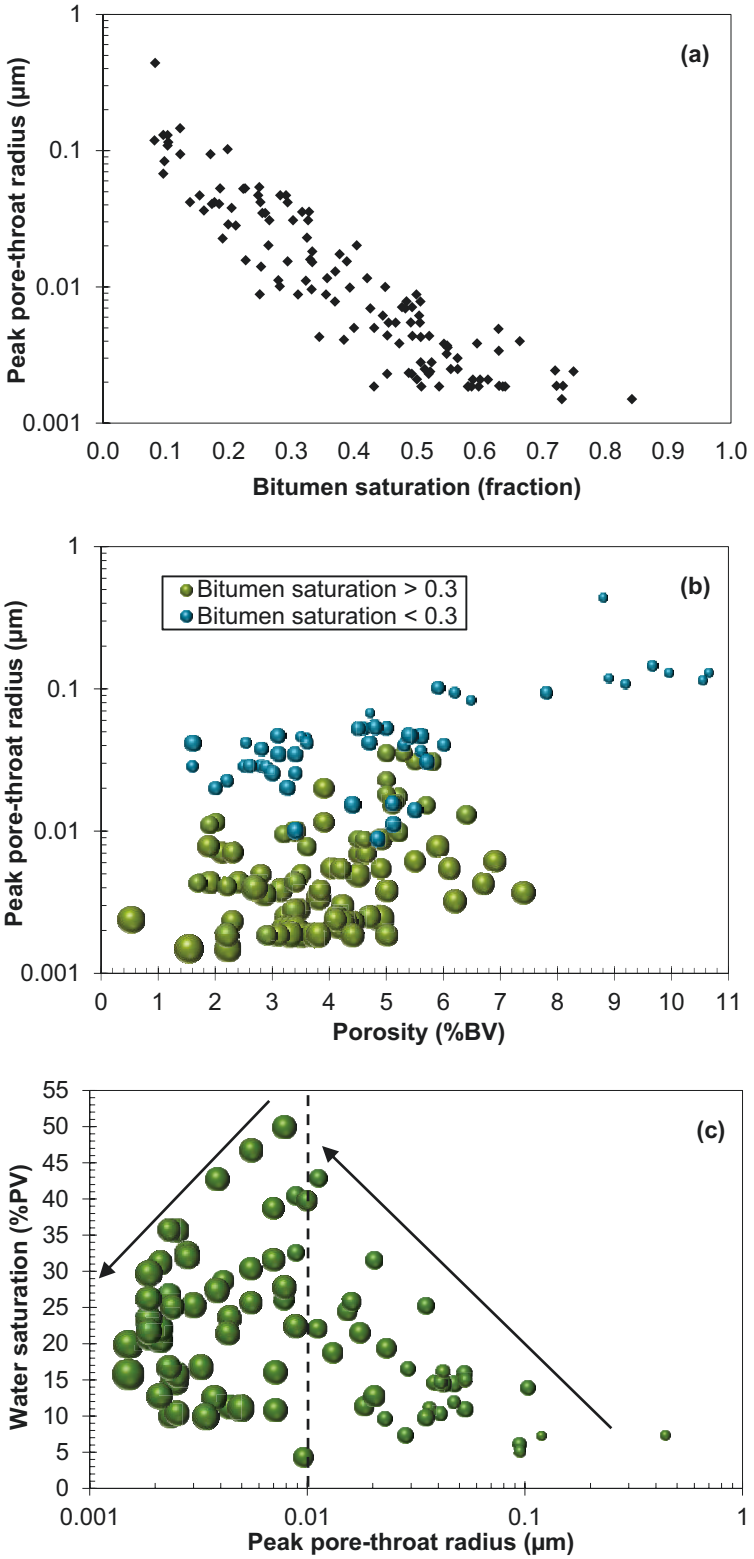

Fig. 5.4: Peak pore-throat radius vs. (a) bitumen saturation and (b) porosity; (c) Initial water saturation vs. peak pore-throat radius for samples from 17 wells. Modified after Wood et al. (2015).

5.2.4 Comparative Oil/Water Imbibition

Lan et al. (2015a) conducted a series of experiments to measure and compare co-current spontaneous imbibition of oil and water for 9 twin plugs from different depths of a well drilled in the Montney Formation. 5 twin plugs were selected from Upper Montney (UMT), and 4 twin plugs were chosen from Lower Montney (LMT). The petrophysical properties of the plugs are listed in Table 5.1. Generally, the UMT samples have higher porosity and permeability compared with LMT samples. Conversely, the total organic carbon (TOC) content of LMT samples is higher than that of UMT samples. The plug is initially saturated with air ($S_w = 0$). To perform the co-current spontaneous imbibition, the bottom face of the dry sample is exposed to oil or water. Dodecane and 2 wt% potassium chloride (KCl) were used as oleic and aqueous phases for the imbibition experiments. The sample was weighed periodically to measure the imbibed mass of oil or water vs. time.

Table 5.1: Petrophysical properties of Upper Montney (UMT) and Lower Montney (LMT) plugs.

Plug name	Depth (m)	Porosity (%BV)	Permeability (mD)	TOC content (wt%)
UMT1	2127.38	6.3	-	0.96
UMT2	2130.39	6.2	3.89×10^{-3}	0.86
UMT3	2137.64	6.6	2.35×10^{-2}	1.17
UMT4	2144.19	8.1	1.05×10^{-1}	0.93
UMT5	2150.96	6.3	4.42×10^{-3}	1.29
LMT1	2323.37	4.3	1.50×10^{-2}	2.08
LMT2	2330.01	2.0	2.33×10^{-3}	1.66
LMT3	2340.45	4.9	2.04×10^{-3}	1.43
LMT4	2347.13	4.5	1.01×10^{-2}	1.74

Figs. 5.5a and 5.5b compare the normalized volumes of oil (I_o) and water (I_w) imbibed into UMT and LMT samples, respectively. I_w (or I_o) is calculated by dividing the total imbibed volume of water (or oil) by the sample PV. The imbibed volume is obtained through dividing the measured imbibed mass by the water or oil density. The imbibition profiles reach an equilibrium state after an initial transition period. The equilibrated imbibed volume of oil is higher than that of water for all twin plugs. This observation indicates that the natural wetting affinity of these samples to oil is higher than that to water.

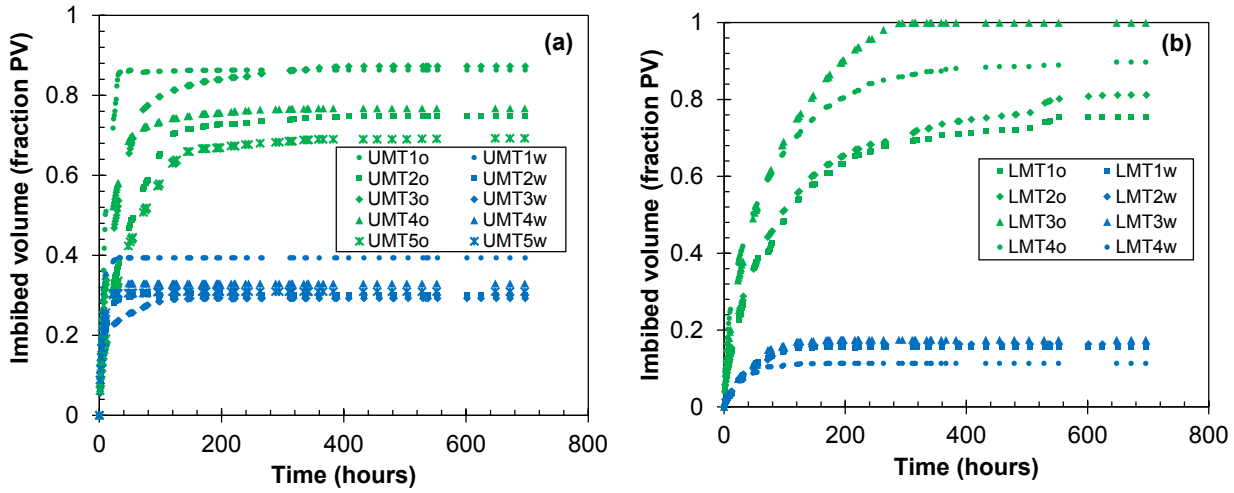

Fig. 5.5: Normalized imbibed volume of oil and water into (a) Upper Montney (UMT) and (b) Lower Montney (LMT) samples.

On the basis of the equilibrated imbibed volume of oil (I_o^{eq}) and water (I_w^{eq}), we define oil wettability index,

$$WI_o = \frac{I_o^{eq}}{I_o^{eq} + I_w^{eq}} \tag{5.1}$$

Fig. 5.6a shows WI_o of UMT and LMT samples vs. TOC content. We observe that the wetting affinity of all samples to oil is stronger than that to water ($WI_o > 0.5$). Although the total oil uptake for LMT samples is lower than that for UMT samples, the oil wettability index for LMT samples is higher than that for UMT samples. This figure also shows that there is a positive correlation between WI_o and TOC content. Because virtually all the TOC content in these Montney samples is solid bitumen/pyrobitumen, we conclude that the strong wetting affinity to oil is caused by the presence of hydrophobic solid bitumen/pyrobitumen (Lan et al., 2015a).

Pores within or coated by solid bitumen/pyrobitumen are water-repellent, and this results in lower imbibition of water. Therefore, ($I_o^{eq} - I_w^{eq}$) should represent the volume of water-repellant pores within the organic matter. Furthermore, the MICP data show that a fraction of the pore space cannot be accessed by mercury even at maximum pressure of 400 MPa (Fig. 5.3).

In Fig. 5.6b, we plot ($I_o^{eq} - I_w^{eq}$) / I_o^{eq} vs. the volume fraction of the pores inaccessible by mercury. In general, the LMT samples with relatively higher volume of inaccessible pores show higher values of ($I_o^{eq} - I_w^{eq}$) / I_o^{eq}. This observation suggests that the small pores are mainly within solid bitumen/pyrobitumen, which is in agreement with FIB/SEM images shown in Fig. 5.1. As

shown in Fig. 5.6b, the data point of LMT2 has a very high value of pore volume inaccessible by mercury. It may be because of very low porosity of LMT2 (2% of bulk volume) among the 9 twin plugs and also its high TOC content (1.66 wt%). As shown in Fig. 5.4b, the samples with low porosity and high bitumen saturation have a smaller peak pore-throat radius and consequently a higher number of organic nanopores. In conclusion, mercury cannot intrude into small nanopores of LMT2 even at a maximum pressure of 400 Mpa. It explains the high inaccessible PV of this sample, as shown in Fig. 5.6b.

In summary, the previous discussions suggest that the Montney rock samples can be characterized as a dual-porosity and dual-wet system. Nanoscale pores are partly represented by the tail part of the pore-throat size distribution from MICP and are inaccessible by mercury. Interpretations of FIB/SEM images, organic petrography, and comparative imbibition data suggest that such pores are mainly within solid bitumen/pyrobitumen, which is strongly water-repellent.

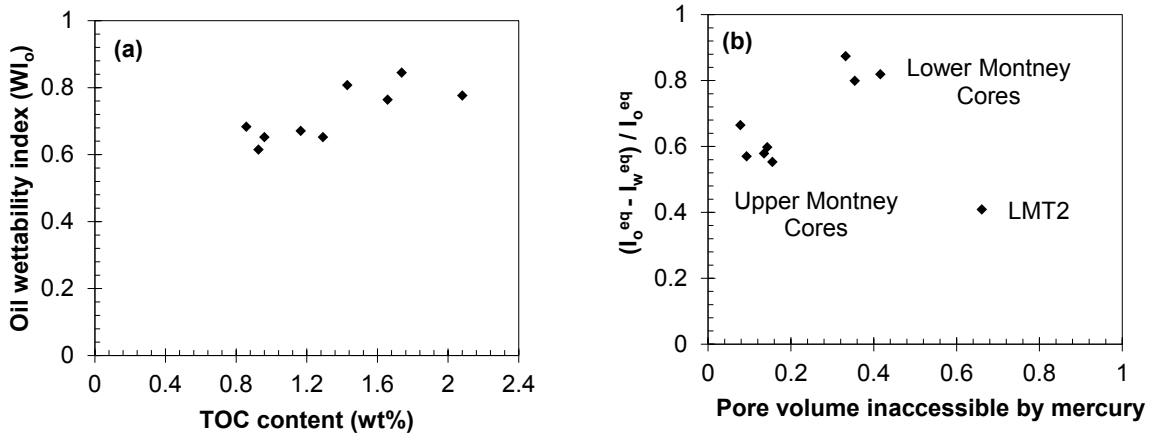

Fig. 5.6: (a) Oil wettability index vs. TOC content. (b) $(I_o^{eq} - I_w^{eq}) / I_o^{eq}$ vs. the volume fraction of the pores inaccessible by mercury.

5.3 Review of Purcell's Model and Its Limitations

Mercury injection is widely used for calculation of PV, pore-throat size distribution, capillary pressure, absolute permeability, and relative permeability. Absolute permeability (k, md) can be calculated from the Purcell's equation (Purcell, 1949) as follows,

$$k = 10.6566 \times (\sigma \times \cos\theta)^2 \times F_1 \times \varphi \times \int_0^1 \frac{dS_{air}}{P_c^2} \quad (5.2)$$

where σ is the air/mercury surface tension (dynes/cm), θ is the contact angle from mercury phase, F_1 is the lithology factor, φ is the porosity (fraction of bulk volume), S_{air} is the air saturation

(fraction of PV), and P_c is the capillary pressure (psi) corresponding to mercury pressure at each step of mercury injection. F_1 with the average value of 0.216 is introduced to this model to account for the effects of rock tortuosity and deviation from a bundle of capillary tubes (Purcell, 1949).

The pore-throat size distribution obtained from mercury injection has been used to estimate two-phase relative permeability curves. Assuming a bundle of straight capillary tubes, both water and gas relative permeability at water saturation of S_w are given by (Purcell, 1949),

$$k_{rw}(S_w) = \frac{k_w}{k} = \frac{\int_0^{S_w} \frac{dS_w}{P_c^2}}{\int_0^1 \frac{dS_w}{P_c^2}} \tag{5.3}$$

$$k_{rg}(S_w) = \frac{k_g}{k} = \frac{\int_{S_w}^1 \frac{dS_w}{P_c^2}}{\int_0^1 \frac{dS_w}{P_c^2}} \tag{5.4}$$

where P_c is the capillary pressure, and k is the absolute permeability. These equations were developed by combining the Hagen-Poiseuille law for a bundle of capillary tubes and a probability density function for pore-throat radius (Peters, 2012).

The Purcell's model for calculation of relative permeability has some substantial limitations. For example, from Eqs. 5.3 and 5.4, $k_{rw} + k_{rg} = 1$ always, which is not the case in real porous medium. Purcell's model assumes a bundle of capillary tubes, which neglects phase trapping and the Jamin effect (Jamin, 1860). In real porous medium, $k_{rw} + k_{rg} < 1$, caused by interfacial phenomena such as phase trapping and capillary pressure (Honarpour et al., 1986). To address this limitation, new modifications were established by introducing two different tortuosity factors as a function of wetting- and non-wetting phase saturations (Burdine, 1953; Wyllie and Gardner, 1958).

The second shortcoming of the Purcell's model lies in the negative curvature of k_{rg}. The negative curvature is not observed in measured k_{rg} (Honarpour et al., 1986). Conversely, calculated k_{rw} by Purcell's equation has a positive curvature. The negative curvature of gas relative permeability can be explained by the fact that in all saturations, $k_{rw} + k_{rg} = 1$. The comparison with experimental data also shows that Purcell's prediction of wetting-phase permeability is more accurate than that of the non-wetting phase permeability (Li and Horne, 2006).

The third limitation of the Purcell's model is related to the assumption of uniform wettability, which means that there is one unique wetting phase at any point in the rock. However, for

unconventional rocks, such as the Montney samples discussed here, the oleic phase acts as the wetting phase in organic nanopores, whereas water acts as the wetting phase in inorganic micropores.

5.4 Extension of Purcell's Theory

5.4.1 Relative Permeability of Dual-Wet Systems

Here, we extend the Purcell's model to describe two-phase flow of water and gas in a dual-porosity/dual-wet medium. As mentioned previously, the original Purcell's model was developed for uniform-wet systems. A schematic of pore structure for a uniform-wet system is shown in Fig. 5.7a. In this system, water can flow through both organic nanopores and inorganic micropores. Fig. 5.7b shows the inverse square of capillary pressure from MICP experiment vs. S_w. At any water saturation, S_w, the left and right areas below the curve are proportional to k_{rw} and k_{rg}, respectively (Eqs. 5.3 and 5.4). By increasing water saturation and growing the left-side area, the k_{rw} increases.

Fig. 5.7c shows a schematic of pore structure in a dual-wet system. Part I represents the small (nanoscale) pores within organic matter. Part II represents microscale pores among inorganic minerals. Let us consider pore-scale positioning of water and gas when $S_w = S_{wa}$. If the system is uniformly water-wet, pores within the range of $0 < r < r_{Swa}$ will fill with water, where r_{Swa} is the radius of the largest pore that water fills. However, in the proposed model, pores within the range of $0 < r < r_{org}$ are strongly water-repellant; and r_{org} is the radius of the largest pore in the organic matter (Part I). Therefore, the water phase should be placed in Part II which is assumed to be water-wet, in the presence of gas. This means pores within the range of $r_{org} < r < r_{Swa}$ will fill with water, as shown in Fig. 5.7c.

It is important to mention that the model proposed in Fig. 5.7c has two limitations. First, we assume that pores smaller than r_{org} are water-repellant. In practice, there may be some clay minerals in pores smaller than r_{org}. Clay minerals have high wetting affinity for water adsorption (Dehghanpour et al., 2013). Hence, these small nanopores will be a conduit for flow of water. However, in the Montney rock samples, Wood (2015) showed that the clay materials with large surface area are generally enclosed by, or substantially are coated with, organic matter in the form of solid bitumen/pyrobitumen. Therefore, nanopores within clay minerals remain water-repellant.

The second shortcoming of the proposed dual-wet model lies in Part II of Fig. 5.7c. On the basis of our model, all pores larger than r_{org} are water-wet. In actual Montney rocks, there might be pores larger than r_{org} that are coated with water-repellant organic matter.

Now, let us consider a pore-throat size distribution obtained from MICP, such as the one shown in Fig. 5.3. Here, we assume that S_{org} is the fraction of the pores within the range of $0 < r < r_{org}$, representing the organic pores. In other words, S_{org} is defined as the volume of water-repellant (gas-wet) pores divided by the total PV. S_w, which is the wetting-phase saturation in MICP data, is related to S_{wa} and S_{org} by,

$$S_w = S_{org} + S_{wa} \tag{5.5}$$

After substituting Eq. 5.5 into Eq. 5.3 and accounting for the absence of water in Part I, the relative permeability to the water phase is given by,

$$k_{rw}(S_{wa}) = \frac{\int_0^{(S_{org}+S_{wa})} \frac{dS_w}{P_c^2} - \int_0^{S_{org}} \frac{dS_w}{P_c^2}}{\int_0^1 \frac{dS_w}{P_c^2}} = \frac{\int_{S_{org}}^{(S_{org}+S_{wa})} \frac{dS_w}{P_c^2}}{\int_0^1 \frac{dS_w}{P_c^2}} \tag{5.6}$$

Similarly, the Eq. 5.7 gives the relative permeability of the gas phase that occupies Part I and the right side of Part II,

$$k_{rg}(S_{wa}) = \frac{\int_{(S_{org}+S_{wa})}^1 \frac{dS_w}{P_c^2} + \int_0^{S_{org}} \frac{dS_w}{P_c^2}}{\int_0^1 \frac{dS_w}{P_c^2}} \tag{5.7}$$

When $S_{org} = 0$, Eqs. 5.6 and 5.7 will be simplified to the original Purcell's equations (Eqs. 5.3 and 5.4). Fig. 5.7d presents the inverse square of capillary pressure vs. water saturation. This figure shows the modified version of the Purcell's model for the dual-wet system (Eqs. 5.6 and 5.7). The difference between Figs. 5.7b and 5.7d is the incorporation of the term $\int_0^{S_{org}} \frac{dS_w}{P_c^2}$ to account for the flow of gas through water-repellant pores. This term is equal to the area under the inverse square of capillary pressure curve from $S_w = 0$ to $S_w = S_{org}$.

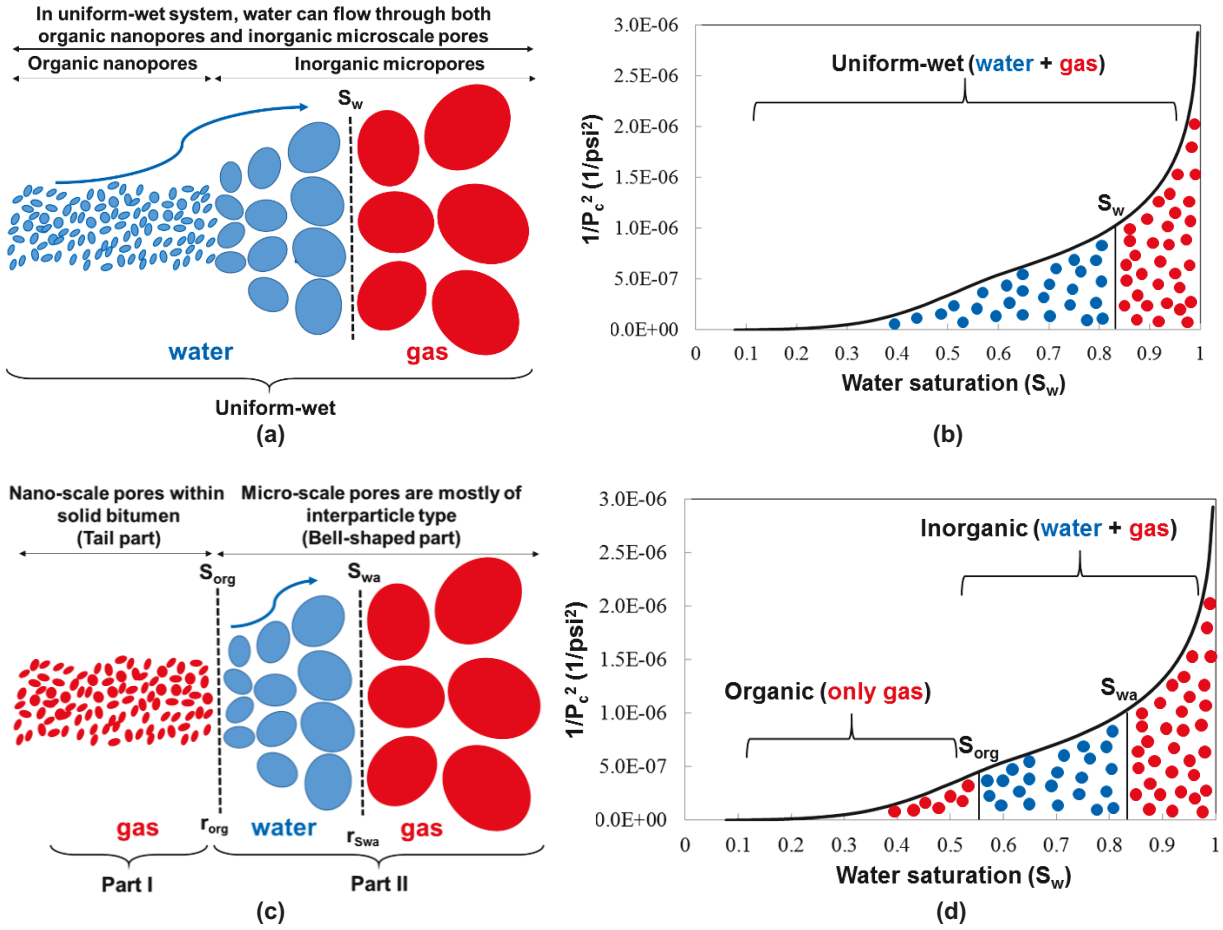

Fig. 5.7: Schematic of pore-throat size in (a) uniform-wet and (c) dual-wet systems. Inverse square of capillary pressure (from MICP data) vs. water saturation in (b) uniform-wet and (d) dual-wet systems. Red and blue colors represent gas and water, respectively.

It is important to mention that the values of r_{org} and S_{org} in Figs. 5.7c and 5.7d are unknown, but can be roughly estimated with pore-throat size distribution from MICP such as Fig. 5.3. Theoretically, we divide the MICP curve into two main parts: 1) small pores within solid bitumen (tail part) and 2) intergranular larger pores (bell-shaped part). Here, we consider two scenarios. First, r_{org} is assumed to be at the intersection of the tail and bell-shaped parts. Second, r_{org} is considered to be at a random point on the left side of the bell-shaped part.

To address the first two drawbacks of the original Purcell's equation, the Wyllie and Gardner's (1958) modifications are applied by multiplying Eqs. 5.6 and 5.7 by S_{wa}^2 and $(1-S_{wa})^2$, respectively. As shown in Eqs. 5.8 and 5.9, these two coefficients are introduced to represent the tortuosity of wetting and non-wetting phases as a function of their saturations (Wyllie and Gardner, 1958; Honarpour et al., 1986). In Eqs. 5.8 and 5.9, we assume zero irreducible water saturation (S_{wir} =

0). After applying Wyllie and Gardner's (1958) modifications, the sum of k_{rg} and k_{rw} is smaller than one, and k_{rg} has a positive curvature. Here, Eqs. 5.8 and 5.9 are called the dual-wet model with normal tortuosity factor,

$$k_{rw}(S_{wa}) = S_{wa}^2 \times \frac{\int_{S_{org}}^{(S_{org}+S_{wa})} \frac{dS_w}{P_c^2}}{\int_0^1 \frac{dS_w}{P_c^2}} \tag{5.8}$$

$$k_{rg}(S_{wa}) = (1 - S_{wa})^2 \times \frac{\int_{(S_{org}+S_{wa})}^{1} \frac{dS_w}{P_c^2} + \int_0^{S_{org}} \frac{dS_w}{P_c^2}}{\int_0^1 \frac{dS_w}{P_c^2}} \tag{5.9}$$

5.4.2 Application of the Proposed Theory

In this section, we apply the proposed model to calculate relative permeability of water and gas for a Montney sample with the MICP data that are shown in Fig. 5.3. A sensitivity analysis is also performed to investigate the effect of S_{org} on relative permeability curves. As shown in Eqs. 5.8 and 5.9, the water and gas relative permeability curves depend on S_{org}, which represents the volume fraction of the pores within organic matter. Here, we used three different values of S_{org}. The first value is $S_{org} = 0$, representing a uniformly water-wet system. For the second assumption, S_{org} is at the start of the tail part, equal to 0.36 for this sample. The third value of S_{org} is considered a random point from the left-side of the bell-shaped part, for example, 0.48.

Fig. 5.8 shows the calculated relative permeability curves (Eqs. 5.8 and 5.9) vs. S_{wa} for the three cases. As shown in this figure, by increasing S_{org} from 0 to 0.36 and then to 0.48, k_{rw} increases whereas k_{rg} decreases, for a fixed S_{wa}. As discussed previously, S_{org} represents the volume fraction of small pores within water-repellent organic matter. Therefore, as shown in Fig. 5.7c, by increasing S_{org}, the fraction of the water-repellent small pores (Part I) increases. Therefore, for a fixed S_{wa} (and S_g), the average size of flow conduits for gas, and consequently, k_{rg}, decreases. A similar argument can be used to explain increasing k_{rw} by increasing S_{org}.

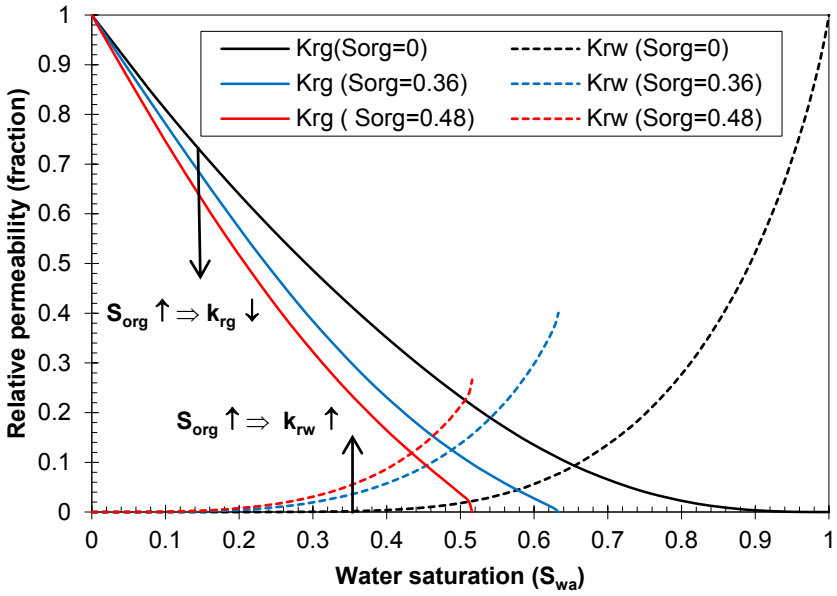

Fig. 5.8: Water and gas relative permeability (Eqs. 5.8 and 5.9) curves at different values of S_{org}. S_{org} = 0 represents a uniformly water-wet system; S_{org} = 0.36 assumes that all the pores in the tail part are within the organic matter and are water-repellant; S_{org} = 0.48 assumes that all the pores in the tail part and some from the bell-shaped part are within the organic matter and are water-repellant.

5.4.3 Verification of the Proposed Dual-Wet Model

This part is divided into two subsections to verify the proposed dual-wet model. To do this, the measured gas relative permeability data of the Montney samples are used. On the basis of the results presented in Fig. 5.8, higher organic material leads to lower k_{rg} for a fixed water saturation. First, we try to test this observation by comparing k_{rg} data of three Montney samples. Second, we calculate k_{rg} by Eq. 5.9 to see if it can match the measured k_{rg} data. To perform this task, MICP data are used to calculate k_{rg} of Montney samples by Eq. 5.9, and the results are then compared with the experimental k_{rg} data.

5.4.3.1 Verification of Dual-Wet Hypothesis

In this part, the measured k_{rg} of three Montney samples is examined to investigate the relationship of organic matter with k_{rg}. Table 5.2 lists the petrophysical properties of these rock samples. The Klinkenberg air permeability is measured and analyzed by CMS-300 automated core measurement system, at ambient temperature and a hydrostatic overburden pressure of 2,000 psig. A pore pressure of 1,000 psig is applied during permeability measurement. A desired pressure drop is established between the upstream and the downstream. Then, pulse-decay is conducted and the

upstream, downstream, and mean pressures are monitored. Air permeability is calculated on the basis of the pulse-decay rate (Tinni et al., 2012; Fathi et al., 2012).

Table 5.2: Petrophysical properties of the Montney plugs.

Plug ID	Depth (m)	Porosity (%BV)	Permeability (mD)	TOC content (wt%)
1	2013.5	4.3	3.40×10^{-4}	0.62
2	2026.1	6.7	4.77×10^{-3}	0.55
3	2023.7	7.7	1.46×10^{-2}	0.51

As shown in Table 5.2, by decreasing the TOC content from Samples 1 through 3, the values of Klinkenberg permeability and porosity increase. This is in agreement with Fig. 5.4a that shows the pore-throat size distribution of the Montney samples is predominantly controlled by the proportion of solid bitumen/pyrobitumen that fills the paleopore volume (Wood et al., 2015). Higher TOC content can block pore throats and decrease the effective porosity and permeability (Lan et al., 2015a; Wood et al., 2015).

Fig. 5.9a presents the measured k_{rg} of the three Montney rock samples. The core sample was fully saturated with simulated formation brine at the start of the test. Then, it was loaded into a centrifuge apparatus and spun under air at incrementally increasing speeds to desaturate it. After the completion of each desaturation cycle, the sample was removed from the centrifuge, wrapped in cellophane, and placed in a humidity bath for 48 hours to allow water redistribution. The water saturation was measured by mass balance, and the sample was then loaded into hydrostatic core holder at a net hydrostatic overburden pressure of 2,000 psig and ambient temperature. Finally, effective permeability to gas at a certain water saturation was measured with a pulse-decay permeameter at 1,000 psig pore pressure.

On the basis of the dual-wet model, a higher amount of organic material (or S_{org}) leads to lower k_{rg}, for a fixed water saturation. Here, it is reasonable to assume that the samples with higher TOC content have higher fraction of water-repellant pores (S_{org}). Consequently, the samples with higher TOC content should show lower k_{rg}, for a fixed water saturation. As can be seen from Fig. 5.9a, Samples 3 and 1 have the maximum and minimum values of k_{rg}, respectively, and Sample 2 lies between them (k_{rg} (3) > k_{rg} (2) > k_{rg} (1)). Besides, Samples 1 and 3 have the maximum and minimum TOC contents, and Sample 2 lies between them (TOC (3) < TOC (2) < TOC (1)). The

inverse relationship between the TOC contents and the measured k_{rg} data, for a fixed water saturation, is in agreement with the proposed dual-wet model (Fig. 5.8).

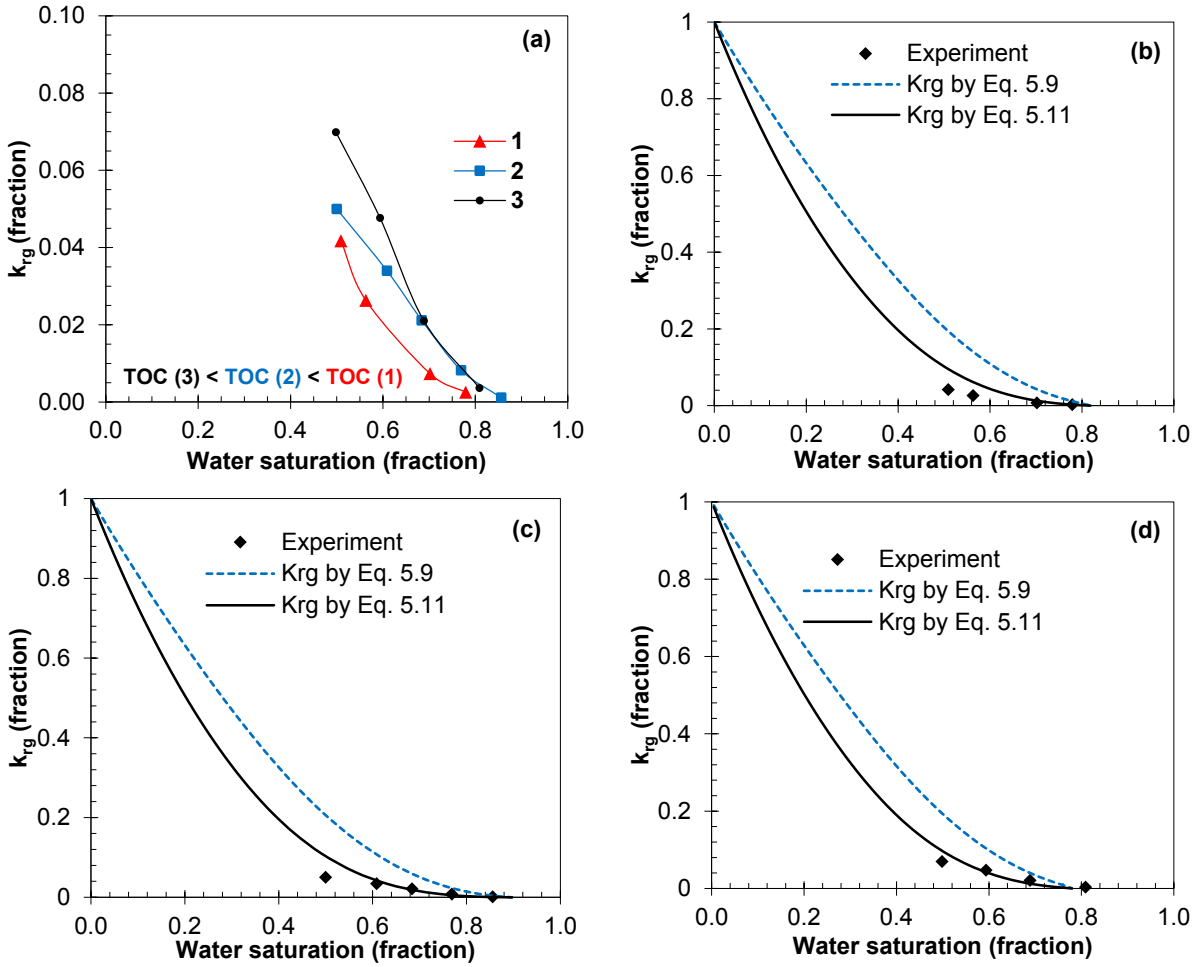

Fig. 5.9: (a) Measured gas relative permeability of the Montney plugs. Comparison of the measured k_{rg} data of (b) Sample 1, (c) Sample 2, and (d) Sample 3 with the values predicted by Eqs. 5.9 and 5.11.

5.4.3.2 Comparison of Measured and Predicted k_{rg}

In this subsection, MICP data of the three Montney samples (Table 5.2) are used to calculate the gas relative permeability by Eq. 5.9. First, we assume $S_{org} = 0$ in Eq. 5.9. The dotted curves in Figs. 5.9b through 5.9d are calculated k_{rg} by using Eq. 5.9. There is a considerable difference between measured and calculated values for the three plugs. As noted previously, we considered the effect of tortuosity by multiplying Eqs. 5.6 and 5.7 by S^2_{wa} and $(1-S_{wa})^2$, respectively. These two coefficients act as tortuosity factors for wetting and non-wetting phases in conventional rocks. Winsauer et al. (1952) used the analogy between the flow of electrical current and fluid flow, and measured the tortuosity of 31 sandstone samples. They concluded that the lower the porosity is,

the longer is the length of the flow path from one end of the porous medium to the other end. The longer the flow path is, the higher is the tortuosity of the porous medium. Therefore, for unconventional rocks, the values of tortuosity are higher than those for conventional sandstone and carbonate rocks. This is caused by ultralow value of porosity in tight and shale rocks.

To have a better match between the measured and calculated k_{rg}, we modified the tortuosity factor of water and gas phases. After optimization, the best match was obtained by changing the exponents of S_{wa} and $(1-S_{wa})$ from 2 to 3. A higher value of this exponent is equivalent to higher tortuosity. For example, in the capillary-tube model (Eqs. 5.3 and 5.4), the exponents are equal to zero, which mean the absence of a tortuosity factors for water and gas. Therefore, the final form of the dual-wet model is given by,

$$k_{rw}(S_{wa}) = S_{wa}^3 \times \frac{\int_{S_{org}}^{(S_{org}+S_{wa})} \frac{dS_w}{P_c^2}}{\int_0^1 \frac{dS_w}{P_c^2}} \tag{5.10}$$

$$k_{rg}(S_{wa}) = (1-S_{wa})^3 \times \frac{\int_{(S_{org}+S_{wa})}^{1} \frac{dS_w}{P_c^2} + \int_0^{S_{org}} \frac{dS_w}{P_c^2}}{\int_0^1 \frac{dS_w}{P_c^2}} \tag{5.11}$$

The solid curves in Figs. 5.9b through 5.9d show the calculated values of k_{rg} by Eq. 5.11, for the three Montney plugs. We observe an acceptable match between the experimental and calculated values. The data reported by Wood (2013) also confirm the high tortuosity of these samples. He presented k_{rg} of 15 plugs from 4 wells in the Montney gas play. For water saturations higher than 0.5, the majority of the k_{rg} data lie below 0.05, which is in the same range of k_{rg} presented in Fig. 5.9.

5.5 Modeling Water Imbibition Using the Dual-Wet Model

In this part, the proposed relative permeability model is applied to simulate co-current water imbibition for two of the Montney plugs (UMT_{3w} and UMT_{4w} in Table 5.1). Then, the simulation results are compared with the measured imbibition data.

A black-oil simulator is used for modeling the two-phase (gas/water) co-current spontaneous imbibition. Fig. 5.10 shows a schematic of the radial simulation-model that is divided into two sections. Part I is composed of 2,400 gridblocks representing the plug. There are 10, 8, and 30 grids in r (radial), θ (angular), and z (height) directions, respectively. The measured porosity and

permeability of the plug are assigned to these gridblocks (Table 5.1). The initial gas saturation and initial pressure are equal to 100% of PV and 14.7 psia, respectively. Part II is composed of one gridblock representing the source of water imbibing into the plug. This gridblock has porosity and permeability of 100% of bulk volume and 10,000 md, respectively. The initial water saturation and initial pressure of this single block are 100% PV and 14.7 psia, respectively. Part II is below Part I to model co-current imbibition of water into the gas-saturated plug. The water imbibes vertically from Part II to Part I, and the gas is displaced in radial direction toward the production wells. The volume of produced gas is equal to the imbibed volume of water from Part II to Part I.

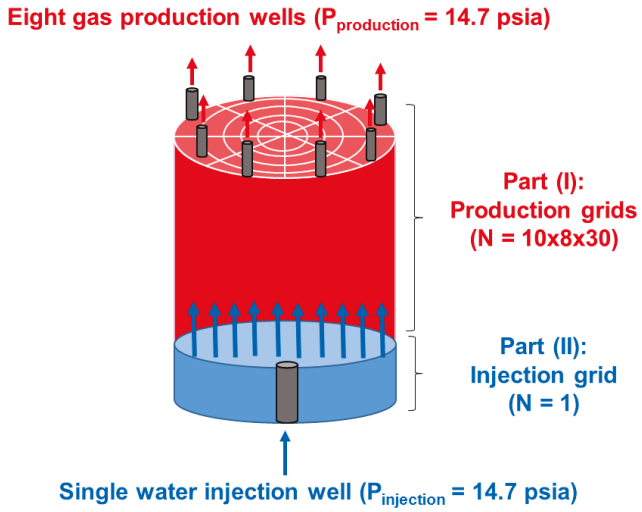

Fig. 5.10: Schematic of simulation model for co-current spontaneous imbibition of water.

The imbibition experiments are conducted at atmospheric pressure. The pressure of the water source remains at a constant value of 14.7 psia, and the gas is produced at 14.7 psia. Two groups of production and injection wells are defined to account for the effects of atmospheric pressure and boundary conditions. The locations of injection and production wells are selected in a way to simulate the actual experimental conditions. In the first group, 8 wells are located at the boundary of Part I. These wells produce gas with a constant bottomhole pressure of 14.7 psia as the constraint. The perforation interval of these wells includes all 30 layers in the z-direction. In the second group, a single well is defined at the center of Part II. This well injects water with a constant bottomhole pressure of 14.7 psia. This injection well stabilizes the pressure of the water source at constant value of 14.7 psia, during spontaneous imbibition.

Two input parameters are needed to start the simulation. The first parameter is the air/water capillary pressure, which is the only driving force for spontaneous imbibition. The Leverett J-function is used to convert the MICP data from a mercury/air to an air/water system. Eqs. 5.12 and 5.13 show the air/water capillary pressure for UMT_{3w} and UMT_{4w}, respectively,

$$P_{cgw}(atm) = 5.77 \times S_w^{-1.66} \quad for\ UMT3_w \tag{5.12}$$

$$P_{cgw}(atm) = 6.01 \times S_w^{-1.60} \quad for\ UMT4_w \tag{5.13}$$

The second parameter is the gas/water relative permeability curve. Here, the proposed dual-wet theory for relative permeability is applied to calculate the gas/water relative permeability by using the MICP data. In Eqs. 5.10 and 5.11, the value of S_{org} is unknown. The measured imbibition data can be used to roughly estimate the value of S_{org}. Water imbibition data for UMT_{3w} and UMT_{4w} show that the equilibrated imbibed volumes water (I_w^{eq}) at the end of the experiments are almost 30% and 32% of PV, respectively. In other words, 70% and 68% of PV are still saturated with air, and are not accessible for water imbibition. On the basis of the dual-wet model, a large fraction of the inaccessible pores for water may be coated by organic matter with low wetting affinity to water. In conclusion, the values of S_{org} are estimated to be approximately 0.7 and 0.68 (fraction PV) for UMT_{3w} and UMT_{4w}, respectively.

To compare the simulation results with the conventional model of relative permeability, the gas/water relative permeability curves are also calculated by assuming a uniformly water-wet system (S_{org} = 0). The results of gas/water relative permeability for the UMT_{3w} and UMT_{4w} samples are shown in Figs. 5.11a and 5.11b, respectively. The main differences between the relative permeability of the dual-wet and uniformly water-wet models are: 1) the curvatures of relative permeability data and 2) the endpoint water saturations. In the uniformly water-wet system, the endpoint water saturation is equal to 1. In other words, water can displace the entire volume of gas from all water-wet and water-repellant pores. For the dual-wet system, the endpoint water saturation is equal to (1-S_{org}). In other words, water can displace only the gas in the water-wet pores with total saturation of (1-S_{org}).

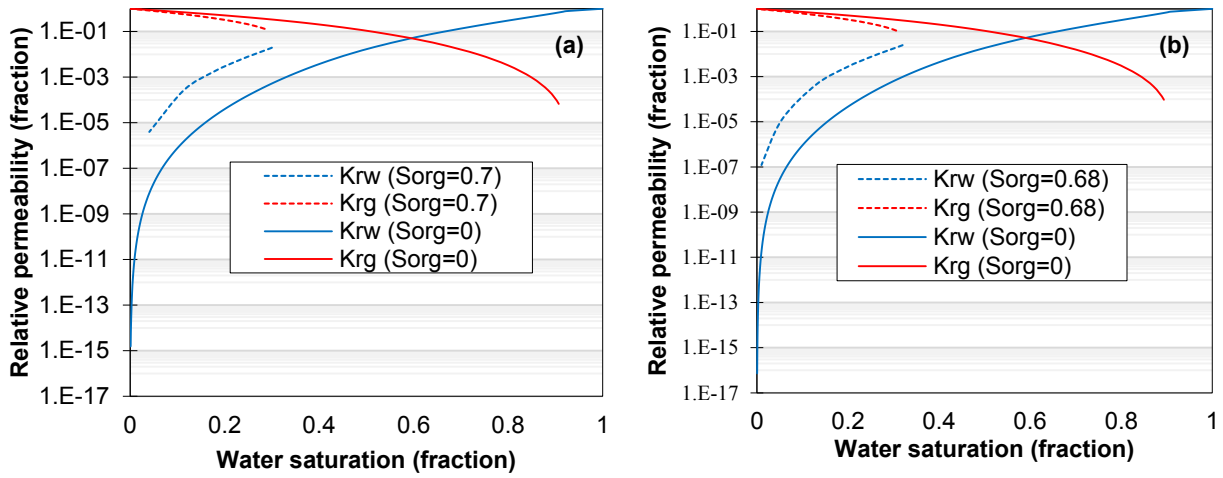

Fig. 5.11: Water and gas relative permeability curves by using the dual-wet and uniformly water-wet models for (a) UMT_{3w} and (b) UMT_{4w}.

Four simulations are run for all four relative permeability curves presented in Figs. 5.11a and 5.11b. Figs. 5.12a and 5.12b compare the simulated and measured water imbibition data for the dual-wet and uniformly water-wet systems, respectively. The dual-wet model (Fig. 5.12a) shows a better match with the measured imbibition data compared with the uniformly water-wet model (Fig. 5.12b). In the uniformly water-wet system, water is allowed to imbibe into all the pores, including water-repellant organic and water-wet inorganic pores. This is the reason for higher simulated imbibed volume of water in the uniformly water-wet system compared with that in the dual-wet system.

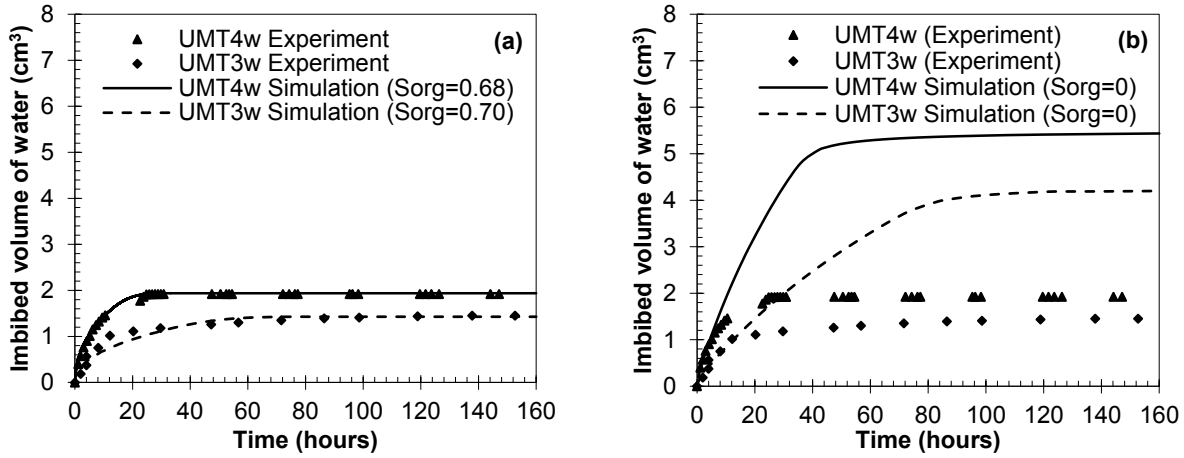

Fig. 5.12: Measured and simulated water imbibition for UMT_{3w} and UMT_{4w} samples by using the (a) dual-wet and (b) uniformly water-wet models.

5.6 Summary

Both aqueous and oleic phases spontaneously imbibe into the Montney plugs. However, the equilibrated oil uptake is significantly higher than the equilibrated water uptake, and the difference is more pronounced for the samples with higher TOC content. Furthermore, the results of FIB/SEM, organic petrography, and MICP analyses suggest that the pore network of the Montney samples can be divided generally into: 1) nanoscale pores within the organic matter mainly composed of solid bitumen/pyrobitumen (Part I) and 2) microscale pores among inorganic minerals (Part II). Part I is usually represented by the tail part at the low end of the pore-throat size distribution from MICP data, whereas Part II is represented by the bell-shaped part at higher pore-throat size. Moreover, the comparative water/oil imbibition data suggest that Part I is strongly water-repellant.

We extended Purcell's model to describe two-phase flow of water and gas through this dual-porosity/dual-wet system. We assumed that gas is the wetting phase in organic pores (Part I), and is the non-wetting phase in inorganic pores (Part II). Therefore, for a certain value of S_w, Part I is fully saturated with gas, whereas Part II is shared with water as the wetting phase and gas as the non-wetting phase. The model results show that increasing the fraction of water-repellant pores reduces gas relative permeability, for a fixed water saturation.

The hypothesis of the dual-wet behavior is in agreement with the measured gas relative permeability data. The Montney plugs with higher TOC content have lower gas relative permeability, for a fixed water saturation. The comparison of the proposed dual-wet model with experimental relative permeability data shows that a higher tortuosity factor is required to match the experimental data.

The applicability of the proposed model was tested with a black-oil simulator to simulate the experimental water-imbibition data. The simulation results with the dual-wet relative permeability model show a very good match with the experimental water-imbibition data.

Nomenclature

BV= Bulk volume, L^3 [cm^3]
F_l = Lithology factor, dimensionless
I_o = Normalized imbibed volume of oil, [%PV]
I_o^{eq} = Equilibrated I_o, L^3/L^3 [%PV]
I_w = Normalized imbibed volume of water, [%PV]
I_w^{eq} = Equilibrated I_w, L^3/L^3 [%PV]
k = Absolute permeability, L^2 [mD]
k_g = Effective gas permeability, L^2 [mD]
k_w = Effective water permeability, L^2 [mD]
k_{rg} = Gas relative permeability, dimensionless
k_{rw} = Water relative permeability, dimensionless
P_c = Capillary pressure, $ML^{-1}t^{-2}$ [pa, Mpa, psi]
PV = Pore volume , L^3 [cm^3]
r = radius, L [μm]
r_{org} = Largest organic r, L [μm]
r_{Swa} = Largest inorganic r at S_{wa}, L [μm]
S_{air} = Air saturation, L^3/L^3 [%PV]
S_{org} = Saturation of organic pores, L^3/L^3 [%PV]
S_w = Water saturation, L^3/L^3 [%PV]
S_{wa} = S_w in a dual-wet system, L^3/L^3 [%PV]
S_{wir} = Irreducible water saturation, L^3/L^3 [%PV]
t = Time, t [hour]
TOC = Total organic carbon, M/M% [wt%]
WI_o = Oil wettability index, dimensionless
θ = Liquid contact angle, degree
σ = Surface tension , Mt^{-2} [mN/m]
μ = Viscosity, $ML^{-1}t^{-1}$ [pa.s, cp]
φ = Effective porosity, L^3/L^3 [%BV]

Abbreviations

FIB = Focused ion beam
LMT = Lower Montney
MICP = Mercury injection capillary pressure
SEM = Scanning electron microscopy
UMT = Upper Montney
XRD = x-ray diffraction

Chapter 6

CO_2-EOR from Dual-Wet Shales

6.1 Introduction

With the decline of conventional resources, attention toward unconventional oil and gas resources has increased considerably (Gonzalez et al., 2013; Law and Curtis, 2002). During the last decade, low-permeability reservoirs have been rapidly developed by horizontal drilling and multistage hydraulic fracturing. Tight-oil production has pushed the US oil supply to 11% of the world total production (US Energy Information Administration, EIA). However, field data and simulation studies show that only 5-14% of the original oil in place can be recovered after massive fracturing operations (Panja and Deo, 2016; Barba, 2015; Clark, 2009). What is the next boom in shale development? More aggressive drilling and fracturing or more effective technologies to recover the remaining oil from existing wells?

Field and laboratory results suggest that rock/fluid interactions after fracturing operations can significantly influence well performance, depending on rock wettability (Dehghanpour et al., 2013 and 2012), reservoir conditions, fracturing fluid formulation (Montgomery, 2013), and shut-in periods (Crafton, 2015; Centurion et al, 2014; Crafton and Noe, 2013). Wettability is an important rock/fluid property that affects the oil recovery (Morrow, 1990), electrical resistivity of rock (Mungan and Moore, 1968), capillary pressure (Anderson, 1987a), water flood behavior (Morrow, 1987), and relative permeability (Yassin et al., 2016; Anderson, 1987b). Evaluation of shale wettability is significant for: 1) investigating water blockage in matrix followed by rapid decline in production rate (Bertoncello et al., 2014), 2) mitigating low fracturing fluid recovery after fracturing operations (Roshan et al., 2016; Ghanbari and Dehghanpour, 2016 and 2015; Cheng, 2012), 3) investigating fracture-face damage and subsequent cleanup strategies after fracturing (Barati et al., 2009), 4) selecting the type of fracturing fluid (water-based or oil-based) and its chemical additives such as surfactants for higher post-flowback hydrocarbon production (Yassin et al., 2018a; Mirchi et al., 2015), 5) investigating the consequences of condensate dropout below

dewpoint pressure (Meng and Sheng, 2016; Sheng et al., 2016), 6) investigating the spatial distribution and morphology of oil-wet and water-wet pores (Yassin et al., 2016), and 7) selecting appropriate capillary pressure and relative permeability curves for reservoir engineering calculations (Yassin et al., 2016).

The results of wettability tests conducted on Bakken (Wang et al., 2012), Wolfcamp (Neog and Schechter, 2016), Eagle Ford (Nguyen et al., 2014), Permian (Alvarez and Schechter, 2017), and Marcellus (Engelder et al., 2014) shale plugs show that the wetting affinity these samples are intermediate-wet to oil-wet. Odusina et al. (2011) used Nuclear Magnetic Resonance (NMR) analysis and studied the wettability of shale samples from Barnett, Floyd, and Woodford Formations. They concluded that the shale samples exhibit mixed-wet behavior, with pores within organic matter contributing to the strong oil-wet behavior. Combined analyses of oil recovery, wettability, and scanning electron microscopy (SEM) results demonstrate that the strong oil-wet characteristics of shale samples is due to the abundant water-repellant pores within organic matter (Yassin et al., 2018a and 2016). As a result, significant volume of oil may be trapped in sub-micron oil-wet pores, mainly within organic matter. Recovering this oil is a real challenge both economically and technically. It has been proposed to add surfactant solutions in fracturing fluids to enhance the oil recovery factor (RF) (Alvarez and Schechter, 2017; Neog and Schechter, 2016; Nguyen et al., 2014; Wang et al., 2012). The results show that using appropriate surfactant solutions can lead to additional oil recovery from oil-wet shales by counter-current imbibition process.

Recently, a large number of experimental (Alharthy et al., 2018; Wang et al., 2017; Huo et al., 2017; Kimbrel et al., 2015) and simulation (Peck et al., 2018; Zuloaga-Molero et al., 2016; Zhu et al., 2015; Li et al., 2015) studies have been conducted to investigate CO_2-enhanced oil recovery (EOR) and CO_2-storage in shale and tight reservoirs. Hawthorne et al. (2014 and 2013) conducted a series of CO_2-soaking tests and investigated the effect of CO_2 exposure time, oil composition, and rock surface area on oil recovery. They proposed a 4-step conceptual mechanism for oil recovery by CO_2: 1) CO_2 rapidly flows through the fractures, 2) CO_2 flows into the rock due to pressure gradient between fracture and matrix, 3) oil expands and migrates into the bulk CO_2 phase in fracture, and 4) oil in the bulk CO_2 phase flows from fractures to the production well. When CO_2 pressure gradient between matrix and fracture becomes small enough, further oil production is based on diffusion mechanism triggered by CO_2 concentration gradient. Wang et al. (2017)

visually investigated CO_2-soaking process by analyzing NMR (nuclear magnetic resonance) transverse relaxation time and MRI (magnetic resonance imaging). They concluded that oil expansion due to CO_2 diffusion is the main mechanism for oil mobilization. Eide et al. (2016) and Darvish et al. (2006) also highlighted the importance of CO_2 diffusion as an oil recovery mechanism.

The results of CO_2-soaking tests in the previous studies (Hawthorne et al., 2014 and 2013) show that the oil-recovery mechanisms from tight matrix are mainly governed by CO_2 dissolution into the oil phase, oil expansion, and oil migration into the bulk CO_2 phase. However, the sequence of aforementioned mechanisms as well as the individual significance of each mechanism on oil recovery are not well understood. Furthermore, the results of tests conducted on tight and shale plugs (Wang et al., 2017; Gamadi et al., 2014) show that increasing CO_2 pressure leads to higher oil RF. This observation was attributed to the stronger miscibility of CO_2 with oil at higher pressures. Oil mobilization mechanism from tight matrix into fracture system at higher CO_2 pressures is still a debatable subject which will be investigated in this chapter by conducting a set of visualization tests.

In Chapter 6, we review the results of Duvernay wettability tests presented in Chapter 2. Then, we analyze the results of oil-recovery tests by brine and CO_2. To explain the results of brine-soaking tests, we interpret the petrophysical properties and liquid/liquid contact angles, measured prior to immersing the oil-saturated plugs in brine. We use a high-pressure and high-temperature visual cell, and visualize the alterations occurring on surface of the plugs during the CO_2-soaking process to understand the role of different mechanisms in oil production from shale plugs. By changing the CO_2 physical state from gaseous to supercritical conditions, we qualitatively investigate the effects of oil expansion and oil extraction mechanisms on oil production. To explain the results of CO_2-soaking tests, we conduct bulk-phase tests and visualize CO_2/oil interactions in the visual cell.

6.2 Materials and Equipment

6.2.1 Shale Plugs

We select 9 twin plugs from Minhik (MIN), Wahigan (WAH), Ferrier (FER), Saxon (SAX), and Cecilia (CEC) wells. We have two twin plugs for each well, except for Saxon with only one

twin plugs. The depth, dry mass, length, effective porosity (φ_{eff}), and pressure-decay permeability (k_{Decay}) of the twin plugs are listed in Table 2.1. All plugs with 3.8 cm in diameter were drilled horizontally from full-diameter cores. The depth of the plugs ranges from 3095 m for MIN1 to 3963 m for CEC2. We test all samples as-received and do not use any washing fluids such as toluene or methanol. More details about the results of XRD analysis and rock-eval pyrolysis are presented in Chapter 2.

6.2.2 Reservoir Fluids

We use reservoir oil and brine collected from the wells next to the cored wells, to conduct contact angle, spontaneous imbibition, and brine-soaking tests. The produced brine is a mixture of slickwater used for hydraulic fracturing, and formation brine. Table 6.1 lists the values of viscosity, surface tension, interfacial tension (IFT), and density of the reservoir fluids at 72°F and atmospheric pressure (0 psig), measured by concentric cylinder rheometer, Wilhelmy plate, Du Noüy ring, and displacement method (Archimedes' principle), respectively. Oil samples from all 4 wells are translucent and have amber or yellowish color (Fig. 6.1). Table 6.1 also lists the total dissolved solids (TDS) ranging from 153,000 (MIN) to 176,000 (WAH) ppm. The reservoir oil and brine are not available for CEC well, and we use FER fluid samples for conducting the tests on the CEC plugs.

Table 6.1: Physical properties of reservoir oil and brine samples at 72°F and 0 psig.

Well	Viscosity (cp)		Surface tension (mN/m)		IFT (mN/m)	Density (g/cm^3)		TDS (ppm)
	Brine	oil	Air/Brine	Air/Oil	Oil/Brine	Brine	oil	Brine
MIN	1.50	1.20	47.8	23.3	17.9	1.048	0.762	153,000
WAH	1.60	2.10	62.5	23.5	27.4	1.111	0.787	176,000
FER	1.62	1.37	51.9	23.2	18.1	1.129	0.747	156,000
SAX	1.48	1.35	46.5	22.3	15.6	1.080	0.771	171,000

We select WAH and FER oil samples for conducting bulk-phase tests between CO_2 and oil. The result of compositional analysis of the WAH oil sample in Fig. 6.1 indicates that the weight fraction of intermediate components is significantly higher than that of heavy components. For instance, cumulative fraction of components between C_7 to C_{14} is 76.04 wt%; while there is no component heavier than C_{42} in WAH oil sample.

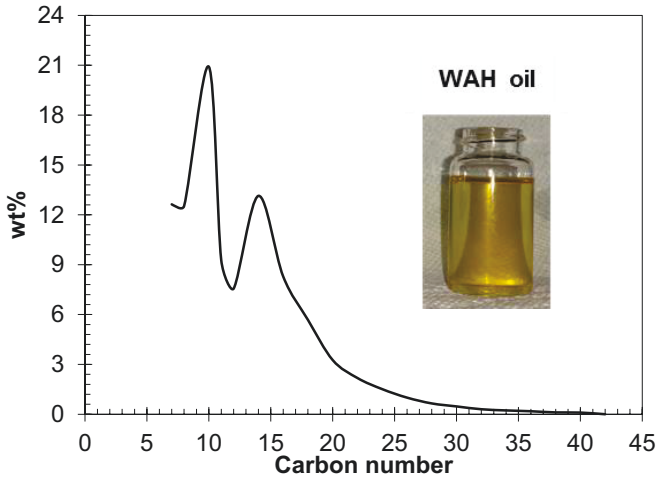

Fig. 6.1: Compositional analysis of the WAH oil sample measured by simulated distillation test.

6.2.3 Visual Cell Setup

Fig. 6.2 shows the custom-designed visual cell setup used for high-pressure and high-temperature visualization tests. The main components of this setup are continuous pulse-free pump, two accumulators, and the visual cell. The continuous pulse-free pump injects deionized (DI) water to the lower part of the accumulators. The maximum operating pressure and flow rate of the pump are 12,000 psig and 29 cm^3/min, respectively. The upper part of one accumulator is filled with oil and the upper part of the second accumulator is charged with CO_2 tank. The total volume and maximum operating pressure of each accumulator are 500 cm^3 and 10,000 psig, respectively. By injecting DI water to the lower part of the accumulators, oil or CO_2 flows from the upper part of the accumulators into the visual cell. Two inlet ports are embedded in the visual cell. The upper and lower inlet ports are used for CO_2 and oil injections, respectively. A heating jacket (amber color) coats the visual cell and a temperature controller adjusts the temperature of the visual cell up to 392°F, with an accuracy of ±0.2°F. A digital pressure transducer connected to a data acquisition system records the pressure of the visual cell with an accuracy of ±2 psig. The visual cell is equipped with two sight glasses, standing maximum pressure of 4,000 psig. We use a high-resolution camera next to the front-side sight glass to record gas/oil interactions during the visualization tests. The rear-side sight glass is equipped with a white light source to provide the required light for the visualization purposes. To protect the sight glasses, a safety pressure valve is used at the upper part of the the visual cell to release the residing gas or liquid when visual-cell pressure exceeds 4,000 psig.

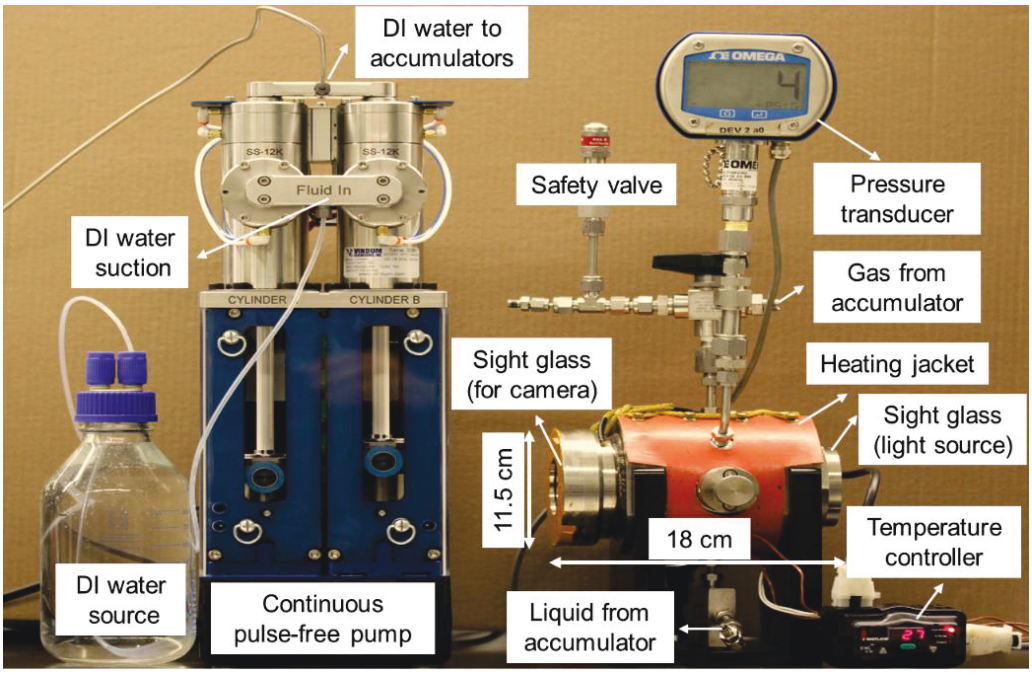

Fig. 6.2: A picture of the visual-cell setup used for investigating CO_2-soaking tests and CO_2/oil interactions under reservoir conditions. The accumulators are not shown in this figure (Yassin et al., 2018).

6.3 Methodology

6.3.1 Evaluation of Wettability

In Chapter 2, we evaluated the wettability of the Duvernay plugs by conducting air/liquid spontaneous-imbibition and contact-angle tests as well as analyzing SEM/EDS images and petrophysical properties.

6.3.2 Oil Recovery by Brine-Soaking Test

In this part, we explain the procedure for conducting brine-soaking tests.

Liquid-Liquid Contact Angle Measurement. We measure the contact angles of oil and brine on polished surfaces of the oil-saturated plugs. For measuring oil (or brine) contact angle, the oil-saturated plug is fully immersed in the brine (or oil) and a droplet of oil (or brine) is placed on the surface of the plug. The camera's software records the droplet shape and determines the equilibrium contact angle.

Soaking Tests with Brine. We fully immerse the oil-saturated shale plug in the brine (Table 6.1), and measure the volume of oil produced and accumulated at the top of the Amott cell. Oil RF

is calculated by diving the equilibrated volume of produced oil by the initial volume of the oil in the plug. Oil-saturated plugs of MIN1, MIN2, WAH1, and FER1 are used for brine-soaking tests.

6.3.3 Oil Recovery by CO_2-Soaking Test

Here, we explain the procedures for conducting: 1) CO_2-soaking and 2) bulk-phase CO_2/oil tests by using the visual cell.

6.3.3.1 Soaking Tests by CO_2

Similar to brine-soaking tests, we soak the oil-saturated plugs (MIN2 and FER1) in CO_2. After weighing the oil-saturated plug, we place it in the visual cell (Fig. 6.2) and run the heating jacket to reach the set temperature (T_{set} = 122°F). The continuous pulse-free pump is used to inject CO_2 into the visual cell until reaching the desired pressure. We record the alterations occurring on the surface of the plug during the soaking process, by using a high-resolution camera.

To finish the test, we vent the CO_2 out of the visual cell and reduce the pressure gradually until reaching 0 psig. Then, the plug is removed from the visual cell and is weighed using a digital balance. The difference between plug's mass before and after CO_2-soaking test is used to calculate oil RF.

6.3.3.2 Bulk-phase CO_2/Oil Interactions

In order to understand CO_2/oil interactions, we conduct bulk-phase tests between CO_2 and oil, in the absence of shale samples. We use the high-pressure and high-temperature visual cell (Fig. 6.2), and conduct the bulk-phase tests:

Step 1**: **Base Oil volume Determination. We fill the first accumulator with WAH (or FER) oil sample and use the continuous pulse-free pump to inject 1.25 mol (242 cm^3 at 72°F and 0 psig) of oil for filling almost half of the visual cell. Then, the visual-cell temperature is set to 122°F (T_{set}) which is higher than critical temperature of CO_2 (T_c = 87.8°F). The volume of oil at atmospheric pressure (0 psig) and T_{set} is considered as the base oil volume ($V_{oil}|_{P=0}$) for calculation of oil expansion factor (EF_{oil}) after CO_2 injection into the visual cell,

$$EF_{oil} = \left(\frac{V_{oil}|_{P'}}{V_{oil}|_{P=0}}\right)_{T_{set}} \tag{6.1}$$

where, $V_{oil}|_{P'}$ is the volume of oil at any elevated pressure ($P' > 0$ psig) during the pressure-buildup (Step 2) and soaking (Step 3) processes. EF_{oil} is equal to 1.00 before introducing CO_2 into the visual cell.

Step 2: Pressure-Buildup Process. The second accumulator is charged with a CO_2 tank, supplying a pressure of ~700 psig. Then, we use continuous pulse-free pump and inject CO_2 from the accumulator into the visual cell, partly filled with oil. We keep injecting CO_2 until the visual-cell pressure builds up from zero to the set pressure (P_{set}) of 2,000 psig. Then, the injection valve is closed and no more CO_2 is injected into the visual cell. P_{set} is considered as the maximum pressure in the bulk-phase tests. CO_2 is supercritical at 122°F and 2,000 psig.

In order to minimize the duration of pressure-buildup process, we run the pump at maximum DI water flow rate of 29 cm^3/min. It takes about 22 minutes to reach P_{set}. A high-resolution camera is used to record the nonequilibrium interactions between the oil phase and the injected CO_2 during the pressure-buildup process. EF_{oil} at P_{set} and T_{set} is referred to as initial EF_{oil} ($EF_{oil,ini}$).

Step 3: Soaking Process. After pressure-buildup process, the visual-cell pressure declines from P_{set} to equilibrium pressure (P_{eq}), indicating nonequilibrium interactions between CO_2 and oil. EF_{oil} at the P_{eq} and T_{set} is referred to as equilibrium EF_{oil} ($EF_{oil,eq}$). Similar to Step 2, we investigate the nonequilibrium interactions at the CO_2/oil interface and within the bulk oil phase.

6.4 Results and Discussions

6.4.1 Wettability Measurement Results

Here, we present a summary of the results of wettability tests presented in Chapter 2. Oil droplets completely spread, while brine droplets form contact angles higher than 60°, suggesting the strong wetting affinity of the shale samples to oil (Fig. 2.5). Fig. 2.6 shows the normalized imbibed volumes of oil (I_o) and brine (I_w) vs. time for the twin plugs. I_o and I_w are calculated by dividing the imbibed volumes of oil and brine, respectively, by the effective pore volume (PV) of the plugs. $I_o > I_w$ for each twin plugs, suggesting that the wetting affinity of the plugs to oil is stronger than that to brine, consistent with the air/liquid contact angle results. According to Fig. 2.6, brine imbibition reaches to equilibrium state faster than oil imbibition. Considering the pore network of rock sample as an idealized bundle of capillary tubes with different pore sizes, the wetting phase first imbibes into the larger pores, followed by filling the smaller pores (Shi et al.,

2018; Handy, 1960). Late equilibrium of oil profiles compared with brine profiles suggests that there are abundant small water-repellant pores with strong wetting affinity to oil.

To verify the existence of water-repellant pores, we investigated SEM images and petrophysical properties of the Duvernay plugs. SEM images of Duvernay samples in Fig. 2.9 show the abundant small pores within the organic matter. Organic matter is expected to have high wetting affinity to oil (Mitchell et al., 1990).

Figs. 2.12a through 2.12e show the crossplots of effective porosity vs. TOC content for shale samples from 5 wells drilled in the Duvernay Formation. Shale samples with higher TOC content generally have higher effective porosity. The positive correlations between effective porosity and TOC content suggest that the majority of pores are within the organic matter. This is consistent with the SEM images (Fig. 2.9), showing the abundant small pores within organic matter. High fraction of hydrophobic organic pores may explain the higher imbibed volume of oil compared with that of brine, and also the late equilibrium of oil.

6.4.2 Oil Recovery by Brine Imbibition

Figs. 6.3a shows an oil droplet with contact angle of 47° equilibrated on the surface of the oil-saturated MIN1 plug, immersed in brine. Fig. 6.3b presents brine contact angle of 153° on the surface of the oil-saturated MIN1 plug, in the presence of oil. The brine contact angle is three times higher than the oil contact angle, indicating that the oil-saturated plug is strongly oil-wet. This observation is consistent with the results of wettability tests presented in the previous section.

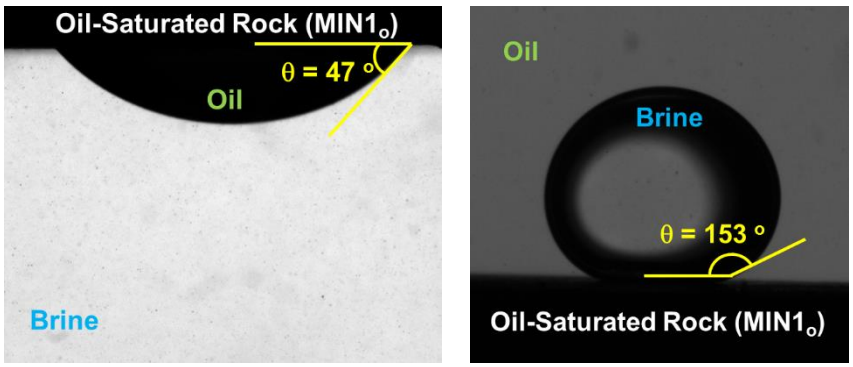

(a) (b)

Fig. 6.3: (a) The contact angle of an oil droplet equilibrated on the surface of oil-saturated MIN1 plug, immersed in brine. (b) The contact angle of a brine droplet equilibrated on the surface of oil-saturated MIN1 plug, immersed in oil.

To investigate imbibition oil recovery, we fully immerse the oil-saturated MIN1 plug in an Amott cell filled with brine. We observe oil droplets attached on the surface of the plug, after 30 days of soaking in brine (Fig. 6.4a). However, the volume of oil accumulated at the top of the cell is negligible. Although the size of oil droplets attached on the surface of the plug increases after 120 days of soaking (Fig. 6.4b), the produced oil volume, and consequently oil RF are negligible. We conduct similar brine-soaking tests on WAH1, FER1, and MIN2 plugs, and observe oil RFs of 0.0%, 1.9%, and 6.2%, respectively, after 120 days.

The results show that brine does not spontaneously imbibe into the oil-saturated plugs. Low imbibition oil recovery by brine is consistent with the results of liquid/liquid contact angle measurements, illustrating brine contact angle of 153°, in the presence of oil (Fig. 6.3b). This observation can be explained by the fact that majority of connected pores are within the organic matter, and brine may not have enough wetting affinity to spontaneously displace the oil out of these hydrophobic organic pores.

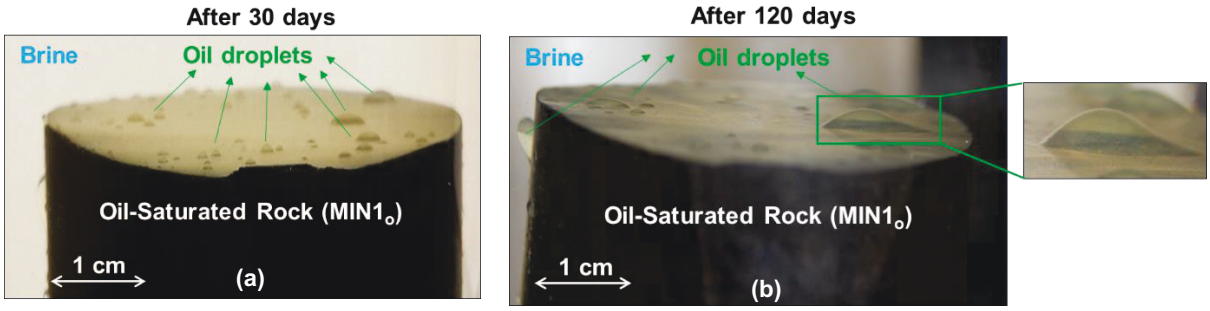

Fig. 6.4: Oil droplets attached on the surface of the oil-saturated MIN1 plug after soaking in brine for (a) 30 and (b) 120 days.

6.4.3 Oil Recovery by CO_2

Here, we present and discuss the results of CO_2-soaking tests and bulk-phase CO_2/oil interactions.

6.4.3.1 Soaking the Oil-saturated Plugs in CO_2

In this subsection, we present the results of soaking oil-saturated plugs in CO_2 at 122°F. During the soaking process, we visualize the end face of the plug to record possible alterations due to CO_2/rock/oil interactions. By increasing the pressure from 0 to 2,000 psig at 122°F, CO_2 physical state changes from gaseous to near-supercritical, and then to supercritical. First, we present our observations at different pressures and then discuss the results.

Gaseous CO_2. The surface of the oil-saturated plug is completely dry before introducing CO_2 into the visual cell at 0 psig and 122°F (Fig. 6.5a). Right after increasing the pressure to 850 psig, the plug's surface becomes partially wet by a liquid phase. CO_2 is a colorless gas at 850 psig. Therefore, the wet area may be attributed to the oil expelled from the plug. The pressure is kept at the constant value of 850 psig for 20 hours during which we do not observe any alterations in the wet area, as shown in Fig. 6.5b (t = 20 hours). Then, we increase the pressure from 850 to 970 psig, and observe that the area of the wet part increases. The pressure is kept at the constant value of 970 psig for 30 hours during which the wet area does not change, as shown in Fig. 6.5c (t = 50 hours).

Near-supercritical CO_2. We continue CO_2 injection and increase the pressure from 970 to 1,030 psig (Fig. 6.5d), which is close to P_c = 1,055.3 psig. Comparing Fig. 6.5d with 6.5c illustrates that the wet area shrinks, and the plug's surface becomes relatively dry. By increasing the pressure from 1,030 to 1,080 psig, CO_2 becomes supercritical, and the plug's surface becomes completely dry, as shown in Fig. 6.5e [Video 1].

Supercritical CO_2. Fig. 6.5f shows that after increasing the pressure to 1,380 psig, the plug's surface becomes partially-wet again. It appears that oil is preferentially produced along several layers parallel to the depositional laminations. These layers may be induced micro-fractures along bedding planes, created after reducing confining stress (Handwerger et al., 2011). By further CO_2 injection and increasing the pressure from 1,380 to 2,000 psig, the wet surface of the plug gradually dries out, as shown in Figs. 6.5f through 6.5h [Video 2].

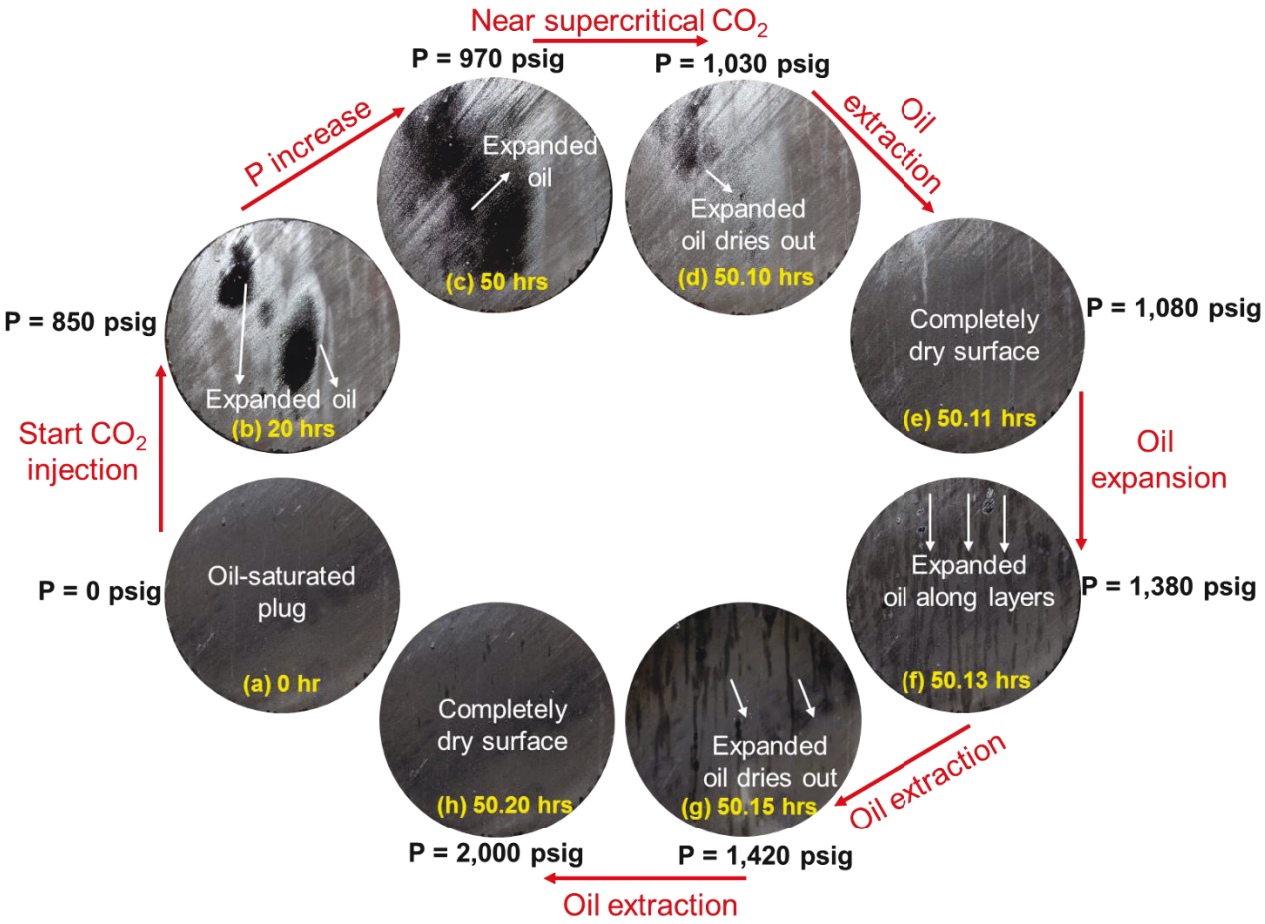

Fig. 6.5: Pictures of oil-saturated MIN2 plug soaked in CO_2 at T_{set} = 122°F and (a) 0, (b) 850, (c) 970, (d) 1,030, (e) 1,080, (f) 1,380, (g) 1,420, and (h) 2,000 psig. CO_2 is at supercritical state at 122°F and pressures higher than P_c = 1,055.3 psig. The diameter of the shale plug is 3.8 cm.

We soak MIN2 plug in supercritical CO_2 at 2,000 psig for 110 hours. After the soaking process, we gradually vent the CO_2 out and reduce visual-cell pressure to atmospheric pressure. When pressure drops below 800 psig, we observe accumulation of condensed oil droplets at the bottom of the visual cell. The condensed droplets are the oil extracted by supercritical CO_2. MIN2 plug is weighted after the soaking process, and oil RF is 82% of the initial oil which is much higher than oil RF of 6.2% by soaking the plug in brine.

A similar soaking process was conducted on the oil-saturated FER1 plug, and oil RF was 45% after 75 hours of soaking process. Lower oil RF of FER1 compared with oil RF of MIN2 is due to shorter CO_2 soaking time in FER1 test. Figs. 6.6a through 6.6f show the end face of FER1 as pressure increases from 0 to 2,000 psig. Similar to MIN2 test, the wet part shrinks and becomes relatively dry by changing the CO_2 physical state from gaseous to near-supercritical, and then to supercritical (Figs. 6.6b through 6.6d). By increasing CO_2 pressure to 1,245 psig (Figs. 6.6e), the

wet parts appear along parallel layers. As more CO_2 is injected and the pressure increases to 2,000 psig, the wet surface of the plug gradually dries out (Fig. 6.6f).

Fig. 6.7 shows the significantly higher oil RFs in CO_2-soaking tests compared with oil RFs in brine-soaking tests, for MIN2 and FER1 plugs.

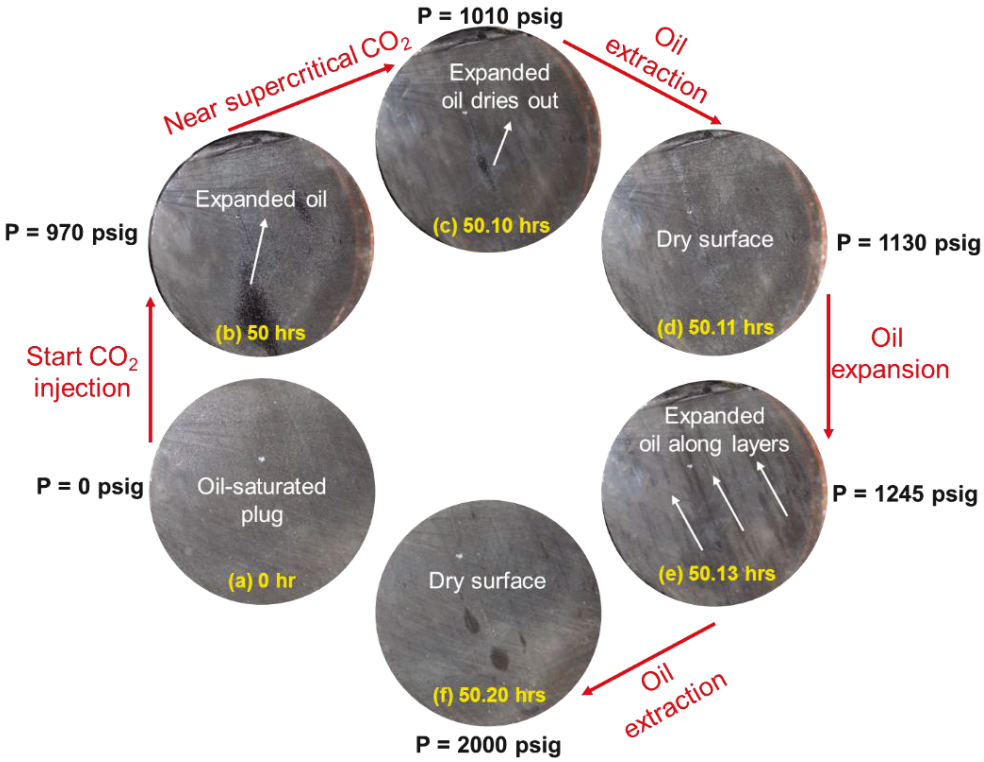

Fig. 6.6: Pictures of oil-saturated FER1 plug soaked in CO_2 at T_{set} = 122°F and (a) 0, (b) 970, (c) 1,010, (d) 1,130, (e) 1,245, and (f) 2,000. CO_2 is at supercritical state at 122°F and pressures higher than P_c = 1,055.3 psig. The diameter of the shale plug is 3.8 cm.

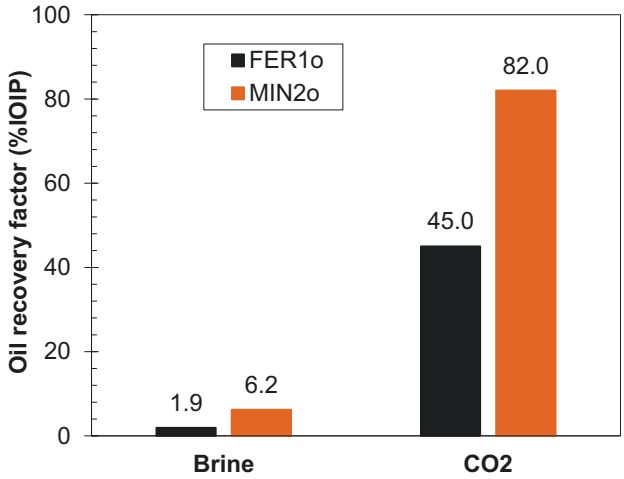

Fig. 6.7: Oil recovery factors after soaking the oil-saturated FER1 and MIN2 plugs in brine and CO_2.

The results suggest that gaseous CO_2 can diffuse into the oil-saturated plug, dissolve into and expand the oil phase, as shown by the wet areas in Figs. 6.5b and 6.5c. By approaching to near-supercritical conditions, the wet areas dry out, suggesting extraction of the expanded oil into the bulk CO_2 phase (Figs. 6.5d and 6.5e). To explain this observation, we need to consider the physical properties of CO_2 at pressures above and below P_c. According to Fig. 6.8, CO_2 density increases considerably as its physical state changes from gaseous to supercritical. Supercritical CO_2 with high density is a supersolvent with a stronger affinity for extraction of organic compounds compared with gaseous CO_2 (Hawthorne, 1990). Therefore, as gaseous CO_2 converts to supercritical CO_2, the expanded oil on the rock surface (Fig. 6.5c) is extracted into the bulk CO_2 phase, and the wet surface dries out (Figs. 6.5d and 6.5e). Oil extraction by supercritical CO_2 will be investigated by visualization of the bulk-phase CO_2/oil interactions.

Figs. 6.5f through 6.5h show the occurrence of a three-step mechanism when CO_2 is in supercritical state: 1) CO_2 diffuses into the oil-saturated plug and dissolves into the oil phase, 2) CO_2-saturated oil expands and wets the surface of plug, and 3) the expanded oil is extracted into the bulk CO_2 phase. This three-step mechanism may be repeated several times until no more oil is extracted by CO_2. To validate different stages of this conceptual hypothesis, we visually investigate the bulk-phase CO_2/oil interactions in the next part.

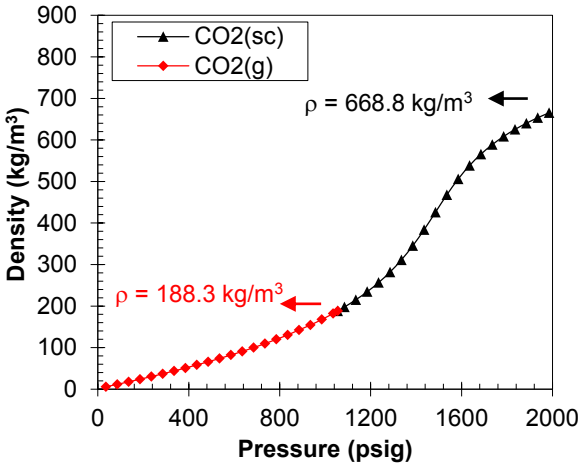

Fig. 6.8: Density of CO_2 vs. pressure at 122°F, based on the available data (NIST).

The results of wettability tests show that majority of the pores are within the organic matter, leading to the strong hydrophobicity of the Duvernay plugs. To investigate the pores invaded by CO_2, we compare the results of wettability tests with those of CO_2-soaking tests. Equilibrated I_w

(I_w^{eq}) in the air/brine imbibition tests (Table 2.8) can be considered as the fraction of hydrophilic pores, mainly bordered by inorganic minerals. For instance, the values of I_w^{eq} for MIN2 and FER1 plugs are 23% and 13% of pore volume, respectively. Oil RFs from CO_2-soaking tests are 82% and 45% for MIN2 and FER1 plugs, respectively. Oil RF > I_w^{eq} for both plugs, suggesting that supercritical CO_2 not only extracts the oil out of hydrophilic inorganic pores, but also extracts a portion of the oil out of hydrophobic organic pores. Conversely, oil RF < I_w^{eq} in the brine-soaking tests, suggesting that brine may displace only a portion of oil out of hydrophilic inorganic pores.

6.4.3.2 Visualization of CO_2/Oil Interactions

To verify the occurrences of 1) CO_2 dissolution, 2) oil expansion, and 3) oil extraction during CO_2-soaking tests, we conduct bulk-phase tests and visualize nonequilibrium interactions between CO_2 and oil in the visual cell at T_{set} = 122°F. Fig. 6.9 shows the oil levels at a) the initial condition of the test for determining the base oil volume, b) the end of the pressure-buildup process when P_{set} = 2,000 psig, and c) the end of the soaking process when P_{eq} = 1,480 psig. The pressure-buildup process for increasing the pressure from 0 to 2,000 psig takes 22 minutes, leading to a significant jump in EF_{oil} (oil expansion factor) from 1.00 to 1.43 ($EF_{oil,ini}$ in Fig. 6.9b). During the soaking process, the pressure drops from P_{set} to P_{eq} in 174 minutes, and EF_{oil} increases from 1.43 ($EF_{oil,ini}$) to 1.53 ($EF_{oil,eq}$ in Fig. 6.9c). CO_2 has a strong affinity to dissolve spontaneously into and expand the oil phase, as shown by the wet areas in CO_2-soaking tests (Figs. 6.5 and 6.6).

Rapid oil expansion right after introducing CO_2 into the visual cell in the buildup process suggests fast CO_2 dissolution into the oil phase. In addition, pressure drop from 2,000 to 1,480 psig as well as EF_{oil} increase from 1.43 to 1.53 indicate further CO_2 dissolution into the oil phase, during the soaking process. It is important to mention that there is no stirrer in the visual cell and the injected CO_2 interacts spontaneously with the oil phase until reaching the equilibrium state. To explain the rapid oil expansion in Fig. 6.9, we investigate the mechanisms leading to CO_2 dissolution into the oil phase by visualizing the interactions in the bulk oil phase and at the CO_2/oil interface.

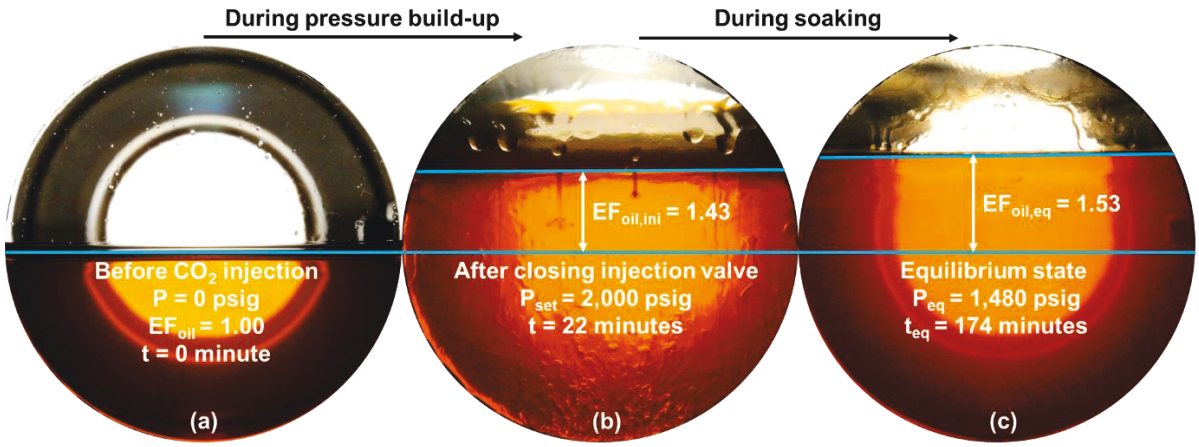

Fig. 6.9: Pictures of oil levels corresponding to (a) the initial condition of the test for determining base oil volume (b) the end of pressure-buildup process at P_{set} = 2,000 psig, and (c) the end of soaking process at P_{eq} = 1,480 psig. The temperature is 122°F and the diameter of the sight glass is 4.8 cm.

Density-Driven Convection in the Bulk Oil Phase. Once CO_2 is introduced into the visual cell, its concentration increases at CO_2/oil interface. The concentration gradient leads to Fickian molecular diffusion of CO_2 into the oil phase. As CO_2 diffuses into the oil phase, the mixture density at the interface increases to a value higher than CO_2-free oil density below the interface. The heavier CO_2/oil mixture moves downward and lighter oil moves upward, leading to density-driven convection, which facilitates CO_2 dissolution into the oil phase (Khosrokhavar, 2016; Farajzadeh et al., 2007).

We observe distinct density-driven fingers once pressure exceeds 1,100 psig [Video 3]. Fig. 6.10a shows unstable fingers moving downward from the CO_2/oil interface toward the bottom of the visual cell during the pressure-buildup process at 1,440 psig (t = 14 minutes and EF_{oil} = 1.15) [Video 4]. Local increase in the density of CO_2/oil mixture forms these fingers which carry the dissolved CO_2 toward the bottom of the cell with lower CO_2 concentration, leading to spontaneous CO_2/oil mixing. The recorded videos show that by injecting more CO_2 and increasing the pressure to a value higher than 1,440 psig, the number of density-driven fingers increases considerably [Video 5]. Higher number of fingers leads to faster dissolution of CO_2, causing 43% increase in the oil volume at P_{set} = 2,000 psig. We conduct a similar bulk-phase test using CO_2 and yellowish FER oil sample. Fig. 6.10b presents a closer view of several fingers moving downward during the pressure-buildup process at 1,230 psig [Video 6].

Rongy et al. (2012) conducted nonequilibrium bulk-phase tests to investigate CO_2/n-C_{10} interactions. They concluded that the equilibrium time under the density-driven convection is

about 50 times shorter than that under only Fickian molecular diffusion. Rapid oil expansion observed in Fig. 6.9 is explained by the density-driven convection, triggered by the local density increase. It is important to mention that density-driven convection does not necessarily occur at the pore scale of the oil-saturated shales with ultralow permeability.

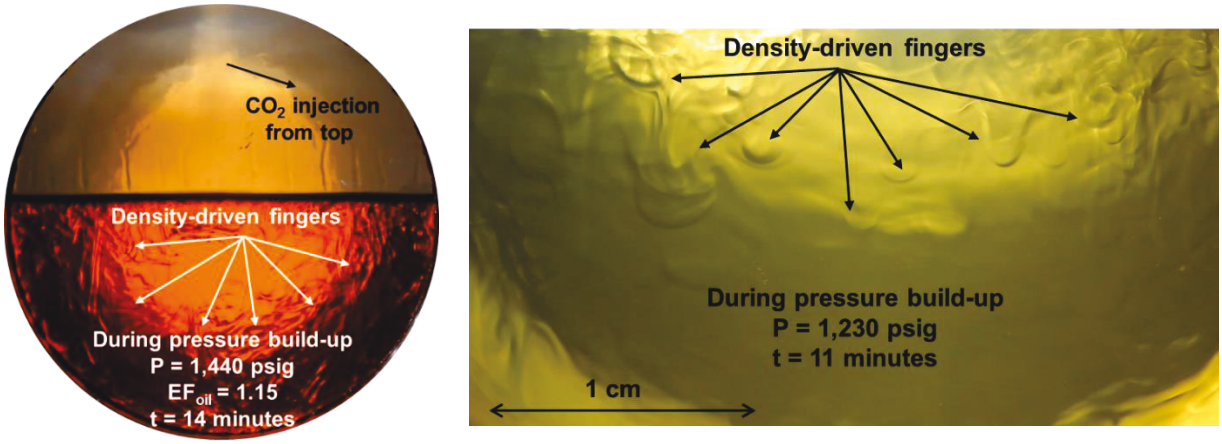

Fig. 6.10: Picture of gravity-induced fingers caused by local density increase during the pressure-buildup process for (a) WAH oil sample at 1,440 psig and (b) FER oil sample at 1,230 psig. The diameter of the sight glass is 4.8 cm.

Extracting and Condensing Flows at the CO_2/Oil Interface. CO_2 behaves as a supercritical fluid when P > 1,055.3 psig (P_c) and T > 87.8°F (T_c) (NIST). In our tests, T_{set} = 122°F, and P increases from 0 to 2,000 psig in 22 minutes during the pressure buildup process. When P < P_c, CO_2 is in the gaseous state, and it is in the supercritical state when P > P_c. We do not observe any specific interactions at the CO_2/oil interface, when CO_2 is in the gaseous state. Once the cell pressure exceeds P_c, we observe two distinct upward and downward flow streams at the CO_2/oil interface, referred to as extracting and condensing flows, respectively, in this study. Fig. 6.11a shows the extracting (upward red arrows) and condensing (downward green arrows) flows at the CO_2/oil interface during the soaking process at 1,525 psig [Video 7]. These flow currents last during the soaking process as pressure declines from 2,000 to 1,480 psig. These flow currents completely cease as pressure drops to the equilibrium value of 1,480 psig.

Fig. 6.11b shows the image of condensing droplets at the CO_2/oil interface. The recorded videos show that as the condensing droplets contact the CO_2/oil interface and cross the interface, the droplets further penetrate into the bulk oil phase [Video 8]. This observation suggests that the density of CO_2/oil mixture is higher than that of the bulk oil phase, causing the condensing droplets

to penetrate into the oil phase. Penetration of the condensing droplets may be considered as a gravity-assisted mechanism, leading to faster dissolution of CO_2 into the oil phase.

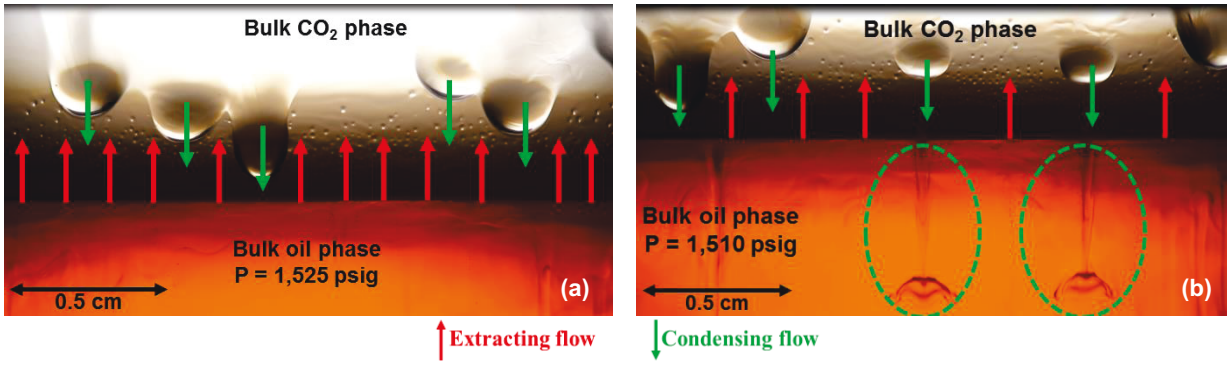

Fig. 6.11: (a) Picture of extracting and condensing flows during the soaking process at 122°F and 1,525 psig (t = 81 minutes). (b) Penetration of condensing droplets into the bulk oil phase during the soaking process at 122°F and 1,510 psig (t = 85 minutes).

The extracting and condensing flows appear when the physical state of CO_2 changes from gaseous to supercritical. To explain these interactions, we investigate the differences between physical properties of gaseous and supercritical CO_2. Supercritical CO_2 has gas-like mass transfer and liquid-like dissolving characteristics (Hawthorne, 1990), which make it a strong candidate for extracting organic compounds. Generally, supercritical fluids are considered as supersolvents (Hawthorne, 1990). Extracting power of supercritical fluids approaches to that of the liquid solvents with similar densities.

Fig. 6.8 shows how CO_2 density increases by increasing pressure at T_{set}. The maximum density of gaseous CO_2 at P_c is 188.3 kg/m^3, which is significantly lower than the density of oil (787 kg/m^3 at 72°F and 0 psig). Due to the large difference between gaseous CO_2 and oil densities, oil solubility in CO_2 and vice versa are limited. Low solubility of oil in gaseous CO_2 may explain the absence of extracting and condensing flows when pressure is lower than P_c. However, density of supercritical CO_2 at P_{set} = 2,000 psig is 668.8 kg/m^3 which is close to the density of oil (787 kg/m^3 at 72°F and 0 psig). The small difference between the densities of supercritical CO_2 and oil enhances their solubilities into each other as shown by the upward extracting and downward condensing flows (Fig. 6.11). In summary, the presence of extracting and condensing flows at the CO_2/oil interface for $P > P_c$ can facilitate CO_2 mixing with the oil phase, leading to rapid oil expansion.

As discussed in the CO_2-soaking tests, the wet areas attributed to the expanded oil dry out, once the CO_2 physical state changes from gaseous to supercritical. Using a similar argument, we conclude that supercritical CO_2 with high density can extract the oil components, leading to oil production from oil-saturated shales (Video 1 and Video 2).

6.5 Limitations of Setup and Tests

1- The total internal volume of the visual cell is 567 cm^3. To calculate the effective internal volume, bulk volume of MIN2 plug (BV = 63.5 cm^3) is subtracted from the total internal volume. We need to inject 7.0 mol of CO_2 to pressurize the system to 2000 psig at 122°F. In CO_2-soaking test of MIN2 plug, the initial oil in the plug is 0.016 mol. As a results CO_2/oil molar ratio is 437 which is very high. In cyclic CO_2 injection (Huff-n-Puff) in a fractured reservoir, the injected CO_2 in a narrow fracture is in contact with matrix and reservoir fluids. The CO_2/oil molar ratio at reservoir conditions would not be as high as 437. To reduce this ratio and mimic the actual reservoir conditions, it is recommended to reduce the total internal volume of the visual cell as much as possible.

2- In CO_2-soaking tests, we report the final oil RF at the end of the test when CO_2 is vented out and pressure is reduced to atmospheric conditions. To report the full curve of oil RF vs. time, it is recommended to cool down the vented mixture of extracted oil/CO_2 and measure the volume of condensed oil at different times. To keep the visual-cell pressure at the constant value of 2,000 psig, a fresh stream of CO_2 must be injected continuously during the ventilation and cooling processes.

3- For pressure-buildup process in bulk-phase CO_2/oil tests, we use the pulse-free pump with maximum DI water flow rate of 29 cm^3/min. Because of the small flow rate, it takes approximately 22 minutes to reach the set pressure. Different pressure-buildup times for different tests affect the comparative analysis of EF_{oil} during the pressure-buildup and soaking processes. To remediate this problem and minimize the pressure-buildup time, we recommend the use of a gas compressor, capable of injecting CO_2 at very high flow rates.

6.6 Summary

The results of wettability tests (Chapter 2) show that the wetting affinity of the Duvernay shales to oil is stronger than that to brine. Strong wetting affinity of shales to oil is attributed to the large

number of hydrophobic pores within the organic matter, confirmed by the scanning electron microscopy (SEM) and energy-dispersive x-ray spectroscopy (EDS) analyses. Furthermore, there is a positive correlation between TOC content and effective porosity of organic-rich shale samples. This positive correlation shows that the pores within the organic matter constitute a significant portion of the effective porosity. Organic porosity of the shale plugs is responsible for significantly higher imbibed volume of oil compared with imbibed volume of brine.

In Chapter 6, we measured and compared oil recovery from dual-wet shale plugs soaked in brine and CO_2. To investigate the mechanisms of oil recovery by CO_2, we used a custom-designed visual cell and visualized the interactions on the surface of plugs at high-pressure and high-temperature conditions. To explain the process of oil recovery from shale plugs, we conducted bulk-phase tests between CO_2 and oil, and visualized CO_2/oil interactions in the visual cell.

The key findings of the EOR tests presented in Chapter 6 are the following.

1- Imbibition oil recovery by brine is less than 7% of the initial oil in place, indicating the weak affinity of oil-filled pores to brine.

2- The results of CO_2-soaking tests show that supercritical CO_2 can diffuse into the oil-saturated plugs and expand the oil. Supercritical CO_2 with high density extracts the expanded oil into the bulk CO_2 phase, leading to oil production. Oil recovery factor by CO_2 is around 82% of initial oil in place, which is much higher than oil recovery by brine imbibition.

3- Comparing the results of oil recovery in CO_2-soaking tests with those of wettability tests suggests that in contrary to brine, supercritical CO_2 can extract a significant portion of the oil out of hydrophobic organic pores.

4- Rapid oil expansion observed in the bulk-phase tests is explained by extracting and condensing flows at the CO_2/oil interface as well as density-driven convection that enhance CO_2 dissolution into the oil phase. It is important to mention that density-driven convection does not necessarily occur at the pore scale of oil-saturated shales with ultralow permeability.

5- Extracting and condensing flows are explained by high density of supercritical CO_2 that enhances the solubility of oil components into CO_2 phase and vice versa.

Nomenclature

BV = Bulk volume, L^3 [cm^3]
EF_{oil} = Oil expansion factor, L^3/L^3
$EF_{oil,eq}$ = Equilibrium EF_{oil} at P_{eq}, L^3/L^3
$EF_{oil,ini}$ = Initial EF_{oil} at P_{set}, L^3/L^3
IOIP = Initial oil in place, L^3 [cm^3]
IFT = Interfacial tension, Mt^{-2} [mN/m]
I_o = Normalized imbibed volume of oil, [%PV]
I_o^{eq} = Equilibrated I_o, L^3/L^3 [%PV]
I_w = Normalized imbibed volume of brine, [%PV]
I_w^{eq} = Equilibrated I_w, L^3/L^3 [%PV]
k_{Decay} = Pressure-decay permeability, L^2 [nD]
P = Pressure, $ML^{-1}t^{-2}$ [psig]
P_c = Critical pressure, $ML^{-1}t^{-2}$ [psig]
P_{eq} = Equilibrium pressure, $ML^{-1}t^{-2}$ [psig]
P_{set} = Set pressure, $ML^{-1}t^{-2}$ [psig]
PV = Pore volume, L^3 [cm^3]
RF = Recovery factor, L^3/L^3 [%IOIP]
TOC = Total organic carbon, M/M% [wt%]
t = Time, t [min]
TDS = Total dissolved solids, M/M [ppm]
T = Temperature, [^oF]
T_c = Critical temperature, [^oF]
T_{set} = Set temperature, [^oF]
$V_{oil}|_{P'}$ = Volume of oil at elevated pressure, L^3 [cm^3]
$V_{oil}|_{P=0}$ = Volume of oil at 0 psig, L^3 [cm^3]
WI_o = Oil wettability index, dimensionless
φ_{eff} = Effective porosity, L^3/L^3 [%BV]
θ = Contact angle, degree
ρ = Density, ML^{-3} [kg/m^3]

Abbreviations

CEC = Cecilia
CO_2 = Carbon dioxide
$CO_{2(g)}$ = Gaseous CO_2
$CO_{2(sc)}$ = Supercritical CO_2
EDS = Energy-dispersive x-ray spectroscopy
EOR = Enhanced oil recovery
FER = Ferrier
LD = Lower Duvernay
MIN = Minhik
ppm = Parts per million
SAX = Saxon
SEM = Scanning electron microscopy
TRA = Tight-rock analysis
WAH = Wahigan
WCSB = Western Canadian Sedimentary Basin
XRD = x-ray diffraction

Chapter 7

Understanding Nonequilibrium CO_2/Oil Interactions

7.1 Introduction

Oil production from unconventional resources including shale and tight formations has been expanded by the development of hydraulic-fracturing and horizontal-drilling techniques during the last decade. For most of the unconventional resources, the primary oil-production rate declines rapidly, leading to a very low oil recovery (less than 10% of original oil in place) (Cherian et al., 2012; Hoffman, 2012; Liu et al., 2014). Carbon dioxide (CO_2)-based enhanced oil recovery (EOR) has been the focus of many studies (Wang and Gu, 2011; Han and Gu, 2014; Pu et al., 2016; Yu et al., 2016; Habibi et al., 2017), mainly because of the lower minimum miscibility pressure (MMP) of CO_2 with oil compared with other gases such as methane and nitrogen, and because of the higher injectivity index of CO_2 into the tight formations compared with aqueous fluids (Adekunle and Hoffman, 2016).

The main recovery mechanisms in CO_2-EOR processes include oil swelling, vaporization of light- and intermediate-oil components from the oleic phase, condensation of CO_2 and intermediate-gas components into the oleic phase, and oil-viscosity reduction (Holm and Josendal, 1974). The phase behavior of CO_2/oil mixture strongly affects the efficiency of oil displacement in porous medium (Metcalfe and Yarborough, 1979; Gardner et al., 1981; Orr et al., 1981). The extent of hydrocarbon extraction, especially light and intermediate components from the oleic phase, depends on the oil composition and operating conditions such as pressure and temperature (Holm and Josendal, 1982; Klins, 1983; Bahralolom and Orr, 1988). CO_2 behaves as a supercritical fluid ($CO_{2(sc)}$) at pressures and temperatures higher than 1,055.3 psig and 87.8°F, respectively (NIST). To understand how CO_2 interacts with oil at reservoir conditions, it is essential to characterize CO_2/oil interactions at elevated pressures and temperatures.

For EOR purposes, CO_2 not only improves the oil mobility by oil-viscosity reduction, but also extracts light- and intermediate-oil components (C_5-C_{30}) (Klins, 1983), leading to improved miscibility conditions. The density of $CO_{2(sc)}$ is significantly higher than that of gaseous carbon dioxide ($CO_{2(g)}$), which improves the solubility of $CO_{2(sc)}$ in oil (Eckert et al., 1996). In addition, diffusion of light/intermediate components into $CO_{2(sc)}$ is faster than that into liquid carbon dioxide ($CO_{2(l)}$), increasing the rate of mass transfer into the $CO_{2(sc)}$ phase (Hawthorne, 1990).

Accurate and reliable phase behavior and volumetric data are essential elements for proper simulation of recovery processes such as miscible displacement (Danesh, 1998). PVT experiments such as the swelling test (Whitson and Brule´, 2000; Bahralolom et al., 1988; Tsau et al., 2010; Li et al., 2013; Rostami et al., 2017) and MMP measurement (Silva and Orr, 1987; Orr et al., 1993; Adekunle and Hoffman, 2016; Hawthorne et al., 2016) are routinely conducted to characterize the phase behavior of an injected gas/oil mixture at equilibrium conditions. However, nonequilibrium interactions of injected gas and oil at reservoir conditions are poorly understood. Current compositional simulators assume that the injected gas and oil in gridblocks are at the equilibrium conditions (Nghiem and Sammon, 1997). However, thermodynamic equilibrium between the injected gas and oil is not valid when the injected gas bypasses the oil because of viscous fingering and channeling caused by reservoir heterogeneities (Chang et al., 1994). Nghiem and Sammon (1997) developed a nonequilibrium compositional simulator, and compared the results with that of an equilibrium compositional simulator. In their modeling approach, the authors assumed instantaneous thermodynamic equilibrium at the fine scale and derived coarse-scale equations in which the phase behavior is not necessarily at equilibrium conditions. Their nonequilibrium upscaling approach demonstrated considerable improvements over the equilibrium upscaling approaches. Zubov et al. (2016) applied a new approach to model the effect of nonequilibrium phase transition in a compositional simulator. Key modifications, compared with the equilibrium case, were the calculation modules for phase states, fractions, and compositions. Their nonequilibrium modeling approach provided a tool to control the rates of gas dissolution, condensate evaporation, and gas breakthrough in compositional simulators. Bayestehparvin et al. (2017) showed that in solvent-aided steam-assisted gravity drainage (SAGD), the assumption of instantaneous phase equilibrium between heavy oil and solvent is not valid. The authors developed a nonequilibrium model for diffusion of solvent in heavy oil at the pore scale. The modeling results show that assuming equilibrium conditions in solvent-aided SAGD overestimates oil production

by reducing the viscosity of the oil. In contrast, solvent co-injection under nonequilibrium conditions may lead to lower oil recovery compared with the SAGD process.

Nonequilibrium phase-behavior data are essential for modeling nonequilibrium processes. In Chapter 7, we aim at visualization of nonequilibrium interactions between the injected gas and oil phases. We visualize CO_2/oil interactions under nonequilibrium conditions to understand how CO_2 interacts with oil during CO_2 injection and soaking periods at elevated pressure and temperature conditions; how the physical state (i.e., liquid, gas, and supercritical) of CO_2 affects the CO_2/oil interactions; and the key mechanisms controlling CO_2 dissolution into oil. We conduct 5 visualization tests using a custom-designed visual cell. In the first three tests, we investigate the effect of the physical state of CO_2 on CO_2/oil interactions. Then, we replace the opaque oil with the translucent light oil (LO) to visualize the interactions in the bulk oil phase. Finally, we conduct an $N_{2(sc)}$/oil test to compare the results with those of a $CO_{2(sc)}$/oil test.

7.2 Materials

We use Montney (MTN) and Duvernay (DUV) oil samples with 37.96 and 48.30 °API, respectively. Visualization tests are performed at reservoir conditions. The reservoir pressure and temperature of the target well in the MTN Formation are 2,000 psig and 122°F, respectively. CO_2 and N_2 are supercritical at the reservoir pressure and temperature. Table 7.1 lists the physical properties of oil samples. Compared with the DUV oil sample, MTN oil has higher density, viscosity, and molecular weight (Mw), which corresponds to the higher fraction of its heavier components.

Table 7.1: Physical properties of the MTN and DUV oil samples at 72°F and atmospheric pressure.

Oil	Color	Density (kg/m^3)	Viscosity (cp)	Surface tension (mN/m)	Mw (g/mol)
MTN	Dark brown	835	9.6	26.8	251.78
DUV	Amber	787	2.1	23.5	148.03

Fig. 7.1 presents the compositional analysis of oil samples measured using the simulated distillation test. The compositional analysis indicates that the weight percent (wt%) of intermediate components is significantly higher in the DUV oil sample compared with that in the MTN oil sample. For instance, cumulative weight percentages of components between C_7 and C_{14} are 29.30 and 76.04 wt% for the MTN and DUV oil samples, respectively. Furthermore, the weight percentages of C_{42+} are 15.59 and 0.00 wt% for the MTN and DUV oil samples, respectively,

indicating the presence of heavy components in the MTN oil. The absence of heavy components in the DUV oil sample explains its translucent feature, as shown in Fig. 7.1. The gases injected into the visual cell are CO_2 and N_2 with a purity of 99.9%.

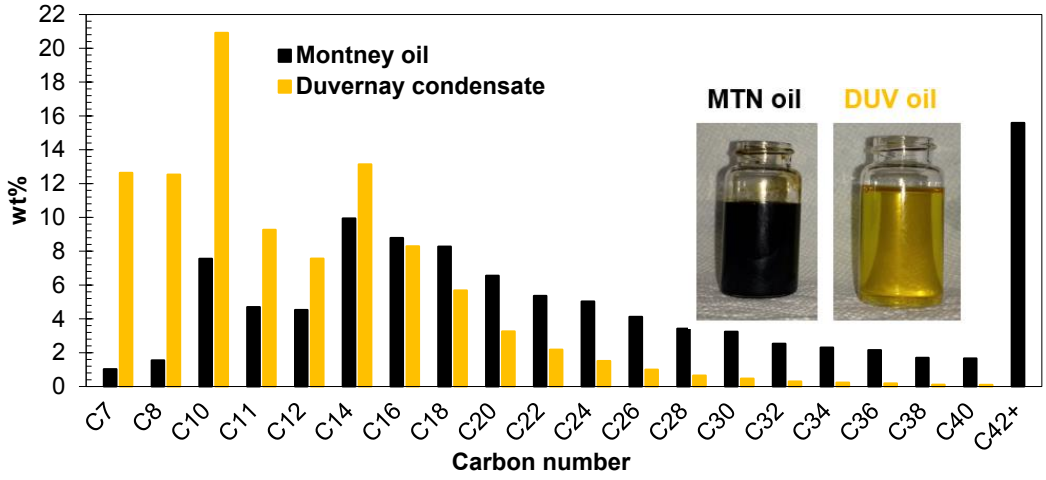

Fig. 7.1: Compositional analysis of the MTN and DUV oil samples measured by simulated distillation test.

Table 7.2 lists the results of a saturates/aromatics/resins/asphaltenes (SARA) test for the MTN oil sample. The cumulative weight percentage of polar components including resins and asphaltenes is 8.5 wt%.

Table 7.2: The results of a SARA test for the MTN oil sample.

Hydrocarbon type	wt%	Polarity
Saturates	67.6	Non-polar
Aromatics	23.9	Non-polar
Resins	7.1	Polar
Asphaltenes	1.4	Polar

7.3 Setup Specifications

Fig. 6.2 in Chapter 6 illustrates the custom-designed visualization setup. The chamber of the visual cell is made of stainless steel (Grade 316) and has two Sapphire sight glasses allowing the visualization of interactions between the injected gas and oil over time. The internal volume of the cell is 567 cm^3 with maximum operating pressure and temperature of 4,000 psig and 392°F, respectively. A heating jacket (the amber coating in Fig. 6.2) controls the visual-cell temperature with an accuracy of ±0.2°F. The visual cell is provided with one Type K thermocouple to monitor the temperature. A pressure gauge monitors the visual-cell pressure with an accuracy of ±2 psig. The front-side sight glass is equipped with a high-resolution camera to record gas/oil interactions during the tests. We place a white light source close to the rear-side sight glass to provide the

required light for the visualization purpose. We use a continuous pulse-free pump to inject deionized (DI) water into the lower part of the accumulators. During DI-water injection, a floating piston moves upward and transfers the oil, CO_2, or N_2 into the visual cell. One of the accumulators injects the oil phase and the other one injects CO_2 or N_2 into the visual cell. The flow-rate range of the pump is 0.0001 to 29 cm^3/min, and it can supply a maximum operating pressure of 12,000 psig. The capacity of each accumulator is 500 cm^3 with a maximum operating pressure of 10,000 psig.

7.4 Methodology

In this part, we explain the procedure of conducting the PVT and visualization tests.

7.4.1 PVT Tests

We conduct PVT tests to measure phase behavior of the CO_2/MTN oil mixture at equilibrium conditions. After cleaning the PVT cell with toluene and applying vacuum on the cell, we inject a specific volume of CO_2 into the cell at room temperature of 72°F. The injected mole of CO_2 is calculated using the CO_2 volume in the cell and the CO_2-density values from the literature (NIST). After that, a specific volume of oil is injected into the PVT cell and the oven temperature is increased to 122°F. To mix CO_2 with the oil sample, we turn on the stirrer for 24 hours. When the temperature of the mixture is stabilized at 122°F, we increase the pressure of the mixture until a single phase is formed by dissolving all the CO_2 in the oil phase. Next, we decrease the pressure of the mixture step by step and measure the relative volume of oil, oil expansion factor (EF_{oil}), and density of the CO_2/oil mixture at each pressure. The relative volume of oil is calculated by dividing the total volume of bulk oil phase at a certain pressure by that at the bubblepoint pressure (P_b). EF_{oil} is calculated by dividing the volume of bulk oil phase at any elevated pressure by the volume of CO_2-free oil (P = 0 psig) at 122°F. In this study, we use overall CO_2 mole fractions of 48.36 and 71.06 mol%. More details regarding the experimental procedure, equipment, and operating conditions are presented elsewhere (Habibi et al., 2017).

7.4.2 Visualization Tests

To investigate nonequilibrium CO_2 (or N_2)/oil interactions under reservoir conditions, we perform 5 sets of visualization tests, which are listed in Table 7.3. All tests in this study include the following three primary steps.

Table 7.3: Design of tests for investigating nonequilibrium interactions between oil and gas (CO_2 and N_2). Oil and LO stand for MTN and DUV oil samples, respectively.

Test number	Test name	Oil type	Injected fluid	CO_2 or N_2 state	CO_2 or N_2 (mol)	Oil (mol)	P_{set} (psig)	T_{set} (^oF)
1	$CO_{2(g)}$/oil	MTN	CO_2	Gas (g)	1.67	0.78	915	122
2	$CO_{2(l)}$/oil	MTN	CO_2	Liquid (l)	1.75	0.78	870	72
3	$CO_{2(sc)}$/oil	MTN	CO_2	Supercritical (sc)	1.95	0.78	2,000	122
4	$CO_{2(sc)}$/LO	DUV	CO_2	Supercritical (sc)	2.67	1.25	2,000	122
5	$N_{2(sc)}$/oil	MTN	N_2	Supercritical (sc)	2.10	0.78	2,000	122

Step 1: Determining the Base Oil Volume. First, the accumulator is filled with oil, and we use the continuous pulse-free pump to fill almost one-half of the visual cell with oil. Then, temperature is set at 122^{o}F, which is the MTN reservoir temperature. The image of the oil level at atmospheric pressure and the set temperature (T_{set}) is captured before gas (CO_2 or N_2) injection. We use this image to calculate the volume of oil (base oil volume). This volume is a basis for evaluating the oil expansion factor (EF_{oil}) after its interaction with the injected CO_2 (or N_2). Similar to the PVT tests, we define EF_{oil} as,

$$EF_{oil} = \left(\frac{V_{oil}|_{P'}}{V_{oil}|_{P=0}}\right)_{T_{set}} \tag{7.1}$$

where, $V_{oil}|_{P'}$ is the volume of oil at any elevated pressure ($P' > 0$ psig) during the pressure-buildup (Step 2) and soaking (Step 3) processes, and $V_{oil}|_{P=0}$ is the base oil volume at P = 0 psig.

Step 2: Pressure-Buildup Process. After Step 1, the gas phase is introduced into the visual cell with the initial pressure of 700 psig. Then, we gradually increase the visual-cell pressure to the set (or maximum) pressure (P_{set}) listed in Table 7.3. P_{set} is considered as the maximum pressure in each test. Depending on the experimental conditions listed in Table 7.3, it takes approximately 7 to 22 minutes to reach the P_{set} value. To minimize the injection time and reduce the gas/oil interactions during the gas-injection process, we apply the maximum pump-flow rate of 29 cm^3/min for DI-water injection into the accumulator. The mass-flow rate of CO_2 (or N_2) injection depends on the accumulator pressure and varies with time during the pressure-buildup process. EF_{oil} at P_{set} and T_{set} is referred to as the initial EF_{oil} ($EF_{oil,ini}$). We use a high-resolution camera to record the interactions between the oil phase and the injected CO_2 (or N_2) during the pressure-buildup process.

The visual-cell pressure is controlled by the amount of injected CO_2 (or N_2) during the pressure-buildup process. However, in PVT tests, there are constant moles of oil and gas in the PVT cell, and the system's pressure is controlled by a floating piston that adjusts the residing fluids' volume.

Step 3: Soaking Process. The visual-cell pressure declines over time, indicating that the system is at nonequilibrium conditions. We visualize the interface of oil and CO_2 (or N_2) during this nonequilibrium period. The images are used to determine the oil volume and to calculate EF_{oil}. We consider equilibrium conditions once the visual-cell pressure is stabilized over time and reaches the equilibrium pressure (P_{eq}). EF_{oil} at T_{set} and P_{eq} is referred to as equilibrium EF_{oil} ($EF_{oil,eq}$).

It is important to mention that in a PVT cell, a stirrer mixes the oil and injected gas and reduces the time needed to reach to the equilibrium conditions. However, there is no stirrer in the visual cell, and the injected gas spontaneously interacts with the oil phase until reaching to the equilibrium state.

Hereafter in this paper, we refer to MTN and DUV oil samples as "oil" and "LO", respectively. CO_2 cannot be in the gaseous state at pressures higher than P_c = 1,055.3 psig. Thus, we conduct $CO_{2(g)}$/oil test (Test 1) at 915 psig and at the reservoir temperature (122°F). Furthermore, CO_2 cannot be in the liquid state at temperatures higher than T_c = 87.8°F. Therefore, we conduct the $CO_{2(l)}$/oil test (Test 2) at room temperature of 72°F and 870 psig, which is close to the saturation pressure of CO_2. The pressure and temperature for Tests 4 and 5 are the same as those for Test 3 (2,000 psig and 122°F). The oil is opaque, and it is not possible to visualize the interactions in the bulk oil phase. To address this problem, we replace the oil with the translucent LO in Test 4 ($CO_{2(sc)}$/LO). In Test 5, we investigate the interactions of $N_{2(sc)}$ with oil ($N_{2(sc)}$/oil) and compare the results with those of Test 3 ($CO_{2(sc)}$/oil). Similar to CO_2, N_2 is supercritical at 2,000 psig and 122°F.

For $CO_{2(g)}$/oil test (Test 1), we inject 235 cm^3 of oil (0.78 mol) to fill almost one-half of the visual cell. Then, the visual-cell temperature is increased to 122°F. We inject approximately 1.67 mol of CO_2 to reach the P_{set} of 915 psig. For the $CO_{2(l)}$/oil test (Test 2), we inject 0.78 mol of oil. Once the CO_2-injection valve is opened, $CO_{2(g)}$ enters the visual cell and the pressure increases to approximately 700 psig. At 72°F and 700 psig, there is no $CO_{2(l)}$ in the visual cell, and the CO_2 phase is in the gaseous state. When pressure reaches to the saturation pressure of 856 psig, $CO_{2(g)}$ turns into $CO_{2(l)}$. By injecting more CO_2, the level of $CO_{2(l)}$ increases without significant change

in the visual-cell pressure. The total injected $CO_{2(l)}$ for Test 2 is approximately 1.75 mol. Tests 3 through 5 are conducted at the MTN reservoir temperature and pressure of 122°F and 2,000 psig, respectively. The type of oil as well as the mole values of oil and injected CO_2 (or N_2) for Tests 3 through 5 are listed in Table 7.3.

It is important to mention that we do not vacuum the visual cell before injecting the gas phase. Therefore, there should be some air in the visual cell during pressure-buildup and soaking processes. Considering air as an ideal gas at 0 psig, the mole values of air at 72°F and 122°F are 0.010 and 0.009 mol, respectively. For the $CO_{2(l)}$/oil test, the mole value of injected CO_2 is 1.67 mol, which is 175 times higher than that of air at 72°F. For other tests, the molar ratio of CO_2/air is higher than 175. Therefore, we ignore the effect of the initial air on the injected gas/oil interactions because of its negligible concentration.

7.5 Results

First, we present the results of PVT tests conducted on the CO_2/MTN-oil mixture. Then, we present our observations from the visualization tests. A comparative analysis among the results of different tests is presented to investigate the nonequilibrium interactions between the injected CO_2 (or N_2) and oil (or LO).

7.5.1 Experimental Observations by the PVT Cell

Figs. 7.2a through 7.2c present the results of PVT tests for CO_2 mole fractions of 48.36 and 71.06 mol% at T = 122°F. Fig. 7.2a shows the crossplot of pressure vs. relative volume of oil. The values of P_b are 945 and 1,302 psig for CO_2 mole fractions of 48.36 and 71.06 mol%, respectively. Fig. 7.2b presents the crossplot of EF_{oil} vs. pressure for pressures higher than P_b. For CO_2 mole fractions of 48.36 and 71.06 mol%, the values of EF_{oil} are 1.21 and 1.38 at reservoir pressure of 2,000 psig, respectively. This result indicates that CO_2 can dissolve into the oil phase and increase the oil volume up to approximately 38%, at CO_2 mole fraction of 71.06 mol%. The density of the CO_2/oil mixture at pressures higher than P_b is presented in Fig. 7.2c. Fig. 7.2c also shows the density of dead oil (CO_2-free oil). Comparing density of the dead oil with density of the CO_2/oil mixture indicates that CO_2 dissolution into the oil phase increases the oil density. For instance, densities of the CO_2/oil mixture at 2,000 psig are 833.6 and 850.3 kg/m^3 for CO_2 mole fractions of 48.36 and 71.06 mol%, respectively, whereas the density of dead oil at 2,000 psig is 829.4

kg/m^3. We use the density values presented in Fig. 7.2c to interpret the results of visualization tests.

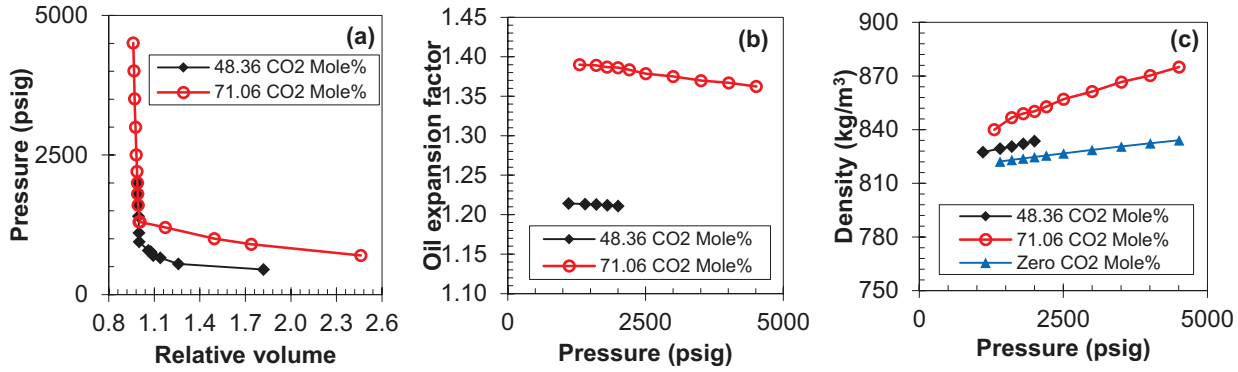

Fig. 7.2: The results of PVT tests for the CO_2/MTN-oil mixture at 122°F. (a) Pressure vs. relative volume of oil; (b) EF_{oil} vs. pressure; and (c) density vs. pressure for CO_2 mole fractions of 48.36 and 71.06 mol%.

7.5.2 Experimental Observations by the Visual Cell

We monitor EF_{oil} and the visual-cell pressure over time. Fig. 7.3 displays images of the oil level for 5 visualization tests. For each test, the captured images correspond to (i) the initial conditions of the test for determining the base oil volume; (ii) the end of the pressure-buildup process at P_{set}; and (iii) the end of the soaking process at P_{eq}. Fig. 7.4 shows the measured pressure vs. time during the soaking process. The pressure-decline rate as well as P_{eq} are different for different tests.

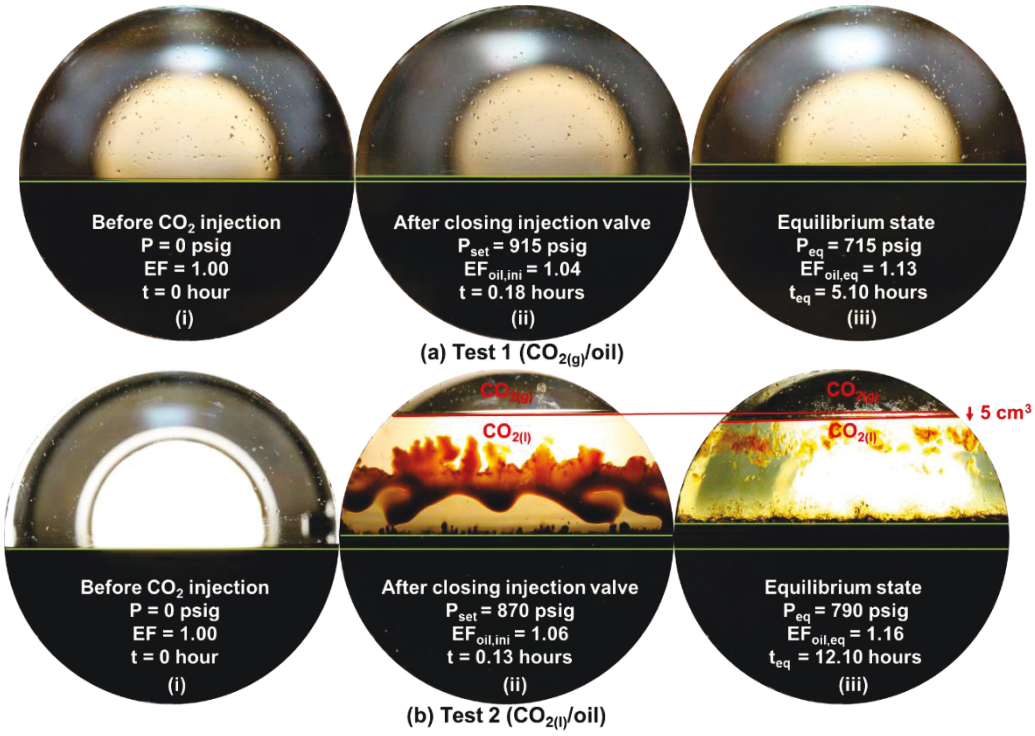

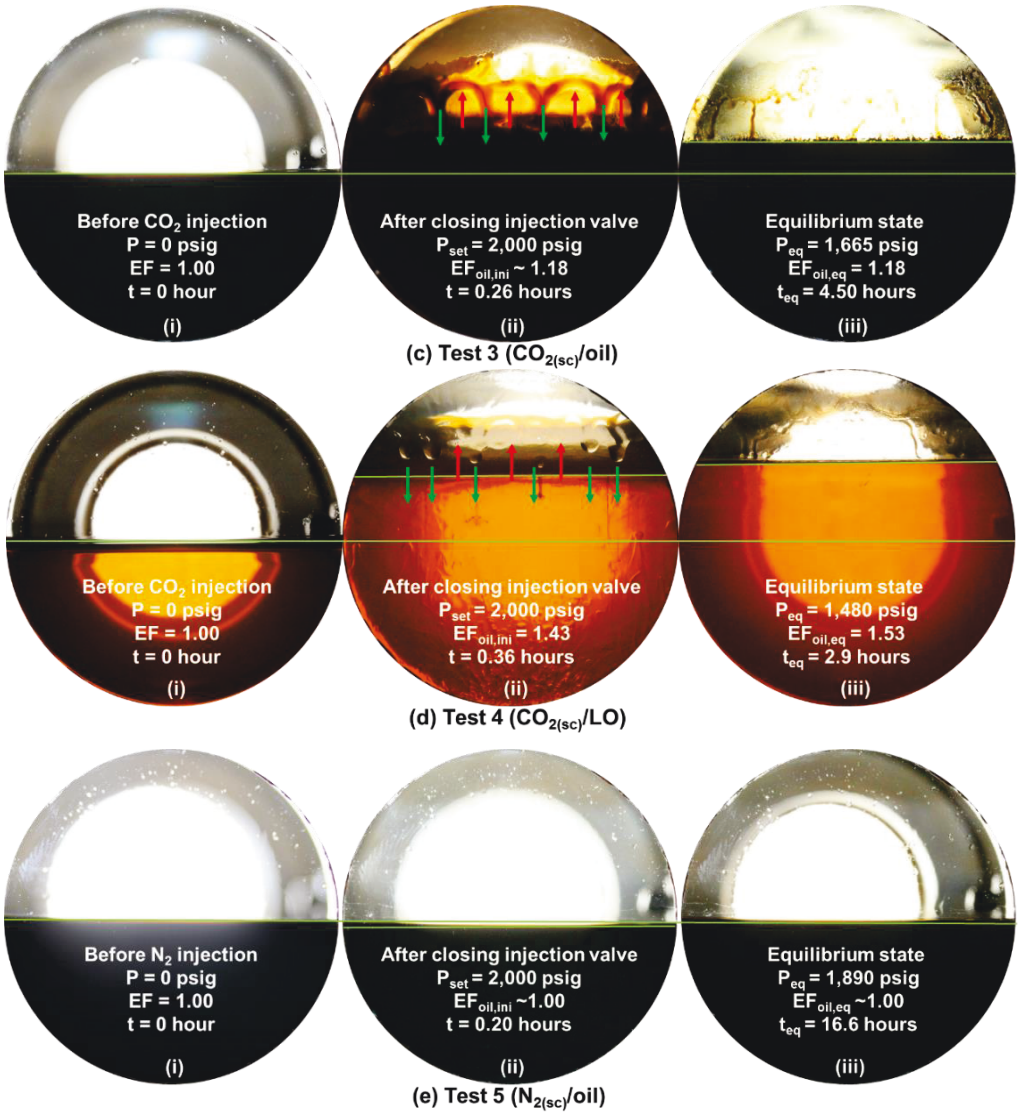

Fig. 7.3: Images of the oil level for (a) $CO_{2(g)}$/oil, (b) $CO_{2(l)}$/oil, (c) $CO_{2(sc)}$/oil, (d) $CO_{2(sc)}$/LO, and (e) $N_{2(sc)}$/oil tests. The pictures correspond to (i) the initial conditions of the test for determination of the base oil volume; (ii) the end of the pressure-buildup process at P_{set}; and (iii) the end of the soaking process at P_{eq}. Upward red and downward green arrows represent extracting and condensing flows, respectively. The white circle in all these figures is caused by the white-light-source reflection used for visualization purposes. The diameter of the sight glass is 4.8 cm.

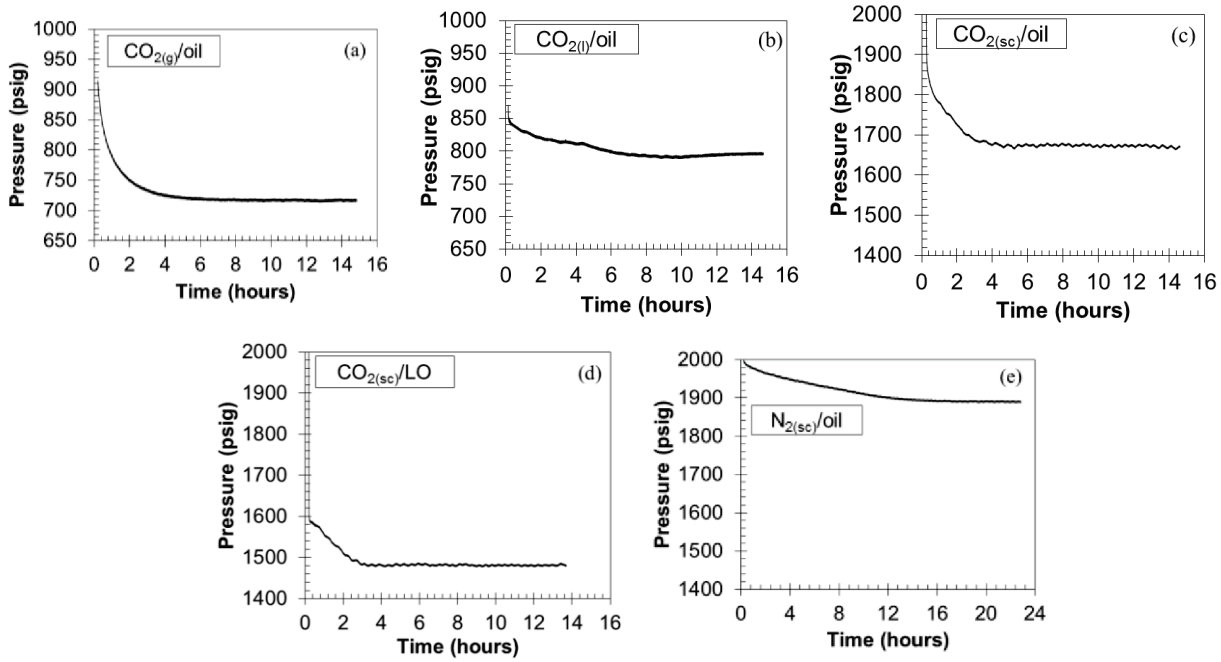

Fig. 7.4: Pressure decline vs. time for (a) $CO_{2(g)}$/oil, (b) $CO_{2(l)}$/oil, (c) $CO_{2(sc)}$/oil, (d) $CO_{2(sc)}$/LO, and (e) $N_{2(sc)}$/oil tests during the soaking process.

7.5.2.1 Test 1. $CO_{2(g)}$/Oil at P_{set} = 915 psig and T_{set} = 122°F

This subsection describes observations from nonequilibrium interactions of the oil with $CO_{2(g)}$. Fig. 7.3a(i) shows the picture of oil level before $CO_{2(g)}$ injection at atmospheric pressure and 122°F. We start $CO_{2(g)}$ injection and increase the pressure from 0 to 915 psig. The pressure-buildup process takes approximately 11 minutes, as shown in Fig. 7.5. According to Fig. 7.3a(ii), $EF_{oil,ini}$ is 1.04 at 915 psig after injection of approximately 1.67 mol of $CO_{2(g)}$ into the visual cell. In fact, $CO_{2(g)}$ dissolves into the oil phase and leads to oil expansion upon injection of $CO_{2(g)}$ into the visual cell. Then, the pressure gradually declines during the soaking process and reaches to the equilibrium value of 715 psig after approximately 5.10 hours (Fig. 7.4a). During the soaking process, EF_{oil} increases to the equilibrium value of 1.13, indicating further dissolution of $CO_{2(g)}$ into the oil phase (Fig. 7.3a(iii)).

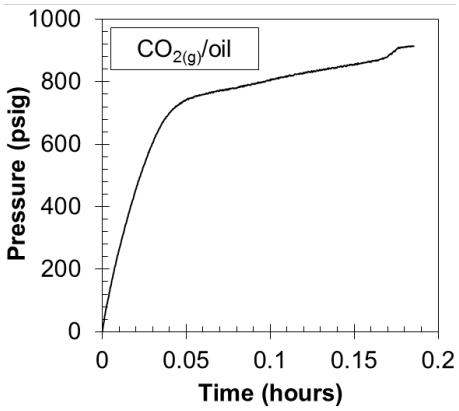

Fig. 7.5: Pressure vs. time during the pressure-buildup process in the $CO_{2(g)}$/oil test. It takes approximately 11 minutes to increase the visual-cell pressure from 0 to 915 psig.

7.5.2.2 Test 2. $CO_{2(l)}$/Oil at P_{set} = 870 psig and T_{set} = 72°F

This subsection describes observations from nonequilibrium interactions of the oil with $CO_{2(l)}$. Fig. 7.3b(i) shows an image of the oil level before $CO_{2(l)}$ injection at atmospheric pressure and 72°F. Fig. 7.3b(ii) shows the $CO_{2(l)}$/oil interface after injection of approximately 1.75 mol of $CO_{2(l)}$ at 72°F and 870 psig. As shown in Fig. 7.3b(ii), we did not completely fill the visual cell with $CO_{2(l)}$. Therefore, at the top of the visual cell, there is still $CO_{2(g)}$ phase in equilibrium with the $CO_{2(l)}$ phase. By doing this, we can visualize the $CO_{2(l)}$ level during the soaking process. According to Fig. 7.3b(ii), EF_{oil} increases from 1.00 to 1.06 during the pressure-buildup process, suggesting the early dissolution of $CO_{2(l)}$ into the oil phase during the pressure-buildup process. During the soaking process, the pressure declines from 870 to 790 psig after approximately 12.10 hours (Fig. 7.4b). EF_{oil} further increases to the equilibrium value of 1.16 (Fig. 7.3b(iii)) during the soaking process, suggesting further dissolution of $CO_{2(l)}$ into the oil phase. A comparison between the upper level of $CO_{2(l)}$ (top of sight glass) in Fig. 7.3b(ii) with that in Fig. 7.3b(iii) shows the downward shift of the $CO_{2(l)}$ level, which is equivalent to 5 cm^3 reduction in the total volume ($CO_{2(l)}$ and oil volumes). This observation also supports the dissolution of $CO_{2(l)}$ into the oil phase.

Fig. 7.3b(ii) shows a brown region attached on the sight glass in the $CO_{2(l)}$ phase. $CO_{2(l)}$ is a transparent colorless phase. Therefore, the brown region might be the oil components transferred from the bulk oil phase toward the bulk $CO_{2(l)}$ phase. This brown region becomes more pronounced as pressure declines during the soaking process. Fig. 7.6 shows that the brown region completely covers the sight glass at 820 psig. The recorded video at 820 psig illustrates two distinct upward- and downward-flow streams at the interface of $CO_{2(l)}$/oil phases. We refer to the upward- and

downward-flow streams as the extracting (upward red arrows in Fig. 7.6) and condensing (downward green arrows in Fig. 7.6) flows, respectively. The extracting and condensing flows last during the soaking process and disappear at P_{eq} = 790 psig, as shown in Fig. 7.3b(iii). It is important to mention that we do not observe extracting and condensing flows for the $CO_{2(g)}$/oil test. There are solid precipitates attached on the sight glass near the interface of $CO_{2(l)}$/oil, which are shown in the magnified image in Fig. 7.6. The chemical characteristics of these solid precipitates are presented in another study (Habibi et al., 2017).

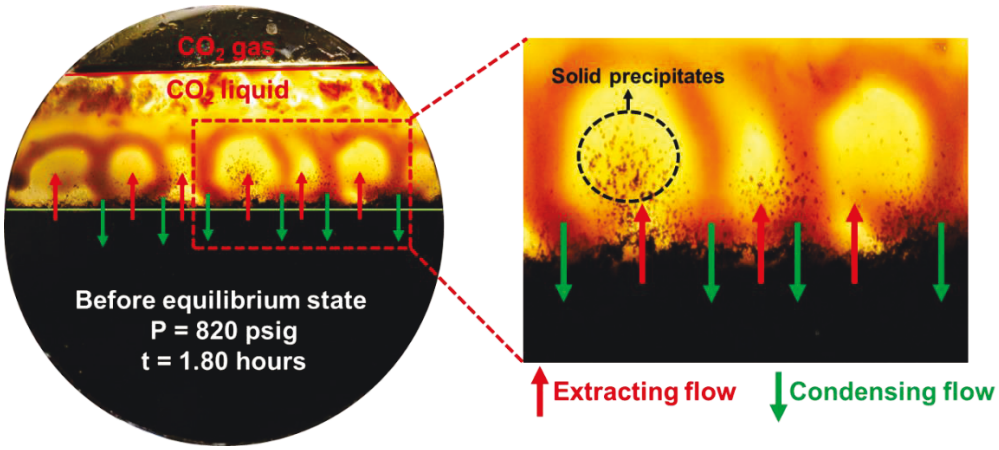

Fig. 7.6: The extracting and condensing flows at the interface of $CO_{2(l)}$/oil during the soaking process at 820 psig and 72°F. The solid precipitates attached on the sight glass are shown in the magnified image. The diameter of the sight glass is 4.8 cm.

7.5.2.3 Test 3. $CO_{2(sc)}$/Oil at P_{set} = 2,000 psig and T_{set} = 122°F

This subsection describes observations from nonequilibrium interactions of the oil with $CO_{2(sc)}$. Fig. 7.3c(i) shows the oil level before $CO_{2(sc)}$ injection at atmospheric pressure and 122°F. Fig. 7.3c(ii) shows the oil level right after closing the CO_2-injection valve at 2,000 psig. According to Fig. 7.3c(ii), the $CO_{2(sc)}$/oil interface is not clear because of the solid precipitates attached on the sight glass. Therefore, we cannot measure the volume of oil accurately. However, $EF_{oil,ini}$ is approximately 1.18 after injection of 1.95 mol of $CO_{2(sc)}$ into the visual cell. Similar to the $CO_{2(g)}$/oil and $CO_{2(l)}$/oil tests, the pressure gradually declines during the soaking process and reaches the equilibrium value of 1,665 psig after approximately 4.5 hours (Fig. 7.4c).

According to Fig. 7.3c(ii), there is a brown region above the $CO_{2(sc)}$/oil interface at 2,000 psig. This region is similar to what we observed in the $CO_{2(l)}$/oil test (Fig. 7.6) in terms of color and location. We record the videos of nonequilibrium interactions at the $CO_{2(sc)}$/oil interface during the

pressure-buildup process. Once the pressure exceeds the critical pressure of CO_2 (1,055.3 psig), the brown region appears above the $CO_{2(sc)}$/oil interface. Figs. 7.7a through 7.7d show a closer view of the $CO_{2(sc)}$/oil interface during the pressure-buildup process at 1,480, 1,570, 1,780, and 1,900 psig, respectively. Similar to the $CO_{2(l)}$/oil test, we observe extracting and condensing flows at the $CO_{2(sc)}$/oil interface, as shown by the upward red and downward green arrows in Fig. 7.7. The color of both downward-condensing and upward-extracting flows turn from light brown to dark brown by increasing the visual-cell pressure. We also observe solid precipitates attached on the sight glass near the $CO_{2(sc)}$/oil interface, as illustrated in Fig. 7.7a. Habibi et al. (2017) reported the results of chemical analysis of these solid precipitates.

As the pressure declines and approaches to P_{eq} = 1,665 psig (Fig. 7.4c), the extracting and condensing flows become less pronounced. At equilibrium conditions, both extracting and condensing flows cease, as shown in Fig. 7.3c(iii).

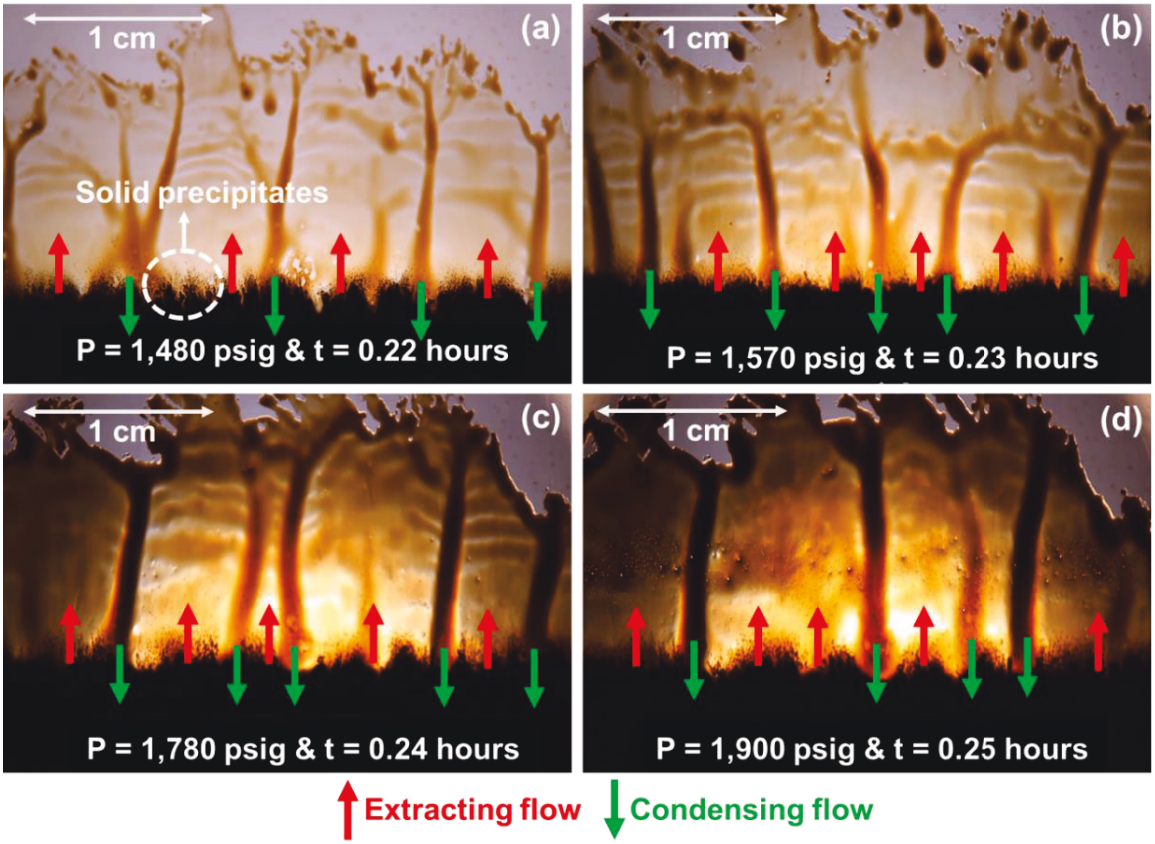

Fig. 7.7: Extracting and condensing flows near the $CO_{2(sc)}$/oil interface at (a) 1,480 psig, (b) 1,570 psig, (c) 1,780 psig, and (d) 1,900 psig during the pressure-buildup process. By increasing the pressure, the color of both downward-condensing and upward extracting flows turns from light brown to dark brown.

7.5.2.4 Test 4. $CO_{2(sc)}$/LO at P_{set} = 2,000 psig and T_{set} = 122°F

In Tests 1 through 3, we investigated the interactions at the interfaces of oil and $CO_{2(g)}$, $CO_{2(l)}$, and $CO_{2(sc)}$. We observe upward-extracting and downward-condensing flows at the CO_2/oil interface for the $CO_{2(l)}$/oil and $CO_{2(sc)}$/oil tests. The oil used in Tests 1 through 3 is opaque, and therefore the CO_2/oil interactions in the bulk of the oil phase are not observable. In Test 4, we use translucent LO to visualize the interactions in the bulk of the LO phase during the pressure-buildup and soaking processes.

Fig. 7.3d(i) shows the LO level before CO_2 injection at atmospheric pressure and 122°F. Approximately 2.67 mol of $CO_{2(sc)}$ is injected into the visual cell to increase its pressure to 2,000 psig. After the pressure-buildup process, $EF_{oil,ini}$ was approximately 1.43 (Fig. 7.3d(ii)). This value is much higher than $EF_{oil,ini}$ of 1.18 shown in Fig. 7.3c(ii) for the $CO_{2(sc)}$/oil test. Fig. 7.3d(iii) shows an image of the LO level at P_{eq} = 1,480 psig. During the soaking process, EF_{oil} increases from 1.43 to the equilibrium value of 1.53, where the visual-cell pressure decreases from 2,000 to 1,480 psig. Fig. 7.4d presents the pressure vs. time during the soaking process. The pressure quickly drops from 2,000 to 1,580 psig in just 3 minutes after closing the CO_2-injection valve. This sharp pressure decline suggests that the dissolution rate of CO_2 in the LO phase is significant. According to Fig. 7.4d, the system reaches P_{eq} = 1,480 psig after approximately 2.9 hours.

Fig. 7.8b shows an image of the LO level after the pressure-buildup process (P = 870 psig). Injection of $CO_{2(g)}$ at 870 psig leads to EF_{oil} of 1.05, which is similar to the EF_{oil} of 1.04 shown in Fig. 7.3a(ii) for the $CO_{2(g)}$/oil test. However, LO expansion significantly increases by injecting more CO_2 and increasing the pressure to the values higher than the critical pressure of CO_2.

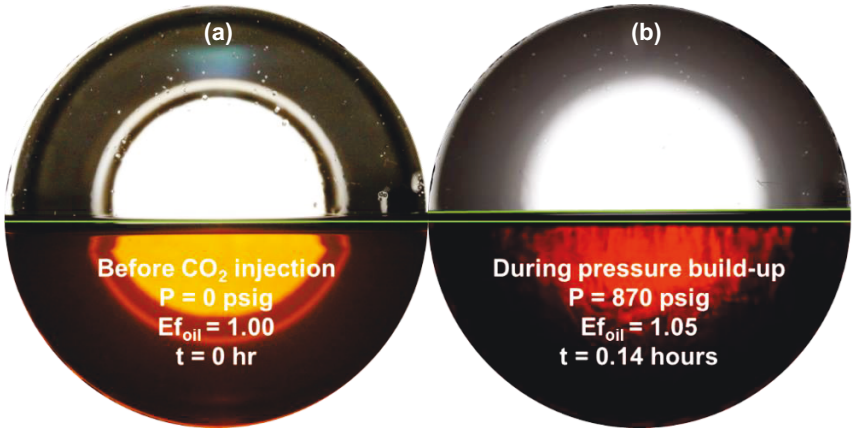

Fig. 7.8: Pictures of the LO level at 122°F: (a) before CO_2 injection at P = 0 psig; (b) after the pressure-buildup process (t = 0.14 hours) at P = 870 psig. The diameter of the sight glass is 4.8 cm.

Similar to the $CO_{2(sc)}$/oil test, we observe extracting and condensing flows at the $CO_{2(sc)}$/LO interface, as shown in Fig. 7.3d(ii). Fig. 7.9 shows the magnified image of the $CO_{2(sc)}$/LO interface. We observe a large number of small gas bubbles moving upward toward the bulk $CO_{2(sc)}$ phase (upward red arrows). Moreover, there are several droplets condensing downward toward the bulk LO phase (downward green arrows). The condensing flows pass through the interface and enter the bulk LO phase. Figs. 7.10a through 7.10c show the magnified images of two droplets at three different times. The time frame between Figs. 7.10a and 7.10c is approximately 1 second. After crossing the interface, the droplets further penetrate into the bulk LO phase.

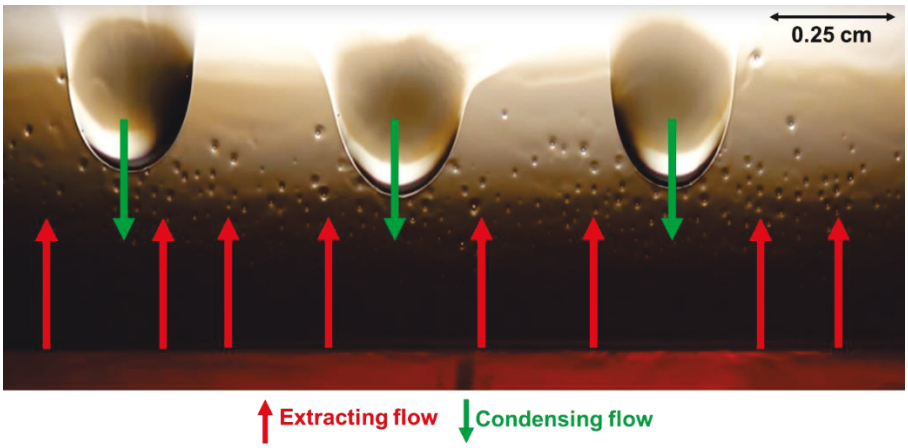

Fig. 7.9: The magnified image of extracting and condensing flows during the soaking process (t = 1.30 hours) at the $CO_{2(sc)}$/LO interface at 122°F and 1,540 psig.

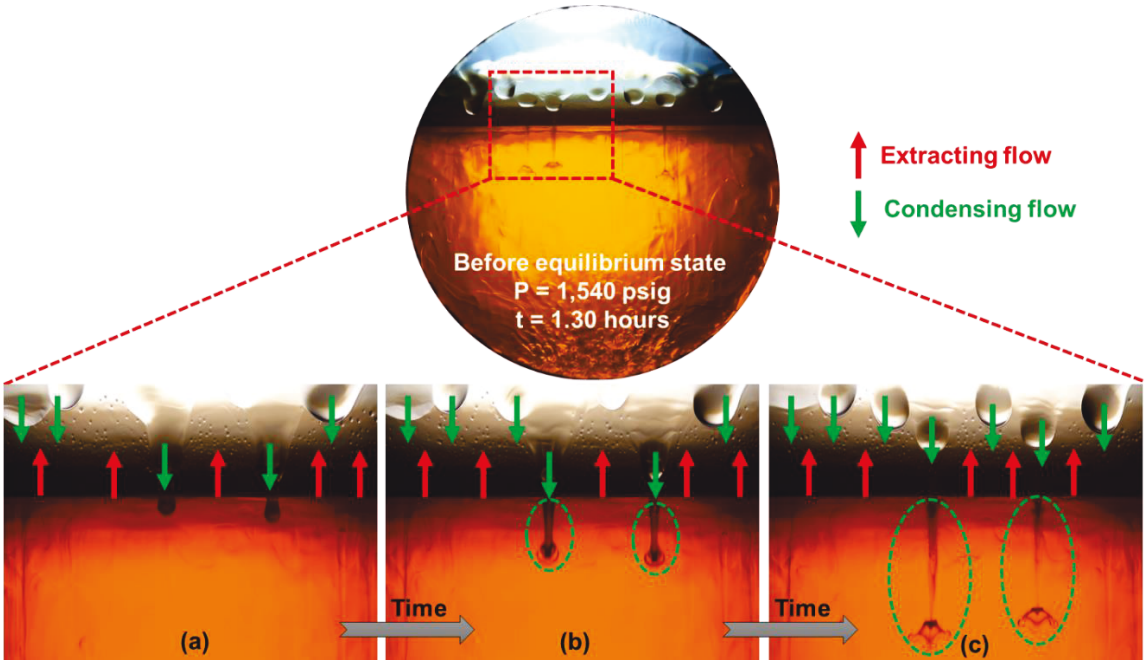

Fig. 7.10: Penetration of condensing flows into the bulk LO phase during the soaking process (t = 1.30 hours) at 122°F and 1,540 psig. The time frame between (a) and (c) is approximately 1 second.

7.5.2.5 Test 5. $N_{2(sc)}$/Oil at P_{set} = 2,000 psig and T_{set} = 122°F

In Test 5, we replaced CO_2 with N_2, which is in its supercritical state at 2,000 psig and 122°F. Fig. 7.3e(i) shows an image of the oil level before $N_{2(sc)}$ injection at atmospheric pressure and 122°F. Injection of $N_{2(sc)}$ (approximately 2.10 mol) increases the pressure to 2,000 psig (Fig. 7.3e(ii)). Comparing Fig. 7.3e(i) with Fig. 7.3e(ii) indicates that the oil phase is compressed after pressurizing the cell to 2,000 psig. More specifically, the oil volume in Fig. 7.3e(ii) is approximately 98% of its initial volume before $N_{2(sc)}$ injection. Fig. 7.11 shows a close view of the compressed-oil phase at 2,000 psig. This observation suggests that $N_{2(sc)}$ dissolution into the oil phase is not significant. Therefore, most of the injected $N_{2(sc)}$ remains at the top of the visual cell and compresses the oil phase. In other words, $N_{2(sc)}$ acts like a piston during the pressure-buildup process and reduces the oil volume. Fig. 7.3e(iii) illustrates the oil level at P_{eq} = 1,890 psig. The soaking process takes approximately 16.6 hours (Fig. 7.4e), which is approximately four times longer than that for the $CO_{2(sc)}$/oil test. The oil volume increases to its initial value during the soaking process, suggesting the gradual dissolution of $N_{2(sc)}$ into the oil phase over time. $N_{2(sc)}$ dissolution during the soaking process can compensate for the oil compression during the pressure-buildup process, increasing the oil volume to its initial value. At the end of this test, N_2 is vented out of the visual cell. During the ventilation process, gas bubbles come out of the oil phase (Fig. 7.12). Because the oil phase retrieved its initial volume after the ventilation process, these bubbles are probably the dissolved N_2.

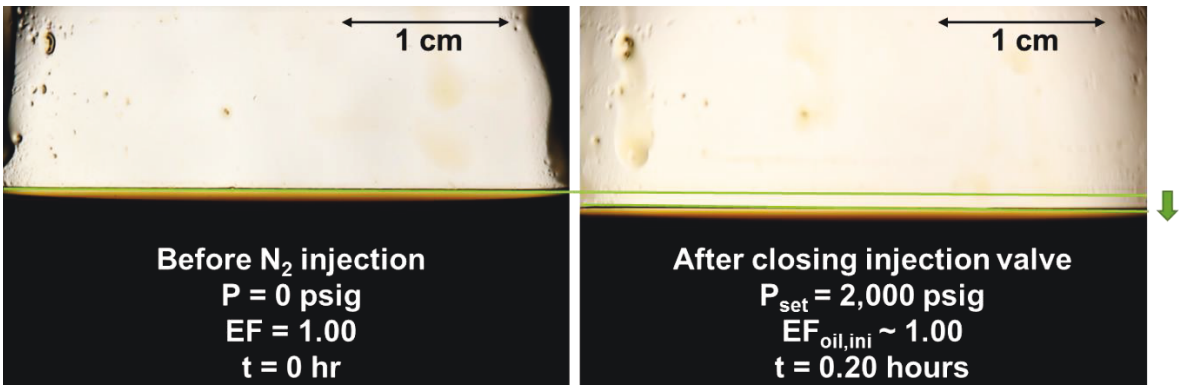

Fig. 7.11: Oil phase at 122°F (a) before $N_{2(sc)}$ injection at P = 0 psig and (b) after $N_{2(sc)}$ injection at P = 2,000 psig. The oil phase is compressed by increasing the pressure from 0 to 2,000 psig. The oil volume at 2,000 psig is approximately 98% of its initial volume before $N_{2(sc)}$ injection.

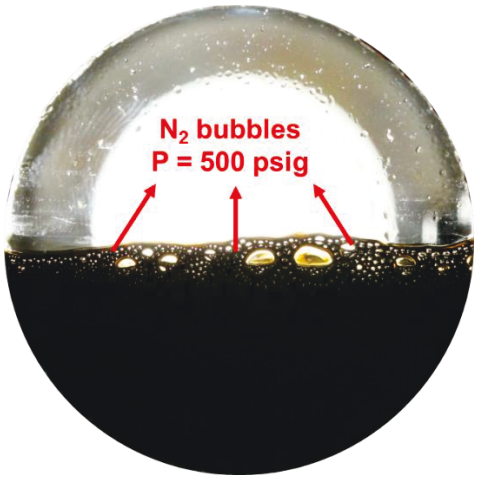

Fig. 7.12: Gas bubbles coming out of the oil phase during the venting of N_2 out of the visual cell at 500 psig. The diameter of the sight glass is 4.8 cm.

7.6 Discussions

Table 7.4 summarizes the key results of the 5 visualization tests. The primary goal of this study is to investigate nonequilibrium $CO_{2(sc)}$/oil interactions under MTN reservoir conditions. Test 3 ($CO_{2(sc)}$/oil) is more representative of the MTN reservoir conditions because it is conducted at the MTN reservoir pressure and temperature. Hereafter, we compare the results of other tests with Test 3.

Table 7.4: The values of EF_{oil} and equilibrium time for visualization tests.

Test number	Test name	P_{set} (psig)	P_{eq} (psig)	$EF_{oil,ini}$	$EF_{oil,eq}$	Equilibrium time (hours)
1	$CO_{2(g)}$/oil	915	715	1.04	1.13	5.1
2	$CO_{2(l)}$/oil	870	790	1.06	1.16	12.1
3	$CO_{2(sc)}$/oil	2,000	1,665	~1.18	1.18	4.5
4	$CO_{2(sc)}$/LO	2,000	1,480	1.43	1.53	2.9
5	$N_{2(sc)}$/oil	2,000	1,890	~1.00	~1.00	16.6

7.6.1 Interactions at the Two-Phase Interface

In this subsection, we explain the reasons for extracting and condensing flows at the CO_2/oil interface.

7.6.1.1 Effect of Physical State of CO_2

The results of Tests 2 through 4 show that there are extracting and condensing flows at the two-phase interface when $CO_{2(sc)}$ or $CO_{2(l)}$ interacts with oil (or LO) (Figs. 7.6, 7.7, and 7.9). We do not observe extracting and condensing flows for the $CO_{2(g)}$/oil and $N_{2(sc)}$/oil tests. Supercritical fluids are generally considered as supersolvents (Hawthorne, 1990). The ability of a supercritical

fluid to dissolve the solute approaches that of the liquid solvent, where their densities approach each other. Furthermore, the maximum solubility of an organic compound is usually higher in liquid solvents than in supercritical fluids (Hawthorne, 1990). Therefore, a possible explanation for the formation of the extracting and condensing flows at the two-phase interface is high densities of $CO_{2(sc)}$ and $CO_{2(l)}$, which are close to the oil-phase (or LO-phase) density. The similarity between densities of the interacting solvent (CO_2) and solute (oil) phases enhances their solubility into each other (Friedrich et al., 1982; Hawthorne, 1990). Fig. 7.13a presents the density of CO_2 vs. pressure at 72°F. $CO_{2(l)}$ has a high density of 755.3 kg/m^3 at P_{set} = 870 psig in the $CO_{2(l)}$/oil test. Oil density is 837.5 kg/m^3 at 72°F and 870 psig. The small difference between oil and $CO_{2(l)}$ densities enhances the solubility of oil components into $CO_{2(l)}$, and vice versa. According to Fig. 7.6, the extracting and condensing flows at the $CO_{2(l)}$/oil interface may be an indication of oil solubility in the $CO_{2(l)}$ phase and vice versa.

Fig. 7.13b presents the density of CO_2 vs. pressure at 122°F. The density of $CO_{2(g)}$ is 149.4 kg/m^3 at P_{set} = 915 psig in the $CO_{2(g)}$/oil test, which is much lower than the density of oil at 122°F and 915 psig (823.3 kg/m^3). Because of the large difference between the $CO_{2(g)}$ and oil densities, oil solubility in $CO_{2(g)}$ (and vice versa) is not very high. The lower solubility of oil in $CO_{2(g)}$ compared with that in $CO_{2(l)}$ can explain the lower extent of extracting and condensing flows in the $CO_{2(g)}$/oil test (Fig. 7.3 a(ii)). As pressure exceeds the CO_2 critical pressure (1,055.3 psig), CO_2 density increases significantly. $CO_{2(sc)}$ and oil densities are 668.8 and 829.4 kg/m^3, respectively, at 2,000 psig and 122°F. The small difference between the densities of $CO_{2(sc)}$ and oil enhances their solubilities into each other, as shown by the upward-extracting and downward-condensing flows (Figs. 7.3c(ii) and 7.7). Although we did not observe extracting and condensing flows in the $CO_{2(g)}$/oil test, it does not necessarily mean the absence of extracting and condensing flows at the $CO_{2(g)}$/oil interface.

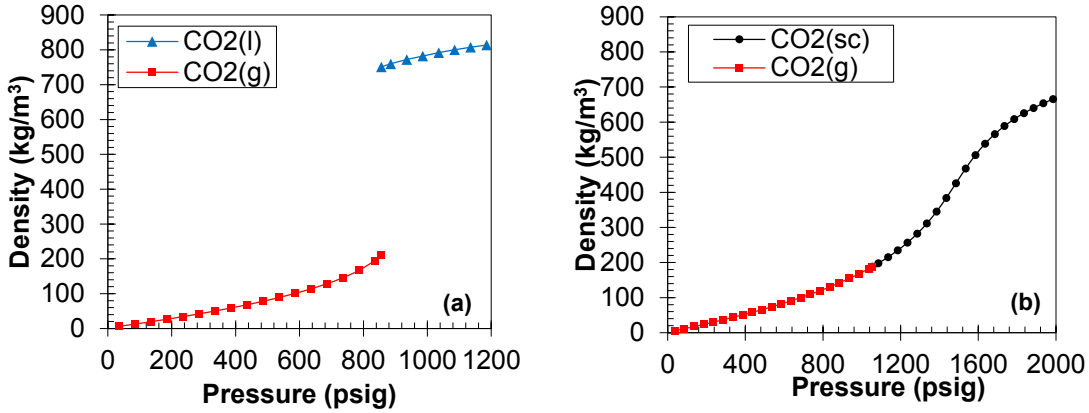

Fig. 7.13: (a) Densities of $CO_{2(l)}$ and $CO_{2(g)}$ vs. pressure at T = 72°F. The density of $CO_{2(l)}$ is equal to 755.3 kg/m^3 at 72°F and 870 psig. (b) The density of CO_2 vs. pressure at T = 122°F. Densities of $CO_{2(g)}$ and $CO_{2(sc)}$ at 915 and 2,000 psig are 149.4 and 668.8 kg/m^3, respectively. The presented data are extracted from NIST.

7.6.1.2 Density of Condensing Flows

We captured the images of condensing flows over time during the $CO_{2(sc)}$/LO test. As the condensing flows contact the interface of $CO_{2(sc)}$/LO and cross the interface, the droplets penetrate farther into the bulk LO phase (Fig. 7.10). This observation suggests that the density of the CO_2/LO mixture is higher than that of the bulk LO phase. The density difference causes the condensing flows to penetrate into the LO phase. Penetration of condensing flows during the soaking process may be considered as a gravity-assisted mechanism, leading to faster dissolution of $CO_{2(sc)}$ into the LO phase.

To explain the penetration of condensing droplets into the LO phase, we investigate the results of PVT tests presented in Fig. 7.2. Fig. 7.2c shows the density of the CO_2/oil mixture as well as the density of dead oil (CO_2-free oil). The density of the CO_2/oil mixture is relatively higher than the density of dead oil at a constant pressure value. Furthermore, higher concentration of CO_2 in the oil phase increases the mixture density. For instance, densities of CO_2/oil mixture at 2,000 psig are 833.6 and 850.3 kg/m^3 when the CO_2 mole fractions are 48.36 and 71.06 mol%, respectively. At similar conditions, the density of dead oil is 829.4 kg/m^3. We did not conduct PVT tests on the CO_2/LO mixture. However, the higher density of the CO_2/LO mixture than that of the dead LO may explain the penetration of condensing droplets into the LO phase (Fig. 7.10).

Similarly, Lansangan and Smith (1993) conducted a series of PVT tests using CO_2 and 8 West Texas oil samples. The authors measured equilibrium density of CO_2-rich and oil-rich mixtures over conditions ranging from 105 to 165°F and from 1,185 to 2,335 psig. The results illustrated

that the densities of CO_2/oil mixtures increase with dilution of the crude oil with CO_2. To explain this observation, they considered the complex crude oil as an ideal multicomponent mixture of n-alkanes. The n-alkanes are nonpolar symmetric molecules with no permanent dipoles. However, the presence of quadrupolar molecules such as CO_2 can induce dipolar moments in n-alkane molecules. Therefore, when CO_2 molecules dissolve into the crude oil, CO_2 serves as a catalyst that polarizes the n-alkane molecules, resulting in superimposition of attractive Coulombic forces on the London dispersion forces (Lansangan and Smith, 1993). Thus, dissolution of CO_2 into oil promotes agglomeration of denser oil molecules, leading to higher density of the CO_2/oil mixture compared with that of CO_2-free oil.

7.6.1.3 $N_{2(sc)}$/Oil Test

N_2 is supercritical at 2,000 psig and 122°F in Test 5. However, we did not observe extracting and condensing flows at the $N_{2(sc)}$/oil interface. To explain this result, we interpret the N_2 density vs. pressure curve presented in Fig. 7.14. N_2 density increases linearly by conversion of $N_{2(g)}$ into $N_{2(sc)}$. The density of $N_{2(sc)}$ is 139.1 kg/m^3 at 2,000 psig and 122°F, which is far lower than that of oil (829.4 kg/m^3). One possible explanation for the absence of extracting and condensing flows at the $N_{2(sc)}$/oil interface could be the large difference between densities of $N_{2(sc)}$ and oil. In addition, weaker $N_{2(sc)}$/oil interactions compared with those for the $CO_{2(sc)}$/oil system result in higher MMP for $N_{2(sc)}$. MMP is the minimum pressure required to eliminate the interfacial tension between oil and injected gas (N_2 and CO_2). Hawthorne et al. (2016) conducted the capillary-rise/vanishing-interfacial-tension tests to evaluate the MMP between oil and different fluids such as CO_2, N_2, and methane. The results of MMP measurements at 107°F showed that the MMP between the Bakken oil and CO_2 (1,285 ± 37 psig) is much lower than that between the Bakken oil and N_2 (22,370 ± 840 psig).

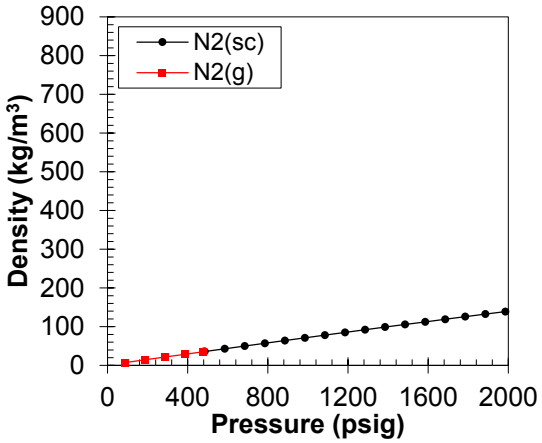

Fig. 7.14: N_2 density as a function of pressure at 122°F. Densities of oil and $N_{2(sc)}$ at 2,000 psig and 122°F are 829.4 and 139.1 kg/m^3, respectively. The presented data are extracted from NIST.

7.6.2 Oil Expansion Factor (EF_{oil})

In this subsection, we investigate the driving mechanisms for dissolution of CO_2 into the oil phase, which can lead to oil expansion. We discuss the effect of the physical state of CO_2 on EF_{oil} during the pressure-buildup and soaking processes.

The results of Tests 1 through 3 show that CO_2 in all of its physical states (gas, liquid, and supercritical) can dissolve into the oil phase and cause oil expansion (Figs. 7.3a through 7.3c). Table 7.4 lists $EF_{oil,ini}$ and $EF_{oil,eq}$ at the end of the pressure-buildup and soaking processes, respectively. The pressure-buildup process takes approximately 7 to 22 minutes to complete. However, the equilibrium condition (end of the soaking process) is obtained after a few hours, as listed in Table 7.4. For $CO_{2(g)}$/oil and $CO_{2(l)}$/oil tests, most of the oil expansion occurs during the soaking process. However, for the $CO_{2(sc)}$/oil test, most of the oil expansion occurs during the pressure-buildup process. For instance, $EF_{oil,ini}$ values for $CO_{2(g)}$/oil and $CO_{2(l)}$/oil tests are 1.04 and 1.06, respectively. During the soaking process, EF_{oil} values for $CO_{2(g)}$/oil and $CO_{2(l)}$/oil tests increase to equilibrium values of 1.13 and 1.16, respectively. On the other hand, $EF_{oil,ini}$ for the $CO_{2(sc)}$/oil test is approximately 1.18, and it remains almost constant during the soaking process. For the $CO_{2(sc)}$/LO test, $EF_{oil,ini}$ is 1.43, and EF_{oil} increases to 1.53 during the soaking process. The results of Tests 3 and 4 show that oil and LO expansions mainly occur during the pressure-buildup process when CO_2 is in the supercritical state. These observations suggest that the rate of CO_2 dissolution, and consequently the rate of oil expansion, depends on the physical state of CO_2.

Fig. 7.13b shows the density of CO_2 as a function of pressure at 122°F. The density of CO_2 increases significantly by conversion of $CO_{2(g)}$ into $CO_{2(sc)}$. For example, $CO_{2(g)}$ at 915 psig and $CO_{2(sc)}$ at 2,000 psig have densities of 149.4 and 668.8 kg/m^3, respectively. At 2,000 psig and 122°F, oil density is 829.4 kg/m^3. Immediately after $CO_{2(sc)}$ injection into the visual cell, the concentration of $CO_{2(sc)}$ at the vicinity of the $CO_{2(sc)}$/oil interface is higher than that in the bulk oil phase. The CO_2 concentration gradient between the bulk oil phase and that at the $CO_{2(sc)}$/oil interface leads to Fickian diffusion of CO_2 into the bulk oil phase (Rongy et al., 2012). As $CO_{2(sc)}$ with high density dissolves into the oil phase, the $CO_{2(sc)}$/oil mixture density at the interface increases to a value higher than the density of CO_2-free oil (Crawford et al., 1963; Lansangan and Smith, 1993). Therefore, the oil density at the $CO_{2(sc)}$/oil interface is higher than that in the bulk oil phase, leading to a density-driven convection phenomenon. In other words, heavier and lighter CO_2/oil mixtures move downward and upward, respectively, during the CO_2/oil interactions (Khosrokhavar, 2016; Farajzadeh et al., 2007). The density-driven convection causes CO_2 dissolution into the oil phase, leading to fast mixing of CO_2 into the oil phase (Rongy et al., 2012).

We observe gravity-induced fingers in the $CO_{2(sc)}$/LO test during the pressure-buildup process at 1,230 psig (Fig. 7.15a). By increasing the pressure from 1,230 to 1,550 psig, the density of $CO_{2(sc)}$ increases from 254.5 to 479.9 kg/m^3. Compared with the lower pressure condition (Fig. 7.15a), increasing pressure increases the number of gravity-induced fingers (Fig. 7.15b). Higher $CO_{2(sc)}$ density at higher pressure values causes more-pronounced local density increase in the LO phase, and consequently increases the number of gravity-induced fingers. Formation of gravity-induced fingers enhances $CO_{2(sc)}$ dissolution into the LO and oil phases, explaining the fast expansion of LO and oil right after $CO_{2(sc)}$ injection into the visual cell. Rongy et al. (2012) investigated the nonequilibrium interactions of the binary mixture of CO_2 and n-C_{10} experimentally and mathematically. They concluded that compared with the Fickian-diffusion mechanism, equilibrium conditions were achieved approximately 50 times faster when the density-driven convection expedites the mixing of CO_2 into n-C_{10}. Khosrokhavar et al. (2014) developed a Schlieren setup to observe the gravity-induced fingers using refractive-index variations. They visually detected the beginning and development of gravity-induced fingers caused by local density increase after the contact of $CO_{2(sc)}$ with n-C_{10}.

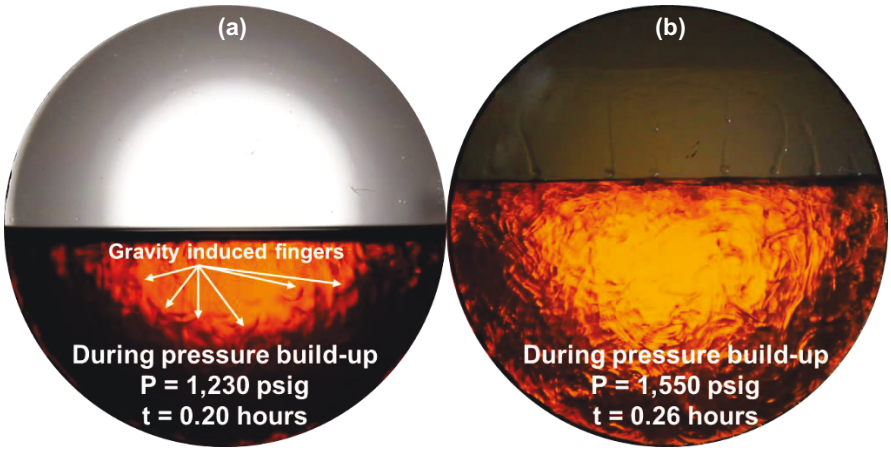

Fig. 7.15: Picture of gravity-induced fingers caused by local density increase in the $CO_{2(sc)}$/LO test. The images are captured at (a) 1,230 and (b) 1,550 psig, during the pressure-buildup process at 122°F.

The system's pressure and temperature influence the extracting and condensing flows. We observe extracting and condensing flows at the CO_2/oil interface for $CO_{2(l)}$/oil and $CO_{2(sc)}$/oil tests (Figs. 7.6 and 7.7). The extracting and condensing flows enhance the mixing, and thus dissolution of CO_2 into the oil phase. However, during the pressure-buildup process, the oil-expansion rate in the $CO_{2(l)}$/oil test is lower than that in the $CO_{2(sc)}$/oil test. The diffusion coefficient strongly depends on temperature (Treybal, 1980). During the $CO_{2(sc)}$/oil test, the temperature is 122°F, which is higher than that for the $CO_{2(l)}$/oil test (72°F). Thus, the diffusion coefficient of CO_2 is higher in the $CO_{2(sc)}$/oil system compared with that in the $CO_{2(l)}$/oil system. Faster mass transfer in the $CO_{2(sc)}$/oil system can be a possible reason for the faster expansion rate compared with that in the $CO_{2(l)}$/oil system. In addition, the viscosity of $CO_{2(sc)}$ is one order of magnitude lower than that of $CO_{2(l)}$ (Hawthorne, 1990). Therefore, lower viscosity of $CO_{2(sc)}$ enhances its mass-transfer characteristics, leading to faster oil expansion during pressure-buildup process in the $CO_{2(sc)}$/oil test compared with that in $CO_{2(l)}$/oil test.

For the $N_{2(sc)}$/oil system, right after $N_{2(sc)}$ injection into the visual cell, $N_{2(sc)}$ concentration at the $N_{2(sc)}$/oil interface is higher than that in the bulk oil phase. Thus, N_2 diffuses from the $N_{2(sc)}$/oil interface into the bulk oil phase. As $N_{2(sc)}$ dissolves into the oil phase, the $N_{2(sc)}$/oil mixture density at the interface decreases to a value lower than the density of $N_{2(sc)}$-free oil. Therefore, the lighter $N_{2(sc)}$/oil mixture at the $N_{2(sc)}$/oil interface remains on top of the initial denser oil below the interface, and does not move downward. In other words, density-driven convection likely does not occur in the $N_{2(sc)}$/oil system.

7.6.3 Pressure Decline vs. Time

According to Fig. 7.4, the visual-cell pressure decreases during the soaking process for all tests. The pressure-decline rate is relatively sharp at the beginning of the soaking process, and it gradually stabilizes while approaching equilibrium conditions. In general, the sharper the pressure-decline rate, the lower the equilibrium time. Dissolution of CO_2 into the oil (or LO) phase explains the pressure decline observed during the soaking process (Ghasemi et al., 2017; Habibi et al., 2017). The viscosity of the interacting oil (or LO) phase affects the rate of dissolution of CO_2 molecules. More specifically, LO has lower viscosity than the oil (Table 7.1). Thus, it is easier for CO_2 to mix with the LO phase compared with the oil phase. Furthermore, LO has a higher fraction of lighter components compared with the oil phase (Fig. 7.1), facilitating CO_2 dissolution into the LO phase. Higher CO_2-dissolution rate into the LO phase leads to faster pressure decline in the $CO_{2(sc)}$/LO system compared with that in the $CO_{2(sc)}$/oil system. In addition, among all the tests, the $CO_{2(sc)}$/LO system has the sharpest pressure decline during the soaking period, where the pressure drops from 2,000 to approximately 1,480 psig in less than 3 hours. One explanation for this observation is the high solubility of $CO_{2(sc)}$ in LO. The density-driven convection in the $CO_{2(sc)}$/LO system (Fig. 7.15) facilitates mixing of CO_2 in the LO phase, expediting the pressure decline. Rongy et al. (2012) modeled the nonequilibrium CO_2 dissolution into n-C_{10} and compared the simulated pressure decline with the experimental data. They assumed the Fickian-diffusion mechanism in their model. Their results indicate that it takes approximatively 100 hours to reach to the equilibrium pressure when diffusion is the only mass-transfer mechanism. Accounting for density-driven convection reduces the equilibrium time to 2 hours. They concluded that the rapid pressure decline in the CO_2/n-C_{10} system is mainly attributed to the density-driven convection, which enhances CO_2 dissolution into the n-C_{10} phase.

Among all the tests, the $N_{2(sc)}$/oil system has the least pressure decline during the soaking process, where the pressure drops from 2,000 to approximately 1,890 psig. In addition, the equilibrium time for the $N_{2(sc)}$/oil system is nearly 16.6 hours, which is the highest among all tests (Table 7.4). The solubility of $N_{2(sc)}$ in oil is significantly lower than $CO_{2(sc)}$ solubility in oil (Bahralolom and Orr, 1988), reducing the total amount of pressure decline during the soaking process, at a specific temperature.

7.7 Limitations of Setup and Tests

There are limitations associated with the proposed experimental procedure/setup, which we discuss in this subsection.

1- We used material balance and the real-gas law to calculate the injected moles of CO_2 (or N_2) listed in Table 7.3. To do this, the final mole value of CO_2 (or N_2) is subtracted from its initial value in the accumulator. CO_2 is in gaseous state in the accumulator at the start of the pressure-buildup process. However, at the end of pressure-buildup process, some of the $CO_{2(g)}$ may be converted to $CO_{2(l)}$ in the accumulator. Thus, there are some uncertainties in the calculation of the mole values of $CO_{2(g)}$ and $CO_{2(l)}$ at final conditions using the real-gas law.

2- We used the captured images (during the tests) to obtain EF_{oil} by analyzing the oil/LO level. However, there are solid precipitates on the sight glass, which can cause errors in finding the accurate oil/LO level. Therefore, the presented EF_{oil} values may not be very accurate, especially where significant solid precipitates are present on the sight glass.

3- The accumulator and its residing CO_2 (or N_2) are at laboratory temperature of 72°F. When we start injecting CO_2 (or N_2) into the visual cell, the temperature of oil in the visual cell drops from 122°F to approximately 117°F during pressure-buildup process. This temperature fluctuation may affect $EF_{oil,ini}$ measured at the end of the pressure-buildup process. It is important to mention that the visual-cell temperature returns to 122°F nearly 10 minutes after ceasing the CO_2 (or N_2) injection into the visual cell.

4- For pressurizing the visual cell with CO_2 (or N_2), we use the pulse-free pump with maximum DI water flow rate of 29 cm^3/min. Because of the small flow rate, it takes approximately 7 to 22 minutes to reach the set pressure. Different pressure-buildup times for different tests affect the comparative analysis of EF_{oil} during the pressure-buildup and soaking processes. To remediate this problem, we recommend the use of a gas compressor capable of injecting CO_2 (or N_2) at high flow rates to minimize the pressure-buildup time.

7.8 Industrial Application

Understanding the mechanisms of CO_2 dissolution into oil phase is essential for EOR from oil reservoirs. Characterization of these mechanisms requires an improved understanding of nonequilibrium interactions between solute and solvent under in-situ conditions. The experimental

results of this study indicate that the density-driven convection along with the extracting and condensing flows at the $CO_{2(sc)}$/oil interface are the primary mechanisms controlling the CO_2/oil interactions. Cyclic CO_2 processes such as CO_2 huff-n-puff are considered as efficient EOR methods in tight and shale formations (Carpenter, 2018). The results of this study can also help the oil industry to optimize the operating parameters such as CO_2-slug size, CO_2-soaking time, and number of CO_2-injection cycles.

7.9 Summary

In Chapter 7, we used a custom-designed visual cell to investigate nonequilibrium CO_2/oil interactions under high-pressure and high-temperature conditions. We visualized the CO_2/oil interface and measured the visual-cell pressure over time. We performed 5 sets of visualization tests. The first three tests aimed at investigating interactions of gaseous (g), liquid (l), and supercritical (sc) CO_2 with a Montney (MTN) oil sample. In the fourth test, to visualize the interactions in the bulk oil phase, we replaced the opaque MTN oil with a translucent Duvernay (DUV) light oil (LO). Finally, we conducted an $N_{2(sc)}$/oil test to compare the results with those of $CO_{2(sc)}$/oil test. We also compared the results of nonequilibrium CO_2/oil interactions with those obtained from conventional pressure/volume/temperature (PVT) tests. The key findings of this chapter are the following.

1- Oil expands as soon as CO_2 is injected into the visual cell. The rate of oil expansion depends on the physical state of CO_2. For $CO_{2(sc)}$, oil rapidly expands during the pressure-buildup process. However, for $CO_{2(g)}$ and $CO_{2(l)}$, oil expansion mainly occurs during the soaking process. Rapid oil expansion in the $CO_{2(sc)}$/oil test is explained by density-driven convection as well as extracting and condensing flows at the $CO_{2(sc)}$/oil interface that enhance the mixing of $CO_{2(sc)}$ with oil.

2- Extracting and condensing flows occur when CO_2 is in either liquid state or supercritical state. Extracting and condensing flows can be explained by high densities of $CO_{2(l)}$ and $CO_{2(sc)}$ that enhance the solubility of oil components in the CO_2 phase and vice versa.

3- The density of the CO_2/oil mixture is higher than the density of the CO_2-free oil phase. The density difference causes the condensing flows to penetrate into the oil phase. Penetration of the condensing flows during the soaking process can be considered as a gravity-assisted mechanism, leading to faster dissolution of $CO_{2(sc)}$ into oil.

Nomenclature

EF_{oil} = Oil expansion factor, L^3/L^3
$EF_{oil,eq}$ = Equilibrium EF_{oil} at P_{eq}, L^3/L^3
$EF_{oil,ini}$ = Initial EF_{oil} at P_{set}, L^3/L^3
MMP = Minimum miscibility pressure, $ML^{-1}t^{-2}$ [psig]
Mw = Molecular weight, [g/mol]
P = Pressure, $ML^{-1}t^{-2}$ [psig]
P_b = Bubblepoint pressure, $ML^{-1}t^{-2}$ [psig]
P_c = Critical pressure, $ML^{-1}t^{-2}$ [psig]
P_{eq} = Equilibrium pressure, $ML^{-1}t^{-2}$ [psig]
P_{set} = Set pressure, $ML^{-1}t^{-2}$ [psig]
t = Time, t [hour]
T = Temperature [^oF]
T_c = Critical temperature, [^oF]
T_{set} = Set temperature, [^oF]
$V_{oil}|_{P'}$ = Volume of oil at elevated P, L^3 [cm^3]
$V_{oil}|_{P=0}$ = Volume of oil at 0 psig, L^3 [cm^3]
ρ = Density, ML^{-3} [kg/m^3]

Abbreviations

CO_2 = Carbon dioxide
$CO_{2(g)}$ = Gaseous CO_2
$CO_{2(l)}$ = Liquid CO_2
$CO_{2(sc)}$ = Supercritical CO_2
DI water = Deionized water
DUV = Duvernay
EOR = Enhanced oil recovery
LO = Light oil
MTN = Montney
N_2 = Nitrogen
$N_{2(g)}$ = Gaseous N_2
$N_{2(sc)}$ = Supercritical N_2
PVT = Pressure/Volume/Temperature

Chapter 8

Conclusions and Recommendations

This study presents the results of wettability and EOR tests conducted on unconventional rocks with dual-wet pore network. Key petrophysical properties affecting wettability of Duvernay shale and Montney tight siltstone samples are investigated in this thesis. Using the results of wettability tests, new mathematical models and experimental methods are proposed to characterize dual-wet pore networks. At the end of this dissertation, the mechanisms of CO_2-EOR from oil-saturated shale plugs are visually investigated by using a custom-designed visual cell.

8.1 Conclusions

- The wetting affinity of the organic-rich Duvernay samples to oil is much stronger than that to brine, making a dual-wet system. High wetting affinity to oil is attributed to large number of hydrophobic nanopores within the organic matter, confirmed by the SEM/EDS (scanning electron microscopy/energy-dispersive x-ray spectroscopy) analyses as well as the positive correlations between TOC (total organic carbon) content and effective porosity.
- Hydrophobic nanopores within organic matter and hydrophilic micropores bordered by inorganic minerals may explain late equilibrium of oil and early equilibrium of brine in spontaneous-imbibition tests, respectively.
- Powdering the Duvernay shale plugs generates more hydrophobic surface areas that subsequently increase the wetting affinity of crushed shale packs to oil. Higher accessibility to static organic carbon (SOC) may be responsible for the stronger hydrophobicity of crushed shale packs compared with plugs.
- The positive correlations of pressure-decay permeability and effective porosity with TOC content of Duvernay samples indicate that the pores within the organic matter constitute a significant portion of effective pore volume. The samples with higher TOC content generally imbibe higher oil volume and have higher oil wettability index.

- Higher kerogen maturity level results in higher number of organic pores. Shale samples with higher thermal maturity (gas window) have higher number of organic pores with possibly stronger conductivity to each other, compared with less mature samples (oil window).
- Kerogen maturity level affects the connectivity of organic pores, and subsequently the imbibition process. The organic pores in the highly mature (gas window) shale samples are well connected, leading to higher imbibed volume of oil in the samples with higher TOC content. However, Imbibed volume of oil decreases with TOC content in the less mature (oil window) samples, which may be explained by poorly connected organic pores in the less mature samples.
- Kerogen maturity level affects the free hydrocarbons content (S_1) of shale samples. Free hydrocarbons in less mature (oil window) samples reduce the accessible pore space for oil imbibition, leading to the negative correlation of imbibed volume of oil with TOC content.
- Cumulative pore space of shale samples filled by brine in spontaneous- and forced-imbibition tests is about three times higher than that in mercury injection capillary pressure (MICP) test. Therefore, pore size distribution estimated by brine would be more representative than that estimated by MICP.
- The range of peak pore-size of organic pores ($D_{peak\text{-}org}$) estimated by forced brine-imbibition is consistent with the 2-D visualization of organic pores using SEM analysis.
- Minimum pore diameter (D_{min}) detected by forced mercury-injection at 55,110 psig is 3.8 nm. D_{min} detected by brine injection at 9,500 psig is 1.2 nm. Therefore, brine injection can be used to characterize smaller pore sizes at significantly lower pressures compared with mercury.
- The comparative water/oil imbibition data suggest that Montney siltstone samples have dual-wet pore network, which is similar to the Duvernay samples. SEM analysis, organic petrography, and MICP data show that the pore network of the Montney samples can be divided into: 1) nanoscale pores within the organic matter mainly composed of solid bitumen/pyrobitumen (Part I) and 2) microscale pores among

inorganic minerals (Part II). Part I is represented by the tail part at the low end of the pore-throat size distribution from MICP data, whereas Part II is represented by the bell-shaped part at higher pore-throat size.

- Based on the modified Purcell's model for gas/water relative permeability of unconventional rocks, by increasing the fraction of hydrophobic organic pores (S_{org}), gas relative permeability (k_{rg}) decreases, for a fixed water saturation. By increasing the fraction of water-repellant nanopores (higher S_{org}), the average size of conduits for gas flow and then k_{rg} are reduced.
- Imbibition oil recovery by brine is less than 7% of the initial oil in place, indicating the poor affinity of oil-filled pores to brine.
- Supercritical CO_2 can diffuse into the oil-saturated plugs and expand the oil phase. Supercritical CO_2 with high density extracts the expanded oil into the bulk CO_2 phase, leading to oil production. Oil recovery factor by CO_2 is around 82% of initial oil in place, which is much higher than oil recovery factor by brine imbibition.
- Comparing the results of oil recovery in CO_2-soaking tests with those of wettability tests suggests that in contrary to brine, supercritical CO_2 can extract a significant portion of the oil out of hydrophobic organic pores.
- Oil expands as soon as CO_2 is injected into the visual cell. However, the rate of oil expansion depends on the physical state of CO_2. When CO_2 is supercritical ($CO_{2(sc)}$), oil expansion is faster than liquid ($CO_{2(l)}$) and gaseous ($CO_{2(g)}$) cases. Rapid oil expansion in the $CO_{2(sc)}$/oil test is explained by density-driven convection as well as extracting and condensing flows at the $CO_{2(sc)}$/oil interface.
- Extracting and condensing flows occur when CO_2 is in either liquid state or supercritical state. Extracting and condensing flows can be explained by high densities of $CO_{2(l)}$ and $CO_{2(sc)}$ that enhance the solubility of oil components in the CO_2 phase and vice versa.
- The density of the CO_2/oil mixture is higher than the density of the CO_2-free oil phase. The density difference causes the condensing flows to penetrate into the oil phase. Penetration of the condensing flows during the soaking process can be considered as a gravity-assisted mechanism, leading to faster dissolution of $CO_{2(sc)}$ into oil phase.

8.2 Recommendations

- We used oxygen index (OI) as an indicator of kerogen maturity level, and investigated its correlation with oil wettability index (WI_o) in Chapters 2 and 3. OI is not generally used for quantifying thermal maturity of shales. Vitrinite reflectance ($\%R_o$) is a measure of the percentage of incident light reflected from the surface of vitrinite particles. Vitrinite reflectance is typically used for determining the maturity level of organic matter. To study the effect of kerogen maturity level on wettability, it is recommended to measure $\%R_o$ and investigate its possible correlation with WI_o.
- In forced brine-imbibition test (Chapter 4), we reduced the pressure to atmospheric conditions and took the plug out of the accumulator to measure incremental brine saturation. This pressure drop in the forced-imbibition test leads to capillary-pressure hysteresis effects that influence the brine saturation, and subsequently the estimation of organic pore size distribution (PSD_{org}). It is recommended to custom design a new setup and apply the volume-balance method (similar to MICP test) for measuring the incremental brine saturation at each incremental pressure step.
- The CO_2/oil molar ratio in CO_2-soaking tests (Chapter 6) is much higher than that at reservoir conditions. To reduce this ratio and mimic fractured reservoir conditions, it is recommended to reduce the total internal volume of the visual cell as much as possible.
- To report the full curve of oil RF vs. time in CO_2-soaking tests (Chapter 6), it is recommended to cool down the vented mixture of extracted oil/CO_2 and measure the volume of the condensed oil at different times. Furthermore, measuring the composition of the condensed oil by simulated distillation technique would be useful for investigating the produced oil components at different soaking times.
- In CO_2-EOR tests for unconventional rocks, CO_2/oil/rock interactions are typically investigated. Water-based fluids are commonly used for fracturing the unconventional formations. Load water recovery during flowback process is typically less than 10%. In other words, more than 90% of the injected fracturing water remains in reservoir. As a result, the injected CO_2 for EOR is in contact with oil, rock, and also water. CO_2 dissolution into water makes carbonated water that has an acidic effect for reaction with

carbonate minerals such as calcite and dolomite. Investigating the interactions of carbonated water with oil-saturated shale plugs is a missing factor that has not been considered so far.

- In the bulk-phase CO_2/oil tests (Chapter 7), taking fluid samples from extracting and condensing flows, and measuring their compositions would be helpful in better understanding of the nonequilibrium interactions.

Bibliography

Adekunle, O. and B. T. Hoffman (2016). Experimental and Analytical Methods to Determine Minimum Miscibility Pressure (MMP) for Bakken Formation Crude Oil. Journal of Petroleum Science and Engineering 146: 170-182. https://doi.org/10.1016/j.petrol.2016.04.013

Adesida, A. G., Akkutlu, I., Resasco, D. E., & Rai, C. S. (2011). Characterization of Barnett Shale Kerogen Pore Size Distribution Using DFT Analysis and Grand Canonical Monte Carlo Simulations. Society of Petroleum Engineers. https://doi.org/10.2118/147397-MS

Ahmed, U., & Meehan, D. N., (2016). Unconventional Oil and Gas Resources: Exploitation and Development. CRC Press.

Akkutlu, I. Y., & Fathi, E. (2012). Multiscale Gas Transport in Shales with Local Kerogen Heterogeneities. Society of Petroleum Engineers. https://doi.org/10.2118/146422-PA

Al Hinai, A., Rezaee, R., Esteban, L., & Labani, M. (2014). Comparisons of Pore Size Distribution: A Case From The Western Australian Gas Shale Formations. Journal of Unconventional Oil and Gas Resources, 8, 1-13. https://doi.org/10.1016/j.juogr.2014.06.002

Alharthy, N., Teklu, T. W., Kazemi, H., Graves, R. M., Hawthorne, S. B., Braunberger, J., & Kurtoglu, B. (2018). Enhanced Oil Recovery in Liquid-Rich Shale Reservoirs: Laboratory to Field. Society of Petroleum Engineers. https://doi.org/10.2118/175034-PA

Alvarez, J. O., & Schechter, D. S. (2017). Wettability Alteration and Spontaneous Imbibition in Unconventional Liquid Reservoirs by Surfactant Additives. Society of Petroleum Engineers. https://doi.org/10.2118/177057-PA

American Petroleum Institute. (1962). API Recommended Practices for Laboratory Testing of Surface Active Agents for Well Stimulation, American Petroleum Institute, Production Department.

Amott, E., (1959). Observations Relating to the Wettability of Porous Rock. Society of Petroleum Engineers.

Anderson, W. G. (1986a). Wettability Literature Survey- Part 2: Wettability Measurement. Society of Petroleum Engineers. https://doi.org/10.2118/13933-PA

Anderson, W. G. (1986b). Wettability Literature Survey-Part 3: The Effects of Wettability on the Electrical Properties of Porous Media. Journal of Petroleum Technology, 38(12), 1-371. https://doi.org/10.2118/13934-PA

Anderson, W. G. (1987a). Wettability Literature Survey- Part 4: Effects of Wettability on Capillary Pressure. Society of Petroleum Engineers. https://doi.org/10.2118/15271-PA

Anderson, W. G. (1987b). Wettability Literature Survey Part 5: The Effects of Wettability on Relative Permeability. Society of Petroleum Engineers. https://doi.org/10.2118/16323-PA

Bahralolom, I. M. and F. M. Orr, Jr. (1988). Solubility and Extraction in Multiple-Contact Miscible Displacements: Comparison of N_2 and CO_2 Flow Visualization Experiments. SPE Reservoir Engineering 3(01): 213-219. https://doi.org/10.2118/15079-PA

Bahralolom, I. M., R. E. Bretz and F. M. Orr, Jr. (1988). Experimental Investigation of the Interaction of Phase Behavior With Microscopic Heterogeneity in a CO_2 Flood. SPE Reservoir Engineering 3(02): 662-672. https://doi.org/10.2118/14147-PA

Barati, R., Hutchins, R. D., Friedel, T., Ayoub, J. A., Dessinges, M. N., & England, K. W. (2009). Fracture Impact of Yield Stress and Fracture-face Damage on Production with a Three-phase 2D Model. SPE Production & Operations, 24(02), 336-345. https://doi.org/10.2118/111457-PA

Barba, R. E. (2015). Liquids Rich Organic Shale Recovery Factor Application. In SPE Annual Technical Conference and Exhibition. Society of Petroleum Engineers. https://doi.org/10.2118/174994-MS

Baskin, D. K. (1997). Atomic H/C Ratio of Kerogen as an Estimate of Thermal Maturity and Organic Matter Conversion. AAPG bulletin, 81(9), 1437-1450.

Batycky, J.P., McCaffery, F.G., Hodgins, P.K. and Fisher, D.B., (1981). Interpreting Relative Permeability and Wettability from Unsteady-State Displacement Measurements. Society of Petroleum Engineers Journal, 21(03), pp.296-308. http://dx.doi.org/10.2118/9403-PA

Bayestehparvin, B., Abedi, J., & Farouq Ali, S. M. (2017). Development of a Non-Equilibrium Pore Scale Reservoir Simulator. Society of Petroleum Engineers. https://doi.org/10.2118/185010-MS

Begum, M., Reza Yassin, M., Dehghanpour, H., & Dunn, L. (2017). Rock-Fluid Interactions in the Duvernay Formation: Measurement of Wettability and Imbibition Oil Recovery. Society of Petroleum Engineers. https://doi.org/10.2118/185065-MS

Benner, F.C., Dodd, C.G. and Bartell, F.E., (1942). Evaluation of Effective Displacement Pressures for Petroleum Oil-Water Silica Systems. In Drilling and Production Practice. American Petroleum Institute.

Bernard, G. G. (1967). Effect of Floodwater Salinity on Recovery of Oil from Cores Containing Clays. In SPE California Regional Meeting. Society of Petroleum Engineers. https://doi.org/10.2118/1725-MS

Bertoncello, A., Wallace, J., Blyton, C., Honarpour, M. and Kabir, C.S., (2014). Imbibition and Water Blockage in Unconventional Reservoirs: Well Management Implications during Flowback and Early Production. In SPE/EAGE European Unconventional Resources Conference and Exhibition. http://dx.doi.org/10.2118/167698-PA

Binazadeh, M., Xu, M., Zolfaghari, A. and Dehghanpour, H., (2016). Effect of Electrostatic Interactions on Water Uptake of Gas Shales: The Interplay of Solution Ionic Strength and Electrostatic Double Layer. Energy & Fuels, 30(2), pp.992-1001. http://dx.doi.org/10.1021/acs.energyfuels.5b02990

Bobek, J. E., Mattax, C. C., & Denekas, M. O. (1958). Reservoir Rock Wettability - Its Significance and Evaluation (SPE-895-G). Society of Petroleum Engineers.

Borysenko, A., Clennell, B., Sedev, R., Burgar, I., Ralston, J., Raven, M., Dewhurst, D. and Liu, K., (2009). Experimental Investigations of the Wettability of Clays and Shales. Journal of Geophysical Research: Solid Earth, 114(B7). https://doi.org/10.1029/2008JB005928

Boult, P. J., Theologou, P. N., & Foden, J. (1997). Capillary Seals within the Eromanga Basin, Australia: Implications for Exploration and Production. Memoirs-American Association of Petroleum Geologists, 143-168.

Boyd, C.E., (1995). Bottom Soils, Sediment, and Pond Aquaculture. Springer Science & Business Media.

Britt, L. K. (1985). Optimized Oilwell Fracturing of Moderate-Permeability Reservoirs. Society of Petroleum Engineers. https://doi.org/10.2118/14371-MS

Brown, R.J. and Fatt, I., (1956). Measurements of Fractional Wettability of Oil Fields' Rocks by the Nuclear Magnetic Relaxation Method. In Fall Meeting of the Petroleum Branch of AIME. Society of Petroleum Engineers. http://dx.doi.org/10.2118/743-G

Brunauer, S., Deming, L.S., Deming, W.E. and Teller, E., (1940). On a Theory of the Van Der Waals Adsorption of Gases. Journal of the American Chemical society, 62(7), pp.1723-1732.

Brunauer, S., Emmett, P. H., & Teller, E. (1938). Adsorption of Gases in Multimolecular Layers. Journal of the American chemical society, 60(2), 309-319.

Buckley, J. S. (2001). Effective Wettability of Minerals Exposed to Crude Oil. Current Opinion in Colloid & Interface Science, 6(3), 191-196. https://doi.org/10.1016/S1359-0294(01)00083-8

Burdine, N., (1953). Relative Permeability Calculations from Pore Size Distribution Data. Journal of Petroleum Technology, 5(03), pp.71-78. http://dx.doi.org/10.2118/225-PA

Cai, J., & Yu, B. (2011). A Discussion of the Effect of Tortuosity on the Capillary Imbibition in Porous Media. Transport in porous media, 89 (2), 251-263. https://doi.org/10.1007/s11242-011-9767-0

Cai, J., Hu, X., Standnes, D. C., & You, L. (2012). An Analytical Model for Spontaneous Imbibition in Fractal Porous Media Including Gravity. Colloids and Surfaces A: Physicochemical and Engineering Aspects, 414, 228-233. https://doi.org/10.1016/j.colsurfa.2012.08.047

Cantisano, M.T., Restrepo, D.P., Cespedes, S., Toelke, J., Grader, A., Suhrer, M. and Walls, J., (2013). Relative Permeability in a Shale Formation in Colombia Using Digital Rock Physics. In Unconventional Resources Technology Conference. Society of Exploration Geophysicists, American Association of Petroleum Geologists, Society of Petroleum Engineers. http://dx.doi.org/10.1190/URTEC2013-092

Cao, Q., & Zhou, W. (2015). Characteristic and Controlling Factors of Organic Pores in Continental Shale Gas Reservoir of Chang 7th of Yanchang Formation, Ordos Basin. Acta Geologica Sinica-English Edition, 89(s1), 1-2. https://doi.org/10.1111/1755-6724.12302_1

Carman, P.C., (1937). Fluid Flow Through Granular Beds. Trans. Inst. Chem. Eng., 15, pp.150-166.

Carpenter, C., (2018). A Review of Improved-Oil-Recovery Methods in North American Unconventional Reservoirs. Journal of Petroleum Technology, 70(01), pp.42-44. https://doi.org/10.2118/0118-0042-JPT

Cassie, A.B.D. and Baxter, S., (1944). Wettability of Porous Surfaces. Transactions of the Faraday Society, 40, pp.546-551.

Centurion, S., Junca-Laplace, J. P., Cade, R., & Presley, G. (2014). Lessons Learned From an Eagle Ford Shale Completion Evaluation. In SPE Annual Technical Conference and Exhibition. Society of Petroleum Engineers. https://doi.org/10.2118/170827-MS

Chalmers, G. R. and Bustin, R. M. (2012). Geological Evaluation of Halfway-Doig–Montney Hybrid Gas Shale-Tight Gas Reservoir, Northeastern British Columbia. Marine and Petroleum Geology 38 (1): 53-72. http://dx.doi.org/10.1016/j.marpetgeo.2012.08.004

Chalmers, G. R., Bustin, R. M., & Power, I. M. (2012). Characterization of Gas Shale Pore Systems by Porosimetry, Pycnometry, Surface Area, and Field Emission Scanning Electron Microscopy/Transmission Electron Microscopy Image Analyses: Examples from the Barnett, Woodford, Haynesville, Marcellus, and Doig Units. AAPG bulletin, 96(6), 1099-1119. https://doi.org/10.1306/10171111052

Chandler, R., Koplik, J., Lerman, K., & Willemsen, J. F. (1982). Capillary Displacement and Percolation in Porous Media. Journal of Fluid Mechanics, 119, 249-267. https://doi.org/10.1017/S0022112082001335

Chang, Y.B., Lim, M. T., Pope, G. A., & Sepehrnoori, K. (1994). CO_2 Flow Patterns Under Multiphase Flow: Heterogeneous Field-Scale Conditions. Society of Petroleum Engineers. https://doi.org/10.2118/22654-PA

Chatzis, I., & Dullien, F. A. L. (1983). Dynamic Immiscible Displacement Mechanisms in Pore Doublets: Theory versus Experiment. Journal of Colloid and Interface Science, 91(1), 199-222. https://doi.org/10.1016/0021-9797(83)90326-0

Chenevert, M. E. (1989). Lecture: Diffusion of Water and Ions into Shales. In ISRM International Symposium. International Society for Rock Mechanics.

Chenevert, M.E., (1970). Shale Alteration by Water Adsorption. Journal of Petroleum Technology, 22(09), pp.1-141. https://doi.org/10.2118/2401-PA

Cheng, Y., (2012). Impact of Water Dynamics in Fractures on the Performance of Hydraulically Fractured Wells in Gas-shale Reservoirs. Journal of Canadian Petroleum Technology 51 (02): 143-151. https://doi.org/10.2118/127863-PA

Cherian, B. V., E. S. Stacey, R. Lewis, F. O. Iwere, R. N. Heim and S. M. Higgins (2012). Evaluating Horizontal Well Completion Effectiveness in a Field Development Program. SPE Hydraulic Fracturing Technology Conference. The Woodlands, Texas, USA, Society of Petroleum Engineers. https://doi.org/10.2118/152177-MS

Clark, A. J. (2009). Determination of Recovery Factor in the Bakken Formation, Mountrail County, ND. In SPE Annual Technical Conference and Exhibition. Society of Petroleum Engineers. https://doi.org/10.2118/133719-STU

Clarkson, C.R., Solano, N., Bustin, R.M., Bustin, A.M.M., Chalmers, G.R.L., He, L., Melnichenko, Y.B., Radliński, A.P. and Blach, T.P., (2013). Pore Structure Characterization of North American Shale Gas Reservoirs Using USANS/SANS, Gas Adsorption, and Mercury Intrusion. Fuel, 103, pp.606-616. https://doi.org/10.1016/j.fuel.2012.06.119

Crafton, J. (2015). Maximize Recovery by Minimizing Production Delays and Shut-ins. Journal of Petroleum Technology, 67(06), 32-36. https://doi.org/10.2118/0615-0032-JPT

Crafton, J. W., & Noe, S. (2013). Factors Affecting Early Well Productivity in Six Shale Plays. In SPE Annual Technical Conference and Exhibition. Society of Petroleum Engineers. https://doi.org/10.2118/166101-MS

Craig, F.F., (1971). The Reservoir Engineering Aspects of Water Flooding (Vol. 3, pp. 45-47). New York, NY: HL Doherty Memorial Fund of AIME.

Craig, V.S., Ninham, B.W. and Pashley, R.M., (1993). The Effect of Electrolytes on Bubble Coalescence in Water. The Journal of Physical Chemistry, 97(39), pp.10192-10197.

Crawford, H. R., G. H. Neill, B. J. Bucy and P. B. Crawford (1963). Carbon Dioxide - A Multipurpose Additive for Effective Well Stimulation. Journal of Petroleum Technology 15(03): 237-242. https://doi.org/10.2118/571-PA

Curtis, M. E., Ambrose, R. J., Sondergeld, C. H., & Rai, C. S. (2011). Transmission and Scanning Electron Microscopy Investigation of Pore Connectivity of Gas Shales on the Nanoscale. Society of Petroleum Engineers. https://doi.org/10.2118/144391-MS

Curtis, M. E., Sondergeld, C. H., Ambrose, R. J., & Rai, C. S. (2012). Microstructural Investigation of Gas Shales in Two and Three Dimensions Using Nanometer-Scale Resolution Imaging Microstructure of Gas Shales. AAPG bulletin, 96(4), 665-677. https://doi.org/10.1306/08151110188

Dacy, J. M. (2010). Core Tests for Relative Permeability of Unconventional Gas Reservoirs. Presented at the SPE Annual Technical Conference and Exhibition. http://dx.doi.org/10.2118/135427-MS

Dake, L.P., Fundamentals of Reservoir Engineering (1977), Elsevier Scientific Publishing Company, Amsterdam, 1977.

Danesh, A. (1998). PVT and Phase Behaviour of Petroleum Reservoir Fluids (Vol. 47). Elsevier.

Darvish, G. R., Lindeberg, E. G. B., Holt, T., Kleppe, J., & Utne, S. A. (2006). Reservoir Conditions Laboratory Experiments of CO_2 Injection into Fractured Cores. Society of Petroleum Engineers. https://doi.org/10.2118/99650-MS.

Dehghanpour, H., Lan, Q., Saeed, Y., Fei, H. and Qi, Z., (2013). Spontaneous Imbibition of Brine and Oil in Gas Shales: Effect of Water Adsorption and Resulting Microfractures. Energy & Fuels, 27(6), pp.3039-3049. http:// dx.doi.org/10.1021/ef4002814

Dehghanpour, H., Xu, M. and Habibi, A., (2015). Wettability of Gas Shale Reservoirs. Fundamentals of Gas Shale Reservoirs, pp.341-359. https://doi.org/10.1002/9781119039228.ch16

Dehghanpour, H., Zubair, H.A., Chhabra, A. and Ullah, A., (2012). Liquid Intake of Organic Shales. Energy & Fuels, 26(9), pp.5750-5758. https://doi.org/10.1021/ef3009794

Dernaika, M., Jallad, O.A., Koronfol, S., Suhrer, M., Teh, W.J., Walls, J., Matar, S., Murthy, N. and Zekraoui, M., (2015). Petrophysical and Fluid Flow Properties of a Tight Carbonate Source Rock Using Digital Rock Physics. Society of Exploration Geophysicists, American Association of Petroleum Geologists, Society of Petroleum Engineers. http://dx.doi.org/10.2118/172959-MS

Donaldson, E. C., Thomas, R. D., & Lorenz, P. B. (1969). Wettability Determination and Its Effect on Recovery Efficiency. Society of Petroleum Engineers. https://doi.org/10.2118/2338-PA

Drummond, C., & Israelachvili, J. (2004). Fundamental Studies of Crude Oil–surface Water Interactions and Its Relationship to Reservoir Wettability. Journal of Petroleum Science and Engineering, 45(1-2), 61-81. https://doi.org/10.1016/j.petrol.2004.04.007

Dunn, L. A., & Humenjuk, J. (2014). The Duvernay Formation: Integrating Sedimentology, Sequence Stratigraphy and Geophysics to Identify Sweet Spots in a Liquids-Rich Shale Play, Kaybob Alberta. Unconventional Resources Technology Conference.
https://doi.org/10.15530/URTEC-2014-1922713

Eckert, C. A., Knutson, B. L., & Debenedetti, P. G. (1996). Supercritical Fluids as Solvents for Chemical and Materials Processing. Nature, 383(6598), 313-318.
https://doi.org/10.1038/383313a0

Eide, Ø., Fernø, M. A., Alcorn, Z., & Graue, A. (2016). Visualization of Carbon Dioxide Enhanced Oil Recovery by Diffusion in Fractured Chalk. Society of Petroleum Engineers.
https://doi.org/10.2118/170920-PA

Engelder, T., Cathles, L. M., & Bryndzia, L. T. (2014). The Fate of Residual Treatment Water in Gas Shale. Journal of Unconventional Oil and Gas Resources, 7, 33-48.
https://doi.org/10.1016/j.juogr.2014.03.002

Ezulike, O.D. (2017). Complementary Workflows for Analyzing Multiphase Flowback and Post-flowback Production Data in Unconventional Reservoirs (Doctoral dissertation, University of Alberta). https://doi.org/10.7939/R3N29PM5M

Farajzadeh, R., Salimi, H., Zitha, P. L., & Bruining, H. (2007). Numerical Simulation of Density-driven Natural Convection in Porous Media with Application for CO_2 Injection Projects. International Journal of Heat and Mass Transfer, 50(25), 5054-5064. https://doi.org/10.1016/j.ijheatmasstransfer.2007.08.019

Fathi, E., Tinni, A., & Akkutlu, I. Y. (2012). Shale Gas Correction to Klinkenberg Slip Theory. Society of Petroleum Engineers. https://doi.org/10.2118/154977-MS

Fothergill, P., Boskovic, D., Schoellkopf, N., Murphy, P., & Mukati, M. A. (2014). Regional Modelling of the Late Devonian Duvernay Formation, Western Alberta, Canada. Unconventional Resources Technology Conference. https://doi.org/10.15530/URTEC-2014-1923935

Frantz, J. K. and Jochen, V. (2005). Shale Gas, Schlumberger shale gas white paper. Marketing Communications.

Freeman, M.J., (2012). Lithological, Diagenetic, and Organic Controls on Reservoir Quality in the Lower Triasic Montney Formation, Pouce Coupe, Alberta.

Friedrich, J. P., List, G. R., & Heakin, A. J. (1982). Petroleum-free Extraction of Oil from Soybeans with Supercritical CO_2. Journal of the American Oil Chemists' Society, 59(7), 288-292. https://doi.org/10.1007/BF02662228

Gamadi, T. D., Sheng, J. J., Soliman, M. Y., Menouar, H., Watson, M. C., & Emadibaladehi, H. (2014). An Experimental Study of Cyclic CO_2 Injection to Improve Shale Oil Recovery. Society of Petroleum Engineers. https://doi.org/10.2118/169142-MS

Gardner, J. W., F. M. Orr and P. D. Patel (1981). The Effect of Phase Behavior on CO_2-flood Displacement Efficiency. Journal of Petroleum Technology 33(11): 2067-2081. https://doi.org/10.2118/8367-PA

Ghanbari, E. and Dehghanpour, H., (2015). Impact of Rock Fabric on Water Imbibition and Salt Diffusion in Gas Shales. International Journal of Coal Geology, 138, pp.55-67. https://doi.org/10.1016/j.coal.2014.11.003

Ghanbari, E. and Dehghanpour, H., (2016). The Fate of Fracturing Water: A Field and Simulation Study. Fuel, 163, pp.282-294. https://doi.org/10.1016/j.fuel.2015.09.040

Ghanbari, E., Abbasi, M. A., Dehghanpour, H., & Bearinger, D. (2013). Flowback Volumetric and Chemical Analysis for Evaluating Load Recovery and Its Impact on Early-Time Production. Society of Petroleum Engineers. https://doi.org/10.2118/167165-MS

Ghasemi, M., Astutik, W., Alavian, S. A., Whitson, C. H., Sigalas, L., Olsen, D., & Suicmez, V. S. (2017). Determining Diffusion Coefficients for Carbon Dioxide Injection in Oil-Saturated Chalk by Use of a Constant-Volume-Diffusion Method. Society of Petroleum Engineers. https://doi.org/10.2118/179550-PA

Gonzalez, J., Lewis, R., Hemingway, J., Grau, J., Rylander, E. and Pirie, I., (2013). Determination of Formation Organic Carbon Content Using a New Neutron-Induced Gamma Ray Spectroscopy Service that Directly Measures Carbon. In Unconventional Resources Technology Conference (pp. 1100-1109). http://dx.doi.org/10.1190/URTEC2013-112

Graham, J. W. (1958). Reverse-Wetting Logging. Society of Petroleum Engineers.

Gruener, S., Hermes, H.E., Schillinger, B., Egelhaaf, S.U. and Huber, P., (2016). Capillary Rise Dynamics of Liquid Hydrocarbons in Mesoporous Silica as Explored By Gravimetry, Optical and Neutron Imaging: Nano-Rheology and Determination of Pore Size Distributions from the Shape of Imbibition Fronts. Colloids and Surfaces A: Physicochemical and Engineering Aspects, 496, pp.13-27. https://doi.org/10.1016/j.colsurfa.2015.09.055

Gruener, S., Sadjadi, Z., Hermes, H.E., Kityk, A.V., Knorr, K., Egelhaaf, S.U., Rieger, H. and Huber, P., (2012). Anomalous Front Broadening During Spontaneous Imbibition in a Matrix with Elongated Pores. Proceedings of the National Academy of Sciences, 109(26), pp.10245-10250. https://doi.org/10.1073/pnas.1119352109

Gupta, I., Jernigen, J., Curtis, M., Rai, C., & Sondergeld, C. (2018). Water-Wet or Oil-Wet: is it Really That Simple in Shales? (SPWLA-2018-v59n3a2). Petrophysics, 59(03), 308-317.

Habibi, A., Dehghanpour, H., Binazadeh, M., Bryan, D. and Uswak, G., (2016). Advances in Understanding Wettability of Tight Oil Formations: A Montney Case Study. SPE Reservoir Evaluation & Engineering, 19(04), pp.583-603. http://dx.doi.org/10.2118/175157-PA

Habibi, A., Yassin, M.R., Dehghanpour, H., and Bryan, D. (2017). Experimental Investigation of CO_2-oil Interactions in Tight Rocks: A Montney Case Study. Fuel 203: 853-867. https://doi.org/10.1016/j.fuel.2017.04.077

Han, L. and Y. Gu (2014). Optimization of Miscible CO_2 Water-Alternating-Gas Injection in the Bakken Formation. Energy & Fuels 28(11): 6811-6819. https://doi.org/10.1021/ef501547x

Handwerger, D. A., Keller, J., & Vaughn, K. (2011). Improved Petrophysical Core Measurements on Tight Shale Reservoirs Using Retort and Crushed Samples. Society of Petroleum Engineers. https://doi.org/10.2118/147456-MS

Handwerger, D. A., Willberg, D. M., Pagels, M., Rowland, B., & Keller, J. (2012). Reconciling Retort versus Dean Stark Measurements on Tight Shales. Society of Petroleum Engineers. https://doi.org/10.2118/159976-MS

Handy, L. L. (1960). Determination of Effective Capillary Pressures for Porous Media from Imbibition Data (SPE-1361-G). Society of Petroleum Engineers.

Hawthorne, S. B. (1990). Analytical-Scale Supercritical Fluid Extraction. Analytical Chemistry, 62(11), 633A-642A. https://doi.org/10.1021/ac00210a001

Hawthorne, S. B., D. J. Miller, L. Jin and C. D. Gorecki (2016). Rapid and Simple Capillary-Rise/Vanishing Interfacial Tension Method To Determine Crude Oil Minimum Miscibility Pressure: Pure and Mixed CO_2, Methane, and Ethane. Energy & Fuels 30(8): 6365-6372. https://doi.org/10.1021/acs.energyfuels.6b01151

Hawthorne, S. B., Gorecki, C. D., Sorensen, J. A., Miller, D. J., Harju, J. A., & Melzer, L. S. (2014). Hydrocarbon Mobilization Mechanisms Using CO_2 in an Unconventional Oil Play. Energy Procedia, 63, 7717-7723.

Hawthorne, S. B., Gorecki, C. D., Sorensen, J. A., Steadman, E. N., Harju, J. A., & Melzer, S. (2013). Hydrocarbon Mobilization Mechanisms from Upper, Middle, and Lower Bakken Reservoir Rocks Exposed to CO_2. Society of Petroleum Engineers. https://doi.org/10.2118/167200-MS

Hensen, E. J., & Smit, B. (2002). Why Clays Swell. The Journal of Physical Chemistry B, 106(49), 12664-12667. https://doi.org/10.1021/jp0264883

Hetényi, M. (1998). Oxygen Index as an Indicator of Early Organic Maturity. Organic geochemistry, 29(1-3), 63-77. https://doi.org/10.1016/S0146-6380(98)00060-6

Hoffman, B. T. (2012). Comparison of Various Gases for Enhanced Recovery from Shale Oil Reservoirs. SPE Improved Oil Recovery Symposium. Tulsa, Oklahoma, USA, Society of Petroleum Engineers. https://doi.org/10.2118/154329-MS

Holm, L. W. and V. A. Josendal (1974). Mechanisms of Oil Displacement By Carbon Dioxide. Journal of Petroleum Technology 26(12): 1427-1438. https://doi.org/10.2118/4736-PA

Holm, L. W. and V. A. Josendal (1982). Effect of Oil Composition on Miscible-Type Displacement by Carbon Dioxide. Society of Petroleum Engineers Journal 22(01): 87-98. https://doi.org/10.2118/8814-PA

Holmberg, K., Shah, D. O., & Schwuger, M. J. (2002). Handbook of Applied Surface and Colloid Chemistry (Vol. 1). John Wiley & Sons.

Honarpour, M. M., Koederitz, F., and Herbert, A. (1986). Relative Permeability of Petroleum Reservoirs. Boca Raton, Florida: CRC Press.

http://www.cspg.org/cspg/documents

https://info.drillinginfo.com/

https://www.csur.com/

https://www.eia.gov/

https://www.elarasystems.com/may-2018-hydraulic-fracturing/

https://www.rockstone-research.com

Hu, Y., Devegowda, D. and Sigal, R., (2016). A Microscopic Characterization of Wettability in Shale Kerogen with Varying Maturity Levels. Journal of Natural Gas Science and Engineering, 33, pp.1078-1086. https://doi.org/10.1016/j.jngse.2016.06.014

Hu, Y., Devegowda, D., & Sigal, R. F. (2014). Impact of Maturity on Kerogen Pore Wettability: A Modeling Study. Society of Petroleum Engineers. https://doi.org/10.2118/170915-MS

Hunt, J.M. (1979) Petroleum Geochemistry and Geology. W.H. Freeman and Company, San Francisco.

Huo, P., Zhang, D., Yang, Z., Li, W., Zhang, J., & Jia, S. (2017). CO_2 Geological Sequestration: Displacement Behavior of Shale Gas Methane by Carbon Dioxide Injection. International Journal of Greenhouse Gas Control, 66, 48-59. https://doi.org/10.1016/j.ijggc.2017.09.001

Jamin, J. M. (1860). Memoir on Equilibrium and Movement of Liquids in Porous Substances. Compt. Rend 50: 172–176.

Jarvie, D. M. (2014). Components and Processes Affecting Producibility and Commerciality of Shale Resource Systems. Geologica Acta, 12(4), 307-325.

Jarvie, D.M., (2012). Shale Resource Systems for Oil and Gas: Part 2-Shale-Oil Resource Systems.

Johnson, R. E., and R. H. Dettre (1969). Wettability and Contact Angles. Surface and Colloid Science: 85-153.

Kale, S. V., Rai, C. S., & Sondergeld, C. H. (2010). Petrophysical Characterization of Barnett Shale. Society of Petroleum Engineers. http://dx.doi.org/10.2118/131770-MS

Keneti, A., & Wong, R. C. K. (2010). Investigation of Anisotropic Behavior of Montney Shale under Indirect Tensile Strength Test. Society of Petroleum Engineers. https://doi.org/10.2118/138104-MS

Khlaifat, A. L., Qutob, H., & Barakat, N. (2011). Tight Gas Sands Development is Critical to Future World Energy Resources. Society of Petroleum Engineers. https://doi.org/10.2118/142049-MS

Khosrokhavar, R. (2016). Visualization and Numerical Investigation of Natural Convection Flow of CO_2 in Aqueous and Oleic Systems. In Mechanisms for CO_2 Sequestration in Geological Formations and Enhanced Gas Recovery (pp. 7-31). Springer International Publishing. https://doi.org/10.1007/978-3-319-23087-0_2

Khosrokhavar, R., Elsinga, G., Farajzadeh, R., & Bruining, H. (2014). Visualization and Investigation of Natural Convection Flow of CO_2 in Aqueous and Oleic Systems. Journal of Petroleum Science and Engineering, 122, 230-239. https://doi.org/10.1016/j.petrol.2014.07.016

Kibria, M. G., Hu, Q., Liu, H., Zhang, Y., & Kang, J. (2018). Pore Structure, Wettability, and Spontaneous Imbibition of Woodford Shale, Permian Basin, West Texas. Marine and Petroleum Geology, 91, 735-748. https://doi.org/10.1016/j.marpetgeo.2018.02.001

Kimbrel, E. H., Herring, A. L., Armstrong, R. T., Lunati, I., Bay, B. K., & Wildenschild, D. (2015). Experimental Characterization of Nonwetting Phase Trapping and Implications for Geologic CO_2 Sequestration. International Journal of Greenhouse Gas Control, 42, 1-15. https://doi.org/10.1016/j.ijggc.2015.07.011

Klaver, J., Desbois, G., Urai, J. L., & Littke, R. (2012). BIB-SEM Study of the Pore Space Morphology in Early Mature Posidonia Shale from the Hils Area, Germany. International Journal of Coal Geology, 103, 12-25. https://doi.org/10.1016/j.coal.2012.06.012

Klins, M. A. (1983). Carbon Dioxide Flooding: Basic Mechanism and Project Design Boston, USA, International Human Resources Development Corporation.

Krohn, C. E. (1988). Fractal Measurements of Sandstones, Shales, and Carbonates. Journal of Geophysical Research: Solid Earth, 93(B4), 3297-3305. https://doi.org/10.1029/JB093iB04p03297

Kuila, U., & Prasad, M. (2013). Specific Surface Area and Pore-size Distribution in Clays and Shales. Geophysical Prospecting, 61(2), 341-362. https://doi.org/10.1111/1365-2478.12028

Labani, M. M., Rezaee, R., Saeedi, A., & Al Hinai, A. (2013). Evaluation of Pore Size Spectrum of Gas Shale Reservoirs Using Low Pressure Nitrogen Adsorption, Gas Expansion and Mercury Porosimetry: A Case Study from the Perth and Canning Basins, Western Australia. Journal of Petroleum Science and Engineering, 112, 7-16. https://doi.org/10.1016/j.petrol.2013.11.022

Lafargue, E., Marquis, F., & Pillot, D. (1998). Rock-Eval 6 Applications in Hydrocarbon Exploration, Production, and Soil Contamination Studies. Revue de L'institut Français du Pétrole, 53(4), 421-437. https://doi.org/10.2516/ogst:1998036

Lan, Q., Dehghanpour, H., Wood, J. and Sanei, H., (2015a). Wettability of the Montney Tight Gas Formation. SPE Reservoir Evaluation & Engineering, 18(03), pp.417-431. http://dx.doi.org/10.2118/171620-PA

Lan, Q., Xu, M., Binazadeh, M., Dehghanpour, H., & Wood, J. M. (2015b). A Comparative Investigation of Shale Wettability: The Significance of Pore Connectivity. Journal of Natural Gas Science and Engineering, 27, 1174-1188. https://doi.org/10.1016/j.jngse.2015.09.064

Lan, Q., Xu, M., Dehghanpour, H., & Wood, J. (2014). Advances in Understanding Wettability of Tight and Shale Gas Formations. Society of Petroleum Engineers.
https://doi.org/10.2118/170969-MS

Lansangan, R. M., & Smith, J. L. (1993). Viscosity, Density, and Composition Measurements of CO_2/West Texas Oil Systems. Society of Petroleum Engineers.
https://doi.org/10.2118/21017-PA

Laplace, P. S. (1805). Traite de Mechanique Celeste (Gauthier-Villars, Paris), Vol. 4, Supplements au Livre X.

Law, B. E., & Curtis, J. B. (2002). Introduction to Unconventional Petroleum Systems. AAPG bulletin, 86(11), 1851-1852.

Law, B.E., (2002). Basin-centered Gas Systems. AAPG bulletin, 86(11), pp.1891-1919. https://doi.org/10.1306/61EEDDB4-173E-11D7-8645000102C1865D

Law, C.A., (1999). Chapter 6: Evaluating Source Rocks. Treatise of Petroleum Geology/Handbook of Petroleum Geology: Exploring for Oil and Gas Traps.

Lenormand, R. Capillary Pressure and Pore Size Distribution from Water Injection: A Feasibility Study. SCA2012-41 Presented at the International Symposium of The Society Of Core Analysis Held in Aberdeen, Scotland, UK, 27-30 August, 2012.

Li, B., Mehmani, A., Chen, J., Georgi, D.T. and Jin, G., (2013). The Condition of Capillary Condensation and Its Effects on Adsorption Isotherms of Unconventional Gas Condensate Reservoirs. In SPE Annual Technical Conference and Exhibition. Society of Petroleum Engineers.
https://doi.org/10.2118/166162-MS

Li, H., S. Zheng and D. Yang (2013). Enhanced Swelling Effect and Viscosity Reduction of Solvent(s)/CO_2/Heavy-Oil Systems. SPE Journal 18(04): 695-707.
https://doi.org/10.2118/150168-PA

Li, K. and Horne, R.N., (2006). Comparison of Methods to Calculate Relative Permeability from Capillary Pressure in Consolidated Water-wet Porous Media. Water Resources Research, 42(6). https://doi.org/10.1029/2005WR004482

Li, K., & Zhao, H. (2012). Fractal Prediction Model of Spontaneous Imbibition Rate. Transport in Porous Media, 91(2), 363-376. https://doi.org/10.1007/s11242-011-9848-0

Li, L., Khorsandi, S., Johns, R. T., & Dilmore, R. M. (2015). CO_2 Enhanced Oil Recovery and Storage Using a Gravity-enhanced Process. International Journal of Greenhouse Gas Control, 42, 502-515. https://doi.org/10.1016/j.ijggc.2015.09.006

Liu, G., J. A. Sorensen, J. R. Braunberger, R. Klenner, J. Ge, C. D. Gorecki, E. N. Steadman and J. A. Harju (2014). CO_2-Based Enhanced Oil Recovery from Unconventional Reservoirs: A Case Study of the Bakken Formation. SPE Unconventional Resources Conference. https://doi.org/10.2118/168979-MS

Loucks, R. G., Reed, R. M., Ruppel, S. C., & Jarvie, D. M. (2009). Morphology, Genesis, and Distribution of Nanometer-scale Pores in Siliceous Mudstones of the Mississippian Barnett Shale. Journal of sedimentary research, 79(12), 848-861. https://doi.org/10.2110/jsr.2009.092

Low, W.S., (2012). The New Millennium Gold Rush. Duvernay Shale, BMO Capital Markets.

Lucas, R. (1918). Rate of Capillary Ascension of Liquids, Kolloid Z, 23, 15-22

Makhanov, K., Habibi, A., Dehghanpour, H. and Kuru, E., (2014). Liquid Uptake of Gas Shales: A Workflow to Estimate Water Loss During Shut-in Periods After Fracturing Operations. Journal of Unconventional Oil and Gas Resources, 7, pp.22-32. https://doi.org/10.1016/j.juogr.2014.04.001

Mandelbrot, B. (1967). How Long is the Coast Of Britain? Statistical Self-similarity and Fractional Dimension. Science, 156 (3775), 636-638. https://doi.org/10.1126/science.156.3775.636

Mandelbrot, B.B., Pignoni, R. (1983). The Fractal Geometry of Nature, WH freeman New York.

Meng, X., & Sheng, J. J. (2016). Experimental Study on Revaporization Mechanism of Huff-n-Puff Gas Injection to Enhance Condensate Recovery in Shale Gas Condensate Reservoirs. Society of Petroleum Engineers. https://doi.org/10.2118/179537-MS

Metcalfe, R. S. and L. Yarborough (1979). The Effect of Phase Equilibria on the CO_2 Displacement Mechanism. Society of Petroleum Engineers Journal 19(04): 242-252. https://doi.org/10.2118/7061-PA

Mirchi, V., Saraji, S., Goual, L., & Piri, M. (2015). Dynamic Interfacial Tension and Wettability of Shale in the Presence Of Surfactants at Reservoir Conditions. Fuel, 148, 127-138. https://doi.org/10.1016/j.fuel.2015.01.077

Mitchell, A. G., Hazell, L. B., & Webb, K. J. (1990). Wettability Determination: Pore Surface Analysis. In SPE Annual Technical Conference and Exhibition. Society of Petroleum Engineers. https://doi.org/10.2118/20505-MS

Montgomery, C. T., & Smith, M. B. (2010). Hydraulic Fracturing: History of an Enduring Technology. Society of Petroleum Engineers. https://doi.org/10.2118/1210-0026-JPT

Montgomery, C., (2013). Fracturing fluids. In ISRM International Conference for Effective and Sustainable Hydraulic Fracturing. International Society for Rock Mechanics.

Morrow, N. R. (1987). A Review of the Effects of Initial Saturation, Pore Structure and Wettability on Oil Recovery by Water flooding.

Morrow, N. R. (1990). Wettability and Its Effect on Oil Recovery. Society of Petroleum Engineers. https://doi.org/10.2118/21621-PA

Mungan, N., & Moore, E. J. (1968). Certain Wettability Effects on Electrical Resistivity in Porous Media. Journal of Canadian Petroleum Technology, 7(01), 20-25.

Munson, E. O. (2015). Reservoir Characterization of the Duvernay Formation, Alberta: A Pore-to Basin-scale Investigation (Doctoral Dissertation, University of British Columbia). https://doi.org/10.14288/1.0166722

Nasralla, R. A., & Nasr-El-Din, H. A. (2014). Double-layer Expansion: Is it a Primary Mechanism of Improved Oil Recovery by Low-salinity Water Flooding? SPE Reservoir Evaluation & Engineering, 17(01), 49-59. https://doi.org/10.2118/154334-PA

National Institute of Standards and Technology (NIST); http://webbook.nist.gov/chemistry/fluid/.

Neog, A., & Schechter, D. S. (2016). Investigation of Surfactant Induced Wettability Alteration in Wolfcamp Shale for Hydraulic Fracturing and EOR Applications. SPE Improved Oil Recovery Conference. Tulsa, Oklahoma, USA: Society of Petroleum Engineers. http://dx.doi.org/10.2118/179600-MS

Neuzil, C. E. (2000). Osmotic Generation of 'Anomalous' Fluid Pressures in Geological Environments. Nature, 403(6766), 182. https://doi.org/10.1038/35003174

Nghiem, L. X., & Sammon, P. H. (1997). A Non-Equilibrium Equation-of-State Compositional Simulator. Society of Petroleum Engineers. https://doi.org/10.2118/37980-MS

Nguyen, D., Wang, D., Oladapo, A., Zhang, J., Sickorez, J., Butler, R., & Mueller, B. (2014). Evaluation of Surfactants for Oil Recovery Potential in Shale Reservoirs. Society of Petroleum Engineers. https://doi.org/10.2118/169085-MS

Nieto, J., Bercha, R., & Chan, J. (2009). Shale Gas Petrophysics - Montney and Muskwa, Are They Barnett Look-Alikes? Society of Petrophysicists and Well-Log Analysts.

Odusina, E. O., Sondergeld, C. H., & Rai, C. S. (2011). NMR Study of Shale Wettability. Society of Petroleum Engineers. https://doi.org/10.2118/147371-MS

Orr, F. M., Jr., A. D. Yu and C. L. Lien (1981). Phase Behavior of CO_2 and Crude Oil in Low-Temperature Reservoirs. Society of Petroleum Engineers Journal 21(04): 480-492. https://doi.org/10.2118/8813-PA

Orr, F. M., Jr., R. T. Johns and B. Dindoruk (1993). Development of Miscibility in Four-Component CO_2 Floods. SPE Reservoir Engineering 8(02): 135-142. https://doi.org/10.2118/22637-PA

Panja, P., & Deo, M. (2016). Factors that Control Condensate Production from Shales: Surrogate Reservoir Models and Uncertainty Analysis. SPE Reservoir Evaluation & Engineering, 19(01), 130-141. https://doi.org/10.2118/179720-PA

Passey, Q. R., Bohacs, K., Esch, W. L., Klimentidis, R., & Sinha, S. (2010). From Oil-Prone Source Rock to Gas-Producing Shale Reservoir - Geologic and Petrophysical Characterization of Unconventional Shale Gas Reservoirs. Society of Petroleum Engineers. https://doi.org/10.2118/131350-MS

Peck, W.D., Azzolina, N.A., Ge, J., Bosshart, N.W., Burton-Kelly, M.E., Gorecki, C.D., Gorz, A.J., Ayash, S.C., Nakles, D.V. and Melzer, L.S., (2018). Quantifying CO_2 Storage Efficiency Factors in Hydrocarbon Reservoirs: A Detailed Look at CO_2 Enhanced Oil Recovery. International Journal of Greenhouse Gas Control, 69, pp.41-51. https://doi.org/10.1016/j.ijggc.2017.12.005

Peng, S., Zhang, T., Ellis, G. S., & Lewan, M. D. (2015). Variation of Wettability of Organic-Rich Shales With Thermal Maturity and the Implications for Oil and Gas Distributions. In AAPG Annual Convention and Exhibition.

Peters, E. (2012). Advanced Petrophysics: Volume 2: Dispersion, Interfacial Phenomena/Wettability, Capillarity/Capillary Pressure, Relative Permeability. Greenleaf Book Group.

Poiseuille, J. L. (1844). Recherches Expérimentales sur le Mouvement des Liquides Dans les Tubes de Très-Petits Diamètres. Imprimerie Royale.

Pu, W., B. Wei, F. Jin, Y. Li, H. Jia, P. Liu and Z. Tang (2016). Experimental Investigation of CO_2 Huff-n-Puff Process for Enhancing Oil Recovery in Tight Reservoirs. Chemical Engineering Research and Design 111: 269-276. https://doi.org/10.1016/j.cherd.2016.05.012

Purcell, W. R. (1949). Capillary Pressures - Their Measurement Using Mercury and the Calculation of Permeability Therefrom. Society of Petroleum Engineers. https://doi.org/10.2118/949039-G

Ransohoff, T. C., Gauglitz, P. A., & Radke, C. J. (1987). Snap-Off of Gas Bubbles in Smoothly Constricted Noncircular Capillaries. AIChE Journal, 33(5), 753-765. https://doi.org/10.1002/aic.690330508

Reisberg, J. and Doscher, T.M., (1956). Interfacial Phenomena in Crude Oil-Water Systems. Producers monthly, 21(1), pp.43-50.

Rongy, L., Haugen, K. B., & Firoozabadi, A. (2012). Mixing from Fickian Diffusion and Natural Convection in Binary Non-equilibrium Fluid Phases. AIChE journal, 58(5), 1336-1345. https://doi.org/10.1002/aic.12685

Roshan, H., Al-Yaseri, A. Z., Sarmadivaleh, M., & Iglauer, S. (2016). On Wettability of Shale Rocks. Journal of Colloid and Interface Science, 475, 104-111. https://doi.org/10.1016/j.jcis.2016.04.041

Rostami, B., Pourafshary, P., Fathollahi, A., Yassin, M.R., Hassani, K., Khosravi, M., Mohammadifard, M. and Dangkooban, A., (2017). A New Approach to Characterize the Performance of Heavy Oil Recovery Due to Various Gas Injection. International Journal of Multiphase Flow. https://doi.org/10.1016/j.ijmultiphaseflow.2017.10.014

Sadjadi, Z., & Rieger, H. (2013). Scaling Theory for Spontaneous Imbibition in Random Networks of Elongated Pores. Physical review letters, 110(14), 144502. https://doi.org/10.1103/PhysRevLett.110.144502

Sanei, H., Wood, J.M., Ardakani, O.H., Clarkson, C.R. and Jiang, C., (2015). Characterization of Organic Matter Fractions in an Unconventional Tight Gas Siltstone Reservoir. International Journal of Coal Geology, 150, pp.296-305. https://doi.org/10.1016/j.coal.2015.04.004

Schön, J., (2011). Physical Properties of Rocks: A Workbook. vol. 8 (Elsevier).

Sharma, M.M. and Wunderlich, R.W., (1987). The Alteration of Rock Properties Due to Interactions with Drilling-Fluid Components. Journal of Petroleum Science and Engineering, 1(2), pp.127-143. https://doi.org/10.1016/0920-4105(87)90004-0

Sheng, J., Sheng, J. J., & Li, L. (2016). A Comparison Study on Huff-n-Puff Gas Injection and Chemical Relative Permeability Modification to Mitigate Condensate Blocking in Fractured Shale Gas Condensate Reservoirs. Society of Petroleum Engineers. https://doi.org/10.2118/180201-MS

Shi, Y., Yassin, M. R., & Dehghanpour, H. (2018). A Modified Model for Spontaneous Imbibition of Wetting Phase into Fractal Porous Media. Colloids and Surfaces A: Physicochemical and Engineering Aspects, 543, 64-75. https://doi.org/10.1016/j.colsurfa.2017.12.052

Shi, Y., Yassin, M.R., Yuan, L. and Dehghanpour, H., (2019). Modelling Imbibition Data for Determining Size Distribution of Organic and Inorganic Pores in Unconventional Rocks. International Journal of Coal Geology, 201, pp.26-43. https://doi.org/10.1016/j.coal.2018.11.010

Shouxiang, M., Morrow, N.R. and Zhang, X., (1997). Generalized Scaling of Spontaneous Imbibition Data for Strongly Water-Wet Systems. Journal of Petroleum Science and Engineering, 18(3-4), pp.165-178. https://doi.org/10.1016/S0920-4105(97)00020-X

Siddiqui, M.A.Q., Ali, S., Fei, H. and Roshan, H., (2018). Current understanding of shale wettability: A review on contact angle measurements. Earth-Science Reviews. https://doi.org/10.1016/j.earscirev.2018.04.002

Silva, M. K. and F. M. Orr, Jr. (1987). Effect of Oil Composition on Minimum Miscibility Pressure-Part 1: Solubility of Hydrocarbons in Dense CO_2. SPE Reservoir Engineering 2(04): 468-478. https://doi.org/10.2118/14149-PA

Stark, P., Chew, K., & Jackson, P. (2008). Importance of Unconventional Oil Resources in Shaping the Far East Energy Future. International Petroleum Technology Conference. https://doi.org/10.2523/IPTC-12743-MS

Stoakes, F. A. (1980). Nature and Control of Shale Basin Fill and Its Effect on Reef Growth and Termination: Upper Devonian Duvernay and Ireton Formations of Alberta, Canada. Bulletin of Canadian Petroleum Geology, 28(3), 345-410.

Sulucarnain, I.D., Sondergeld, C.H. and Rai, C.S., (2012). An NMR Study of Shale Wettability and Effective Surface Relaxivity. In SPE Canadian Unconventional Resources Conference. Society of Petroleum Engineers. http://dx.doi.org/10.2118/162236-MS

Switzer, S.B., Holland, W.G., Christie, D.S., Graf, G.C., Hedinger, A.S., McAuley, R.J., Wierzbicki, R.A., Packard, J.J., Mossop, G.D. and Shetsen, I., (1994). Devonian Woodbend-Winterburn Strata of the Western Canada Sedimentary Basin. Geological Atlas of the Western Canada Sedimentary Basin: Canadian Society of Petroleum Geologists and Alberta Research Council, pp.165-202.

Takahashi, S., & Kovscek, A. R. (2010). Spontaneous Countercurrent Imbibition and Forced Displacement Characteristics of Low-permeability, Siliceous Shale Rocks. Journal of Petroleum Science and Engineering, 71(1-2), 47-55. https://doi.org/10.1016/j.petrol.2010.01.003

Tiab, D., Donaldson, E.C. and Lyczkowski, R.W., (1997). Petrophysics: Theory and Practice of Measuring Reservoir Rock and Fluid Transport Properties. Gulf Professional Publishing.

Tinni, A., Fathi, E., Agarwal, R., Sondergeld, C. H., Akkutlu, I. Y., & Rai, C. S. (2012). Shale Permeability Measurements on Plugs and Crushed Samples. Society of Petroleum Engineers. https://doi.org/10.2118/162235-MS

Tissot, B. P., & Welte, D. H. (1984). Petroleum Formation and Occurrence. New York, Tokyo: Springer-Verlag.

Treybal, R. E. (1980). Mass Transfer Operations. New York.

Tsau, J.S., L. H. Bui and G. P. Willhite (2010). Swelling/Extraction Test of a Small Sample Size for Phase Behavior Study. SPE Improved Oil Recovery Symposium. Tulsa, Oklahoma, USA, Society of Petroleum Engineers. https://doi.org/10.2118/129728-MS

Van Krevelen, D. W. (1950). Graphical-Statistical Method for the Study of Structure and Reaction Processes of Coal. Fuel, 29, 269-284.

Wang, D., Butler, R., Zhang, J., & Seright, R. (2012). Wettability Survey in Bakken Shale With Surfactant-Formulation Imbibition. Society of Petroleum Engineers. https://doi.org/10.2118/153853-PA

Wang, F.P. and Reed, R.M., (2009). Pore Networks and Fluid Flow in Gas Shales. In SPE Annual Technical Conference and Exhibition. Society of Petroleum Engineers. https://doi.org/10.2118/124253-MS

Wang, H., Lun, Z., Lv, C., Lang, D., Ji, B., Luo, M., Pan, W., Wang, R. and Gong, K., (2017). Measurement and Visualization of Tight Rock Exposed to CO_2 Using NMR Relaxometry and MRI. Scientific reports, 7, p.44354. https://doi.org/10.1038/srep44354

Wang, Q., Chen, X., Jha, A. N., & Rogers, H. (2014). Natural gas from shale Formation–The Evolution, Evidences and Challenges of Shale Gas Revolution in United States. Renewable and Sustainable Energy Reviews, 30, 1-28. https://doi.org/10.1016/j.rser.2013.08.065

Wang, S., Feng, Q., Javadpour, F., Xia, T. and Li, Z., (2015). Oil Adsorption in Shale Nanopores and Its Effect on Recoverable Oil-In-Place. International Journal of Coal Geology, 147, pp.9-24. https://doi.org/10.1016/j.coal.2015.06.002

Wang, X. and Y. Gu (2011). Oil Recovery and Permeability Reduction of a Tight Sandstone Reservoir in Immiscible and Miscible CO_2 Flooding Processes. Industrial & Engineering Chemistry Research 50(4): 2388-2399. https://doi.org/10.1021/ie1016046

Washburn, E.W. (1921). The Dynamics of Capillary Flow, Physical review, 17, 273.

Weber, G., Green, J., (1981). Guide to oil shale. National Conference of State Legislatures.

Weissenborn, P.K. and Pugh, R.J., (1996). Surface Tension of Aqueous Solutions of Electrolytes: Relationship with Ion Hydration, Oxygen Solubility, and Bubble Coalescence. Journal of colloid and interface science, 184(2), pp.550-563. https://doi.org/10.1006/jcis.1996.0651

Wenzel, R.N., (1936). Resistance of Solid Surfaces to Wetting By Water. Industrial & Engineering Chemistry, 28(8), pp.988-994.

Whitson, C. H., & Brulé, M. R. (2000). Phase Behavior. Richardson, TX: Henry L. Doherty Memorial Fund of AIME, Society of Petroleum Engineers.

Winsauer, W.O., Shearin Jr, H.M., Masson, P.H. and Williams, M., 1952. Resistivity of Brine-saturated Sands in Relation to Pore Geometry. AAPG bulletin, 36(2), pp.253-277.

Wood, J. (2013). Water Distribution in the Montney Tight Gas Play of the Western Canadian Sedimentary Basin: Significance for Resource Evaluation. Society of Petroleum Engineers. https://doi.org/10.2118/161824-PA

Wood, J. M. (2015). Crushed-Rock versus Full-Diameter Core Samples for Water-Saturation Determination in a Tight-Gas Siltstone Play. Society of Petroleum Engineers. https://doi.org/10.2118/174548-PA

Wood, J.M., Sanei, H., Curtis, M.E. and Clarkson, C.R., (2015). Solid Bitumen as a Determinant of Reservoir Quality in an Unconventional Tight Gas Siltstone Play. International Journal of Coal Geology, 150, pp.287-295. https://doi.org/10.1016/j.coal.2015.03.015

Wu, J., & Yu, B. (2007). A Fractal Resistance Model for Flow through Porous Media. International Journal of Heat and Mass Transfer, 50(19-20), 3925-3932. https://doi.org/10.1016/j.ijheatmasstransfer.2007.02.009

Wyllie, M. R. J. and Gardner, G. H. F. (1958). The Generalized Kozeny-Carman Equation: Its application to Problems of Multiphase Flow in Porous Media: Part 2-A Novel Approach to Problems of Fluid Flow. World Oil 146: 8–16.

Xiong, X., Devegowda, D., Michel Villazon, G. G., Sigal, R. F., & Civan, F. (2012). A Fully-Coupled Free and Adsorptive Phase Transport Model for Shale Gas Reservoirs Including Non-Darcy Flow Effects. Society of Petroleum Engineers. https://doi.org/10.2118/159758-MS

Xu, M. and Dehghanpour, H., (2014). Advances in Understanding Wettability of Gas Shales. Energy & Fuels, 28(7), pp.4362-4375. http://dx. doi.org/10.1021/ef500428y

Yassin, M. R., Begum, M., & Dehghanpour, H. (2017). Organic Shale Wettability and Its Relationship to Other Petrophysical Properties: A Duvernay Case Study, International Journal of Coal Geology, Volume 169, Pages 74-91. https://doi.org/10.1016/j.coal.2016.11.015

Yassin, M. R., Dehghanpour, H., Begum, M., & Dunn, L. (2018a). Evaluation of Imbibition Oil Recovery in the Duvernay Formation. Society of Petroleum Engineers. https://doi.org/10.2118/185065-PA

Yassin, M. R., Habibi, A., Zolfaghari, A., Eghbali, S., & Dehghanpour, H. (2018b). An Experimental Study of Nonequilibrium Carbon Dioxide/Oil Interactions. Society of Petroleum Engineers. https://doi.org/10.2118/187093-PA

Yassin, M.R., Dehghanpour, H., Wood, J. and Lan, Q., (2016). A Theory for Relative Permeability of Unconventional Rocks with Dual-wettability Pore Network. SPE Journal, 21(06), pp.1-970. http://dx. doi.org/10.2118/178549-PA

Young, T. (1805). III. An Essay on the Cohesion of Fluids. Philosophical Transactions of the Royal Society of London, 95, 65-87.

Yu, B., & Cheng, P. (2002). A Fractal Permeability Model for Bi-Dispersed Porous Media. International Journal of Heat and Mass Transfer, 45(14), 2983-2993. https://doi.org/10.1016/S0017-9310(02)00014-5

Yu, B., Cai, J., & Zou, M. (2009). On the Physical Properties of Apparent Two-Phase Fractal Porous Media. Vadose Zone Journal, 8(1), 177-186. https://doi.org/10.2136/vzj2008.0015

Yu, Y., X. Meng and J. J. Sheng (2016). Experimental and Numerical Evaluation of the Potential of Improving Oil Recovery from Shale Plugs by Nitrogen Gas Flooding. Journal of Unconventional Oil and Gas Resources 15: 56-65. https://doi.org/10.1016/j.juogr.2016.05.003

Zahid, S., Bhatti, A. A., Ahmad Khan, H., & Ahmad, T. (2007). Development of Unconventional Gas Resources: Stimulation Perspective. Society of Petroleum Engineers. https://doi.org/10.2118/107053-MS

Zhou, D., Jia, L., Kamath, J., & Kovscek, A. R. (2002). Scaling of Counter-current Imbibition Processes in Low-Permeability Porous Media. Journal of Petroleum Science and Engineering, 33(1-3), 61-74. https://doi.org/10.1016/S0920-4105(01)00176-0

Zhou, S., Yan, G., Xue, H., Guo, W., & Li, X. (2016). 2D And 3D Nanopore Characterization of Gas Shale in Longmaxi Formation Based on FIB-SEM. Marine and Petroleum Geology, 73, 174-180. https://doi.org/10.1016/j.marpetgeo.2016.02.033

Zhu, P., Balhoff, M. T., & Mohanty, K. K. (2015). Simulation of Fracture-to-Fracture Gas Injection in an Oil-Rich Shale. Society of Petroleum Engineers. https://doi.org/10.2118/175131-MS

Zhu, X., Cai, J., Liu, W. and Lu, X., (2016). Occurrence of Stable and Mobile Organic Matter in the Clay-Sized Fraction of Shale: Significance for Petroleum Geology and Carbon Cycle. International Journal of Coal Geology, 160, pp.1-10. https://doi.org/10.1016/j.coal.2016.03.011

Zolfaghari, A., Dehghanpour, H., & Holyk, J. (2017a). Water Sorption Behaviour of Gas Shales: I. Role of Clays. International Journal of Coal Geology, 179, 130-138. https://doi.org/10.1016/j.coal.2017.05.008

Zolfaghari, A., Dehghanpour, H., & Xu, M. (2017b). Water Sorption Behaviour of Gas Shales: II. Pore Size Distribution. International Journal of Coal Geology, 179, 187-195. https://doi.org/10.1016/j.coal.2017.05.009

Zubov, V. R., Indrupskiy, I. M., & Bogachev, K. Y. (2016). Compositional Simulator with Non-equilibrium Phase Transitions. Society of Petroleum Engineers. https://doi.org/10.2118/182001-MS

Zuloaga-Molero, P., Yu, W., Xu, Y., Sepehrnoori, K., & Li, B. (2016). Simulation Study of CO_2-EOR in Tight Oil Reservoirs with Complex Fracture Geometries. Scientific reports, 6, 33445. https://doi.org/10.1038/srep33445

Appendix A

Analytical Solution for Modeling Spontaneous Imbibition Process

Shi et al. (2018 and 2019) modified the imbibition model proposed by Cai et al. (2012) and developed a new analytical solution for non-piston-like imbibition of wetting phase into a fractal porous media.

The imbibition of a Newtonian fluid through a vertical capillary follows the Hagen-Poiseuille's law (Poiseuille, 1844),

$$\frac{d(L_f)}{dt} = \frac{D^2}{32\mu L_f}\left(\frac{4\sigma\cos\theta}{D} - \rho g L_s\right) \tag{A1}$$

In Eq. A1, the second term in the bracket is for the hydrostatic pressure. When hydrostatic pressure is negligible compared with capillary pressure, Eq. A1 is simplified by omitting the hydrostatic pressure term and solved by analytical integration,

$$L_s = \sqrt{\frac{D\sigma\cos\theta}{4\mu\tau^2}}\sqrt{t} \tag{A2}$$

Eq. A2 is almost the same as the Lucas-Washburn equation (Lucas, 1918; Washburn, 1921) except the tortuosity term. The imbibed mass of wetting phase can also be expressed as (Cai and Yu, 2011),

$$m = \frac{\rho\pi}{8}\sqrt{\frac{D^5\sigma\cos\theta}{\mu}}\sqrt{t} \tag{A3}$$

Based on the following equation,

$$N(\geq D) = \left(\frac{D_{max}}{D}\right)^{FD} \tag{A4}$$

The number of capillaries with diameter larger than D in the rock sample (N_f) is obtained by (Yu et al., 2009; Wu and Yu, 2007),

$$N_f(\geq D) = \frac{A_f \times \varphi'}{A_{pu}} N(\geq D) = \frac{4A_f}{\pi D_{max}^{2-FD}} \frac{2-FD}{FD} \frac{\varphi'}{1-\left(\frac{D_{min}}{D_{max}}\right)^{2-FD}} D^{-FD} \tag{A5}$$

where A_{pu} is the cross-sectional area of unit cell and A_f is the total cross-sectional area of rock sample. We name φ' as 'surface porosity', which is the ratio of pore area to cross-sectional area of rock sample. For a bundle of tortuous capillaries, φ' and effective porosity (φ) should follow,

$$\varphi = \frac{PV}{BV} = \frac{A_P \tau L_s}{A_f L_s} = \varphi' \tau \tag{A6}$$

By differentiating Eq. A5 with respect to D, we can calculate the incremental number of capillaries (n(D)) with diameters in the range of D to D + dD (Cai et al., 2012),

$$n(D) = -dN_f = \frac{4A_f}{\pi D_{max}^{2-FD}} \frac{(2-FD)\varphi'}{1-\left(\frac{D_{min}}{D_{max}}\right)^{2-FD}} D^{-(FD+1)} dD \tag{A7}$$

By multiplying the imbibed mass in a single capillary (m in Eq. A3) by Eq. A7, we can calculate the total imbibed mass of liquid in the capillaries with diameter D,

$$M(D) = m \cdot n(D) = \frac{A_f \rho}{2D_{max}^{2-FD}} \frac{(2-FD)\varphi'}{1-\left(\frac{D_{min}}{D_{max}}\right)^{2-FD}} \sqrt{\frac{\sigma \cos\theta}{\mu}} \sqrt{t} D^{1.5-FD} dD \tag{A8}$$

Eq. A8 is valid when the imbibed liquid front has not reached top of the capillary. When liquid reaches top of the capillary with diameter of D, imbibition stops and the total imbibed mass is considered as equilibrated mass,

$$m^{eq}(D) = \frac{\pi D^2}{4} \rho \tau H \tag{A9}$$

Here, m^{eq} is equilibrated mass of liquid in one capillary with diameter of D, H is the height of the rock sample, and (τH) is the actual tortuous length of the capillary. The equilibrated imbibed mass (M^{eq}) in the capillaries with diameter of D is calculated by,

$$M^{eq}(D) = m^{eq} \cdot n(D) = \frac{A_f H \varphi \rho}{D_{max}^{2-FD}} \frac{(2-FD)}{1-\left(\frac{D_{min}}{D_{max}}\right)^{2-FD}} D^{1-FD} dD \tag{A10}$$

Finally, the total imbibed mass of liquid inside all the capillaries (M_T) at time t is calculated by integrating M(D) and $M^{eq}(D)$ from D_{min} to D_{max},

$$M_T = \int_{D_{min}}^{D_C} M(D) + \int_{D_C}^{D_{max}} M^{eq}(D) \tag{A11}$$

where critical diameter D_c is the diameter of the capillaries that are just filled by liquid at time t. Based on Eq. A2, larger capillaries are filled faster than smaller capillaries. Therefore, any capillary with diameter larger than D_c already fills with liquid at time t. The total imbibed mass of liquid (M_T) can be analytically obtained by substituting Eqs. A8 and A10 into Eq. A11,

$$\begin{aligned} M_T = {} & \frac{A_f \rho}{2D_{max}^{2-FD}} \frac{\varphi'}{1-\left(\frac{D_{min}}{D_{max}}\right)^{2-FD}} \sqrt{\frac{\sigma \cos\theta}{\mu}} \left(\frac{2-FD}{2.5-FD}\right) \left[D_C^{2.5-FD} - D_{min}^{2.5-FD}\right] \sqrt{t} \\ & + \frac{A_f \rho H}{D_{max}^{2-FD}} \frac{\varphi}{1-\left(\frac{D_{min}}{D_{max}}\right)^{2-FD}} \left[D_{max}^{2-FD} - D_C^{2-FD}\right] \end{aligned} \tag{A12}$$

Eq. A12 is the final analytical equation for the non-piston-like spontaneous imbibition of wetting phase into a bundle of capillaries with considering the hydrostatic pressure.

To model brine imbibition in the dual-wet system, D, θ, φ, and φ′ are substituted by D_{inorg}, θ_{inorg}, φ_{aw}, and φ'_{aw}, respectively. Eq. A13 presents the final solution,

$$\begin{aligned} M_T = {} & \frac{A_f \rho}{2D_{max}^{2-FD}} \frac{\varphi'_{aw}}{1-\left(\frac{D_{min}}{D_{max}}\right)^{2-FD}} \sqrt{\frac{\sigma \cos\theta_{inorg}}{\mu}} \left(\frac{2-FD}{2.5-FD}\right) \left[D_C^{2.5-FD} - D_{min}^{2.5-FD}\right] \sqrt{t} \\ & + \frac{A_f \rho H}{D_{max}^{2-FD}} \frac{\varphi_{aw}}{1-\left(\frac{D_{min}}{D_{max}}\right)^{2-FD}} \left[D_{max}^{2-FD} - D_C^{2-FD}\right] \end{aligned} \tag{A13}$$

Nomenclature

A_f = Cross-sectional area of plug, L^2 [m^2]
A_p = Pore area of plug's cross-section , L^2 [m^2]
A_{pu} = Cross-sectional area of unit cell, L^2 [m^2]
BV= Bulk volume, L^3 [cm^3, m^3]
D = Pore diameter, L [m]
D_c = Critical diameter, L [m]
D_{inorg} = Inorganic pore diameter, L [m]
D_{max} = Maximum D_{inorg}, , L [m]
D_{min} = Minimum D_{inorg}, , L [m]
FD = Fractal dimension, dimensionless
g = Gravitational acceleration, Lt^{-2} [m/s^2]
H = Height of the plug, L [m]
L_f = Tortuous length of liquid column, L [m]
L_s = Straight length of liquid column, L [m]
m = Imbibed mass in a single capillary at time t, M [kg]
m^{eq} = Equilibrated m^{eq} in a single capillary, M [kg]
M^{eq} = Sum of m^{eq} in capillaries with diameter D, M [kg]
M_T = Total imbibed mass in all capillaries, M [kg]
n = Incremental number of pores
N = Total number of pores with diameter ≥ D
N_f = N in the cross section of rock sample
PV = Pore volume, L^3 [m^3]
t = Time, t [s]
θ = Liquid contact angle, degree
θ_{inorg} = Inorganic brine contact angle, degree
σ = Surface tension of brine, Mt^{-2} [N/m]
ρ = Density of brine, ML^{-3} [kg/m^3]
τ = Tortuosity, dimensionless
μ = Viscosity of brine, $ML^{-1}t^{-1}$ [pa.s]
φ = Effective porosity, L^3/L^3 [%BV]
φ′ = Surface porosity, L^2/L^2
φ_{aw} = Brine porosity, L^3/L^3 [%BV]
φ'_{aw} = Brine surface porosity, L^2/L^2